Islamic Azad University
Majlesi Branch

International Journal of

ADVANCED DESIGN AND MANUFACTURING TECHNOLOGY

Vol. 16, No. 1, March 2023

SUBSCRIPTION FORM

Please enter my annual subscription to the International Quarterly, Journal of Advanced Design and Manufacturing Technology (ADMT), including 4 quarterly issues for the year……Volume……Numbers……

	Internal	***International***
⌗ Institutional	R 600000	€ 400
⌗ Personal	R 400000	€ 300
⌗ Student	R 300000	€ 200
⌗ Single copy	R 100000	€ 80

Name: ***Tel:*** ***Email:***

Mailing Address:

Payment method: Check or money order must be made to order of:
Iran: Account# 0103249224008 CIBA, Melli Bank of Iran
In the Name of: Islamic Azad University, Majlesi Branch

* Please allow 3-5 weeks for delivery Bank order enclosed

stamp

To:
An International Quarterly, Journal of Advanced Design and Manufacturing Technology
Islamic Azad University Majlesi Branch , Esfahan ,IRAN
Mailbox : 84815/119
Tel: (+98) 31 52472907
Tel: (+98) 31 52472290, Ext : 312
Fax: (+98) 31 52472294

CONTENTS

Volume16, No.1, March 2023

This journal has the permission number 87/5265 from Research Deputy of Islamic Azad University.

COPYRIGHT RELEASE

Title of Manuscript:

AUTHOR(S):

I (we) hereby assign and transfer all copyrights in and to the manuscript named above, in all forms and media of expression now known or later developed, to the effective if and when it is accepted for publication in the International Quarterly, ***Journal of Advanced Design and Manufacturing Technology (ADMT)*** by the Islamic Azad University Majlesi Branch.

I (we) also confirm that the manuscript is not in the public domain and is original on my (our) part except for such excerpts copyrighted works as may be included with the written permission of the copyright owners. I (we) further warrant that the manuscript contains no libelous, obscene, or unlawful statements and does not infringe upon or violate any copyright, trademark, or other right or the privacy of others. I (we) warrant that, in the case of sole authorship, that I am (we are) the sole owner of the manuscript and all copyrights therein and have full power and authority to register all copyrights therein and to make this agreement, and that, in the case of multiple authorship, these powers of ownership are shared with all other contributing authors. I (we) acknowledge that the International Journal of Design and Manufacturing Technology (ADMT) is relying on this release in publishing this manuscript in the Journal.

Regarding with the conflicts of interest, submitted manuscript must be accompanied with a statement form the authors disclosing all financial and personnel relationship that might bias their work, if any. Besides, the authors are requested to evident whether impending conflicts do or do not exist. This should cover the proclamation and if there are further details, could be mentioned in the copyright. If an organization encompasses any financial interest in the outcome of the study, the authors are appealed to provide a declaration that have full access to all the data in the study and take complete responsibility for the integrity of the data and the accuracy of the data analysis.

All authors are requested to sign this form upon acceptance of manuscript and fax in to the Editorial Office. It is preferable to be scanned and then submitted through the Journal email.

(1)Author Signature	Print name	Data
(2)Author Signature	Print name	Data
(3)Author Signature	Print name	Data
(4)Author Signature	Print name	Data
(5)Author Signature	Print name	Data
The corresponding Author signature	Print name	Data

The sole responsibility for the whole content(s) of article (views and statements) remains only with the author (s).

PLEASE NOTE: Manuscripts cannot be processed for publication until the publisher has received this signed form. If the manuscript is not published in the Journal, this release will not take effect.

RETURN TO: Editorial Office,
International Journal of Design and Manufacturing Technology (ADMT),
Department of Mechanical Engineering, IAU, Majlesi Branch, Isfahan, Iran
Mail Box: 86315/111

http://Admt.isfahan.iau.ir
Email: Journalmechanic@gmail.com

Int. J. Advanced Design and Manufacturing Technology, 2023, Vol. 16, No. 1, pp. 1-11

DOI: 10.30486/ADMT.2022.1939798.1313 ISSN: 2252-0406 https://admt.isfahan.iau.ir

Effect of Adding a Styrene-Butadiene Rubber Damper to A Sled Sample and Extraction of Its Equivalent Stiffness and Damping

Mohammad Reza Najafi [1]
Department of Mechanical Engineering,
University of Imam Hossein comprehensive, Iran
E-mail: drmrnajafi@ihu.ac.ir

Saeed Mahjoub Moghadas [2, *]
Department of Mechanical Engineering,
University of Imam Hossein comprehensive, Iran
E-mail: smahjoubmoghadas@ihu.ac.ir
*Corresponding author

Received: 7 September 2021, Revised: 20 November 2021, Accepted: 26 November 2021

Abstract: Protection of sled systems from destructive vibrations is inevitably under attraction due to the importance of sled testing in the aerospace industry. A pair of SBR dampers were used between the slipper and the sled body to reduce vertical vibrations, so a design of the sled model was studied. Both equivalent stiffness and equivalent damping of the sled system were obtained to reduce the transmission of vibrations from slippers to the body. A combination of analytical, numerical and experimental test methods was utilized and the results were validated. The stiffness values of 370500 and 391000 N⁄m were obtained from numerical and experimental measurements, respectively. Finally, by designing the sled model, first and second natural frequencies of 12.49 and 19.56 Hz and mode shapes of the sled system were obtained. The results show that the dampers used in the sled have an important role in reducing the transmission of vibrations to the sled body by withstanding the tension and pressure on the slippers.

Keywords: Damper, Equivalent Stiffness, Equivalent Damping, Natural Frequency, Sled Test

Biographical notes: Mohammad Reza Najafi received his Ph.D. in Mechanical Engineering from Imam Hossein comprehensive University, Iran in 2022. His current research interests include vibration and dynamics. **Saeed Mahjoub Moghadas** is an Associate Professor of Mechanical Engineering at Imam Hossein comprehensive University since 1986, Iran. He has received a doctorate with the thesis subject to “Internal Combustion Engines Control and Diagnostics through Instantaneous Speed of Rotation Analysis” at L'ensam university in Paris, France, in 1985. He has authored 20 books and translated 15 others in the field of dynamic, vibration, and control.

Research paper

1 INTRODUCTION

Today, several tests in the aerospace industry are designed and performed using a sled system. This technology is used to achieve supersonic velocities and is widely applicable in space equipment testing [1], projectile penetration [2], parachute [3], pilot seat [4], anti-penetration structures [5], propulsion testing [6], and ultrasonic aerodynamic tests [7]. The main difference of this system from the missile test is its direct movement on the rails until it reaches the target. Slippers are used to truck the system on rails. The slippers slide on the rails to allow the sled to move. A real example of a sled is shown in "Fig. 1".

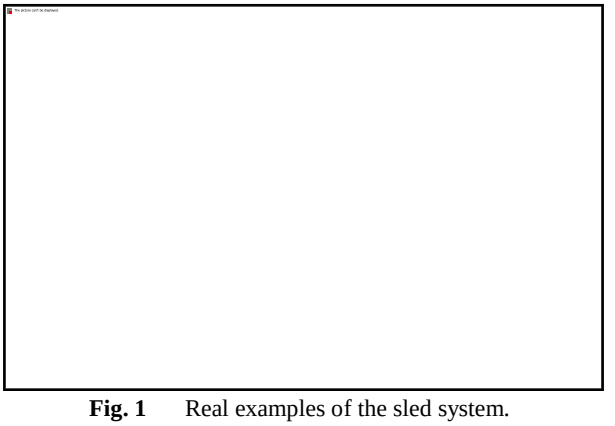

Fig. 1 Real examples of the sled system.

Sled testing technology has attracted the attention of researchers in recent years [8–12]. Impacts from engine propulsion, aerodynamic forces, as well as the impact of slippers on the rails cause significant vibrations to enter the sled structure [13]. Reduction of vibrations on the sled is one of the main problem in this system due to the high-speed motions, that has been attended by many researchers [14–17]. Xiao et al. used a one-degree-of-freedom system for modal analysis of a sled and obtained a damping ratio and mass stiffness matrix, then investigated the natural frequencies of the system using numerical methods [18]. Hauser showed that the vibrational environment in the sled test is a linear function of velocity. He mentioned that the vibrations on the sled are reduced using a pair of rails [19]. Hooser and Hooser used foam to reduce the transmitted vibrations on the explosive material in the middle of the sled body and reported the reduction of vibrations [20]. Lamb developed a structural model of the Holloman sled test and showed that the movement of the sled at critical speeds causes the transmission of vibrations to the rail. This theory was represented through time-frequency analysis of accelerometer data [21]. The vibrations of a system are related to different reasons, which can be carefully examined to determine the main source of vibrations and the effective factors on them. The main reason for vibrations in the sled system is referred to slipper impact on the rail. Considering the sled as a damping system, obtaining damping and equivalent stiffness is one of the main parts of system design. Considering the distance between the surfaces of the slipper colliding with one of the upper, lower, or lateral surfaces of the rail, the resulted vibrations cause vertical or lateral shocks, respectively. Research has shown that most of the rail collisions with the slipper occur in the upper parts of the slipper. In other words, the lateral part does not collide with the rail considerably, and the collision of the lower parts of the slipper with the rail along the sled path can be neglected. The contact of the slipper with the rail in the lower points 1 and 6 is less than 5% and then reaches a maximum of 18%. Variations of applied force on the top of the rail of points 3 and 4 are shown in "Fig. 2" [22]. Turnbull et al. used cable dampers inside the body, as shown in "Fig. 3", to reduce the vibrations on the sled body.

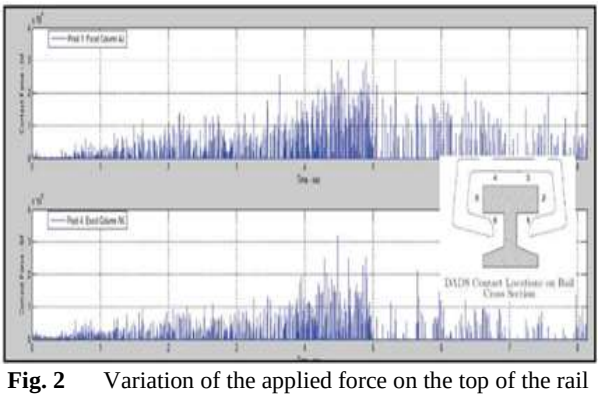

Fig. 2 Variation of the applied force on the top of the rail (points 3 and 4) [22].

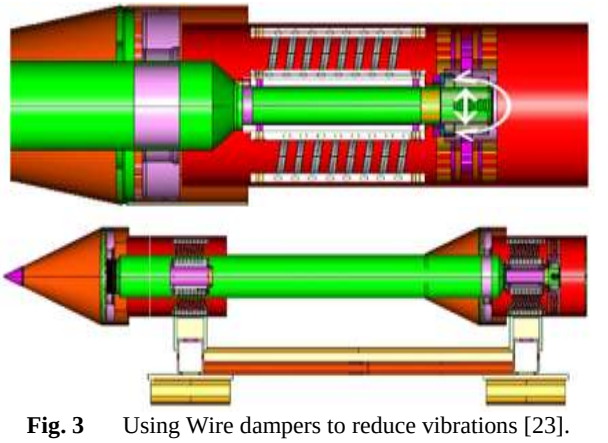

Fig. 3 Using Wire dampers to reduce vibrations [23].

The dampers were installed to withstand and reduce the torsional and vertical vibrations. The results showed that wire cable dampers greatly reduce vibrations in different directions [23]. Styrene-butadiene rubber (SBR), as

composite [24-25] or constituent materials [26], is desirably used in damper to withstand against applied shocks due to better capabilities in comparison with springs[27]. SBR are one of the types of dampers that are identified in different types and applications [28]. The most important features of SBR elastomers are resistance to continuous cycles in terms of fatigue and failure, suspension of vibrations, reversibility against deflection and deformation, high flexibility against impact and shock, high displacement and flexibility capability along with a short distance, simultaneous performance of axial and lateral movements, no need for washers and seals, the ability to deform with low force and, by its nature, apply low force to equipment, low weight, and ease of installation and replacement [29]. In addition, to avoid the resonance phenomenon or reduction of vibration transmission in the system, the natural frequency can be increased by increasing the stiffness of the structure, but this makes the structure heavier and some difficulties for design of system[23]. The main outstanding of the present study, which has not been done by other researchers, is the use of structural elastomer dampers in the connection distance between the slipper and the sled body with a new method which a combination of analytical, numerical, and experimental test methods was utilized. Due to the importance of damping of vertical vibrations, the dampers are used to prevent the transmission of vibrations from the rail to the sled. In this research, SBR elastomer was selected as a novel idea for damping of system vibrations. First, by extracting the stiffness and damping Equations, the equivalent stiffness and equivalent damping of the system are obtained from a combination of analytical, numerical, and experimental methods, and by sled modal analysis, the natural frequency and the role of elastomer are investigated.

2 EQUIVALENT STIFFNESS EXTRACTION

Based on the aforementioned characteristics of SBR elastomer, it is used as a damper in the sled system. Considering the damper at the place where the slipper is attached to the sled body and considering the stiffness of the sled components, the rigidity of the elastomer used in the sled should be obtained.

2.1. Numerical Method

In this method, by obtaining the exact values of Young's modulus, Poisson's ratio, and elastomer density, using Abaqus software, different forces are applied to the part and the displacement of elastomer is obtained. Assuming the spring displacement is linear, the rigidity coefficient is obtained by dividing the amount of force on the displacement. What is available as the hardness coefficient of elastomers as an intrinsic property is their Shore factor. The hardness of materials is divided into two categories A and D based on the amount of Shore value. In our work, the elastomer of type A was selected. To obtain the stiffness of an elastomer, Young's modulus (E_e) should be obtained according to its stiffness value and then calculate its stiffness coefficient according to its geometry [30]. Young's modulus can be determined according to Equation (1) [31].

$$E_e = e^{(0.0235\,(\text{Shore,A}) - 0.6403)} \quad (1)$$

A hardness test was carried out to obtain the elastomer stiffness. This device is shown in “Fig. 4”.

Fig. 4 Hardness Tester.

By measuring the elastomeric shore value and substitution in Equation (1), Young's modulus is obtained. The density was measured equal to 1120 kg/m^3 by obtaining the weight of the elastomer, geometric dimensions and was compared with [32]. By entering different parameters in Abaqus software, the simulation is run. Finally, by entering these values in Abacus software, modeling is done. The number of meshes is 21985 and a type of quad element was selected. In this case, only rectangular elements are used to network and create the finite element network. The element used is C3D8R. This element is in the form of 8 cubic nodes, has a reduced formulation, the ability to control the Hourglass phenomenon and is one of the most widely used elements used in Abaqus software. Fig. 5 shows the elastomer under force.

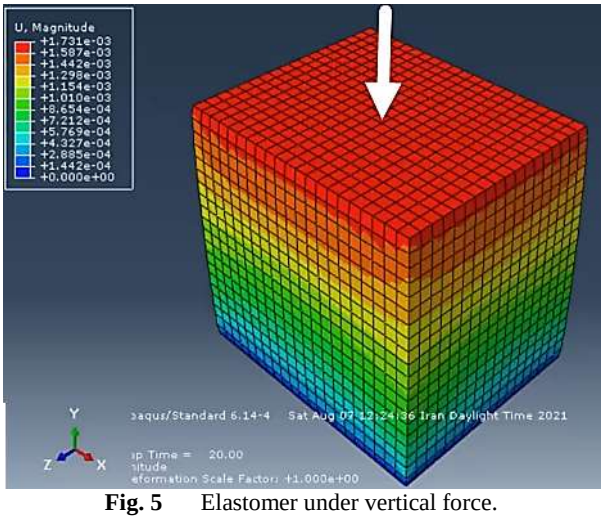

Fig. 5 Elastomer under vertical force.

Fig. **6** also shows the values obtained from the amount of elastomer displacement under different forces.

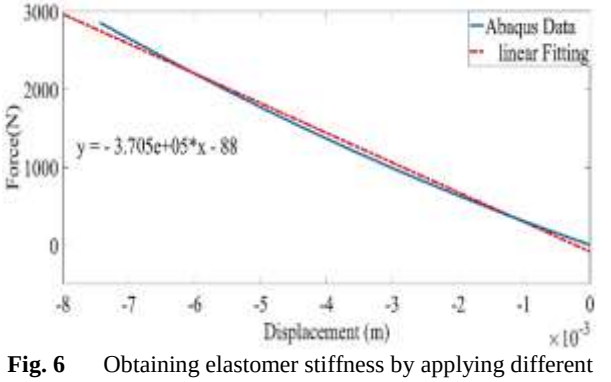

Fig. 6 Obtaining elastomer stiffness by applying different forces.

As can be seen, with increasing force (F) from 1 N to 3000 N, the vertical displacement (x) of the elastomer increases almost linearly. By extrapolating the results obtained from numerical simulation, the red dashed line is fitted to the blue line of Abaqus data, and the resulted Equation is described below

$$F = -370500x - 88 \quad (2)$$

The slope of the plot is equal to the amount of elastomer stiffness which is 370500 N⁄m.

2.2. Experimental Method

Harmonic dynamics test device was used to measure equivalent stiffness. This test was performed in Iran's spare parts manufacturing company, which is engaged in manufacturing various types of dampers and suspension systems for car manufacturing companies. The test apparatus is shown in "Fig. 7".

Fig. 7 Harmonic dynamics testing device of Iran spare parts manufacturing company.

The damper was fixed between plates, and a preload force was applied to prevent any gap between them. Next, the applied force to the elastomer and the resulted displacement is recorded and is monitored using the computer connected to the device. Fig. **8** shows the experiment performed at different frequencies and amplitudes of vibration.

Fig. 8 The harmonic dynamics testing device at the moment of applying force on the elastomer.

With the experiment, the elastomer stiffness was 391000 N⁄m that both experimental and numerical results are described in "Table 1". The values have a difference of less than 5% so the simulation results are confirmed.

Table 1 Amounts of experimental and numerical stiffness

Error percentage	Experimental stiffness (kN⁄m)	Numerical stiffness (kN⁄m)
5%	391	370.5

3 EXTRACTION OF EQUIVALENT DAMPING FACTOR

The present work contains a structural damping type. To obtain equivalent damping, we must first examine the

vibrations with structural damping or hysteresis damping.

3.1. Obtaining Structural Damping Coefficient

When an object deforms, it absorbs and dissipates energy. The energy loss caused by friction between the inner planes and the material deforms is called structural or solid damping. In the case of stress-strain curves, the area of the closed hysteresis curve represents the dissipative energy in each cycle [33–35]. As shown in "Fig. 9", the area of this loop shows the dissipative energy due to structural damping for the unit volume of an object in a cycle [36].

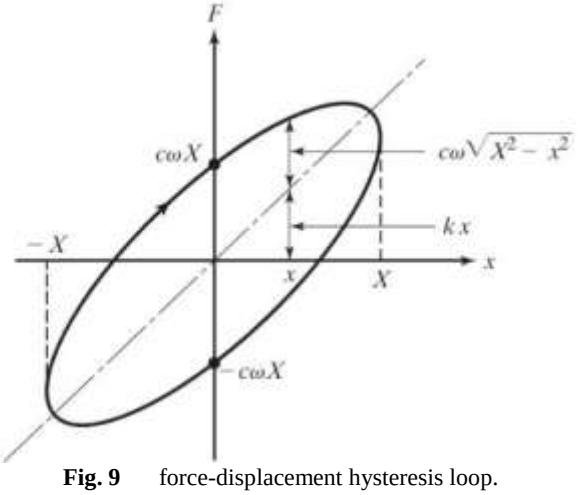

Fig. 9 force-displacement hysteresis loop.

Consider a system of one degree of freedom with structural damping capability as shown in "Fig. 10".

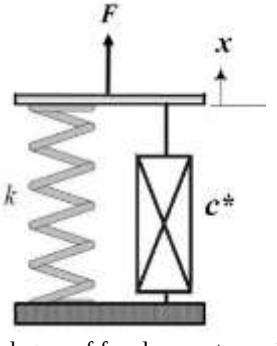

Fig. 10 One- degree of freedom system with structural damping capability.

The Equation of motion of the system is according to (3):

$$F = kx + c\dot{x} \tag{3}$$

Where, k relies on stiffness. Considering the harmonic motion, there is [37]:

$$F(t) = kx \pm c\omega \sqrt{X^2 - x^2} \tag{4}$$

Where, X is the amplitude of the vibration displacement. Thus, to obtain the amount of energy (ΔE_s), there is:

$$\Delta E_s = \int_0^{2\pi/\omega} (k\,X \sin\omega t \pm c\,X\cos\omega t)\,(\omega\,X\cos\omega t)\,dt = \pi\omega c X^2 \tag{5}$$

According to experiments, the energy loss per cycle is proportional to the stiffness of the material and the square of displacement and does not depend on the frequency [38]. To achieve damping behavior, we consider the damping coefficient c as follows [38]:

$$c = \frac{c^*}{\omega} \tag{6}$$

Where, c* is called the structural damping constant. Thus, using Equation (5), there is:

$$\Delta E_s = \pi c^* X^2 \tag{7}$$

With considering the parallel spring and damper, it can be obtained for harmonic motion $x = X\,e^{i\omega t}$ as the following Equation (8):

$$F = k\,X\,e^{i\omega t} + i\omega c\,X\,e^{i\omega t} = (k + i\omega c)\,x = (k + i\,c^*)\,x \tag{8}$$

Where, $k + ic^*$ is called mixed stiffness as Equation (9):

$$k + i\,c^* = k\left(1 + i\frac{c^*}{k}\right) = k(1 + i\,\beta) \tag{9}$$

The dimensionless constant β is called the structural damping ratio. Using Equation (7) the energy loss in a cycle can be written as Equation (10):

$$\Delta E_s = \pi\,\beta\,k\,X^2 \tag{10}$$

Since the value of ΔE_S is low, the motion can be considered harmonic. Referring to [39], equality of the energy stored in the spring and the energy loss value in a cycle, the constant amount of structural damping can be considered as a logarithmic reduction and defined as Equation (11):

$$\delta_l = \ln\frac{X_1}{X_2} = \ln(1+\pi\beta) \cong \pi\beta \tag{11}$$

If the structure behaves similarly to one degree of freedom system, the damping ratio can be defined as (12) [40]:

$$\xi_{eq} = \frac{c_{eq}}{c_c} = \frac{c_{eq}}{2m\,\omega_n} \tag{12}$$

To determine the equivalent damping ratio, considering Equation (11), there is:

$$\xi_{eq} = \frac{\beta\,k}{2m\,\omega_n{}^2} = \frac{\beta}{2} = \frac{c^*}{2k} \tag{13}$$

On the other hand, the equivalent damping constant is obtained from Equation (14):

$$c_{eq} = 2\sqrt{k\,m}.\ \frac{\beta}{2} = \beta\sqrt{k\,m} = \frac{\beta\,k}{\omega} = \frac{c^*}{\omega} \tag{14}$$

Thus, considering Equation (13), there is:

$$\beta = \frac{2\delta_l}{\sqrt{4\pi^2+\delta_l{}^2}} \tag{15}$$

3.2. Forced Movement of The System with Structural Damping

One degree of freedom system was considered with structural damping capability that is under the harmonic force as shown in "Fig. 11".

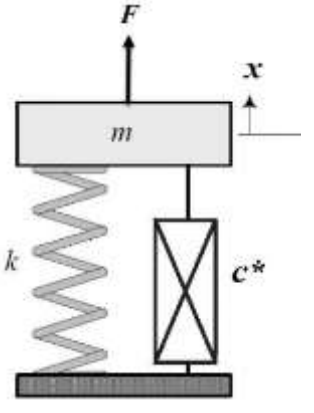

Fig. 11 One degree of freedom system with structural damping.

The Equation of motion of the system according to Equation (14) is obtained as Equation (16):

$$m\ddot{x} + \frac{\beta\,k}{\omega}\dot{x} + kx = F\sin\omega t \tag{16}$$

Where, the term of $((\beta\,k)/\omega)\,\dot{x}$ demonstrates the structural damping force. Considering the harmonic force, the stable solution of the Equation is considered to be as Equation (17):

$$x_p(t) = X\sin(\omega t - \varphi) \tag{17}$$

Thus, there is:

$$X = \frac{F}{k\sqrt{(1-r^2)^2+\beta^2}} \tag{18}$$

$$\varphi = \tan^{-1}\frac{\beta}{1-r^2} \tag{19}$$

That term r of represent frequency ratio. According to experiments performed on materials and structures under harmonic load, it has been observed that the stress will exceed the strain by a constant angle δ. Therefore, for the harmonic strain $\varepsilon = \varepsilon_0\sin(\omega t)$, the stress response is obtained as (20) [37]:

$$\begin{aligned}&\sigma(t) = \sigma_0\,sin(\omega t+\delta) = \\ &\sigma_0\,cos\delta\,sin\omega t + \sigma_0\,sin\delta\,cos\omega t = \\ &\sigma_0\,cos\delta\,sin\omega t + \sigma_0\,sin\delta\,sin\left(\omega t+\frac{\pi}{2}\right)\end{aligned} \tag{20}$$

The first term of Equation (20) is in the same phase with strain, while the second term of stress is 90 degrees with strain difference. By substituting $i = \sqrt{(-1)}$, there is [40]:

$$\sigma(t) = \sigma_0\,cos\delta\,sin\omega t + i\,\sigma_0\,sin\delta\ \ sin\omega t \tag{21}$$

With the definition of a composite module (E^*), there is:

$$E^* = \frac{\sigma}{\varepsilon} = \frac{\sigma_0}{\varepsilon_0}cos\delta + i\frac{\sigma_0}{\varepsilon_0}sin\delta \tag{22}$$

We define quantities of E' and E" as storage modulus and waste modulus respectively, as is shown in Equations (23) and (24):

$$E' = \left(\frac{\sigma_0}{\varepsilon_0}\right)cos\delta \tag{23}$$

$$E'' = \left(\frac{\sigma_0}{\varepsilon_0}\right) sin\delta \tag{24}$$

So, Equation (25) is written:

$$E^* = E' + i\,E'' \tag{25}$$

Thus the stress response of linear viscoelastic materials to a harmonic strain input will be (26) [41]:

$$\sigma(t) = \varepsilon_0 \left(E' sin\omega t + E'' cos\omega t\right) \tag{26}$$

Where, ε_0 is the strain amplitude. The storage modulus is proportional to the average energy stored in a cycle, while the dissipation modulus is proportional to the average energy loss in a cycle [42]. The loss coefficient of η is dimensionless and is a measure of hysteresis damping in a structure, defined as (27) [41]:

$$\eta = \frac{E''}{E'} = tan\delta \tag{27}$$

The dissipation coefficient relates the wasted energy to the stored energy during the deformation cycle [43]. In other words, there is:

$$\frac{c^*}{k} = \eta \tag{28}$$

By substituting Equation (14) to (16), the free motion Equation of the system is obtained as (29):

$$m\ddot{x} + \frac{c^*}{\omega}\dot{x} + kx = 0 \tag{29}$$

Considering $x = X\,e^{i\omega t}$, there is:

$$\dot{x} = i\omega x \tag{30}$$

Therefore,

$$\frac{c^*}{\omega}\dot{x} = i\,c^* x \tag{31}$$

By using relations (31) and (29) there is:

$$m\ddot{x} + \left(k + i\,c^*\right)x = 0 \tag{32}$$

So, there is:

$$k + i\,c^* = k\left(1 + \frac{i\,c^*}{k}\right) = k\left(1 + i\,\eta\right) = k^* \tag{33}$$

Where, k is static stiffness and k* is complex stiffness. Finally, the Equation of motion is obtained as follows:

$$m\ddot{x} + k^* x = 0 \tag{34}$$

It describes that the combined effects of tensile strength, elasticity, and hysteresis capabilities can be represented as complex stiffness. Various experimental studies have been performed to obtain the loss coefficient. Environmental conditions such as temperature, type of test and are effective in determining the loss factor. "Table 2" shows the values of the loss coefficient η for SBR elastomer in various studies for ambient temperatures between 0 and 50 ° C.

Table 2 Loss coefficient values for SBR elastomer

SBR elastomer dissipation reference	Reference
0.2-0.3	[38]
0.15-0.45	[44]
0.18-0.36	[45]
0.22-0.4	[46]
0.15-0.4	[47]
0.28-0.12	[48]
0.05-0.45	[49]
0.1-0.3	[50]

Considering the obtained results, the value of the SBR loss coefficient decreased with increasing temperature in the range of 0 to 50 °C, so the range of 0.25-0.35 can be predicted for the SBR loss coefficient at 25 °C.

3.3. Experimental Test

An experimental test is used to obtain elastomer damping using the aforementioned dynamic test device. The elastomer under test is shown in "Fig. 12".

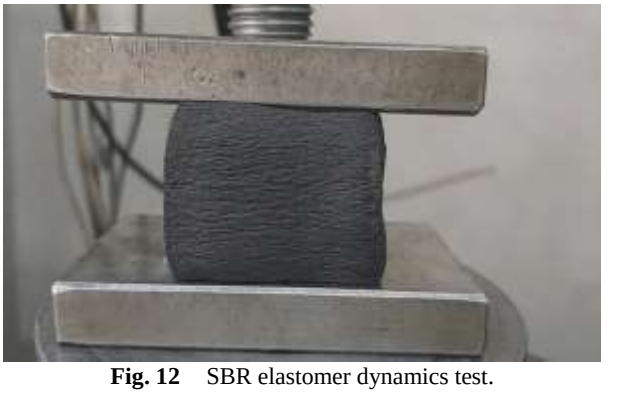

Fig. 12 SBR elastomer dynamics test.

The procedure of the test is done by placing the elastomer in the device and adjusting it precisely to prevent from any distance between the device and the elastomer, so different frequencies were transmitted into the device which displayed the amount of tanφ at different frequencies. Considering Equation (19), tanφ is related to the two-dimensional value of the damping ratio of the structures, which can be expressed as following:

$$tan\varphi = \frac{\beta}{(1-r^2)} \tag{35}$$

The method for obtaining the natural frequency of elastomer was done first by designing the elastomer model in Abaqus software and entering the geometric characteristics and related parameters such as density and Poisson's ratio, the shape of elastomer different modes is obtained. Finally, due to the importance of vertical displacement of the elastomer in the present problem, the natural frequency of the elastomer is obtained using the results related to the mode shape. Considering the applied frequency value and the natural frequency of the elastomer, the frequency ratio of (r) is obtained, and the damping ratio of the structures can be obtained according to Equation (35) and the term of tanφ. The natural frequency of elastomer is shown in "Fig. 13".

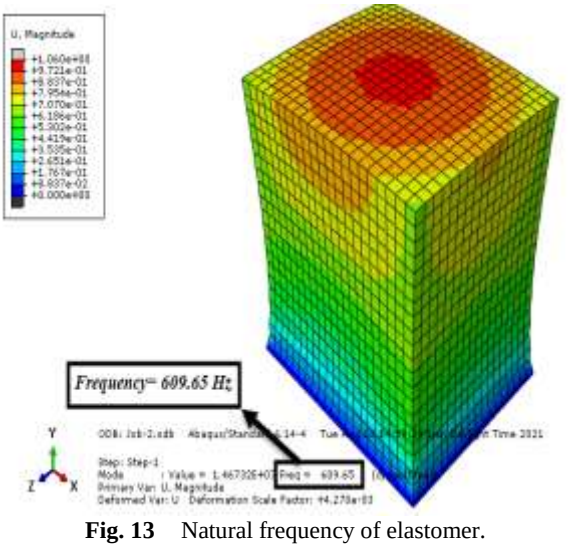

Fig. 13 Natural frequency of elastomer.

By substituting the values obtained in Equation (35), the value of β is extracted. "

Table **3**" shows the structural damping ratio of the system using experimental measurement of the phase difference between the force and displacement at different frequencies.

Table 3 Phase difference between force and displacement at different frequencies in the experimental experiment

β	tanφ	frequency
0.306	0.306	5
0.307	0.308	10
0.308	0.31	15
0.314	0.323	25
0.316	0.327	50
0.318	0.329	100

The differences between the mentioned values are negligible. The dimensionless value of the structural damping ratio is considered to be 0.31, and equivalent damping ratio (ξ_{eq}) is defined as:

$$\xi_{eq} = \frac{\beta}{2} = \frac{c^*}{2k} \rightarrow \xi_{eq} \cong 0.155 \tag{36}$$

Finally, by converting the unit of the natural frequency of the damper to radians per second and using Equation (14), the equivalent damping ratio is obtained as Equation (37):

$$c_{eq} = \frac{\beta k}{\omega} = \frac{0.31 \times 370000}{3830} = 29.94 \text{ N.s/m} \tag{37}$$

Considering the 25 grams weighs of the damper, the value of Ceq is validated, thus the loss factor values are compared. For this purpose, using Equation (14), the value of c^* is obtained as follows:

$$c^* = c_{eq}\ \omega = 29.94 \times 3830 = 114 \text{ kN.s/m} \tag{38}$$

Considering Eq. (38), the loss coefficient (η) is determined as following:

$$\eta = \frac{c^*}{k} \rightarrow \eta \cong 0.3 \tag{39}$$

The obtained results are in good agreement with the results of previous researches mentioned in "Table 2", and the amount of equivalent damping is validated. By obtaining the equivalent damping and stiffness, the values of the various parameters of the sled, which determine the design parameters of the sled in our present work, are described in "Table 4".

Table 4 Values of different parameters of the designed sled.

Parameter	Value	Unit
Sled mass	14.69	kg
Slipper mass	0.79	kg
Equivalent stiffness	370	kN/m
Second level torque	0.877	kgm^2
Equivalent Damping	29.01	N.s/m
Sled length	810	mm
Sled diameter	105	mm

4 SLED MODELING

Figure 14 represents the designed sled system and the dampers on the top of the slipper. The main body, which includes the propulsion and projectile engines, is considered as an integrated part, so two semi-circular rolled pieces, which are connected like a belt, are provided to restrain the main body. The dampers are connected from the bottom and top to the slipper and the belts, respectively. The belts are joined together with screws.

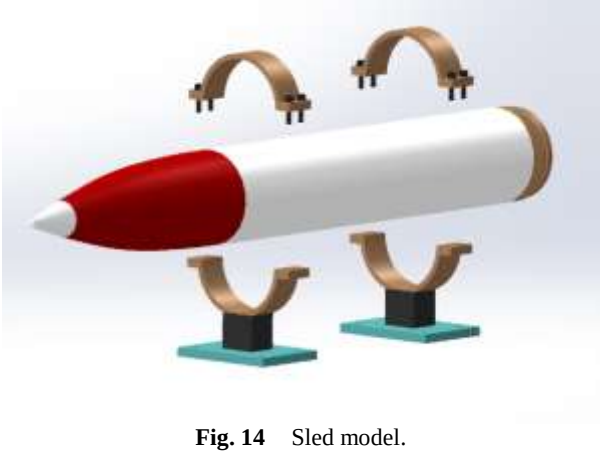

Fig. 14 Sled model.

4.1. Natural Frequencies and Shape of Modes

Fig. 15 shows the sled modal analysis for the first mode of the system. The first mode is related to the torsional vibrations around the center of mass of the sled. The first mode of the natural frequency is equal to 12.49 Hz. Due to the rigidity of the sled body, the amount of torsional vibration is small. The present condition demonstrates that one of the dampers is stretched and the other is under pressure.

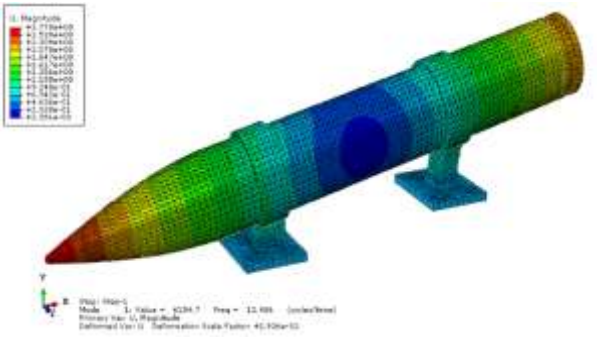

Fig. 15 The first (torsional) mode of the sled.

Fig. 16 shows the second mode of vibration which is related to the transverse vibration of the sled. In this case, the sled vibrates vertically without torsional motion, and the vibration rate of the two slippers is equal to each other. In this case, the second mode of the natural frequency is 19.56 Hz. The dampers are both stretched.

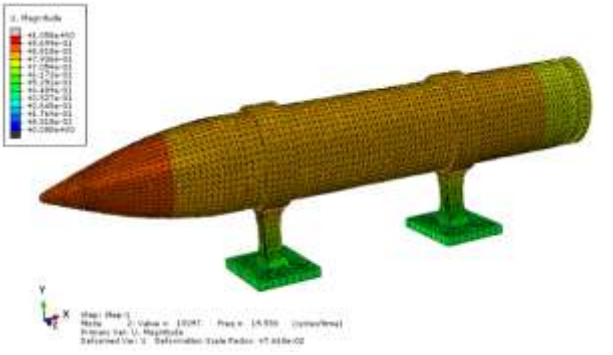

Fig. 16 Second (transverse) sled mode.

By examining the vibration modes and considering the rigidity of the sled body, the importance of the role of slippers in sled is determined that if the damper is not used, the vibrations will be transmitted to the sled body. Also, the use of elastomer dampers are the convenient choice because they can withstand pressure and tension, and do not transmit any displacement.

5 CONCLUSION

In this paper, the idea of using elastomer dampers to reduce the transmission of vibrations from the slipper to the sled body was investigated. First, by the relations governing the problem, equivalent stiffness and equivalent damping of the system were extracted from a combination of analytical, numerical, and experimental methods. So the stiffness values of 370500 and 391000 N⁄m were obtained numerically and experimentally. The difference between values was less than 5% so the results were confirmed. Then, by locating the damper and designing an example of a sled system, natural

frequencies and system modes were obtained. The first and second modes of the natural frequency are equal to 12.49 and 19.56 Hz. The results showed the highest tension and pressure is applied on the dampers and elastomeric dampers prevent the transmission of vibrations and displacement of the sled body.

REFERENCES

[1] DeLeon, A., Palazotto, A. N., Shock Wave Investigation of High Speed Asperity Collision with Finite Element Modeling (January), 2020, pp. 1–20, Doi: 10.2514/6.2020-0316.

[2] Liu, J., Wang, W., and Zhao, F., Analysis of Wear for a Rocket Sled Slipper, MS&E, Vol. 398, No. 1, 12017, 2018.

[3] Gallon, J. C., Clark, I. G., Rivellini, T. P., and Adams, D. S., Witkowski A: Low Density Supersonic Decelerator Parachute Decelerator System, AIAA Aerodyn Decelerator Syst Conf, 2013, (March), 2013, pp. 1–14, Doi: 10.2514/6.2013-1329.

[4] Zhu, Y., Zhao, X., and Zhang, S., Computational Studies of Aircraft Life-Support Systems (January), 2011, pp. 1–16, Doi: 10.2514/6.2011-1045.

[5] Liu, Jun., Zhao, H., Gu, K., and Wang, W., An Analysis of Dynamic Response of a Rocket Sled. DEStech Trans Comput Sci Eng (aiea), 2017, pp. 956–67, Doi: 10.12783/dtcse/aiea2017/15034.

[6] Connell, T. L., Santi, S. A., Risha, G. A., Muller, B. A., and Batzel, T. D., Experiment and Semi-Empirical Modeling of Lab-Scale Hybrid Rocket Performance, 45th AIAA/ASME/SAE/ASEE Jt Propuls Conf Exhib (August), 2009, pp. 1–12.

[7] Doig, G., Barber, T. J., Leonardi, E., Neely, A. J., Kleine, H., and Coton, F., Aerodynamics of a Supersonic Projectile in Proximity to a Solid Surface, AIAA J, Vol. 48, No. 12, 2010, pp. 2916–30, Doi: 10.2514/1.J050505.

[8] Boardman, B., Uber, R., Baker, W., and Palazotto, A. N., Modeling Nonlinear Heat Transfer for Pin-on-Disc Sliding System, (January), 2020, pp. 1–22, Doi: 10.2514/6.2020-0973.

[9] Rodney, D., Gadot, B., Martinez, O., du Roscoat, S., Orge ´as L Reversible Dilatancy in Entangled Single-Wire Materials, Vol. 15, 2016, pp. 72–78.

[10] Tang, R. Y., Finite Element Structural Analysis of a Machine Gun Based on ANSYS, Nanjing Univ Sci Technol, 2007, pp. 17–37.

[11] Gao, W., Kessissoglou, N. J., Dynamic Response Analysis of Stochastic Truss Structures under Non-stationary Random Excitation using the Random Factor Method, Comput Methods Appl Mech Engrgy, Vol. 196, 2007, pp. 2765–73.

[12] Gerasimov, S. I., Erofeev, V. I., Calculation of Flexural-and-Torsional Vibrations of a Rocket Track Rail, J Mach Manuf Reliab, Vol. 45, No. 3, 2016, pp. 211–3.

[13] Liu, J., Wang, W., Zhao, F., and Gong, M., Comparison of Two Rocket Sled Slipper Materials for Resistance to Wear, AIP Conf Proc 1890(October), 2017, Doi: 10.1063/1.5005321.

[14] Hale, C. S., Palazotto, A. N., and Baker, W. P., Engineering Approach for The Evaluation of Mechanical Wear Considering the Experimental Holloman High-Speed Test Track, J Eng Mech, Vol. 138, No. 9, 2012, pp. 1127–40, Doi: 10.1061/(ASCE)EM.1943-7889.0000409.

[15] Shockley, J. A., Zetterstrom, S., 50 Years of The Central Inertial and GPS Test Facility, US Air Force T E Days 2009 (February), 2009, pp. 1–32, Doi: 10.2514/6.2009-1724.

[16] Zhang, J., Dynamic Coupling Analysis of Rocket Propelled Sled Using Multibody-Finite Element Method, Vol. 18, No. 4, 2014, pp. 25–30.

[17] Deleon, A., Baker, W. P., and Palazotto, A. N., Evaluation of a Nonlinear Melt Region Produced Within a High Speed Environment, AIAA/ASCE/AHS/ASC Struct Struct Dyn Mater Conf 2018 (210049), 2018, pp. 1–17, Doi: 10.2514/6.2018-0187.

[18] Xiao, J., Zhang, W., Xue, Q., Gao, W., and Zhang, L., Modal Analysis for Single Track Sled (Pmsms), 2018.

[19] Hooser, M., Soft Sled – The Low Vibration Sled Test Capability at The Holloman High Speed Test Track, 2018 Aerodyn Meas Technol Gr Test Conf (February), 2018, pp. 1–12, Doi: 10.2514/6.2018-3872.

[20] Hooser, M., Hooser, C., Soft Sled Design Evaluation Report, 2016.

[21] Lamb, J. L., Critical Velocities for Rocket Sled Excitation of Rail Resonance, Johns Hopkins APL Tech Dig Applied Phys Lab, Vol. 21, No. 3, 2000, pp. 448–58.

[22] Buentello Hernandez, R. G., Palazotto, A. N., and Le, K. H., 3D Finite Element Modeling of High-Speed Sliding Wear, Collect Tech Pap-AIAA/ASME/ASCE/AHS/ASC Struct Struct Dyn Mater Conf, 2013, pp. 1–20.

[23] Turnbull, D., Hooser, C., Hooser, M., and Myers, J., Soft Sled Test Capability at the Holloman High Speed Test Track. US Air Force T&E Days, 2010.

[24] Bahadar, A., Zwawi, M., Development of SWCNTs-Reinforced EPDM/SBR Matrices for Shock Absorbing Applications, Mater Res Express, Vol. 7, No. 2, 2020, pp. 025310, Doi: 10.1088/2053-1591/AB71CE.

[25] Liu, F., Zheng, M., Liu, X., Ding, X., Wang, F., and Wang, Q., Performance Evaluation of Waterborne Epoxy Resin-SBR Composite Modified Emulsified Asphalt Fog Seal, Constr Build Mater, Vol. 301, 2021, pp. 124106.

[26] Yang, L., Wang, L., Guo, H., and Du, A., Compressive Fatigue Behavior of Gum and Filled SBR Vulcanizates. Polymers (Basel), Vol. 13, No. 9, 2021, pp. 1497.

[27] Gil, A., Huang, A., Madrid, P., and Jiménez, L., Analysis of SBR Polymer Adapted to an Automobile Damping System, Journal of Undergraduate Research, Vol. 1, No. 2, 2015.

[28] Fu, Y., Kabir, I. I., Yeoh, G. H., and Peng, Z., A Review on Polymer-Based Materials for Underwater Sound Absorption, Polym Test, 2021, pp. 107115.

[29] Akyüz, S., Dari, M. E., Esiyok, Y. E., and Ermeydan, M. A., Effects of NR/SBR Ratio on Mechanical Properties and Artificial Mechanical Performance of Anti-Vibration Bushings, Iran Polym J, Vol. 30, No. 12, 2021, pp. 1317–28.
[30] Dudea-Simon, M., Dudea, S. M., Schiau, C., Ciortea, R., Mualuțan, A., Simon, V., Burde, A., Ciurea, A., and Mihu, D., Inter-and Intraobserver Reproducibility of Strain and 2D Shear Wave Elastography--a Phantom Study, Med Ultrason, 2021.
[31] Krmela, J., Material input for tire simulation, 2019.
[32] Asme, A., Ahs, A., Structures ASC, A01-25011 (c), 2001.
[33] Pinsker, W., Structural Damping, J Aeronaut Sci, 1949, pp. 699.
[34] Ungar, E. E., The Status of Engineering Knowledge Concerning the Damping of Built-Up Structures, J Sound Vib, Vol. 26, No. 1, 1973, pp. 141–54, Doi: 10.1016/S0022-460X(73)80210-X.
[35] Scanlan, R. H., Mendelson, A., Structural Damping, AIAA J, Vol. 1, No. 4, 1963, pp. 938–9, Doi: 10.2514/3.1684.
[36] Singiresu, S. R., and et al., Mechanical Vibrations, Addison Wesley Boston, Reading, MA, 1958.
[37] Chakraborty, Bikash Chandra Ratna, D., Polymer for Vibration Damping Appliction, 2020, pp. 348.
[38] Lazan, B. J., Damping of Materials and Members In Structural Mechanics, Pergamon Press LTD, Oxford, England, 1968, pp. 317.
[39] Orban, F., Damping of Materials and Members in Structures, Journal of Physics: Conference Series, Vol. 268, 2011, pp. 12022.
[40] Al-Gahtany, S. A., Mechanical Properties oof Styrene Butadiene Rubber-/Ethylene Propylene Diene Monomer Rubber-Based Conductive Blends, J Elastomers Plast, Vol. 45, No. 4, 2013, pp. 367–89, Doi: 10.1177/0095244312454035.
[41] Mohseni, A., Shakouri, M., Natural Frequency, Damping and Forced Responses of Sandwich Plates with Viscoelastic Core and Graphene Nanoplatelets Reinforced Face Sheets, JVC/Journal Vib Control, Vol. 26, No. 15–16, 2020, pp. 1165–77, Doi: 10.1177/1077546319893453.
[42] Schramm, G., A Practical Approach to Rheology and Rheometry, Hardcover – Illustrated, January 1, 1994.
[43] Riande, E., Díaz-Calleja, R., Prolongo, M. G., Masegosa, R. M., and Salom, C., Polymer Viscoelasticity : Stress and Strain In Practice, Boca Raton, 2014, pp. 904, https://doi.org/10.1201/9781482293241.
[44] Bahadar, A., Zwawi, M., Development of SWCNTs-Reinforced EPDM/SBR Matrices for Shock Absorbing Applications, Mater Res Express, Vol. 7, No. 2, 2020, pp. 25310.
[45] Araujo-Morera, J., Hernández Santana, M., Verdejo, R., and López-Manchado, M. A., Giving a Second Opportunity to Tire Waste: an Alternative Path for the Development of Sustainable Self-Healing Styrene-Butadiene Rubber Compounds Overcoming the Magic Triangle of Tires, Polymers (Basel), Vol. 11, No. 122019, pp. 2122.
[46] McKeen, L. W., The Effect of UV Light and Weather on Plastics and Elastomers, William Andrew, Hardcover ISBN: 9780128164570, 2019.
[47] Schaefer, R. J., Mechanical Properties of Rubber, Harris' Shock Vib Handbook, Sixth Ed A Piersol, T Paez (Eds), McGraw-Hill Co Inc, 2010, pp. 31–3.
[48] Mondal, D., Ghorai, S., Rana, D., De, D., and Chattopadhyay, D., The Rubber--Filler Interaction and Reinforcement in Styrene Butadiene Rubber/Devulcanize Natural Rubber Composites with Silica--Graphene Oxide, Polym Compos, Vol. 40, S2, 2019, E1559-E1572.
[49] Chakraborty, B. C., Ratna, D., Polymers for Vibration Damping Applications. Elsevier, Paperback ISBN: 9780128192528, 2020.
[50] Praveen, S., Chattopadhyay, P. K., Jayendran, S., Chakraborty, B. C., and Chattopadhyay, S., Effect of Nanoclay on The Mechanical and Damping Properties of Aramid Short Fibre-Filled Styrene Butadiene Rubber Composites, Polym Int, Vol. 59, No. 2, 2010, pp. 187–97.

Int. J. Advanced Design and Manufacturing Technology, 2023, Vol. 16, No. 1, pp. 13-27

DOI: 10.30486/admt.2022.1951472.1338 ISSN: 2252-0406 https://admt.isfahan.iau.ir

Vibration Analysis of an Imperfect Single-Layer Graphene Sheet using Quasi-3d Theory and Isogeometric Approach

Heidar Fazeli[1], Armen Adamian[2,] *, Ahmad Hosseini-Sianaki[3]

Department of Mechanical Engineering, Central Tehran Branch, Islamic Azad University, Tehran, Iran
E-mail: hei.fazeli.eng@iauctb.ac.ir, arm.adamian@iauctb.ac.ir, a_h_sianaki@iauctb.ac.ir
*Corresponding author

Received: 1 February 2022, Revised: 25 April 2022, Accepted: 30 April 2022

Abstract: In this study, the size-dependent free vibration analysis of a geometrically imperfect single-layer graphene sheet (SLGS) is studied by an isogeometric approach along with the quasi-3D shear and normal deformation theory. Initial geometric imperfections alter the natural frequencies of the graphene sheets that may exist inherently or purposely created by researchers. The initial curvature is modelled by an analytical function in the governing Equations of the plate. A 4-variable quasi-3D theory with a seventh-order distribution function is used to include both shear deformation and thickness stretching influences. A weak form of a nonlocal plate for free vibration analysis is derived that requires the first-order continuity of the displacement fields. Inherent high-order continuity of non-uniform rational B-spline (NURBS) basis functions in isogeometric analysis can meet this condition. A comparison between the present study and other published works reveals the efficiency and accuracy of the proposed method in imperfect SLGS. The results of the present study show a significant effect of initial geometric imperfection on the natural frequency of single-layer graphene sheets.

Keywords: Fundamental Frequency, Imperfection Sensitivity, Initial Geometric Imperfection, Isogeometric Analysis, Single-Layer Graphene

Biographical notes: Heidar Fazeli is a Ph.D. student of mechanical engineering at Central Tehran Branch, IAU, Tehran, Iran. He received his MSc in Mechanical Engineering from Iran University of Science and technology in 2011. **Armen Adamian** is an assistant professor of Mechanical Engineering at the Central Tehran Branch, IAU. He received his Ph.D. in Mechanical Engineering from University of California Los Angeles in 1986. His current research focuses on modal analysis, nanocomposites, structural dynamics. **Ahmad Hosseini-Sianaki** is an assistant professor of Mechanical Engineering at Central Tehran Branch, IAU. He received his Ph.D. in Mechanical engineering from the University of Sussex, England in 1990. His current research focuses on vibration systems and applications of smart materials in engineering and biomechanics.

Research paper

1 INTRODUCTION

In recent years, the invaluable mechanical, electrical, chemical, and thermal properties of nanostructures have encouraged researchers to study and use them in various engineering fields such as biomedical, nanocomposite, and micro/nano-electromechanical systems (MEMS/NEMS) [1].

Single-layer graphene sheet (SLGS) is a carbon-based nanostructure that has become a useful material in sensitive sensors such as nano-resonators, mass sensors, and strain sensors due to its unique properties such as high resonance frequencies and high elastic modulus, [2]. The geometric configuration for the graphene sheet has an essential effect on the mentioned properties that deformation can change them [3]. The pristine graphene sheet can be considered as a flat plate where the carbon atoms are inside a perfect hexagonal lattice. But different defects may appear in these sheets due to the production process. Based on how a defect is formed, it can be classified into three groups: adding carbon or other atoms (adatoms), eliminating carbon atoms from the graphene structure (vacancies) and rearrangement of carbon atoms (such as stone-wales) [4]. With the defects mentioned above, the graphene sheet remains 2D, however researchers [5] have shown that in the presence of some other defects, "graphene reshapes to a 3D state to minimize its energy". This out-of-plane defect is called the initial geometric imperfection [4]. Although the last defect may inevitably occur in a sheet, researchers have recently been able to determine the type and position of defects using manipulated processes to achieve desirable engineered defective graphene sheets [6-7]. Since the imperfection can change the mechanical properties of graphene sheets, understanding the behaviour of the imperfect graphene sheet will help to have an optimal design.

Suleimani et al. [8] analyzed the post-buckling behavior of an SLGS that has an initial geometric imperfection. Jomezadeh et al. [9] investigated the effects of initial configuration for graphene on bending stiffness by extracting non-local Equations for a single-layered graphene sheet with initial curvature. Jalali et al. [4] studied the effect of initial geometric imperfection on graphene sheet vibrations using molecular dynamics and a continuum approach. They observed that the out-of-plane defects increased the natural frequencies of graphene sheets. Implementing precise and controlled experiments at nanoscale is very costly, so researchers have turned to numerical simulations and theoretical analysis to find mechanical properties of nanostructures. There are three approaches available to researchers to implement numerical analysis: molecular dynamics (MD) simulation, continuum methods and combined continuum and molecular dynamics methods. Since molecular dynamics simulation is time-consuming, continuum methods have grown significantly in recent years. When the specimen size is of the order of internal length scale of the material, classical continuum theories are no longer appropriate and the use of nonlocal theories is essential [9]. Eringen's nonlocal elasticity theory [10] is one of the most popular continuum theories known, in which the stress at any point in the body, besides the strain at that point, depends on the strain in all the neighbouring regions in the continuum environment. The nonlocal theory considers inter-atomic forces and applies the internal length scale to the stress-strain Equations [11]. This theory can analyse the behaviour of large Nano-scale structures without having to solve a large number of Equations [12]. This theory, when considering the small-scale effects, provides a satisfactory analysis in comparison with the molecular dynamic's method [13]. From the continuum perspective, an SLGS can be considered as a nanoplate, and hence well-known plate theories can be employed to investigate the vibration response. Classical Plate Theory (CLPT) and first-order shear deformation theory are well-known theories in the analysis of small-scale structures that are used for thin and moderately thick plates, respectively [14-15]. Although the FSDT can be used to analyze moderately thick plates, it's always faced with the problem of selecting the shear correction factor and the shear locking phenomenon. To avoid using the shear correction factors and increase accuracy, researchers use various high-order shear deformation theories [16], [11]. Higher-order theories often have many unknown variables. To reduce the number of variables without decreasing the accuracy, Senthilnathan et al. [17] developed a Refined Plate Theory (RPT) using four independent variables. Subsequently, this theory was used in various nanoscale problems. The buckling and free vibration analysis of orthotropic graphene sheets and nanoplates using RPT was examined by Narendar et al. [18]. Also, Shimpi [19] and Malekzadeh and Shojaee [12] examined the vibrations of a nonlocal rectangular plate using the RPT and the DQM approach. Sarrami-Forushani and Azhari [11] studied the buckling and vibrations of thick rectangular graphene nanoplates using RPT and the finite strip method. In the theories mentioned above, the effects of thickness stretching are neglected, while these effects must be considered in the case of 3D strain $(\varepsilon_z \neq 0)$. For this purpose, high-order shear and normal deformation theories named quasi-3D can be used [20]. Zenkour [21] presented a four variables quasi-3D theory for the static analysis of FGM plates. Subsequently, this quasi-3D theory was used to analyze the bending behavior of FGM plates using the Navier approach [22]. Also, in various papers, the vibrations of plates and nanoplates are investigated using polynomial and non-

polynomial high order shear and normal deformation theory [20], [23-25]. In nanoplates modeling using RPT and quasi-3D theories, the displacement field requires at least C^1 continuity, whereas conventional finite element methods have C^0 continuity and cannot be used easily without adding variables [26]. For this purpose, Hughes et al. [27] presented a numerical method combining computer-aided design and Finite Element Analysis (FEA) based on Galerkin's weak form, named isogeometric analysis (IGA). In this method, a non-uniform rational B-spline basis function (NURBS) is used to describe the structure and also the solution field approximation simultaneously. These B-splines can easily meet the requirements of high-order continuity. Subsequently, because of unique features such as accurate geometry representation, and no need for high-level meshing and continuity, the IGA is widely used in analyzing plates and nanoplates with various plate theories such as FSDT [8], RPT, and quasi-3D theory [20-23], [25], [28].

As mentioned in the literature review, no study has been carried out on the nonlocal vibration analysis of SLGS with an initial geometric imperfection using the quasi-3D theory based on the IGA approach. In the present work, a four-variables quasi-3d theory is proposed to represent the displacement Equations of the plate. The initial geometric imperfection is given as a parametric function and two types of imperfections (sinusoidal and L1 types) are investigated. Using Eringen's nonlocal theory, small-scale effects are applied in the stress-strain Equation. A discrete system of Equations is extracted using the Hamilton principle and is solved by the isogeometric method. The effects of the imperfection amplitude, nonlocal parameter, plate geometrical parameters, and boundary conditions on the imperfection sensitivity and natural frequency of SLGS have been investigated. The comparison between present study and other published works indicates the efficiency and accuracy of the proposed method in imperfect SLGS.

2 GOVERNING EQUATIONS

2.1. Higher-Order Plate Theories

A rectangular graphene sheet that in the continuum approach is assumed as a nanoplate with length a, width b, and the uniform thickness h, is depicted in "Fig. 1".

If the thickness to side ratio for the nanoplate is very small, classical and first-order shear deformation theories can be used, but as the thickness increases, these theories are not accurate enough due to the lack of the shear effects consideration. By taking into account the shear effects, higher-order terms appear in the plate displacement field. Soldatos [29], using the generalized higher-order shear deformation theory, showed the displacement field as:

$$\begin{aligned} u(x,y,z) &= u_0(x,y) - zw_{,x}(x,y) + f(z)\beta_x(x,y) \\ v(x,y,z) &= v_0(x,y) - zw_{,y}(x,y) + f(z)\beta_y(x,y) \\ w(x,y) &= w_0(x,y) \end{aligned} \quad (1)$$

Where, u_0, v_0, and w_0 are the mid-plane displacements of the sheet along x, y, and z, and β_x, β_y are rotations about yz and xz plane, respectively. As it can be seen, in this theory, five variables are used.

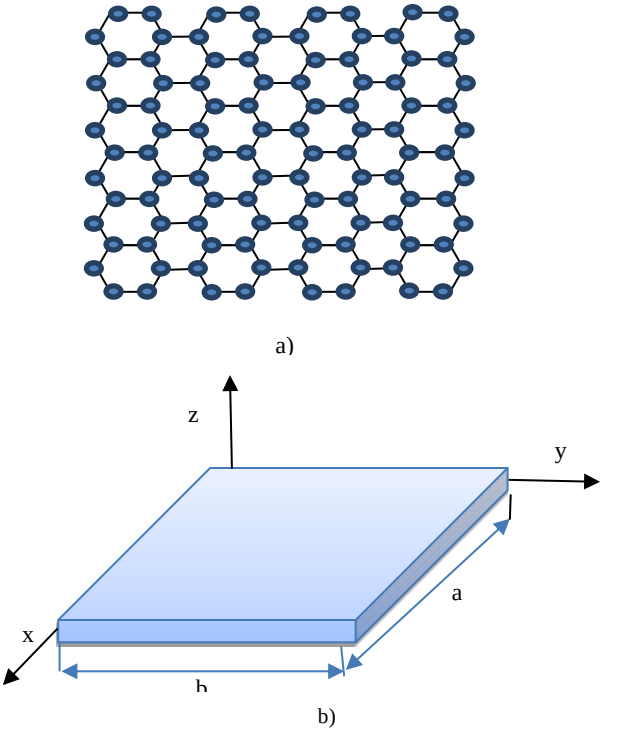

Fig. 1 Single-layer graphene Sheet: (a): Hexagonal lattice, and (b): Continuum model.

Senthilnathan [17] has introduced a refined plate theory (RPT) which uses four unknown variables:

$$\begin{aligned} u(x,y,z) &= u_0(x,y) - zw^b{}_{,x}(x,y) + g(z)w^s{}_{,x}(x,y) \\ v(x,y,z) &= v_0(x,y) - zw^b{}_{,y}(x,y) + g(z)w^s{}_{,y}(x,y) \\ w(x,y) &= w^b(x,y) + w^s(x,y) \end{aligned} \quad (2)$$

Where, w^b and w^s are the bending and shear deformations of the plate in the z-direction, respectively, and $g(z)=f(z)-z$. In the plate theories mentioned above, the effect of thickness stretching in the z-direction is not considered. To overcome this shortcoming, Zenkour

[21] presented a quasi-3D plate theory which has four unknown variables:

$$\begin{aligned} u(x,y,z) &= u_0(x,y) - zw^b{}_{,x}(x,y) + f(z)w^s{}_{,x}(x,y) \\ v(x,y,z) &= v_0(x,y) - zw^b{}_{,y}(x.y) + f(z)w^s{}_{,y}(x,y) \\ w(x,y,z) &= w^b(x,y) + \phi(z)w^s(x,y) \end{aligned} \quad (3)$$

The refined plate theory ("Eq. (2)") can be obtained by replacing $\phi(z)=1$ and *f(z)=g(z)* in "Eq. (3)". Different distribution functions have been used in various papers. In "Table 1", some of these functions are given based on the RPT and quasi-3D theory.

Table 1 Distribution functions used in various papers

Model	ε_z	*f(z)*	*Φ(z)*
Soldatos RPT [29]	*=0*	$h\,sinh\left(\frac{z}{h}\right) - z\,cosh\left(\frac{1}{2}\right)$	1
Nguyen RPT [30]	*=0*	$\frac{7}{8}z - \frac{2}{h^2}z^3 + \frac{2}{h^4}z^5$	1
Nguyen RPT [31]	*=0*	$tan^{-1}(sin(\pi z/h))$	1
Nguyen Quasi-3D [20]	*≠0*	$\frac{\pi}{h}z - \frac{9\pi}{5h^3}z^3 + \frac{28\pi}{25h^5}z^5$	$\frac{1}{8}f'(z)$
Zenkour Quasi-3D [22]	*≠0*	$h\,sinh\left(\frac{z}{h}\right) - \frac{4z^3}{3h^2}cosh\left(\frac{1}{2}\right)$	$\frac{1}{12}f'(z)$
Nguyen Quasi-3D [23]	*≠0*	$-8z + \frac{10}{h^2}z^3 + \frac{6}{5h^4}z^5 + \frac{8}{7h^6}z^7$	$\frac{3}{20}f'(z)$
Thai Quasi-3D [32]	*≠0*	$\frac{h}{\pi}sin(\frac{\pi z}{h})$	$f'(z)$
Gupta Quasi-3D [35]	*≠0*	$\frac{-hcosh^2\left(\frac{k}{2}\right)}{\sqrt{(1+\frac{k^2}{4})}-1}(sinh^{-1}\left(\frac{kz}{h}\right) - \left(\frac{kz}{h}\right))$	$kcosh^2(kz/h)$

In the presence of the initial geometric imperfection, the plate will become three-dimensional. Assuming that the initial geometric imperfection in the nanoplate exists only in the transverse direction, the displacement Equation can be corrected as follows [4], [8]:

$$\begin{aligned} u(x,y,z) &= u_0(x,y) - zw^b{}_{,x}(x,y) + f(z)w^s{}_{,x}(x,y) \\ v(x,y,z) &= v_0(x,y) - zw^b{}_{,y}(x,y) + f(z)w^s{}_{,y}(x,y) \\ w(x,y,z) &= w^b(x,y) + \phi(z)w^s(x,y) + w^i(x,y) \end{aligned} \quad (4)$$

Where, $w^i(x,y)$ denotes the initial geometric imperfection function in the nanoplate.

2.2. Size-Dependent Plate Theory

By using Eringen's nonlocal elasticity theory, the stress-strain relations are simplified in the following way:

$$\left(1-\mu\nabla^2\right)\sigma_{ij} = C_{ijkl}\varepsilon_{kl} \quad (5)$$

Where, $\mu=(e_0a_0)^2$ is the small-scale parameter (e_0 and a_0 are respectively the material constant, and the internal characteristic length) and ∇^2 is the Laplacian operator. Using "Eq. (5)", nonlocal constitutive Equations for a nonlocal plate can be expressed by:

$$\begin{bmatrix}\sigma_{xx}\\ \sigma_{yy}\\ \sigma_{zz}\\ \sigma_{xy}\\ \tau_{xz}\\ \tau_{yz}\end{bmatrix} - \mu\nabla^2\begin{bmatrix}\sigma_{xx}\\ \sigma_{yy}\\ \sigma_{zz}\\ \sigma_{xy}\\ \tau_{xz}\\ \tau_{yz}\end{bmatrix} = \begin{bmatrix} C_{11} & C_{12} & C_{13} & 0 & 0 & 0 \\ C_{21} & C_{22} & C_{23} & 0 & 0 & 0 \\ C_{31} & C_{32} & C_{33} & 0 & 0 & 0 \\ 0 & 0 & 0 & C_{66} & 0 & 0 \\ 0 & 0 & 0 & 0 & C_{55} & 0 \\ 0 & 0 & 0 & 0 & 0 & C_{44} \end{bmatrix}\begin{bmatrix}\varepsilon_{xx}\\ \varepsilon_{yy}\\ \varepsilon_{zz}\\ \gamma_{xy}\\ \gamma_{xz}\\ \gamma_{yz}\end{bmatrix} \quad (6)$$

If the quasi-3D theory is used, the elastic constants for the state $\varepsilon_z \neq 0$ will be [21]:

$$C_{11}=C_{22}=C_{33}=\frac{E(1-\nu)}{(1-2\nu)(1+\nu)}$$
$$C_{12}=C_{21}=C_{13}=C_{31}=C_{23}=C_{32}=\frac{E\nu}{(1-2\nu)(1+\nu)} \quad (7)$$
$$C_{44}=C_{55}=C_{66}=\frac{E}{2(1+\nu)}$$

However, if the RPT is used, the elastic constants for the plane stress state $(\varepsilon_z=0)$ can be written as:

$$C_{11}=C_{22}=\frac{E}{1-\nu^2}, \qquad C_{12}=C_{21}=\frac{E\nu}{1-\nu^2}$$
$$C_{13}=C_{31}=C_{23}=C_{32}=C_{32}=0 \quad (8)$$
$$C_{44}=C_{55}=C_{66}=\frac{E}{2(1+\nu)}$$

Using "Eq. (4)", the Von Karman [22] strain-displacement relationship at a chosen point on the sheet can be described as:

$$\varepsilon=\begin{bmatrix}\varepsilon_{xx}\\ \varepsilon_{yy}\\ \gamma_{xy}\end{bmatrix}=\varepsilon_0+z\varepsilon_1+f(z)\varepsilon_2+\Phi(z)\varepsilon_3$$
$$\gamma=\begin{bmatrix}\gamma_{xz}\\ \gamma_{yz}\end{bmatrix}=\left[f'(z)+\Phi(z)\right]\varepsilon_s,\ \varepsilon_z=\Phi'(z)w^s \quad (9)$$

Where:

$$\varepsilon_0=\begin{bmatrix}u_{0,x}+w^b{}_{,x}w^i{}_{,x}\\ v_{0,y}+w^b{}_{,y}w^i{}_{,y}\\ u_{0,y}+v_{0,x}+w^b{}_{,x}w^i{}_{,y}+w^b{}_{,y}w^i{}_{,x}\end{bmatrix},$$
$$\varepsilon_1=-\begin{bmatrix}w^b{}_{,xx}\\ w^b{}_{,yy}\\ 2w^b{}_{,xy}\end{bmatrix},\varepsilon_2=\begin{bmatrix}w^s{}_{,xx}\\ w^s{}_{,yy}\\ 2w^s{}_{,xy}\end{bmatrix}, \quad (10)$$
$$\varepsilon_3=\begin{bmatrix}w^s{}_{,x}w^i{}_{,x}\\ w^s{}_{,y}w^i{}_{,y}\\ w^s{}_{,x}w^i{}_{,y}+w^s{}_{,y}w^i{}_{,x}\end{bmatrix},\ \varepsilon_s=\begin{bmatrix}w^s{}_{,x}\\ w^s{}_{,y}\end{bmatrix}$$

The stress resultants can be considered as:

$$(N_{ij},M^b{}_{ij},M^s{}_{ij},M^i{}_{ij})=\int_{-\frac{h}{2}}^{\frac{h}{2}}\sigma_{ij}\left(1,z,f(z),\Phi(z)\right)dz\ ,ij=xx,yy,xy$$

$$R_z=\int_{-\frac{h}{2}}^{\frac{h}{2}}\sigma_{zz}\Phi'(z)dz \quad (11)$$
$$Q_{ij}=\int_{-\frac{h}{2}}^{\frac{h}{2}}\tau_{ij}\left(f'(z)+\Phi(z)\right)dz \quad ,ij=xz,yz$$

Now using Eqs. (9) to (11), Eq. (6) can be rewritten as stress resultants:

$$\begin{bmatrix}N\\ M^b\\ M^s\\ M^i\\ R_z\end{bmatrix}-\mu\nabla^2\begin{bmatrix}N\\ M^b\\ M^s\\ M^i\\ R_z\end{bmatrix}=D^b\varepsilon^b\ ,\quad Q-\mu\nabla^2Q=D^s\varepsilon^s \quad (12)$$

Where the material matrices are:

$$D^b=\begin{bmatrix}A & B & E & K & X\\ & D & F & L & Y^b\\ & & H & O & Y^s\\ & & & P^1 & Y^i\\ sym & & & & Z_{33}\end{bmatrix}$$
$$(A_{ij},B_{ij},D_{ij},E_{ij},F_{ij},H_{ij},K_{ij},L_{ij},O_{ij},P_{ij})=$$
$$\int_{-\frac{h}{2}}^{\frac{h}{2}}\begin{pmatrix}1,z,z^2,f(z),zf(z),\left(f(z)\right)^2\\ ,\Phi(z),z\Phi(z),f(z)\Phi(z),\left(\Phi(z)\right)^2\end{pmatrix}\bar{C}_{ij}dz \quad (13)$$

$$(X_{ij},Y^b{}_{ij},Y^s{}_{ij},Y^i{}_{ij})=$$
$$\int_{-\frac{h}{2}}^{\frac{h}{2}}(\Phi'(z),z\Phi'(z),f(z)\Phi'(z),\Phi(z)\Phi'(z))\hat{C}_{ij}dz$$

$$Z_{33}=\int_{-\frac{h}{2}}^{\frac{h}{2}}(\Phi'(z))^2C_{33}dz$$
$$,D^s{}_{ij}=\int_{-\frac{h}{2}}^{\frac{h}{2}}\left(f'(z)+\Phi(z)\right)^2\tilde{C}_{ij}dz \quad (14)$$

In which:

$$\bar{C}_{ij}=\begin{bmatrix} C_{11} & C_{12} & 0 \\ & C_{22} & 0 \\ sym & & C_{66} \end{bmatrix},\qquad \hat{C}_{ij}=\begin{bmatrix} C_{13} \\ C_{23} \\ 0 \end{bmatrix},$$
$$\tilde{C}_{ij}=\begin{bmatrix} C_{55} & 0 \\ 0 & C_{44} \end{bmatrix} \tag{15}$$

And also, the strain tensor ε^b is:

$$\varepsilon^b=\begin{bmatrix} \varepsilon_0 \\ \varepsilon_1 \\ \varepsilon_2 \\ \varepsilon_3 \\ w^s \end{bmatrix} \tag{16}$$

To derive the governing Equations of the graphene sheet, Hamilton's principle is expressed as:

$$\int_0^t \left(\delta U+\delta V-\delta T\right)dt=0 \tag{17}$$

The variation of strain energy can be expressed by:

$$\delta U=\int_V(\sigma^T\delta\varepsilon)dV=\int_A\int_{-\frac{h}{2}}^{\frac{h}{2}}(\begin{bmatrix} \sigma_{xx} \\ \sigma_{yy} \\ \sigma_{xy} \end{bmatrix}^T\delta(\begin{bmatrix} \varepsilon_{xx} \\ \varepsilon_{yy} \\ \gamma_{xy} \end{bmatrix})$$
$$+\begin{bmatrix} \tau_{xz} \\ \tau_{yz} \end{bmatrix}^T\delta\left(\begin{bmatrix} \gamma_{xz} \\ \gamma_{yz} \end{bmatrix}\right)+{\sigma_{zz}}^T\delta\varepsilon_z)dzdA=$$
$$\int_A(N_{xx}(\delta u_{0,x}+w^i{}_{,x}\delta w^b{}_{,x})+N_{yy}\left(\delta v_{0,y}+w^i{}_{,y}\delta w^b{}_{,y}\right)$$
$$+N_{xy}\left(\delta u_{0,y}+\delta v_{0,x}+w^i{}_{,y}\delta w^b{}_{,x}+w^i{}_{,x}\delta w^b{}_{,y}\right)+$$
$$M^b{}_{xx}\left(-\delta w^b{}_{,xx}\right)+M^b{}_{yy}\left(-\delta w^b{}_{,yy}\right)+M^b{}_{xy}\left(-2\delta w^b{}_{,x}\right) \tag{18}$$
$$+M^s{}_{xx}\left(\delta w^s{}_{,xx}\right)+M^s{}_{yy}\left(\delta w^s{}_{,yy}\right)+M^s{}_{xy}\left(2\delta w^s{}_{,xy}\right)+$$
$$M^i{}_{xx}\left(w^i{}_{,x}\delta w^s{}_{,x}\right)+M^i{}_{yy}\left(w^i{}_{,y}\delta w^s{}_{,y}\right)+$$
$$M^i{}_{xy}\left(w^i{}_{,y}\delta w^s{}_{,x}+w^i{}_{,x}\delta w^s{}_{,y}\right)+Q_{xz}\left(\delta w^s{}_{,x}\right)+Q_{yz}\left(\delta w^s{}_{,y}\right)$$
$$+R_z\delta w^s)dA$$

Also, the variation of work done by external forces is:

$$\delta V=\int_V(-q\delta w)dV=\int_A\int_{-\frac{h}{2}}^{\frac{h}{2}}q\delta(w^b+\phi(z)w^s+w^i)dzdA \tag{19}$$

Since $\delta w^i=0$ and q=0, therefore:

$$\delta V=-\int_A\int_{-\frac{h}{2}}^{\frac{h}{2}}q(\delta w^b+\phi(z)\delta w^s)dzdA=$$
$$-\int_A q(\delta w^b+\phi(\frac{h}{2})\delta w^s)dA=0 \tag{20}$$

The variation of kinetic energy can also be written as:

$$\delta T=\int_V\rho\dot{\bar{u}}^T\delta\dot{\bar{u}}dV \tag{21}$$

Considering $u=\begin{bmatrix} u_0 & -w^b{}_{,x} & w^s{}_{,x} & v_0 & -w^b{}_{,y} & w^s{}_{,y} & w^b & w^s & 0 \end{bmatrix}^T$, the above Equation can be expressed as:

$$\delta T=-\int_A\int_{-\frac{h}{2}}^{\frac{h}{2}}\rho(\left(\dot{u}_0-z\dot{w}^b_{,x}+f\left(z\right)\dot{w}^s_{,x}\right)\begin{pmatrix}\delta\dot{u}_0-z\delta\dot{w}^b_{,x}\\+f\left(z\right)\delta\dot{w}^s_{,x}\end{pmatrix}$$
$$+\left(\dot{v}_0-z\dot{w}^b_{,y}+f\left(z\right)\dot{w}^s_{,y}\right)\left(\delta\dot{v}_0-z\delta\dot{w}^b_{,y}+f\left(z\right)\delta\dot{w}^s_{,y}\right) \tag{22}$$
$$+(\dot{w}^b+\phi(z)\dot{w}^s)(\delta\dot{w}^b+\phi(z)\delta\dot{w}^s))dzdA$$

"Eq. (22)" can be simply rewritten as:

$$\delta T=\int_V\ddot{\bar{u}}^T m\delta\dot{\bar{u}}dV \tag{23}$$

In which the mass matrix is defined as:

$$m=\begin{bmatrix} m_0 & 0 & 0 \\ 0 & m_0 & 0 \\ 0 & 0 & m_1 \end{bmatrix},\ m_0=\begin{bmatrix} I_1 & I_2 & I_4 \\ I_2 & I_3 & I_5 \\ I_4 & I_5 & I_6 \end{bmatrix},$$
$$m_1=\begin{bmatrix} I_1 & I_7 & 0 \\ I_7 & I_8 & 0 \\ 0 & 0 & 0 \end{bmatrix} \tag{24}$$

$$I_1,I_2,I_3,I_4,I_5,I_6,I_7,I_8=$$
$$\int_{-\frac{h}{2}}^{\frac{h}{2}}\rho(1,z,z^2,f\left(z\right),zf\left(z\right),\left(f\left(z\right)\right)^2,\Phi(z),\left(\Phi(z)\right)^2)dz \tag{25}$$

The governing Equations for the plate in the displacement form can be obtained by inserting "Eqs. (18), (20), and (23)" in "Eq. (17)", and then integrating by parts and sorting gives:

$$
\begin{aligned}
&\delta u_0: \quad N_{xx,x}+N_{xy,y}=I_1\ddot{u}_0-I_2\ddot{w}^b_{,x}+I_4\ddot{w}^s_{,x}\\
&\delta v_0: \quad N_{yy,y}+N_{xy,x}=I_1\ddot{v}_0-I_2\ddot{w}^b_{,y}+I_4\ddot{w}^s_{,y}\\
&\delta w^b:(N_{xx}w^i{}_{,x})_{,x}+(N_{yy}w^i{}_{,y})_{,y}+(N_{xy}w^i{}_{,y})_{,x}\\
&+(N_{xy}w^i{}_{,x})_{,y}+M^b{}_{xx,xx}+M^b{}_{yy,yy}-2M^b{}_{xy,xy}=\\
&I_1\ddot{w}^b+I_2\left(\ddot{u}_{0,x}+\ddot{v}_{0,y}\right)-I_3\left(\ddot{w}^b_{,xx}+\ddot{w}^b_{,yy}\right)+\\
&I_5\left(\ddot{w}^s_{,xx}+\ddot{w}^s_{,yy}\right)+I_7\ddot{w}^s\\
&\delta w^s: \ -M^s{}_{xx,xx}-M^s{}_{yy,yy}-2M^s{}_{xy,xy}-R_z+Q_{xz,x}\\
&+Q_{yz,y}+(M^i{}_{xx}w^i{}_{,x})_{,x}+(M^i{}_{yy}w^i{}_{,y})_{,y}+(M^i{}_{xy}w^i{}_{,x})_{,y}\\
&+(M^i{}_{xy}w^i{}_{,y})_{,x}=-I_4\left(\ddot{u}_{0,x}+\ddot{v}_{0,y}\right)+I_5\left(\ddot{w}^b_{,xx}+\ddot{w}^b_{,yy}\right)\\
&-I_6\left(\ddot{w}^s_{,xx}+\ddot{w}^s_{,yy}\right)+I_7\ddot{w}^b+I_8\ddot{w}^s
\end{aligned}
\tag{26}
$$

After inserting "Eqs (10) to (15)" in "Eq. (26)", the above Equations must be pre-multiplied by $\delta u_0, \delta v_0, \delta w^b, \delta w^s$, respectively and integrated by part in a region to extract the nonlocal weak form. Readers can refer to [20] for further explanation. The nonlocal weak form for the free vibration problem is summarized in the following:

$$
\begin{aligned}
&\int_A((\delta\varepsilon^b)^T D^b\varepsilon^b dA+\int_A((\delta\varepsilon^s)^T D^s\varepsilon^s dA+\\
&\int_A(\delta u^T-\mu\nabla^2\delta u^T)m\ddot{u}\,dA
\end{aligned}
\tag{27}
$$

As it can be seen from "Eq. (27)", the plate transverse deflection variables (w^b, w^s) appear in the form of third-order derivatives due to the nonlocal effects and are accompanied by the Laplacian operator. So, the interpolation functions in the conventional finite element method must have at least a third-degree derivative and satisfy the C^1 continuity, which cannot easily be accomplished. Therefore, the isogeometric approach along with NURBS basis functions can be used well to solve nonlocal SLGS Equations using RPT and quasi-3D theory.

3 IGA FOR FREE VIBRATION PROBLEM

3.1. Summary of NURBS Basis Functions

The NURBS basis functions are applied in both modeling geometries and finite element analysis in IGA. In one dimensional parametric space $(\xi\in[0,1])$, NURBS basis functions are composed of a set of non-decreasing real numbers $K(\xi)=\{\xi1=0,\xi2,\ldots,\xi_i,\ldots,\xi_{n+p+1}=1\}$, that are called knot vectors (ξ_i, *p, n* are knots, the polynomial order, and the number of basis functions, respectively), and a set of control points.

Each B-spline has a C^∞ continuity inside the knot space and a C^{p-1}continuity at a single knot. The continuity at a knot where repeats k times, is C^{p-k}. The i'th B-spline basis function is written as the following recursive form [23]:

$$
\begin{aligned}
&N_{i,0}(\xi)=\begin{cases}1 & if\ \ \xi_i\le\xi\le\xi_{i+1}\\ 0 & else\end{cases} \qquad \text{for } p=0\\
&N_{i,p}(\xi)=\frac{\xi-\xi_i}{\xi_{i+p}-\xi_i}N_{i,p-1}(\xi)+\frac{\xi_{i+p+1}-\xi}{\xi_{i+p+1}-\xi_{i+1}}N_{i+1,p-1}(\xi)\\
&\text{for } p\ge1
\end{aligned}
\tag{28}
$$

The two-dimensional basis functions are obtained by the tensor product of two one-dimensional B-spline basis functions as:

$$
N_I(\xi,\eta)=N_{i,p}(\xi)N_{j,q}(\eta) \tag{29}
$$

Where, $N_{i,p}(\xi)$ and $N_{j,q}(\eta)$ are the B-spline basis functions with an order of p in the ξ direction and order of q in the η direction, respectively. Fig. 2 shows the B-spline basis functions.

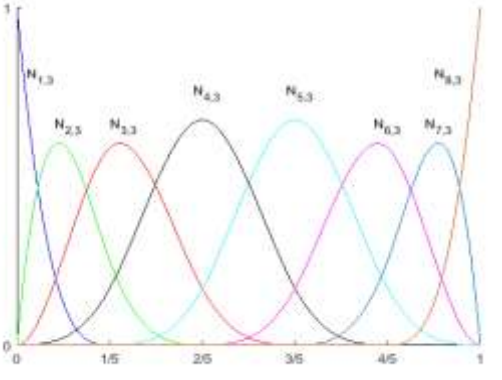

Fig. 2 Cubic basis functions for open non-uniform knot vector $\xi=\{0,0,0,0,\frac{1}{5},\frac{2}{5},\frac{3}{5},\frac{4}{5},1,1,1,1\}$.

B-spline basis functions cannot accurately represent cone shapes like circles and ellipses. Using NURBS, these shapes can be displayed accurately. Two dimensional NURBS basis function for a NURBS surface can be derived from the following Equation:

$$
R_I(\xi,\eta)=\frac{N_I(\xi,\eta)W_I}{\sum_{I=1}^{m\times n}(N_I(\xi,\eta)W_I)} \tag{30}
$$

In which W_I shows the two-dimensional weight function.

3.2. Quasi-3D Nanoplate Formulation Based on NURBS Basis Function

The displacement variables using NURBS basis functions can be interpolated as follows:

$$u^h(\xi,\eta)=\sum_{I=1}^{m\times n}\left(R_I(\xi,\eta)u_I\right) \tag{31}$$

Where, $u_I=\begin{bmatrix}u_0 & v_0 & w^b & w^s\end{bmatrix}$ is the degrees of freedom vector associated with the control point I, and $m \times n$ is the number of basis functions. Using "Eq. (31)", the in-plane, normal and shear strains "Eq. (10)" can be rewritten as:

$$\varepsilon_0=\sum_{I=1}^{m\times n}\left(\begin{bmatrix}R_{I,x} & 0 & R_{I,x}w^i{}_{,x} & 0\\ 0 & R_{I,y} & R_{I,y}w^i{}_{,y} & 0\\ R_{I,y} & R_{I,x} & R_{I,x}w^i{}_{,y}+R_{I,y}w^i{}_{,x} & 0\end{bmatrix}\begin{Bmatrix}u_{0I}\\ v_{0I}\\ w^b{}_I\\ w^s{}_I\end{Bmatrix}\right)=$$

$$\sum_{I=1}^{m\times n}B^m{}_I u_I$$

$$\varepsilon_1=\sum_{I=1}^{m\times n}\left(-\begin{bmatrix}0 & 0 & R_{I,xx} & 0\\ 0 & 0 & R_{I,yy} & 0\\ 0 & 0 & 2R_{I,xy} & 0\end{bmatrix}\begin{Bmatrix}u_{0I}\\ v_{0I}\\ w^b{}_I\\ w^s{}_I\end{Bmatrix}\right)=\sum_{I=1}^{m\times n}B^1{}_I u_I$$

$$\varepsilon_2=\sum_{I=1}^{m\times n}\left(\begin{bmatrix}0 & 0 & 0 & R_{I,xx}\\ 0 & 0 & 0 & R_{I,yy}\\ 0 & 0 & 0 & 2R_{I,xy}\end{bmatrix}\begin{Bmatrix}u_{0I}\\ v_{0I}\\ w^b{}_I\\ w^s{}_I\end{Bmatrix}\right)=\sum_{I=1}^{m\times n}B^2{}_I u_I$$

$$\varepsilon_3=\sum_{I=1}^{m\times n}\left(\begin{bmatrix}0 & 0 & 0 & R_{I,x}w^i{}_{,x}\\ 0 & 0 & 0 & R_{I,y}w^i{}_{,y}\\ 0 & 0 & 0 & R_{I,x}w^i{}_{,y}+R_{I,y}w^i{}_{,x}\end{bmatrix}\begin{Bmatrix}u_{0I}\\ v_{0I}\\ w^b{}_I\\ w^s{}_I\end{Bmatrix}\right)$$

$$=\sum_{I=1}^{m\times n}B^3{}_I u_I$$

$$\varepsilon^s=\sum_{I=1}^{m\times n}\left(\begin{bmatrix}0 & 0 & 0 & R_{I,x}\\ 0 & 0 & 0 & R_{I,y}\end{bmatrix}\begin{Bmatrix}u_{0I}\\ v_{0I}\\ w^b{}_I\\ w^s{}_I\end{Bmatrix}\right)=\sum_{I=1}^{m\times n}B^s{}_I u_I \tag{32}$$

Also, according to "Eq. (9)", we can write:

$$\varepsilon_z=\sum_{I=1}^{m\times n}\left(\begin{bmatrix}0 & 0 & 0 & R_I\end{bmatrix}\begin{Bmatrix}u_{0I}\\ v_{0I}\\ w^b{}_I\\ w^s{}_I\end{Bmatrix}\right)=\sum_{I=1}^{m\times n}B^z{}_I u_I \tag{33}$$

The free vibration Equations in matrix form can be obtained by inserting "Eqs. (32), (33)" in "Eq. (27)":

$$\left(\left[K\right]+\omega^2\left[M\right]\right)u=0 \tag{34}$$

In which the general stiffness and mass matrices are:

$$K=\int_A\left(\begin{bmatrix}B^m\\ B^1\\ B^2\\ B^3\\ B^z\end{bmatrix}^T\boldsymbol{D^b}\begin{bmatrix}B^m\\ B^1\\ B^2\\ B^3\\ B^z\end{bmatrix}+\left(B^s\right)^T\boldsymbol{D^s}B^s\right)dA$$

$$M=\int_A\left(\left(\begin{bmatrix}R_1\\ R_2\\ R_3\end{bmatrix}^T-\mu\nabla^2\begin{bmatrix}R_1\\ R_2\\ R_3\end{bmatrix}^T\right)\boldsymbol{m}\begin{bmatrix}R_1\\ R_2\\ R_3\end{bmatrix}\right)dA \tag{35}$$

Where:

$$R_1=\begin{bmatrix}R_I & 0 & 0 & 0\\ 0 & 0 & -R_{I,x} & 0\\ 0 & 0 & 0 & R_{I,x}\end{bmatrix},\ R_2=\begin{bmatrix}0 & R_I & 0 & 0\\ 0 & 0 & -R_{I,y} & 0\\ 0 & 0 & 0 & R_{I,y}\end{bmatrix}$$

$$,\ R_3=\begin{bmatrix}0 & 0 & R_I & R_I\\ 0 & 0 & 0 & 0\\ 0 & 0 & 0 & 0\end{bmatrix} \tag{36}$$

4 NUMERICAL RESULTS AND DISCUSSION

In this section, the vibration behavior of a geometrically imperfect graphene sheet has been investigated. Numerical integrations have been implemented using 4×4 Gaussian quadrature points with cubic NURBS elements. A seventh-order polynomial distribution function f(z) is chosen to satisfy the zero-traction boundary conditions at the top and bottom surfaces of the plate. Therefore, there is no need to select the shear correction factor. The coefficients are obtained by performing the optimization method in such a way that the difference between present results and results from other researchers are minimized.

$$f(z)=\frac{11z}{8}-\frac{11z^3}{6h^2}+\frac{7z^5}{20h^4}-\frac{z^7}{h^6}$$
$$\phi(z)=\frac{1}{3}f'(z) \tag{37}$$

The boundary conditions on the edges of the plate are considered as:

Simply supported (S):

$$\begin{aligned} v_0 &= w^b = w^s = 0 \qquad at \quad x=0,a \\ u_0 &= w^b = w^s = 0 \qquad at \quad y=0,b \end{aligned} \tag{38}$$

Clamped (C):

$$\begin{aligned} &u_0 = v_0 = w^b = w^s = 0 \\ &w^b{}_{,x} = w^b{}_{,y} = w^s{}_{,x} = w^s{}_{,y} = 0 \end{aligned} \quad \text{at all edges} \tag{39}$$

The Dirichlet boundary conditions can easily be applied in the same way as traditional FEM. For normal slopes e.g., $w^b{}_{,x}$, $w^b{}_{,y}, w^s{}_{,x}$ and $w^s{}_{,y}$, Auricchio et al. [33] presented a simple and appropriate solution. In addition to displacements at the boundary control points, they imposed zero values for transverse bending and shear displacements adjacent to the boundary control points.
To investigate the convergence, a pristine square SLGS with Young modulus E=1.06 TPa, thickness h=0.34 nm, density ρ= 2250 $\frac{kg}{m^3}$, and a width of a=10 nm is used. Both localized (μ=0) and nonlocalized (μ=1) assumptions, and simply supported boundary conditions (SSSS) are implemented. The fundamental frequencies for several elements are given in "Table 2". To carry out the best comparison with existing papers, a refined plate theory is used.

Table 2 Convergence of fundamental frequency (THZ) for pristine SLGS (a=10, v=0.25)

		$\mu=0$	$\mu=1$
Element Mesh	7 × 7	0.068915	0.062979
	9 × 9	0.068914	0.062978
	11 × 11	0.068913	0.062978
	13 × 13	0.068913	0.062978
	RPT [11]	0.068917	0.062981
	CPT [34]	0.069126	0.063172

As it can be seen, responses converge after applying 11 grid points. Therefore, in continuing this study, a mesh of 11×11 cubic NURBS elements is used in the numerical calculations. This mesh and the corresponding control points are shown in "Fig. 3".

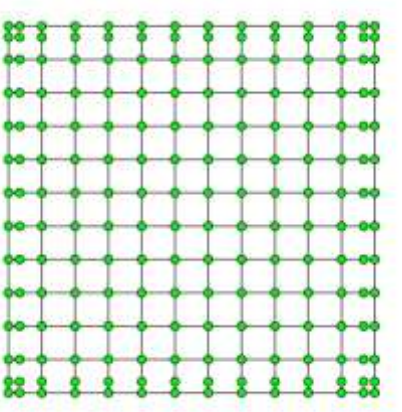

Fig. 3 Control point net and element mesh for SLGS.

To verify the present results, first a nonlocal pristine graphene sheet (without geometric imperfection) and then a localized imperfect graphene sheet are analyzed, and the results are compared with published papers. A pristine graphene sheet with the specifications mentioned before and a length of 5 nm and 10 nm are considered. Simply supported boundary condition is applied, and results for different aspect ratios and nonlocal parameters are shown in "Table 3".

Table 3 Fundamental frequencies (THZ) of SSSS pristine SLGS(v=0.25)

μ	a	$\frac{b}{a}$	Present RPT	Present quasi-3D	RPT [11]	CPT [34]
0	5	1	0.273212	0.278897	0.273201	0.276505
		2	0.171514	0.175296	0.171533	0.172833
		3	0.152583	0.155983	0.152608	0.153636
	10	1	0.068913	0.070522	0.068917	0.069126
		2	0.043120	0.044140	0.043126	0.043208
		3	0.038337	0.039246	0.038344	0.038409
1	5	1	0.204233	0.208482	0.204224	0.206694
		2	0.140346	0.143441	0.140361	0.141425
		3	0.127212	0.130047	0.127233	0.128090
	10	1	0.062978	0.064447	0.062981	0.063172
		2	0.040683	0.041646	0.040689	0.040767
		3	0.036393	0.037256	0.036400	0.036462

The fundamental frequencies obtained using present RPT and quasi-3D methods are compared with the results from other researchers. Results are in good agreement with the RPT [11] and CPT [34]. Due to stretching effects, Quasi-3D theory gives larger responses than RPT and CPT. For thinner sheets (a = 10), frequencies for different plate theories are very close to each other, while in thicker sheets (a = 5), they are somewhat different. As the nonlocal parameter increases, the fundamental frequency decreases due to a decrease in the sheet stiffness.

In the presence of initial geometric imperfection, the plate is no longer a sheet and becomes three-dimensional. Therefore, in this case, "Eq. (4)" along with geometric imperfection-function is used. Although the imperfection function can exist in various forms, to study the amplitude, frequency and defect location parametrically, the initial geometric imperfection is represented as a three-dimensional surface as [35]:

$$w^i(x,y) = \xi\, h\, sech\left(\frac{\delta_1(x-x_c)}{a}\right)\cos\left(\frac{\mu_1\pi(x-x_c)}{a}\right) \operatorname{sech}\left(\frac{\delta_2(y-y_c)}{b}\right)\cos\left(\frac{\mu_2\pi(y-y_c)}{b}\right) \quad (40)$$

Where, ξ is the amplitude to thickness ratio, (x_c, y_c) is the position of the bulge maximum amplitude, (μ_1, μ_2) are imperfection half wave numbers in the x and y directions, respectively and (δ_1, δ_2) determine the localize degree of imperfection. In "Eq. (41)", hyperbolic functions determine the extension of the bulge, and trigonometric functions generate bulges with a maximum value in (x_c, y_c). Therefore, they create a wide range of initial geometric imperfection modes [35]. Two of these imperfections are shown in "Fig. 4".

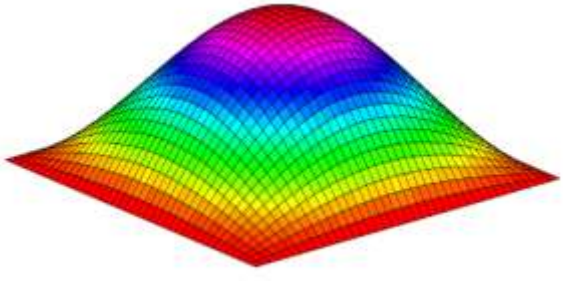

(a): Sine type: $\delta_1 = \delta_2 = 0,\ \mu_1 = \mu_2 = 1,\ \frac{x_c}{a} = \frac{y_c}{b} = 0.5$

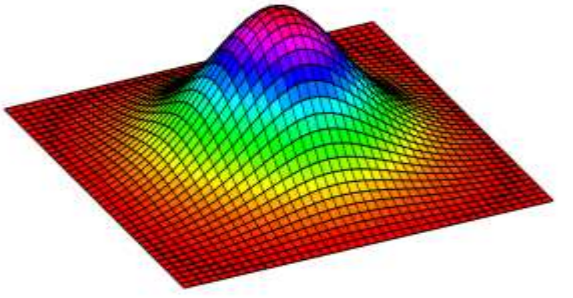

(b): L1 type: $\delta_1 = \delta_2 = 5,\ \mu_1 = \mu_2 = 1,\ \frac{x_c}{a} = \frac{y_c}{b} = 0.5$

Fig. 4 Sinusoidal and L1 type imperfection modes.

Fig. 5 shows variations of the imperfection sensitivity with imperfection amplitude (ξ) for a square SLGS with a Poisson ratio of 0.16. Imperfection sensitivity is defined as $S = \left|\frac{\omega^* - \bar{\omega}}{\bar{\omega}}\right| \times 100$, where $\bar{\omega}, \omega^*$, are the fundamental frequencies for perfect and imperfect SLGS, respectively. The sinusoidal imperfection type and SSSS boundary condition are considered here. As shown, the imperfection sensitivity increases with an increase in imperfection amplitude, since the stiffness and consequently the natural frequency of the plate increases. If the bulge maximum amplitude value approaches the plate thickness $(\xi = 1)$, then the natural frequency will reach twice the natural frequency of the perfect SLGS. Also, a greater thickness to side ratio gives a higher imperfection sensitivity. The amount of this increase is more visible for larger imperfection amplitudes.

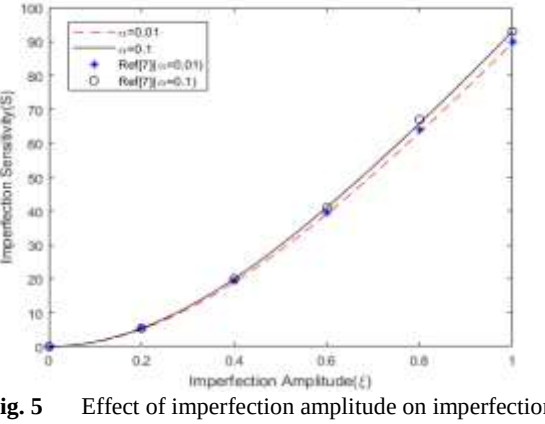

Fig. 5 Effect of imperfection amplitude on imperfection sensitivity for local square SLGS.

The variations of imperfection sensitivity for geometrically imperfect square SLGS with imperfection amplitude 'ξ' and the nonlocal parameter are depicted in "Fig. 6".

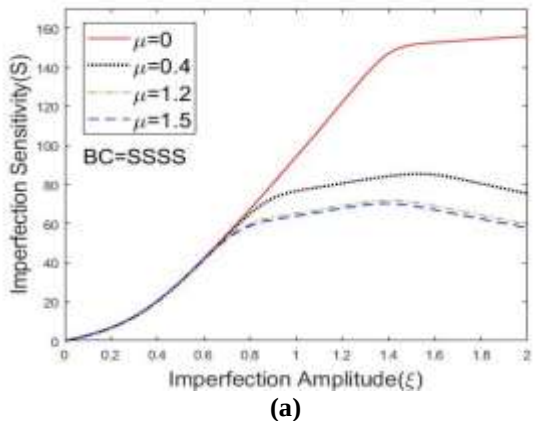

(a)

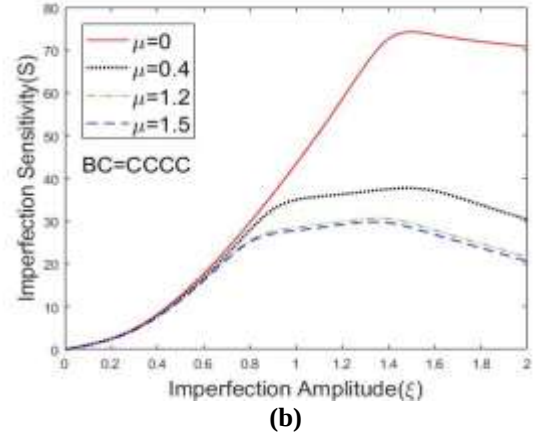

(b)

Fig. 6 Effect of imperfection amplitude on imperfection sensitivity for square SLGS (a=2 nm).

The sinusoidal imperfection type with a=2 nm is considered. In the SSSS boundary condition, for ξ<0.7, the imperfection sensitivity is independent of the nonlocal parameter. In this state, classical continuum and nonlocal theories give the same results. For higher imperfection amplitude, imperfection sensitivity decreases with increasing nonlocal parameter. For large imperfection amplitude (ξ>1.4), the imperfection sensitivity for nonlocal SLGS decreases. In local plates, with increasing d, the stiffness of the sheet and consequently the natural frequency always increases. In nonlocal sheets, with increasing ξ, the sheet stiffness as well as the natural frequency increase. But for larger ξ, the stiffness-softening phenomenon occurs in the sheet and the natural frequency of the sheet begins to decrease again. Also, the imperfection sensitivity for the large nonlocal parameter is less affected by the imperfection amplitude, while at lower nonlocal parameters, especially for the local plate, its effect is more visible. In the CCCC boundary condition, the variation of imperfection sensitivity is somewhat similar to SSSS, but it depends on the nonlocal parameter over a wider range of ξ and is independent of this parameter for ξ<0.3. Also, imperfection sensitivity in SLGS with clamped edges is lower than simply-supported edges. In other words, the geometric imperfection has less effect on the natural frequency of the clamped geometrically imperfect SLGS.

The effects of the imperfection extension parameter (δ) on imperfection sensitivity for SSSS and CCCC boundary conditions are shown in "Fig. 7". The results are depicted for several imperfection amplitudes ξ. As shown for the SSSS boundary condition, an increase in δ, which indicates a greater concentration of imperfection at the center of the nanoplate, decreases the imperfection sensitivity while decreasing δ and approaching to sinusoidal type, the imperfection sensitivity increases. When δ tends to large values, the imperfection sensitivity converges to a constant value for all ξ. For the CCCC boundary condition, as δ increases, the imperfection sensitivity increases first and then starts decreasing, so that the maximum value of imperfection sensitivity for all ξ occurs near δ=3.

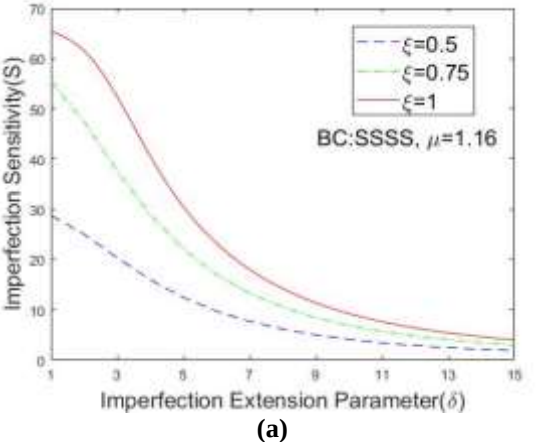

(a)

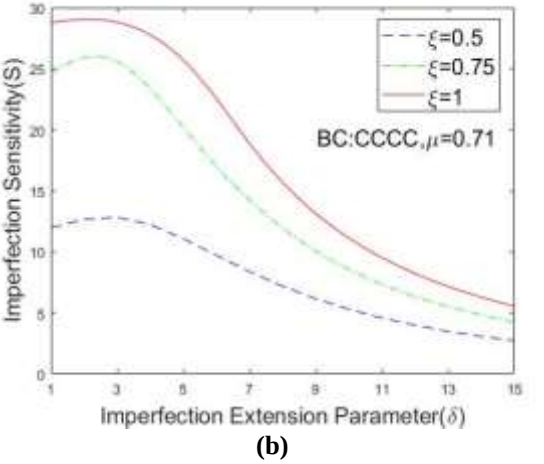

(b)

Fig. 7 Effect of imperfection extension parameter on imperfection sensitivity of square SLGS (a=2 nm).

Variations of frequency parameter (for geometrically imperfect SLGS) with imperfection amplitude and a/h

ratio, for both clamped and simply supported boundary conditions, are shown in "Fig. 8".

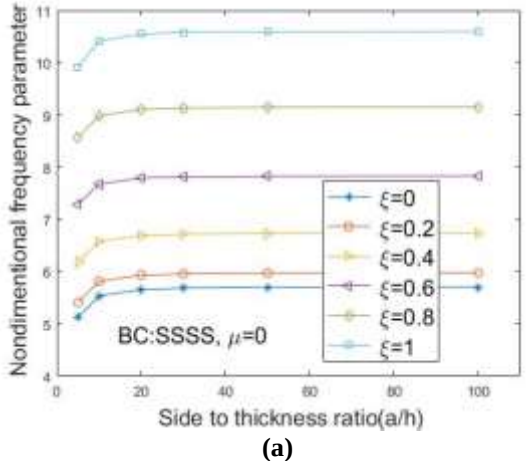

(a)

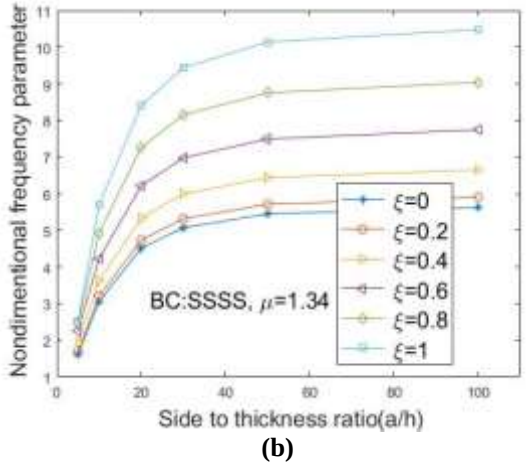

(b)

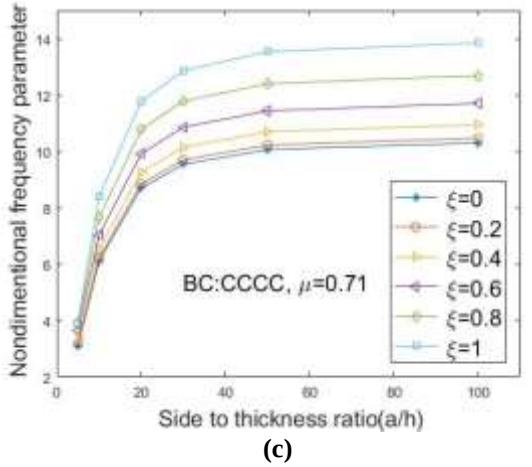

(c)

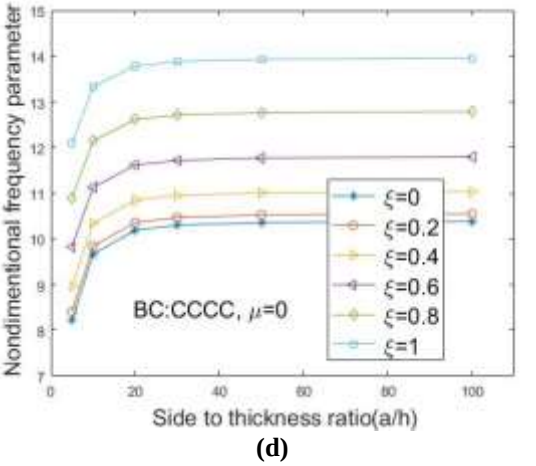

(d)

Fig. 8 The variation of frequency parameter of square SLGS with side to thickness ratio.

Both local $\mu = 0$ and nonlocal plates $(\mu \neq 0)$ are considered. The non-dimensional frequency parameter is considered as $\hat{\omega}=\omega\left(a^2/h\right)\sqrt{\rho(1-\nu^2)/E}$. It is observed that for both SSSS and CCCC boundary conditions, the frequency parameter for each ξ increases first with increasing side to thickness ratio and then converges to a constant value. Also, the frequency parameter increases with increasing ξ for all side to thickness ratios. The change in the frequency parameter between ξ=0 and ξ =1, for the SSSS boundary condition, is greater than that for the CCCC boundary condition. Therefore, it can be seen that the CCCC boundary condition reduces the effects of the geometric imperfection on the frequency parameter. Also, it can be seen that for the same boundary condition, the frequency parameter value in the non-local plate is less than that for the local plate. Another important point is that the non-local parameter at lower *a/h* has a greater effect on the frequency parameter. In other words, the geometric imperfection has a more significant effect on thick plates.

The effect of aspect ratio on the frequency parameter for nonlocal SLGS, for several imperfection amplitudes, is shown in "Fig. 9" for CCCC and SSSS boundary conditions. As it can be seen, the frequency parameter value decreases with increasing the aspect ratio. Also, the change in the frequency parameter between ξ=0 and ξ=1 decreases with increasing the aspect ratio. In other words, decreasing the aspect ratio results in greater effect of geometric imperfection on the non-dimensional frequency parameter.

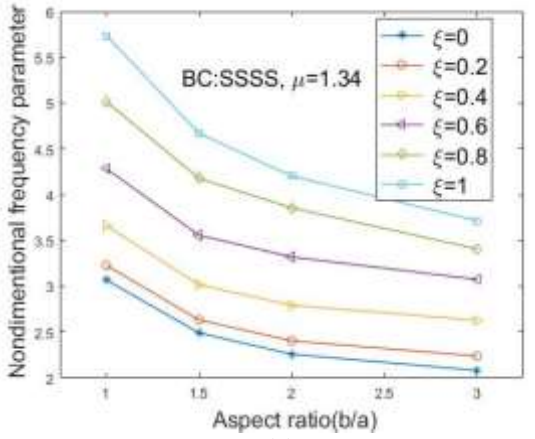

(a)

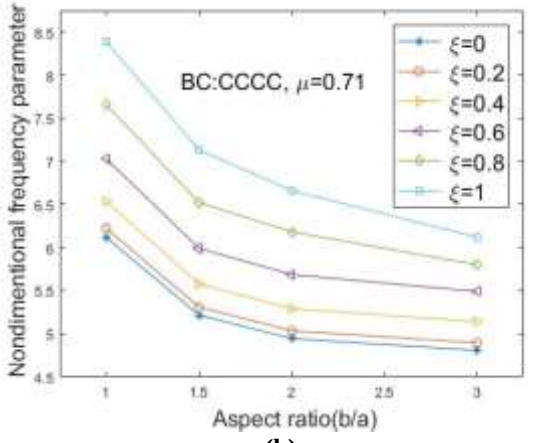

(b)

Fig. 9 Effect of aspect ratio on nondimensional frequency parameter of nonlocal SLGS (a/h=10).

As results show, the natural frequency of geometrically imperfect graphene sheets is significantly influenced by the nonlocal parameter. Therefore, it is necessary to use the appropriate value for this parameter. Ansari et al. [36] obtained the nonlocal parameter for pristine SLGS for simply supported and clamped boundary conditions. They proposed 1.41 (SSSS) and 0.87 (CCCC) for zigzag and 1.34 (SSSS) and 0.74 (CCCC) for armchair SLGS. Jalali et al. [4] compared the fundamental frequency for the pristine SLGS obtained from the continuum approach with that derived from the molecular dynamics method to find the appropriate nonlocal parameter and then used this parameter to analyze the geometrically imperfect SLGS.

In the present study, to find the appropriate nonlocal parameter value for geometrically imperfect SLGS, the fundamental frequencies of a pristine and localized imperfect ($\delta_1=\delta_2=5$, $\xi=1$) SLGS are investigated and shown in Table 4. The errors relative to molecular dynamics (MD) results reported by Jalali et al. [4] are also shown in the table. At $\mu=1.34$, the error for both pristine and localized SLGS are acceptable and this value for the nonlocal parameter can be used to analyze imperfect SLGS.

Table 4 Fundamental frequencies (THZ) for pristine and localized imperfect SLGS (a=2 nm, SSSS)

		Imperfection	
μ	Theory	Pristine	L1 Type
0	Present Study	1.580	2.142
	Jalali [4]	1.510	2.068
1.16	Present Study	0.609(4%)	0.794(7%)
	Jalali [4]	0.584(0%)	0.784(6%)
1.27	Present Study	0.584(0%)	0.764(3%)
1.34	Present Study	0.573(2%)	0.746(1%)
1.41	Present Study	0.560(4%)	0.729(1%)
	MD Jalali [4]	0.584	0.740

"Table 5" presents the fundamental frequencies for sinusoidal and localized imperfect SLGS for the case of simply supported and clamped boundary conditions.

Table 5 Fundamental frequencies (THZ) for SLGS with sinusoidal (δ=0) and localized (δ=5) imperfection (a=2 nm)

			μ			
δ	B.C	ξ	0	1.16	1.34	1.41
0	SSSS	0.7	2.440	0.930	0.874	0.855
		1	3.069	1.007	0.941	0.919
		1.25	3.612	1.038	0.970	0.947
		1.5	3.965	1.044	0.974	0.950
	CCCC	0.7	3.295	1.121	1.050	1.026
		1	3.830	1.191	1.112	1.085
		1.25	4.330	1.207	1.128	1.101
		1.5	4.643	1.200	1.119	1.092
5	SSSS	0.7	1.930	0.733	0.688	0.673
		1	2.142	0.795	0.746	0.729
		1.25	2.302	0.835	0.784	0.766
		1.5	2.446	0.868	0.814	0.795
	CCCC	0.7	3.108	1.097	1.029	1.005
		1	3.391	1.166	1.088	1.062
		1.25	3.605	1.165	1.087	1.061
		1.5	3.796	1.158	1.080	1.054

5 CONCLUSIONS

The size-dependent free vibration analysis and imperfection sensitivity for an imperfect SLGS via NURBS-based IGA, together with the quasi-3D deformation theory, has been examined. The initial geometric imperfection was modeled by inserting an analytical function in the governing Equations. Results show an excellent frequencies comparison for thin SLGS and different frequency values for thick SLGS.

The natural frequencies derived for clamped plates are less sensitive to geometric imperfection than simply supported plates. As the nonlocal parameter increases, the stiffness of the sheet and consequently the natural frequency decreases. The imperfection sensitivity for small values of imperfection amplitude is almost independent of the nonlocal parameter, while for larger values, it reduces by increasing the nonlocal parameter. For a large nonlocal parameter, changes in imperfection amplitude have an insignificant effect on imperfection sensitivity, whereas, for a small nonlocal parameter, imperfection sensitivity is susceptible to imperfection amplitude variations. By increasing the value of the imperfection extension parameter δ, the imperfection sensitivity decreases and converges to a constant value for all imperfection amplitudes. Frequencies for perfect and imperfect SLGS for different nonlocal parameters were extracted, and by comparing with the existing MD analysis, an appropriate and best fit nonlocal parameter value is found.

REFERENCES

[1] Terrones, M., Botello-Méndez, A. R., and Campos-Delgado, J, et al., Graphene and Graphite Nano Ribbons: Morphology, Properties, Synthesis, Defects and Applications, Nano Today, Vol. 5, 2010, pp. 351-372.

[2] Hierold, Ch., Jungen, A., Stampfer, C. H., and Helbling, T., Nano Electromechanical Sensors Based on Carbon Nanotubes, Sensors and Actuators A, Vol. 136, 2007, pp. 51-61.

[3] Wang, C. G., Lan, L., Liu, Y. P., and Tan, H. F., Defect-Guided Wrinkling in Graphene, Computational Materials Science, Vol. 77, 2013, pp. 250–253.

[4] Jalali, S. K., Pugno, N. M., and Jomehzadeh, E., Influence of Out-Of-Plane Defects on Vibration Analysis of Graphene Sheets: molecular and Continuum Approaches, Superlattices and Microstructures, Vol. 91, 2016, pp. 331-344.

[5] Lehtinen, O., Kurasch, S., Krasheninnikov, A. V., and Kaiser, U., Atomic Scale Study of The Life Cycle of a Dislocation in Graphene from Birth to Annihilation, Nat Commun, Vol. 4, 2013, 2098.

[6] Robertson, A. W., Allen, C. S., Wu, Y. A., He, K., Olivier, J., Neethling, J., Kirkland, A. I., and Warner, J. H., Spatial Control of Defect Creation in Graphene at The Nanoscale, Nat Commun, Vol. 3, 2012, 1144.

[7] Berthe, M., Yoshida, S., Ebine, Y., Kanazawa, K., Okada, A., Taninaka A., and et al, Reversible Defect Engineering of Single-Walled Carbon Nanotubes Using Scanning Tunneling Microscopy, Nano Lett, Vol. 7, 2007, pp. 3623–3627.

[8] Suleimani, A., Naei, M. H., and Mashhadi, M. M., Nonlocal Post Buckling Analysis of Graphene Sheets with Initial Imperfection Based on First Order Shear Deformation Theory, Results in Physics, Vol. 7, 2017, pp. 1299-1307.

[9] Jomehzadeh, E., Afshar, M. K., Galiotis, C., Shi, X., and Pugno, M. N., Nonlinear Softening and Hardening Nonlocal Bending Stiffness of An Initially Curved Monolayer Graphene, Compos Part B: Eng, Vol. 56, 2017, pp. 123-131.

[10] Eringen, A. C., Nonlocal Continuum Field Theories, Springer, NewYork. 2002.

[11] Sarrami-Foroushani, S., Azhari M., Nonlocal Buckling and Vibration Analysis of Thick Rectangular Nanoplates Using Finite Strip Method Based on Refined Plate Theory, Acta Mechanica, Vol. 227, 2016, pp. 721-742.

[12] Malekzadeh, P., Shojaee, M., Free Vibration of Nanoplates Based on A Nonlocal Two-Variable Refined Plate Theory, Compos. Struct, Vol. 95, 2013, pp. 443–452.

[13] Arash, B., Wang, Q., A Review on The Application of Nonlocal Elastic Models in Modeling of Carbon Nanotubes and Graphenes, Comp Mater Sci, Vol. 51, 2012, pp. 303–313.

[14] Bayati Chaleshtori, B., Hajiahmad, A., and Mohtasebi, S. S., Vibration Analysis of Rectangular Kirchhoff Nano-Plate using Modified Couple Stress Theory and Navier Solution Method, Int J of Advanced Design and Manufacturing Technology, Vol. 14, No. 2, 2021, pp. 85–92.

[15] Nourbakhsh, S. H., Botshekanan Dehkordi, M., and Atrian, A., Free Vibration Analysis of Nanoplates using Differential Transformation Method, Int J of Advanced Design and Manufacturing Technology, Vol. 10, No. 1, 2017, pp. 39-49.

[16] Thai, C. H., Ferreira A. J. M., and Phung-Van, P., Free Vibration Analysis of Functionally Graded Anisotropic Microplates Using Modified Strain Gradient Theory, Engineering Analysis with Boundary Elements, Vol. 117, 2020, pp. 284–298

[17] Senthilnathan, N. R., Lim, S. P., Lee, K. H., and Chow, S. T., Buckling of Shear-Deformable Plates, AIAA J, Vol. 25, 1987, pp. 1268–1271.

[18] Narendar, S., Buckling Analysis of Micro-/Nano-Scale Plates Based on Two-Variable Refined Plate Theory Incorporating Nonlocal Scale Effects, Compos, Struct, Vol. 93, 2011, pp. 3093–3103.

[19] Shimpi, R. P., Refined Plate Theory and Its Variants, AIAA J, Vol. 40, 2002, pp. 137–146.

[20] Nguyen, N. T., Hui, D., Lee, J., and Nguyen-Xuan, H., An Efficient Computational Approach for Size-Dependent Analysis of Functionally Graded Nanoplates, Comput. Methods Appl. Mech. Engrg, Vol. 297, 2015, pp. 191–218.

[21] Zenkour, A. M., Bending Analysis of Functionally Graded Sandwich Plates Using a Simple Four Unknown Shear and Normal Deformations Theory, J. Sandwich Struct. Mater, Vol. 15, 2013, pp. 629–656.

[22] Zenkour, A. M., A Simple Four-Unknown Refined Theory for Bending Analysis of Functionally Graded Plates, Appl. Math. Model, Vol. 37, 2013, pp. 9041–9051.

[23] Nguyen, H. X., Nguyen, T. N., Abdel-Wahab, M., Bordas, S. P. A., Nguyen-Xuan, H., and Vo, T. P., A Refined Quasi-3D Isogeometric Analysis for Functionally Graded Microplates Based on The Modified Couple Stress Theory, Comput. Methods Appl. Mech. Engrg, Vol. 313, 2017, pp. 904–940.

[24] Gupta, A., Talha, M., An Assessment of a Non-Polynomial Based Higher Order Shear and Normal Deformation Theory for Vibration Response of Gradient Plates with Initial Geometric Imperfections, Composites Part B, Vol. 107, 2016, pp. 141-161.
[25] Van Do, V. N., Lee, C. H., Free Vibration Analysis of Fgm Plates with Complex Cutouts by Using Quasi-3d Isogeometric Approach, International Journal of Mechanical Sciences, Vol. 159, 2019, pp. 213–233
[26] Phung-Van, P., Ferreira, A. J. M., Nguyen-Xuan, H., and Wahab, M. A., An Isogeometric Approach for Size-Dependent Geometrically Nonlinear Transient Analysis of Functionally Graded Nanoplates, Composites Part B, Vol. 118, 2017, pp. 125-134.
[27] Hughes, T. J. R., Cottrell, J. A., and Bazilevs, Y., Isogeometricanalysis: CAD, Finite Elements, Nurbs, Exact Geometry and Mesh Refinement, Comput Methods Appl Mech Eng, Vol. 194, 2005, pp. 4135–4195.
[28] Fazeli, H., Adamian, A., and Hosseini‑Sianaki, A., Influence of Initial Geometric Imperfection on Static and Free Vibration Analyses of Porous Fg Nanoplate Using an Isogeometric Approach, Journal of the Brazilian Society of Mechanical Sciences and Engineering, Vol. 43, No. 4, 2021, pp. 200.
[29] Soldatos, K. P., A Transverse Shear Deformation Theory for Homogeneous Monoclinic Plates, Acta Mech, Vol. 94, 1992, pp. 195–220.
[30] Nguyen-Xuan, H., Thai, C. H., and Nguyen-Thoi, T., Isogeometric Finite Element Analysis of Composite Sandwich Plates Using a Higher Order Shear Deformation Theory, Composites Part B, Vol. 55, 2013, pp. 558–574.
[31] Nguyen-Xuan, H., Tran, L. V., Thai, C. H., Kulasegaram, S., and Bordas S., Isogeometric Analysis of Functionally Graded Plates Using a Refined Plate Theory, Composites Part B, Vol. 64, 2014, pp. 222–234.
[32] Thai, H. T., Kim, S. E., A Simple Quasi-3D Sinusoidal Shear Deformation Theory for Functionally Graded Plates, Composite Structures, Vol. 99, 2013, pp. 172–180.
[33] Auricchio, F., Da Veiga, L. B., Buffa, A., Lovadina, C., Reali, and A., Sangalli, G., A Fully Locking-Free Isogeometric Approach for Plane Linear Elasticity Problems: A Stream Function Formulation, Comput. Methods Appl. Mech. Engrg, Vol. 197, 2007, pp. 160–172.
[34] Sarrami-Foroushani, S., Azhari M., Nonlocal Vibration and Buckling Analysis of Single and Multi-Layered Graphene Sheets Using Finite Strip Method Including van Der Waals Effects, Phys. E Low Dimens. Syst. Nanostruct, Vol. 57, 2014, pp. 83–95.
[35] Gupta, A., Talha, M., Nonlinear Flexural and Vibration Response of Geometrically Imperfect Gradient Plates Using Hyperbolic Higher-Order Shear and Normal Deformation Theory, Composites Part B, Vol. 123, 2017, pp. 241-261.
[36] Ansari, R., Sahmani, S., and Arash B., Nonlocal Plate Model for Free Vibrations of Single-Layered Graphene Sheets, Physics Letters A, Vol. 375, 2010, pp. 53–62.

Int. J. Advanced Design and Manufacturing Technology, 2023, Vol. 16, No. 1, pp. 29-37

DOI: 10.30486/admt.2023.1962820.1365 ISSN: 2252-0406 https://admt.isfahan.iau.ir

Design of Structure for a Heavy Duty Mineral Tow Machine by Evaluating the Dynamic and Static Loads

Mehdi Akhondizadeh[1], Meysam Atashafrooz[2, *]
Department of Mechanical Engineering
Sirjan University of Technology, Sirjan, Iran
E-mail: m.akhondizadeh@sirjantech.ac.ir, m.atashafrooz@sirjantech.ac.ir, Meysam.atashafrooz@yahoo.com
*Corresponding author

Received: 7 July 2022, Revised: 5 October 2022, Accepted: 12 October 2022

Abstract: The present manuscript gives the description of findings which took importance during the design and analysis of the structure of heavy duty hauler machine ordered by Gol-e-Gohar iron ore complex in Iran. Stress and deformation analysis was indeed the heart of the project and the key of its success. The challenging problem of evaluation of value and behaviour of active loads was taken under consideration precisely and all participated external forces were included in analysis. Since the present case is a moving structure, the loading evaluation should be included in all critical experienced conditions through the operation. The inertial forces due to acceleration and road bump have the governing role and have been evaluated and considered in analysis. After precise and complete evaluation of external loads and applying the correct boundary conditions, the simulations for stress analysis have been performed in ANSYS. The main findings of the present study were the optimized decision for the geometry of several important load carrying elements and appropriate reinforcement of the risky positions which was the result of the correct knowledge of the mechanics of problem. Finally, the structure was manufactured with the total weight of about 38 ton and load carrying capacity of 120 ton including the dynamic effects. After succeeding in the initial loading, the operational loading in real conditions in mine ramp has been carried out gradually and the machine is currently working in desired predicted form.

Keywords: Dynamic Load, Mechanical Design, Static Load, Stress Analysis, Tow Structure

Biographical notes: Mehdi Akhondizadeh is an assistant professor of Mechanical Engineering in Sirjan University of Technology, Sirjan, Iran. He received his MSc and PhD degrees from Shahid Bahonar University of Kerman in 2009 and 2015, respectively. He has several published papers and researches about the computational and experimental mechanics. **Meysam Atashafrooz** is an associate professor of Mechanical Engineering in Sirjan University of Technology, Sirjan, Iran. He received his MSc and PhD degrees from Shahid Bahonar University of Kerman in 2011 and 2015, respectively. He has several published papers about the computational mechanics and CFD research area.

Research paper

1 INTRODUCTION

Design of the machines requires a range of the engineering knowledge including the load analysis, material knowledge, drawing, stress analysis, cost evaluation and etc. The mechanical engineering knowledge has the higher degree of importance in the design of the heavy duty machines. The factors of style and cost of machines is not as important as the strength of the machine for working in the rough conditions in mine. The experiment-based findings will be very helpful in mechanical engineering design.

Shigley's mechanical engineering design [1] is full of such relations which simplifies the decisions for the engineers. The research results to be usable for all should be described in same language [2]. The computer aid design gradually finds its way into the engineering design by the modelling and analysing programs and software [3]. Computers also simplified the material selection [4]. Mineral machinery has the heaviest duty and so require the thorough load and stress analysis to select the optimized dimensions to have the minimum weight for the required application. Si et al. [5] analysed the force of frame in the dump truck unloading. ANSYS analyses indicated the stress concentration region to enhance it. Yi Dengli [6] analysed the models of tank car in ANSYS to determine the effect of thickness and height of the wave preventer on the deformation, strain and stress under different working conditions to optimize the dimension of elements. Cao et al. [7] performed FEM analysis for the frame of the truck crane. Results showed that the maximum stress is beyond the yield strength which requires the improvement of the frame structure. Through the load analysis of heavy vehicles, the dynamic force due to cross over road bump should be evaluated to determine its importance [8-9]. There are approaches for evaluating this form of loading on vehicle structure and human [10-12]. From the other point of view, choice of the enhanced materials will reduce the total weight and failure risks [13]. However, the cost considerations should be evaluated.

In the present work, it is tried to design a structure for climbing the mineral machinery to transport them in a faster and lower cost way in mine. The effort was paid to precisely determine the static and dynamic loads to have more reliable design. The novelty of work is application of the dynamic relations to evaluate the additional load due to the crossing the machine over the road bump which is one of the main parts of the loading which is precisely took in account here.

2 DESCRIPTION OF NEED

The availability of heavy mineral machines is one of the most important factors in improving the productivity of mineral processing. The term "walking of the machinery" is used when a mineral machine has to travel a relatively long distance through the mine environment. It is not welcomed by industries due to the time wasting and inherent costs and the effort is to avoid of it. The alternative of the walking will be conveying the slow and heavy machines by a faster and lower cost way. The design of a vehicle having such ability was on the agenda.

3 GEOMETRY LAYOUT

The final geometry of any design is the outcome of the designer viewpoint, manufacturing abilities, cost, functionality, experience, inspiring from similar designs and etc. According to these aspects, the present geometry was finalized which requires to be manufactured at another shop and conveyed to the owner company. Planned layout was decided to have the configuration to be built in separate conveyable structures. After assessment, evaluation and discussion, the general schematic of structure was gradually specified. The final decision was that it would compose of five main structures including two side-structures, central structure, axle structure and Jumbo structure.

4 LOADING SUMMARY AND ITS PATH

The loading of the present structure comes of the carrying of a mineral machine, for example an excavator, which its chain wheels insert the excavator weight on the side-structure of the tow machine. The side structures transfer the load to the central structure by the connecting pins. The load then is divided in two parts by transferring from the central structure to the axle from the rear and to the Jumbo from the front. The graphic summary of the approximate path of transferring the excavator weight to the ground, through the tow structure, has been illustrated in “Fig. 1”.

The loading initiates from the weight of the excavator *(w)* which produces F_1 and M_1 at the support of the first load carrying elements of side structure. Intermediate supports were designed in the central structure to take the major component of M_1 on their both sides. They prevent these couples to be applied on the base plate of the central structure. F_1 transfers and distributes on the base plate of the central structure through F_3 and F_4. F_3 and F_4 then transfer to the Jumbo and axle by F_5 and F_6, respectively.

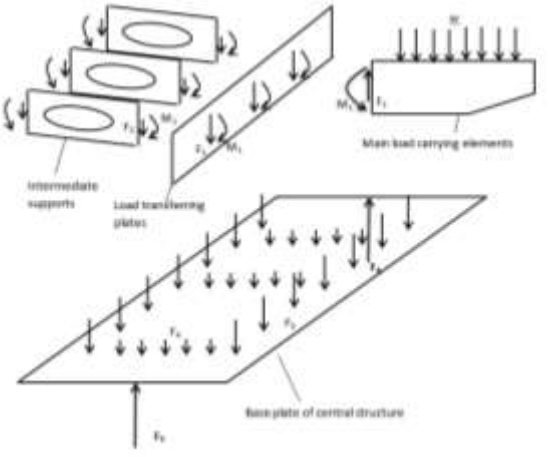

Fig. 1 Load trend from source to the axle.

More evaluations indicated that the structure weight has the noticeable value compared to the design external load. So, the effort was paid on optimizing the structure from the weight point of view to have the maximum strength by the minimum weight. The main load carrying parts were the elements in side-structure which must get the load from the wheels of target machine and transfer it to the central structure. Several choices for these parts, as illustrated in "Fig. 2", have been analysed by ANSYS software to obtain the best choice.

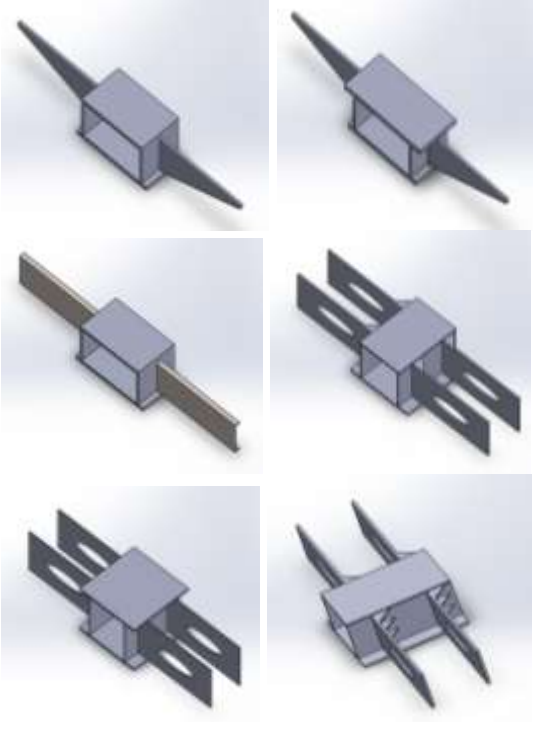

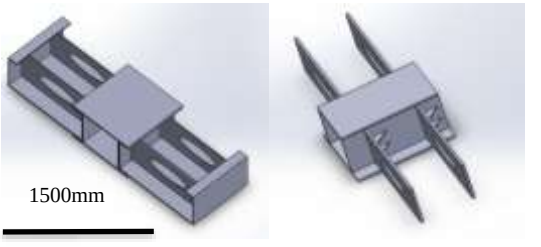

Fig. 2 Elementary options for the main load carrying elements.

The final choice for the main load carrying elements after analyses was as illustrated in "Fig. 3". Since it must have the maximum bending strength, its top and bottom faces were reinforced by small plates. They were also strengthened by additional elements at the support end which must be welded to the central structure.

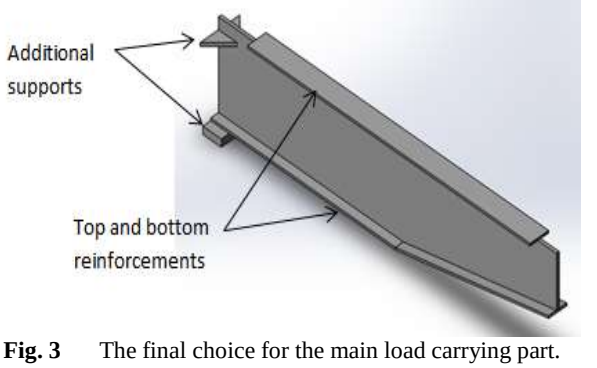

Fig. 3 The final choice for the main load carrying part.

From one end, the main load carrying elements of the side structure are welded on a plate which is considered to be pinned to another plate on the central structure. They are welded to a C-type beam from the other end to compose the rigid side structure. The central structure was reinforced by the intermediate elements which increase its stability. The final design of the combination of the side and central structure has been illustrated in "Fig. 4".

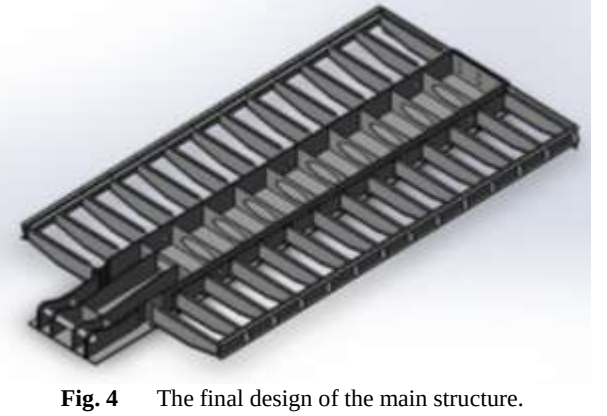

Fig. 4 The final design of the main structure.

5 DESIGN LOAD

The design load is evaluated based on the specifications of CAT390DL hydraulic excavator which its dimension and center of mass of parts are illustrated in "Fig. 5" and their values are given in "Table 1". The total mass of excavator is about 80ton which is applied on the different parts of the main structure through the climbing, positioning in place on side structures, accelerating and decelerating in the mine ramp and crossing over road bump.

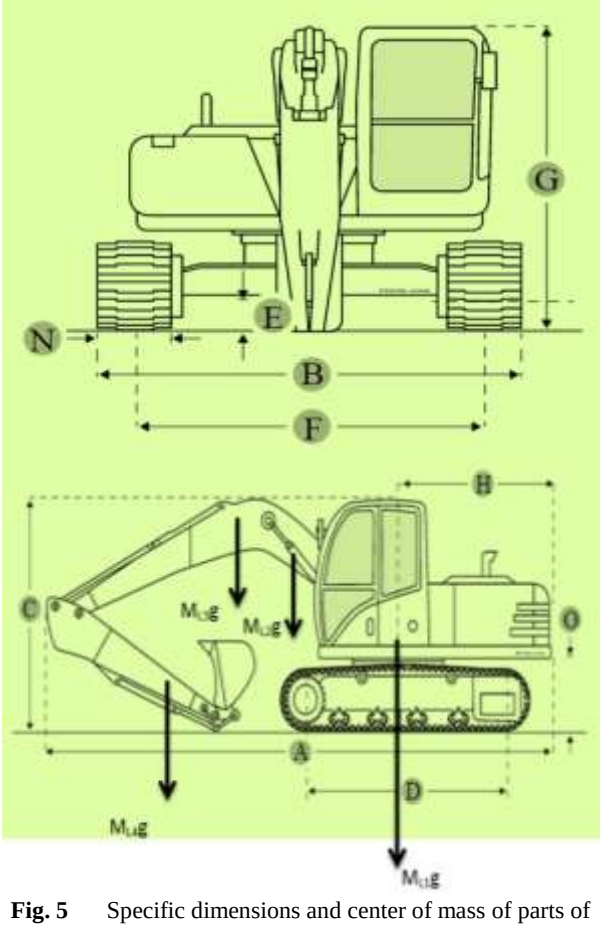

Fig. 5 Specific dimensions and center of mass of parts of CAT390DL hydraulic excavator.

Table 1 Values of specific dimensions and mass of parts of CAT390DL hydraulic excavator

Parameter Name	Value
A	12 m
B	4.6 m
C	3.76 m
D	5.12 m
N	0.9 m
M_{L1}	68 ton
M_{L2}	1.7 ton
M_{L3}	9.7 ton
M_{L4}	5.43 ton

The inertial forces must be included in the applied loads which can be described in two forms: accelerating through the mine ramp and crossing over the road bumps. The schematic of the form of applying these inertial forces is illustrated in "Figs. 6 and 7".

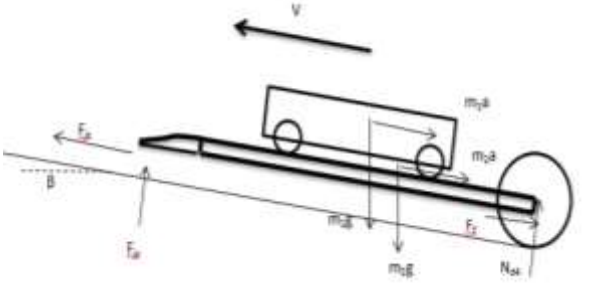

Fig. 6 Force diagram through accelerating of tow at the mine slope.

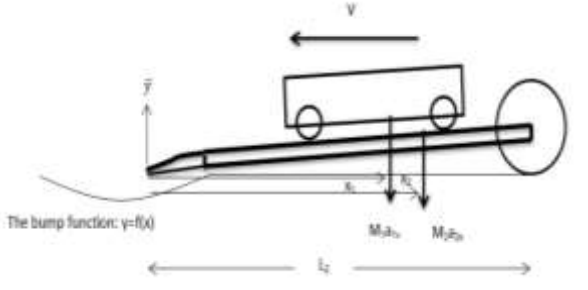

Fig. 7 Inertial forces due to the cross over road bumps.

Obviously, the linear acceleration due to the velocity increment during the motion of the tow does not have a constant value. However, an estimation of inertial force for stress analysis purpose will be obtained by assuming the constant acceleration. The velocity increment Δv over the time Δt gives a constant acceleration as follow:

$$a = \frac{\Delta v}{\Delta t} \tag{1}$$

The other noticeable inertial force will be due to the cross over the road bump. The form of this inertial force, as illustrated in "Fig. 7", is such that the front head of structure experiences a sudden downward-upward motion at the small period of time. It induces a semi-shock force on the target machine and the structure of the conveying machine. The influence of the road bump on the inertial force can be described by the following relations with the help of schematic illustrated in "Fig. 7".

$$Y = f(x) \tag{2}$$

$$\dot{y} = \dot{x}\frac{\partial f}{\partial x} \tag{3}$$

$$\ddot{y} = \ddot{x}\frac{\partial f}{\partial x} + \dot{x}^2\frac{\partial^2 f}{\partial x^2} \quad (4)$$

Assumption:

$$\ddot{x} = 0 \quad (5)$$

Assumption: small structure incline, angular acceleration is:

$$\alpha = \frac{\ddot{y}}{L_2} \quad (6)$$

$$a_{1y}=(L_2-x_1)\alpha \quad (7)$$

$$a_{2y}=(L_2-x_2)\alpha \quad (8)$$

Numerical calculation of the acceleration and inertial force due to the road bump requires an assumed function $f(x)$. The common shape of most road bumps can be estimated by a sector of circle as illustrated in "Fig. 8".

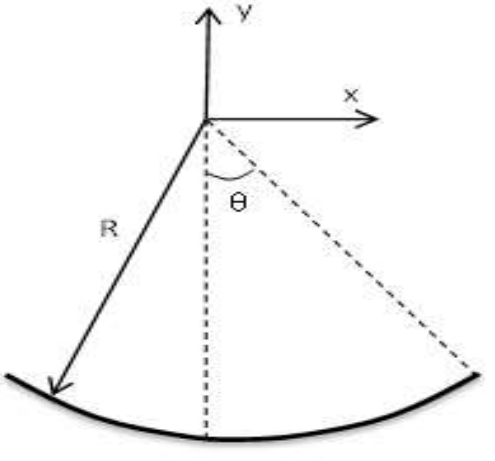

Fig. 8 The sector of circle as the road bump.

$$y = -\sqrt{R^2 - x^2} \quad (9)$$

$$\dot{y} = -\frac{1}{2}(-2x\dot{x})(R^2 - x^2)^{-\frac{1}{2}} \quad (10)$$

$$\ddot{y} = (\dot{x}^2 + x\ddot{x})(R^2 - x^2)^{-\frac{1}{2}} + x\dot{x}\left(-\frac{1}{2}\right)(-2x\dot{x})(R^2 - x^2)^{-\frac{3}{2}} \quad (11)$$

$$\dot{x} = -v, \quad \ddot{x} = 0 \quad (12)$$

$$\ddot{y} = \dot{x}^2(R^2 - x^2)^{-\frac{1}{2}} + x^2\dot{x}^2(R^2 - x^2)^{-\frac{3}{2}} \quad (13)$$

The required parameters and numerical results of the acceleration evaluation are given in "Table 2".

Table 2 Design parameters

Parameter	Value	Parameter	Value
M1(External Load)	80 ton	R	6
M2 (Structure)	30ton	θ	60°
L1 (m)	5.12	v	22km/h
L2 (m)	12.5	a_{1y}	0.56g
X_1(m)	4.5	m/s^2	
X_2	7	a_{2y}	0.58g
X_3	6.25	m/s^2	
β	10°	Δv	30km/h
		Δt	30s
		a	$0.1m/s^2$

6 FINAL LOADING

Not all features of the static and dynamic loads have been cleared. The complete form of the machine was also specified by the partly analyses and decisions. The applied loads and reactions of the axle and Jumbo have been illustrated on the final shape of machine in "Fig. 9". In this figure, F_1 represents the weight of the conveyed machine (excavator) and the dynamic force M_1a_{1y} and F_2 represents the inertial force M_1a. Moreover, the weight of the structure and its inertial force are distributed over the whole structure as the body force.

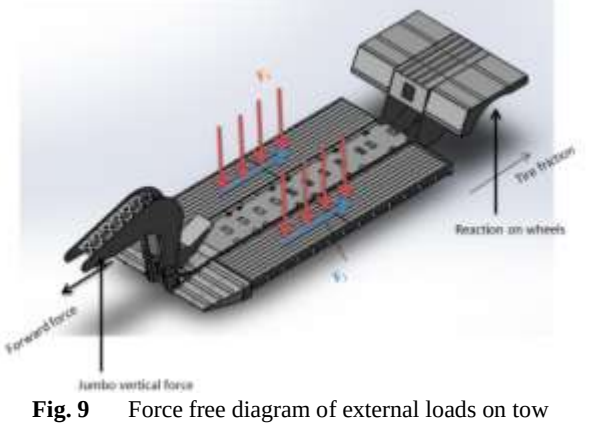

Fig. 9 Force free diagram of external loads on tow structure.

7 LOAD TRANSFERRING ELEMENTS

The form of action of the mechanical elements is described here. The dimension and position of all of elements have been selected such that their maximum load carrying capacity is employed during the different stages of loading. The side structure which is the first component that receives the load has three main parts

including load carrying elements, reinforcing C-type beam and support plate. This beam has the role of load distributing between the main load carrying elements. Without this beam, while the external load receives the first main carrying elements due to the movement of carried machine on the hauler structure, the non-loaded carrying elements do not participate in load carrying and this has the risk of failure of the first carrying elements. At the first stage, the load is applied on the load carrying elements and transfers through it to the support plate to be delivered to the central structure. The elements 1, 2, 3, …, q ("Fig. 10") directly receive the load during the climbing and sitting the excavator on the structure whereas, elements q to N may never directly experience the load but they have the significant effect in increasing the overall strength and stiffness of whole of the side structure by supporting the reinforcing beam.

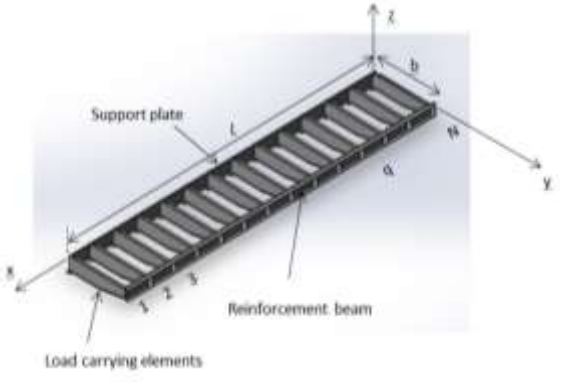

Fig. 10 The main components of the Side structure.

Due to the importance of the main load carrying elements their reaction under loading is discussed in more detail to clear how it transfers the load to the other elements. The deformed shape of these elements after loading is exaggeratedly illustrated in "Fig. 11" and can be given as follow:

$$\vec{U} = u(x,y,z)\vec{\imath} + v(x,y,z)\vec{\jmath} + w(x,y,z)\vec{k} \qquad (14)$$

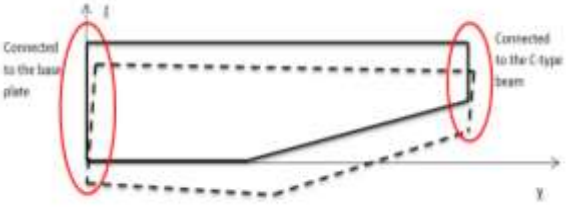

Fig. 11 Exaggerated deformation of the main load carrying element of the side structure.

The base plate and reinforcing beam must show resistant to the displacement at the left and right edges of the main load carrying elements. Such view of the action of the elements will help to appropriate and optimized selection of their type and dimension. The base plate must have the maximum stability under the rotation about the *x*-axis whereas, the reinforcing beam is required to withstand the displacement at the *x* and *z* directions. The base plate is pinned to the central structure at the appropriate regions to have this ability at its best form and the reinforcing beam gets the load from the active load carrying elements (1…q) and transfers it to the inactive ones (q…N) to engage them in the load carrying. This explanation is completed by the force diagram which is illustrated in "Fig. 12".

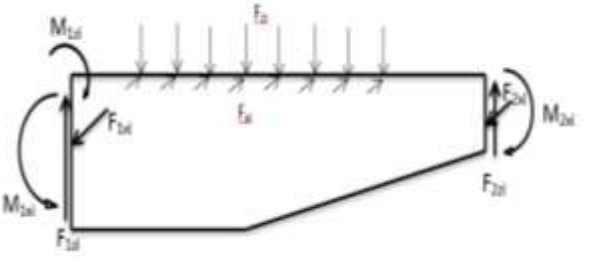

Fig. 12 The force diagram of the main load carrying element of the side structure.

The following relations can be explained by the reactions mathematically:

$$M_{2xi} \propto \frac{\partial v(x,b,z)}{\partial z} \qquad (15)$$

$$F_{2zi} \propto \frac{\partial w(x,b,z)}{\partial x} \qquad (16)$$

$$F_{2xi} \propto \frac{\partial u(x,b,z)}{\partial x} \qquad (17)$$

Based to the described requirements, a C-type beam reinforced against torsion by the small elements as illustrated in "Fig. 13" will give the desired performance in increasing the rigidity of side structure under the heavy weight of external load.

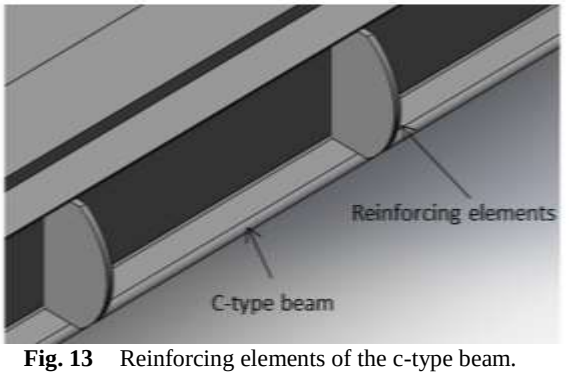

Fig. 13 Reinforcing elements of the c-type beam.

8 CONNECTION OF SIDE STRUCTURE TO THE CENTRAL STRUCTURE

As discussed previously, the required reactions on the connection of side and central structures are M_{1zi}, M_{1xi}, F_{1xi}, F_{1zi} which distribute discretely over the x-axis where there exist a load carrying element. These loads transfer between two steel plates of side and central structures, connected by 6 metric bolts $M_{64\times6}$ grade10.9 spaced $2m$ over the length of the structure. Configuration of the elements and connections is such that the minor part of these loads is received by the base plate of the central structure.

The nature of loads directs the designers to consider the intermediate elements in the central structure which are welded from both sides to the connecting plates to provide their stability and increase the rigidity of the central structure. The configuration is such that the main loads applied on these elements are bending moments from the both sides. (See "Fig. 14").

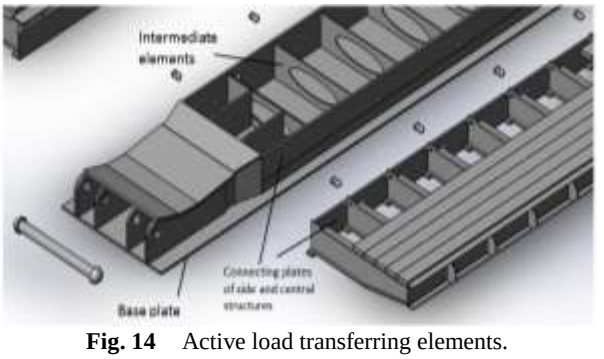

Fig. 14 Active load transferring elements.

9 STRESS ANALYSIS

After the selection of the load carrying elements and indication of the load values, the stress analysis has been performed in ANSYS software. The schematic of loading corresponding to the case in which the machine moves upward on the mine ramp of 10° and also crosses over an assumed road bump has been illustrated in "Fig. 15".

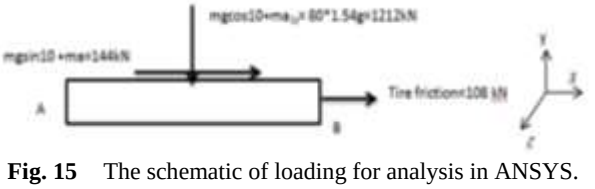

Fig. 15 The schematic of loading for analysis in ANSYS.

In "Fig. 15", *A* represents the side where the central structure is lifted by Jumbo and *B* represents the axle side. The boundary conditions are as follow:

$$\text{At A: } U_x=U_y=U_z=0 \tag{18}$$

$$\text{At B: } U_y=U_z=0 \tag{19}$$

The 8 mm mesh is illustrated in "Fig. 16". The contour of stress and deflection of the whole structure is illustrated in "Figs. 17 and 18", respectively.

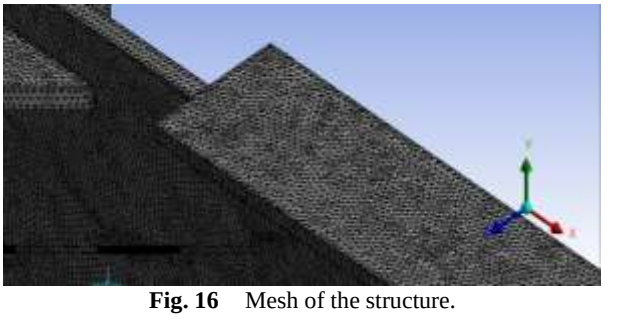

Fig. 16 Mesh of the structure.

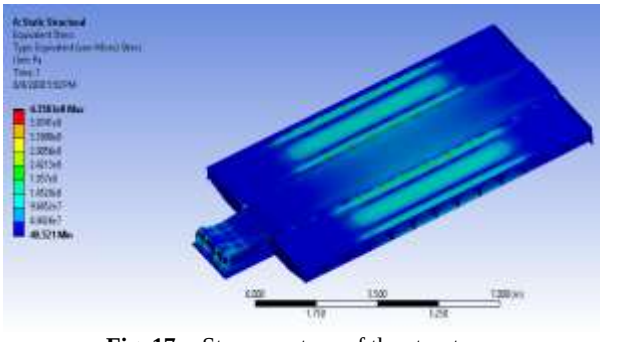

Fig. 17 Stress contour of the structure.

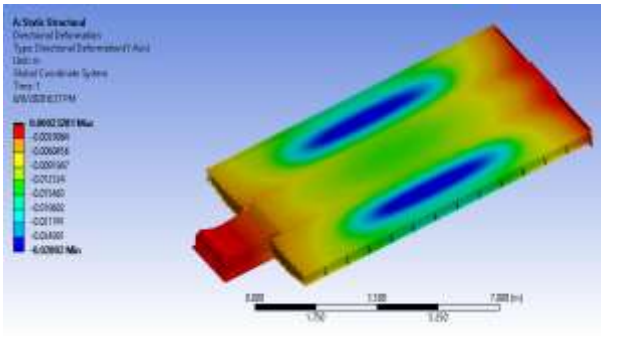

Fig. 18 Deflection of the structure at direction of y.

The results of the finite element analysis indicated that the maximum stress in structure is about 435MPa which is beyond the minimum yield strength of 335MPa of the structure material St52. Extracting the maximum stress of the individual elements which are given in Table 3 revealed that this is not a problem. The maximum stress is lower than the yield strength for all parts except for the connecting elements of the central structure to the jumbo. At this region, the stress concentration at pin holes occurs. Practically, these stresses will be relieved after local plastic deformations.

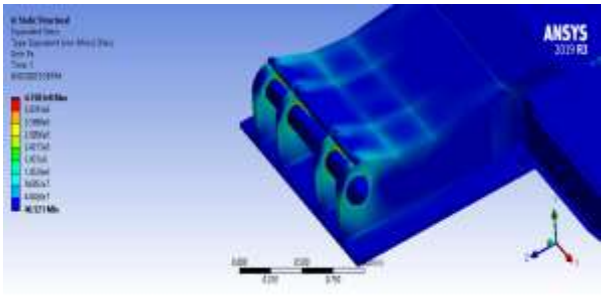

Fig. 19 Stress concentration regions.

Table 3 Values of the maximum stress at individual parts

Part	Max. Stress (MPa)
Main load carrying	174
Connection Side plate	188
Connection pins	89
Central base plate	182
Connection central plate	284
Intermediate supports	119
Pin Jumbo	240
C-type beam	100

Jumbo is another component of the present structure which is composed of the several individual parts and requires load and stress analysis. Jumbo has the role of lifting the head of the main structure by hydraulic pressure after loading. It also transfers the driving force from the haul truck to the main structure during the accelerating. The force diagram of the combination of the main structure and Jumbo has been illustrated in "Fig. 20" which shows how loads apply on Jumbo.

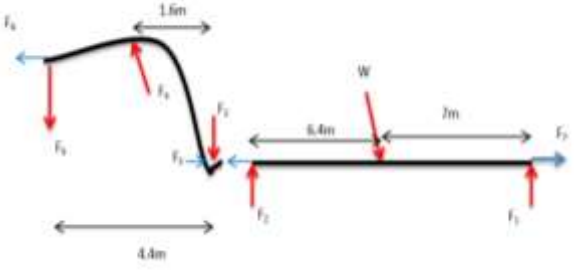

Fig. 20 Force diagram of whole structure with Jumbo.

The jumbo sits on a flat base on haul truck where F_4 is applied. Elsewhere the revolute joint between the haul truck and jumbo produces F_5 and F_6. In fact, F_6 is the driving force which provides the requirements for accelerating the main structure and tire friction. For analysis, the region on which F_4 has been distributed is constrained as $U_y=U_z=0$ and the revolute joint is constrained as $U_x=U_y=U_z=0$. The values of loads are given in "Table 4".

Table 4 Load values (kN) of Figure 20

W	F_1	F_2	F_3	F_4	F_5	F_6	F_7
1224	563	614	319	1010	351	268	108

The stress analysis has been done and stress contour has been illustrated in "Fig. 21".

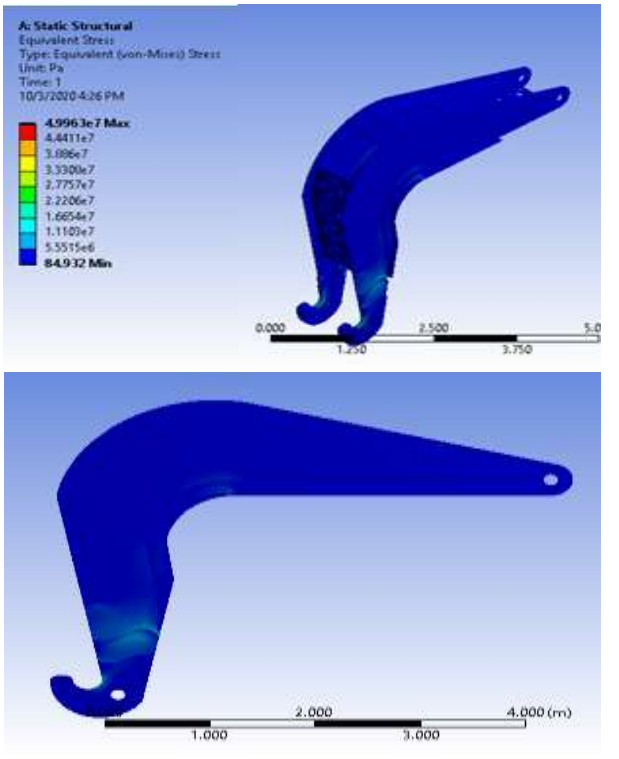

Fig. 21 The stress contour of the Jumbo structure.

The simulations showed that the stress values in jumbo are acceptable. The maximum stress at the stress concentration regions is 49MPa. So, it says that there is no problem for jumbo.

10 CONCLUSION

After the appropriate definition of need for the faster transportation of the mineral machinery, the load analysis and load carrying element selection were performed based on a specified external load. A variety of conditions were taken into account to determine the critical loading condition. Individual stress analysis leads the designer to the appropriate dimension of elements. After that, the 3D model of whole structure was made in Solid works software and was analyzed in ANSYS. The result was the structure which currently passes the initial field tests as illustrated in "Fig. 22" in which the structure conveys a mineral truck of about 70% of the design load.

Fig. 22 Field test of the structure by 70% of design load.

ACKNOWLEDGMENT

Authors would like to appreciate of the Arman Gohar and Gol Gohar companies for their supports during the design and manufacturing of the present structure.

REFERENCES

[1] Budynas, R. G., Nisbett, J. K., Shigley's Mechanical Engineering Design, New York: McGraw-Hill, Vol. 9, 2011.

[2] Finger, S., Dixon, J. R., A Review of Research in Mechanical Engineering Design. Part I: Descriptive, Prescriptive, and Computer-Based Models of Design Processes, Research in Engineering Design, Vol. 1, No. 1, 1989, pp. 51-67.

[3] Ullman, D. G., Toward the Ideal Mechanical Engineering Design Support System, Research in Engineering Design, Vol. 13, No. 2, 2002, pp. 55-64.

[4] Sapuan, S. M., A Knowledge-Based System for Materials Selection in Mechanical Engineering Design, Materials & Design, Vol. 22, No. 8, 2001, pp. 687-695.

[5] Si, J. P., Wang, G. S., and Ding, X. L., Analysis of Dump Truck Unloading Condition Based on ANSYS, In Advanced Materials Research, Vol. 548, 2012, pp. 724-729.

[6] Yi, D., Strength Analysis and Optimization of Tank Truck Based on ANSYS, In Journal of Physics: Conference Series, Vol. 2026, No. 1, 2021, pp. 012058.

[7] Cao, F., Li, J., and Cui, M., Analysis of Frame Structure of Medium and Small Truck Crane, In AIP Conference Proceedings, Vol. 1944, No. 1, 2018, pp. 020065.

[8] Startcev, A., Romanov, S., and Vagina, O., Interaction of Elastic Wheel with Bumps of Rectangular Shape. In International Conference on Industrial Engineering, Springer, Cham, 2019, pp. 621-629.

[9] Desai, R., Guha, A., and Seshu, P., Investigation of Internal Human Body Dynamic Forces Developed During a Vehicle Ride, In the International Conference of IFToMM ITALY, Springer, Cham, 2020, pp. 85-93.

[10] Goenaga, B., Underwood, S., and Fuentes, L., Effect of Speed Bumps on Pavement Condition, Transportation Research Record, Vol. 2674, No. 9, 2020, pp. 66-82.

[11] Tengler, S., Warwas, K., An Effective Algorithm of Uneven Road Surface Modeling and Calculating Reaction Forces for a Vehicle Dynamics Simulation, Coatings, Vol. 11, No. 5, 2021, pp. 535.

[12] Guo, Z., Wu, W., and Yuan, S., Longitudinal-Vertical Dynamics of Wheeled Vehicle under Off-Road Conditions, Vehicle System Dynamics, Vol. 60, No. 2, 2022, pp. 470-490.

[13] Vini, M. H., Daneshmand, S., Effect of Electrically Assisted Accumulative Roll Bonding (EARB) Process on the Mechanical Properties and Microstructure Evolution of AA5083/Al2O3 Composites, Materials Performance and Characterization, Vol. 8, No. 1, 2019, pp. 594-603.

Int. J. Advanced Design and Manufacturing Technology, 2023, Vol. 16, No. 1, pp. 39-44

DOI: 10.30486/admt.2022.1942680.1318 ISSN: 2252-0406 https://admt.isfahan.iau.ir

Strength Improvement of Nano-Structured Titanium Processed by Parallel Tubular Channel Angular Pressing

Ali Amani[1]
Department of Mechanical Engineering, Science and Research Branch, Islamic Azad University, Tehran, Iran
E-mail: a.amani@srbiau.ac.ir

Hamid Soleimanimehr[2, *]
Department of Mechatronics and Computer Engineering, Science and Research Branch, Islamic Azad University, Tehran, Iran
E-mail: soleimanimehr@srbiau.ac.ir
*Corresponding author

Shahram Etemadi Haghighi[3], **Farid Biniyazan**[4]
Department of Mechanical Engineering, Science and Research Branch, Islamic Azad University, Tehran, Iran
E-mail: setemadi@srbiau.ac.ir, farid.biniyazan@srbiau.ac.ir

Received: 15 October 2021, Revised: 3 March 2022, Accepted: 27 March 2022

Abstract: Parallel Tubular Channel Angular Pressing (PTCAP), as a process of Severe Plastic Deformation (SPD), was employed for improving the strength of commercially pure Titanium (Grade 2). In the present research, the tubular samples of pure titanium were severely deformed by one and two passes of PTCAP at the temperature of 450°C. It was found by the results of tensile tests that the yield and ultimate strengths increased by 24% and 29% after applying the second pass of PTCAP, respectively. It was also showed that the Vickers microhardness increased by 46%. Moreover, the micrographs illustrated that the average grain size decreased from ~21 μm in the unprocessed condition to ~143 nm after applying two PTCAP passes. Therefore, applying the technique of PTCAP was successful to produce the nano-structured titanium.

Keywords: Hardness, Microstructure, PTCAP, Strength, Titanium

Biographical notes: Ali Amani received his MSc in Mechanical Engineering from Azad University, Tehran, Iran, in 2019. His current research interest is Wind Energy. **Hamid Soleimanimehr** received his PhD in Mechanical Engineering from Tarbiat Modares University in 2012. He is Assistant Professor at Azad University, Tehran, Iran. His current research interest includes Additive Manufacturing. **Shahram Etemadi Haghighi** is Assistant Professor of Mechanical engineering at Azad University, Tehran, Iran. He received his PhD from Sharif University of Technology in 2012. His current research focuses on Nonlinear Systems. **Farid Biniyazan** received his MSc in Mechanical Engineering from Azad University, Tehran, Iran, in 2018. His current research interests are Formability, and FEM.

Research paper

1 INTRODUCTION

Commercially pure titanium (CP-Ti), as metallic biomaterials, has been used extensively for surgical implants. Titanium is superior to other surgical metals like iron-chromium-nickel alloys (austenitic stainless steels) and cobalt-chromium-based alloys due to high biocompatibility and corrosion resistance. Another favorable property of CP-Ti is that it is more light-weight than other surgical metals. Nevertheless, the main drawback of CP-Ti is its strength. The strength of CP-Ti implants is too low when they are used in load-bearing situations. The addition of alloying elements, such as aluminum and vanadium leads to the significant improvement of titanium's strength. However, the release of aluminum and vanadium ions may cause health problems. Therefore, Al and V ions have aroused concerns about the long-term safety of Ti–6Al–4V alloy implants [1-3].

An alternative method to solve the problem of harmful ion release is to stop using the technique of alloying and improve the strength of pure titanium by nanoscale grain refinement. One of the efficient ways of producing bulk nano-structured materials is the metalworking technique known as Severe Plastic Deformation (SPD). SPD technique is based on the fact that a metal sample is subjected to high plastic strains leading to breaking the coarse grains down into nano-sized (with the size less than 100 nm) grains [4-5].

In order to fabricate nanocrystal line tubes, different SPD methods have been presented. These methods are known as Accumulative Spin Bonding (ASP) [6], High-Pressure Tube Twisting (HPTT) [7], Tubular Channel Angular Pressing (TCAP) [8] and Parallel Tubular Angular Pressing (PTCAP) [9]. PTCAP is a novel method which has some advantages over other methods including the reduction of process force and more strain uniformity in the tube.

Podolskiy et al [10] investigated the microstructure and mechanical properties of CP-Ti by applying equal channel angular pressing (ECAP) at cryogenic temperatures. They achieved higher values of strength and hardness. Also, Zhilyaev et al [11] examined the microstructure and texture homogeneity of ECAP-processed CP-Ti at the elevated temperature of 450°C. They reported that more homogeneous microstructure in mean grain size and texture would be achieved by increasing the pass number of ECAP. To date, there is few research work investigating the microstructure and mechanical properties of CP-Ti processed by PTCAP. The importance and novelty of the research work is to apply the Nano structuring method of PTCAP to CP-Ti at the elevated temperature of 450°C. Successful developments of nanostructured titanium-based medical implants is very important. Nano structuring is a promising technique to further improve the safety, effectiveness and longevity of medical implants made of titanium-based materials. The purpose of present research is to achieve strength improvement in CP-Ti by the Nano structuring technique of PTCAP. For this purpose, tubular samples of titanium were deformed by one and two passes of PTCAP at the temperature of 450°C. Then, the mechanical properties and the microstructure of PTCAP-processed CP-Ti were evaluated by the uniaxial tensile test, micro hardness test, optical microscope (OM) and scanning electron microscope (SEM).

2 MATERIAL AND METHODS

2.1. PTCAP Process

Fig. 1 (a) and (b) schematically illustrate the principle of PTCAP process and die parameters in order to produce nano-structured CP-Ti. As shown in "Fig. 1 (a)", PTCAP process consists of two half passes.

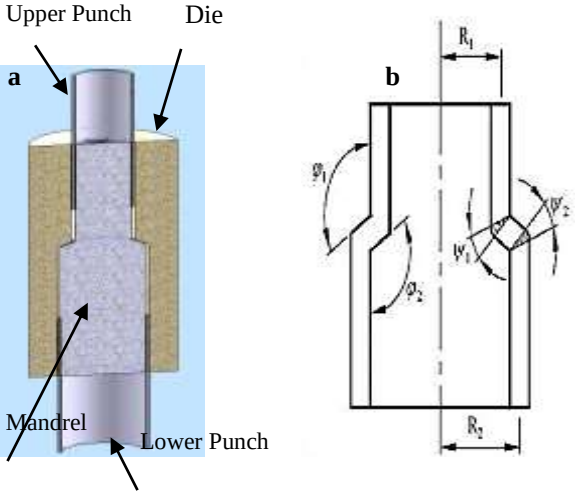

Fig. 1 (a): Schematic illustration of PTCAP process with part label, and (b): Die parameters.

At the first half pass, the tube is pressed into the gap between the mandrel and die including two shear zones in order to enhance the tube diameter to its maximum size. At the second half pass, the tube is pressed back applying the lower punch to reduce the tube diameter to its primary size. The total equivalent strain after N passes of PTCAP can be calculated by the following relationship [9]:

$$\bar{\varepsilon}_{TN} = 2N\left\{\sum_{i=1}^{2}\left[\frac{2\cot\left(\frac{\varphi_i}{2}+\frac{\psi_i}{2}\right)+\psi_i\csc\left(\frac{\varphi_i}{2}+\frac{\psi_i}{2}\right)}{\sqrt{3}}\right]+\frac{2}{\sqrt{3}}\ln\frac{R_2}{R_1}\right\} \quad (1)$$

Where, φ is the channel angle, ψ is the curvature angle, N is the number of cycles, R_1 is the primary radius and R_2 is the secondary radius.

2.2. Experimental Procedures

The studied alloy in this paper was CP-Ti (grade 2) with the chemical composition shown in "Table 1".

Table 1 Chemical composition of CP-Ti Grade 2 (wt.%)

Ti	Fe	C	N	H	O
Balance	0.053	0.012	0.014	0.002	0.059

Cylindrical tubes of 21 mm in outer diameter, 4 mm in thickness, and 36 mm in length were machined. PTCAP die was fabricated as shown in "Fig. 2 (a)" with the parameters of $\varphi_1 = \varphi_2 = 120°$ and $\psi_1 = \psi_2 = 0$. Two passes of PTCAP process at the temperature of 450°C were conducted using hydraulic press of 50 tons capacity operating at ram speed of 10 mm/s. MoS_2 was also used as lubrication. Infrared thermal camera (IR-384H; Cygnus Electronics) was employed in order to control the temperature of PTCAP process at 450°C. To evaluate the mechanical properties of the samples, tensile test at displacement rate of 1mm/min was conducted according to ASTM E8 using Zwick/Roell-Z250 universal testing machine at room temperature. Tensile test results were reported as the average value of three replicates.

The values of the Vickers micro hardness (HV) were measured according to ASTM E384 using Innovates Nova 240 tester with a load of 2.942 N and a dwell time of 10s. In order to achieve a high degree of accuracy, each reported micro hardness datum was the average of five separate measurements. Metallographic analysis was carried out using an OM (Olympus BX51M) and SEM (S-4800, Hitachi).

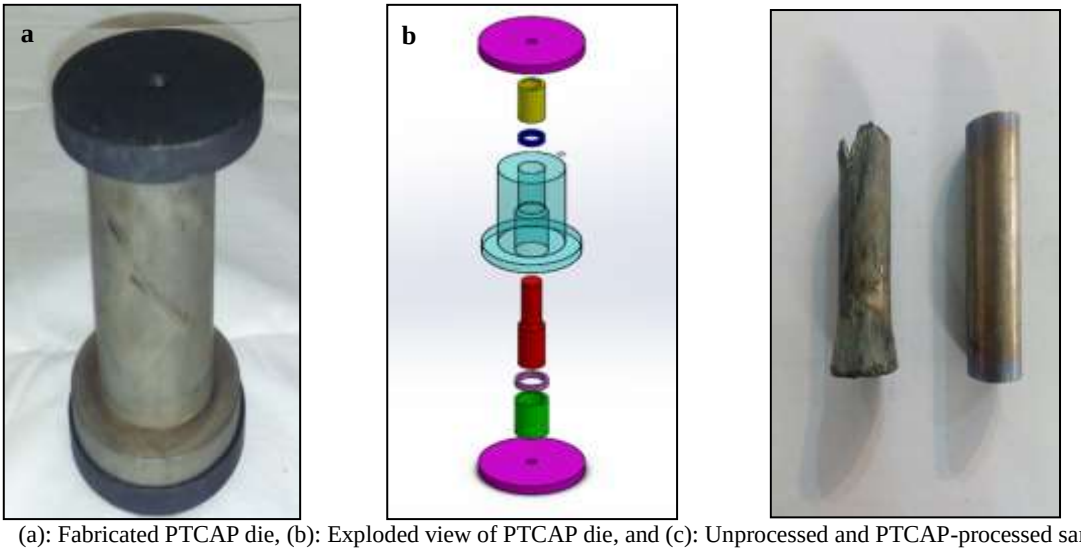

Fig. 2 (a): Fabricated PTCAP die, (b): Exploded view of PTCAP die, and (c): Unprocessed and PTCAP-processed samples.

3 RESULTS AND DISCUSSION

3.1. Tensile and Micro Hardness Tests

Fig. 3 (a) shows the results of tensile tests in 0 pass, 1 pass, and 2 passes of PTCAP process at the temperature of 450°C. As it is seen in "Fig. 3 (a)", there is a satisfactory improvement after two passes of PTCAP with the yield strength increasing from 348 to 449 MPa and the ultimate strength increasing from 508 to 631 MPa. In other words, the yield and ultimate strengths increase by 24% and 29%, respectively. There is also a reasonable ductility in which the elongation decreases from 38% to 27% after two passes of PTCAP process. The same procedure is seen in the results of micro hardness tests. As it is observed in "Fig. 3 (b)", the Vickers micro hardness increases from HV 184 to HV 269 after employing two passes of PTCAP process. In other words, the Vickers micro hardness increases by 46%. "Table 2" summarizes the results of tensile and micro hardness tests.

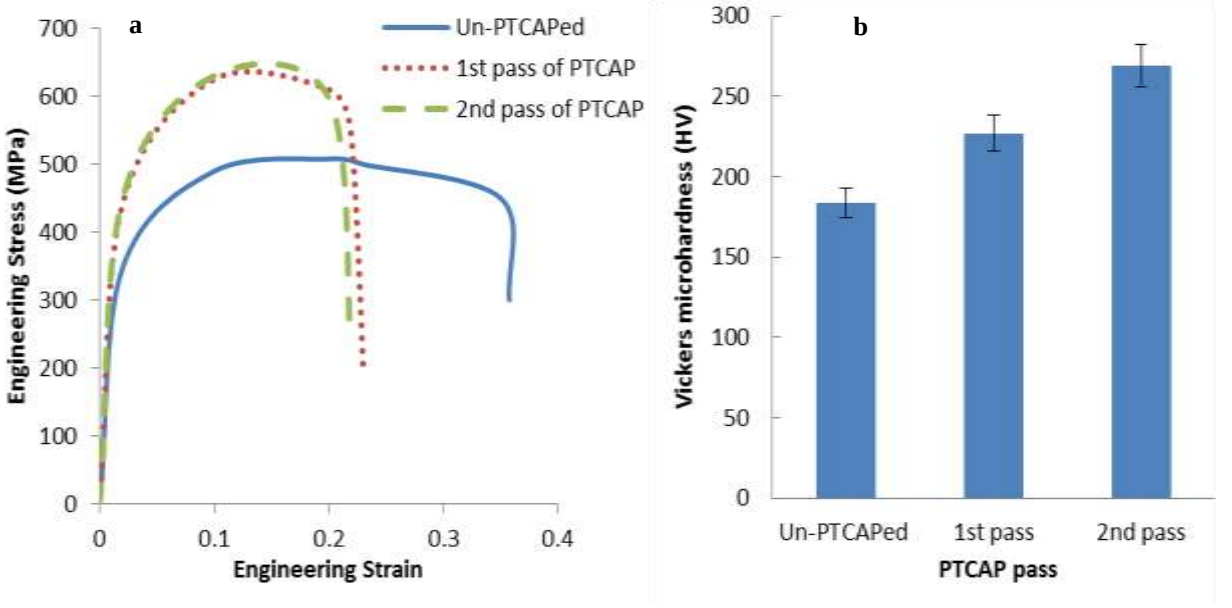

Fig. 3 (a): Engineering stress−strain curves of non-PTCAP and PTCAP-processed specimens, and (b): The average Vickers micro hardness of non-PTCAP and PTCAP-processed specimens.

Table 2 Mechanical properties of CP-Ti before and after PTCAP process

PTCAP pass	Yield Strength (MPa)	Ultimate Strength (MPa)	Elongation (%)	Vickers micro hardness (HV)
0	348	508	38	184
1	442	625	29	227
2	449	631	27	269

3.2. Microstructure Analysis

The significant improvement in the mechanical properties of SPD-processed material is mainly attributed to the grain refinement [12-13] and high-density dislocations [14-15]. In accordance with the Hall−Petch equation, the yield stress, as a criterion for the strength of polycrystalline materials, increases considerably by the grain refinement. The Hall-Petch equation is defined according to following relationship [16]:

$$\sigma_y = \sigma_0 + k_y d^{-1/2} \quad (2)$$

Where, σ_y is the yield stress, σ_0 is the friction stress, k_y is the constant of yielding, and d is the grain size.

In "Fig. 4", the microstructures of CP-Ti before and after applying the PTCAP process are depicted, which the images are obtained by OM and SEM, respectively. In order to identify the behavior of materials, the best way is to examine the microscopic structure [17-19]. It can be observed from "Fig. 4 (a) and (b)" that the grains are refined by PTCAP technique. The magnitude of the average grain size (d) evolved from ~21 μm in un-PTCAPed material down to ~143 nm after employing 2 passes of PTCAP process. Therefore, with respect to Hall-Petch relationship ("Eq. (2)"), the improvement in the strength of CP-Ti is mainly attributed to the nano-sized grains. Another reason of strength improvement in nanostructured titanium could be the existence of high-density dislocations. When the pass number of SPD process increases, accumulative strain as well as dislocations continuously increase. As long as a dislocation cell is newly created, it can absorb the high-density dislocations inside the newborn dislocation cell, and then transfer to the cell wall, therefore the whole dislocation cell comes into being. When these dislocation cells turn into high-angle boundaries, the microstructure could be further refined [20].

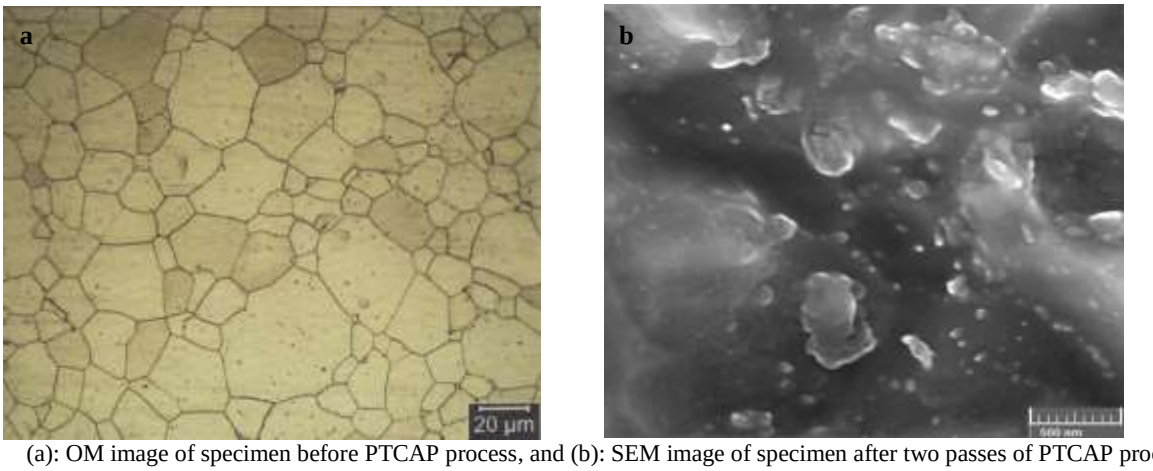

Fig. 4 (a): OM image of specimen before PTCAP process, and (b): SEM image of specimen after two passes of PTCAP process.

Fracture surfaces of non-PTCAP and PTCAP-processed samples after tensile tests are also shown in "Fig. 5 (a) and (b)". According to "Fig. 5 (a)", SEM morpholog shows typical ductile failure with the large-sized dimples. The dimples originate from nucleation, growth and coalescence of micro voids under tensile stresses. It is observed that the fracture surface of non-PTCAP-processed sample includes deep dimples. As it is shown in "Fig. 5 (b)", by applying two passes of PTCAP process, due to the severe deformation, the fracture surface of CP-Ti consists of fine dimples as compare to unprocessed one. Moreover, it is noted that the depth of dimples is reduced in PTCAP-processed sample.

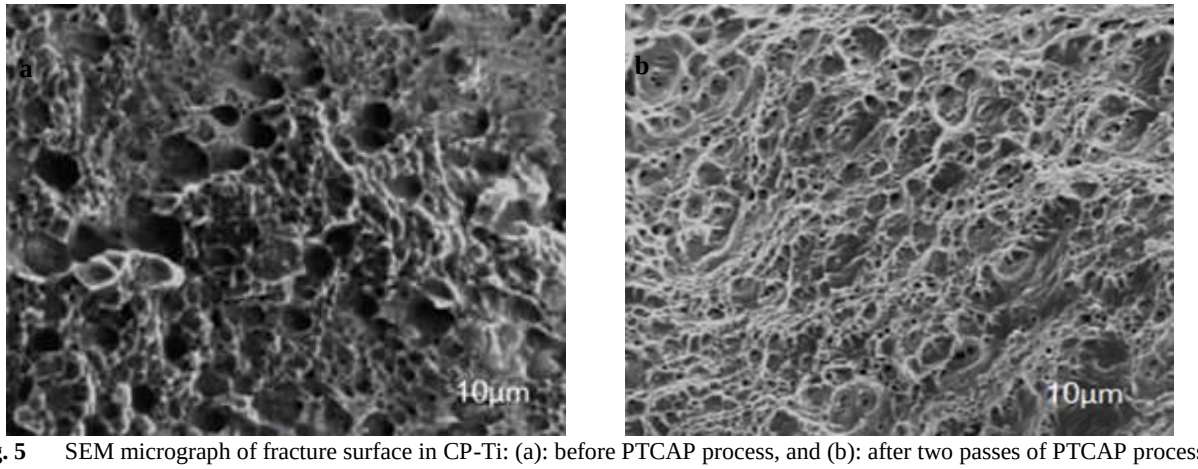

Fig. 5 SEM micrograph of fracture surface in CP-Ti: (a): before PTCAP process, and (b): after two passes of PTCAP process.

4 CONCLUSION

In this research work, tubular samples of CP-Ti (grade 2) were successfully subjected to one and two passes of PTCAP process at the temperature of 450°C. The following conclusions were drawn:

1- The yield and ultimate strengths increased by 24% and 29% after applying two passes of PTCAP process, respectively.

2- The elongation decreased from 38% in the unprocessed condition to 27% after two passes of PTCAP process.

3- The Vickers micro hardness increased from HV 184 in the unprocessed condition to HV 269 after employing two passes of PTCAP process.

4- The average grain size decreased from ~21 µm in the unprocessed condition to ~143 nm after applying two PTCAP passes.

5- The strength improvement in CP-Ti was mainly attributed to the existence of Nano-sized grains.

6- Fracture surface analysis demonstrated that after employing PTCAP process, the number of fine dimples increased considerably.

REFERENCES

[1] Browne, M., Gregson, P. J., Effect of Mechanical Surface Pretreatment on Metal Ion Release, Biomaterials, Vol. 2, No. 4, 2000, pp. 385-392, https://doi.org/10.1016/S0142-9612(99)00200-8.

[2] Zaffe, D., Bertoldi, C., and Consolo, U., Accumulation of Aluminium in Lamellar Bone After Implantation of Titanium Plates, Ti–6Al–4V Screws, Hydroxyapatite Granules, Biomaterials, Vol. 25, No. 17, 2004, pp. 3837-3844, https://doi.org/10.1016/j.biomaterials.2003.10.020.

[3] Geetha, M., Singh, A. K., Asokamani, R., and Gogia, A. K., Ti Based Biomaterials, the Ultimate Choice for Orthopaedic Implants–A Review, Progress in Materials Science, Vol. 54, No. 3, 2009, pp. 397-425, https://doi.org/10.1016/j.pmatsci.2008.06.004.

[4] Morishige, T., Suzuki, Y., and Takenaka, T., Extra-Hardening of SPD-Processed Al-Mg Alloy with Minimum Grain Sizes, Materials Science Forum, Vol. 1016, 2021, pp. 952-956, https://doi.org/10.4028/www.scientific.net/MSF.1016.952.

[5] Krajňák, T., Janeček, M., Minárik, P., Gubicza, J., Hung, P. T., Nový, F., Raab, A., Raab, G., and Asfandiyarov, R., Microstructure Evolution in Cu–0.5 wt% Zr Alloy Processed by a Novel Severe Plastic Deformation Technique of Rotational Constrained Bending, Metals, Vol. 11, No. 1, 2021, pp. 63, https://doi.org/10.3390/met11010063.

[6] Mohebbi, M. S., Akbarzadeh, A., Accumulative Spin-Bonding (ASB) as a Novel SPD Process for Fabrication of Nanostructured Tubes, Materials Science and Engineering: A, Vol. 528, No. 1, 2010, pp. 180-188, https://doi.org/10.1016/j.msea.2010.08.081.

[7] Tóth, L. S., Arzaghi, M., Fundenberger, J. J., Beausir, B., Bouaziz, O., and Arruffat-Massion, R., Severe Plastic Deformation of Metals by High-Pressure Tube Twisting, Scripta Materialia, Vol. 60, No. 3, 2009, pp. 175-177, https://doi.org/10.1016/j.scriptamat.2008.09.029.

[8] Faraji, G., Mashhadi, M. M., and Kim, H. S., Tubular Channel Angular Pressing (TCAP) as a Novel Severe Plastic Deformation Method for Cylindrical Tubes, Materials Letters, Vol. 65, No. 19-20, 2011, pp. 3009-3012, https://doi.org/10.1016/j.matlet.2011.06.039.

[9] Faraji, G., Babaei, A., Mashhadi, M. M., and Abrinia, K., Parallel Tubular Channel Angular Pressing (PTCAP) as a New Severe Plastic Deformation Method for Cylindrical Tubes, Materials Letters, Vol. 77, 2012, pp. 82-85, https://doi.org/10.1016/j.matlet.2012.03.007.

[10] Podolskiy, A. V., Ng, H. P., Psaruk, I. A., Tabachnikova, E. D., and Lapovok, R., Cryogenic Equal Channel Angular Pressing of Commercially Pure Titanium: Microstructure and Properties, Journal of Materials Science, Vol. 49, No. 19, 2014, pp. 6803-6812, https://doi.org/10.1007/s10853-014-8382-1.

[11] Zhilyaev, A., Parkhimovich, N., Raab, G., Popov, V., and Danilenko, V., Microstructure and Texture Homogeneity of ecap Titanium, Reviews on Advanced Materials Science, Vol. 43, 2015, pp. 61-66, http://www.ipme.ru/e-journals/RAMS/no_14315/10_14315_zhilyaev.pdf.

[12] Biniyazan, F., Soleimanimehr, H., Improving Both Strength and Ductility of Al-7075 by Combining Dual Equal Channel Lateral Extrusion with Aging Heat Treatment, Iranian Journal of Science and Technology, Transactions of Mechanical Engineering, Vol. 45, No. 3, 2021, pp. 727-739, https://doi.org/10.1007/s40997-020-00416-y.

[13] Wang, Q., He, X., Deng, Y., Zhao, J., and Guo, X., Experimental Study of Grain Structures Evolution and Constitutive Model of Isothermal Deformed 2A14 Aluminum Alloy, Journal of Materials Research and Technology, Vol. 12, 2021, pp. 2348-2367, https://doi.org/10.1016/j.jmrt.2021.04.025.

[14] Morris, D. G., Gutierrez-Urrutia, I., and Munoz-Morris, M. A., Analysis of Strengthening Mechanisms in A Severely-Plastically-Deformed Al–Mg–Si Alloy with Submicron Grain Size, Journal of Materials Science, Vol. 42, No. 5, 2007, pp. 1439-1443, https://doi.org/10.1007/s10853-006-0564-z.

[15] Picak, S., Wegener, T., Sajadifar, S. V., Sobrero, C., Richter, J., Kim, H., Niendorf, T., and Karaman, I., On the Low-Cycle Fatigue Response of CoCrNiFeMn High Entropy Alloy with Ultra-Fine Grain Structure, Acta Materialia, Vol, 205, 2021, pp. 116540, https://doi.org/10.1016/j.actamat.2020.116540.

[16] Alawadhi, M. Y., Sabbaghianrad, S., Huang, Y., and Langdon, T. G., Evaluating the Paradox of Strength and Ductility in Ultrafine-Grained Oxygen-Free Copper Processed by ECAP at room temperature Materials Science and Engineering: A, Vol. 802, 2021, pp. 140546, https://doi.org/10.1016/j.msea.2020.140546.

[17] Rezaee, B., Kermani, E., Ejlali, S., Biniyazan, F., and Soleimanimehr, H., Nanoparticle Concentration and Heat Treatment Effects on Microstructure and Tribological Behavior of the Ni-P Nanocomposite Coating, Advanced Journal of Science and Engineering, Vol. 2, No. 2, 2021, pp. 71–78, https://doi.org/10.22034/advjscieng21022071.

[18] Rezaee, B., Kermani, E., Biniyazan, F., Ejlali, S., and Soleimanimehr, H., Effect of SiO2 and MoS2 Nanoparticles on Microstructure and Wear Resistance of Electroless Nanocomposite Ni-P-SiO2-MoS2 Coating, Iranian Journal of Manufacturing Engineering, Vol. 7, No. 9, 2020, pp. 65-71, http://www.iranjme.ir/article_120895.html?lang=en.

[19] Kermani, E., Biniyazan, F., Rezaee, B., and Soleimanimehr, H., An Investigation on the Microstructure and Impression Creep Behavior of the Magnesium Alloys, Journal of Modern Processes in Manufacturing and Production, Vol. 9, No. 1, 2020, pp. 43-49, https://mpmpjournal.iaun.ac.ir/article_672268.html.

[20] Roodposhti, P. S., Farahbakhsh, N., Sarkar, A., and Murty, K. L., Microstructural Approach to Equal Channel Angular Processing of Commercially Pure Titanium—A Review, Transactions of Nonferrous Metals Society of China, Vol. 25, No. 3, 2015, pp. 1353–1366, https://doi.org/10.1016/S1003-6326(15)63734-7.

Int. J. Advanced Design and Manufacturing Technology, 2023, Vol. 16, No. 1, pp. 45-56

DOI: 10.30486/admt.2022.1924605.1256 ISSN: 2252-0406 https://admt.isfahan.iau.ir

A New Visual Servoing Method for Grasping and Assembling Objects using Stereo Image Based Feedback

Mahmoud Jeddi[1]
Faculty of Material and Manufacturing Technologies
Malek Ashtar University of Technology, Tehran, Iran
E-mail: m.jedi100@mut.ac.ir

Ahmad Reza Khoogar[2, *]
Faculty of Material and Manufacturing Technologies
Malek Ashtar University of Technology, Tehran, Iran
E-mail: khoogar@mut.ac.ir
* Corresponding author

Received: 25 February 2021, Revised: 8 June 2021, Accepted: 17 June 2021

Abstract: In this paper, an eye-in-hand stereo image-based visual serving controller for industrial 6 degrees of freedom manipulator robots is presented. The visual control algorithms mostly use the relationship between camera speed and changes in image features, to determine the end-effector movement path. One of the main problems of the classical IBVS method is the inability to estimate the distance of the object related to the camera, which requires peripheral equipment such as a laser rangefinder to estimate the depth. In this study, two cameras were mounted on the end-effector of a 6 DOF manipulator robot. The distance of the object to the camera is estimated by the equations associated with the epipolar plane, and the interaction matrix is updated at any time. For increasing response speed, the image interaction matrix was divided into two separate parts related to translational and rotational motion, and it was found that only the translational motion part is affected by distance. The control method separates the camera motion into three-stage based on pure rotation, pure translation, and hybrid motion, which has a better time response compared to the classical IBVS control methods. Additionally, a method for position prediction and trajectory estimation of the moving target in order to use in a real-time grasping task is proposed and developed using Recursive Least Square as the trajectory estimators in the image plane. The simulation results show that the proposed method increases the system response speed and improves the tracking performance.

Keywords: Feature Matching, Image Interaction Matrix, Recursive Least Square, Stereo Image Based Visual Servoing, 6 DOF PILZ Robot

Biographical notes: Mahmoud Jeddi received his MSc in Mechanical Engineering from University of Tabriz 2012. He is currently PhD student in the department of Mechanical Engineering at the Malek Ashtar University of Technology, Tehran, Iran. His current research interests include Robotic, Control and Vision. **Ahmad Reza Khoogar** is Associate Professor of Mechanical Engineering at the Malek Ashtar University of Technology, Tehran, Iran. He received his PhD in Mechanical engineering from The University of Alabama, USA in 1989. His current research interests include Robotic, Control and Artificial Intelligence.

Research paper

1 INTRODUCTION

In recent years, a wide variety of applications regarding autonomous robot behavior in unstructured and unknown environment have been developed. There is a part of vision-based robotic research area called visual servo [1]. Visual servoing guide robots using the vision information. The visual servo is a framework to formalize the vision-based feedback control as a dynamical system. This framework provides rigorous evaluation for developing vision-based control systems, for example, controllability, and asymptotic stability, region of stability, robustness and sensitivity. Since these terms are familiar for control engineers visual servoing became a powerful tool for designing vision-based robotic systems. Visual servoing (VS) is a mature robotic technique having wide applications such as target/feature tracking, manipulator robot grasping [2]. The task in visual servoing, is to control the pose of the robot's end-effector, relative to the target, using visual features extracted from an image of the goal object. Existing VS schemes can be classified as image-based VS (IBVS), position-based VS (PBVS), and hybrid approaches [3]. These two methods are classified based on how the image is used to guide the robot. In PBVS, using image data the position of the end effector relative to the object is estimated and this estimated position is used to generate the robot control signal. In, IBVS image features are used directly to guide the robot. A control signal is generated to guide the robot so that the current features move towards the desired features. Visual servoing system can be single camera or stereo. The camera is usually positioned in either eye-to-hand or eye-in-hand mode. It is called the eye-in-hand where the camera is mounted on the end effector of the robot, but it is called the eye-to-hand when the camera is in a fixed position. This paper presents the eye-in-hand stereo IBVS method to control the end effector of 6 DOF manipulator PILZ robot. In IBVS and PBVS, the tracking error is defined in the image and the Cartesian space respectively, while in hybrid approaches, the error is defined in both spaces [4]. Particular interest in this paper is object pose estimation in IBVS using Recursive Least Square method. The visual control algorithms mostly use the relationship between camera speed and changes in image features (the image interaction matrix), to determine the robot end-effector path. One of the disadvantages of the classic IBVS method is the inability to estimate the depth of the target relative to the camera, which causes the robot to be ineffective in some situations or reduce system response speed. In this study, two cameras were mounted on the end-effector of a 6 DOF manipulator robot. The distance of the object to the camera is estimated by the equations associated with the epipolar plane, and the interaction matrix is updated at any time. For increasing response speed, the image interaction matrix was divided into two separate parts related to translational and rotational motion, and it was found that only the translational motion part is affected by distance. The control method separates the camera motion to three stages based on pure rotation, pure translation, and hybrid motion, which has a better time response compared to the classical IBVS control methods. In this research, it is assumed that two cameras are installed on the robot end-effector. Using the epipolar plane, the depth of the object relative to the camera is estimated at all times. The proposed method can be used for moving and stationary purposes. In some cases, due to the high speed of the moving target, the robot is not able to track and capture it. Therefore, using prediction methods, future positions of features in the image space can be estimated. In this paper, the position of the moving target in the image space was estimated using RLS, and the use of this method could improve the response speed of the system. Another problem with classical IBVS methods is the lack of detection of placement in regular shapes. Using a stereo system solves this problem. The proposed controller also solves the inherent problem of the classic IBVS method, which rotates 180 degrees around the camera axis. The paper is organized as follows. The main contributions are explicitly stated in Section 2. A traditional Image Based Visual Servoing and stereo image based visual servoing scheme are stated in Section 3. In this section the mathematical theory of monocular IBVS is presented and developed. Then, by extending the equations for the stereo approach, the image interaction matrix is calculated, while the description of the Recursive Least square is presented in Section 4. So, position prediction and trajectory estimation of the moving target are added to the proposed stereo-IBVS and make the process faster in a real-time grasping task a method. In Section 5, an intelligent hybrid visual control scheme incorporating developed controllers is explained in details. The proposed approach is evaluated in various simulation scenarios provided. Followed by Section 6 which summarizes findings and the contributions of this study.

1.1. Review of Previous Work

Many studies and methods have been proposed to improve the classical IBVS method. In this method, the control goal is to match the current properties with the desired properties on the image plane. Most studies have reported long convergence times that are not acceptable in industrial applications. In industrial applications, the IBVS method is effective and usable when the system response time is fast and stable. It is possible to reduce the system response time in the IBVS method by increasing the control law gain, but this method has limitations because increasing the gain causes robot instability and unwanted shakings [5]. In addition, traditional IBVS systems are stable only in a limited area around the desired position, and also when the desired

features are far away from the initial features state, the convergence time is long and the singularity points of the image may cause the robot motion to be failed [6]. Xie et al. proposed the idea of using the switching control method in IBVS [7]. In this method, the controller switches in two modes of rotation and translation. By considering the fact that the image interaction matrix is strongly influenced by depth, they used a laser system to determine the depth of the features. In this study, it was shown that switching schemes can solve some of the inherent problems of the IBVS method, such as the inability to rotate 180 degrees around the center of the camera or get stuck in local minima, etc. Also, in this research, all camera parameters are assumed to be known and certain, and the condition for changing between different modes is based on the norm of the features error, which is predefined. This criterion is not directly related to motion separation. In fact, a switch-based control method is required that ensures stability and has a more effective criterion for switching between rotation and translation modes to meet the needs of industrial applications [7]. Another issue with the IBVS method is the dependence of the control system performance on the accuracy of the camera calibration. Although many studies have improved the tracking performance of the IBVS method by using image moments as features or trajectory optimization, none of them considered the camera parameters uncertain and assumed that the camera was well calibrated. In addition, path optimization methods take relatively considerable time to solve the optimization problem in each movement step, which is not suitable for industrial environments [8]. Camera parameters can be obtained by the calibration process. However, in some cases, especially in industrial applications, this is not possible and these parameters may change during an operation [9]. However, most studies in this field are based on the design of the kinematics-based controllers. In other words, they consider the robot as a precise positioning system that has negligible dynamics. Kinematic-based controllers ignore system dynamics and implement a simpler control process. Using a kinematics-based visual servo system is easier than using a dynamics-based control system. However, dynamic-based methods use the robot dynamic model to design the controller, and therefore can provide better control performance in terms of convergence time and guarantee stability compared to the kinematic-based control method. Ghasemi et al. Proposed an adaptive switch control method based on the robot dynamic model for the IBVS system. In this study, three states of pure rotation, pure translation, and hybrid movement were selected as control modes. A different control gain was considered for each control stage. The results showed that the adaptive switch control method has a faster time response and better stability than the two switch methods IBVS and traditional IBVS. However, in this study, the depth of the features is considered as a predefined parameter and the monocular IBVS approach was used for the Vision system, which is unsuitable in industrial environments with uncertain variables [10]. Undoubtedly, one of the most effective human tools in understanding the world and recognizing it is the sense of sight. Understanding the three-dimensional properties of a landscape and finding the geometric information of the objects in it, is one of the most important areas of research in machine vision [11]. By the growth of control systems, in the future we will see smart devices that, while being able to detect objects, route, estimate and maintain distance from passers-by or other devices, and can themselves implement the corresponding route operations [12]. With the increasing use of 3D images for different locations, different sensors are used to simulate high quality visual information [13]. Stereo vision is one of the visual sensors that extracts depth by having at least two images of a scene and based on the adaptation of the stereo [14]. Stereo vision is an emerging method that is inspired by the human visual system and calculates the three-dimensional coordinates of objects using images from left and right cameras and the corresponding stereo equations and algorithms [15]. In robotic applications, the use of stereo vision allows the robot to obtain information about the structure and geometric shape of objects and their location, both relative to the robot and to other objects [16]. The stereo vision model consists of an object and two cameras with a parallel or intersecting optical axis or other layouts that are used to achieve a three-dimensional position of the surrounding environment [17]. Payeur proposed a method based on neural network to predict the trajectory in a robotic environment in real time. His method used the six most recent measurements of the object coordinates as inputs [18]. Hideki Hashimoto describes a control scheme for a robotic manipulator system that uses visual information to position and orientate the end-effector. The control system directly integrates visual data into the servoing process without subdividing the process into determination of the position and orientation of the work piece and inverse kinematic calculation. The feature of the control scheme is the use of neural networks for the determination of the change in joint angles required in order to achieve the desired position and orientation. The proposed system is able to control the robot so that it can approach the desired position and orientation from arbitrary initial ones [19]. It should be noted that the first three columns of the image interaction matrix are related to the translation motion of the end effector and the next three columns are related to its rotational motion. If the motion is divided into translation and rotation parts, the rotational motion is independent of the depth parameter, while the translation motion is dependent on the depth,

which is calculated using the stereo technique at any time and placed in the interaction matrix. This technique gives the chance of overcoming the nonlinearity created by the depth parameter and allows us to use adaptive methods to estimate the camera parameters in stereo eye in hand mode. Therefore, in this paper, the idea of switching between different modes of motion of the robot will be used in such a way that the three modes of pure rotation, pure translation and a hybrid motion for fine tuning will be used. The remaining paper is organized as follows: in section 2, a methodology is presented. In section 3, the adaptive switch controller for stereo IBVS considering the three movement states is designed. In section 4, simulation results are presented and finally, conclusion remarks are given and the advantage of the presented method is explained in section 5.

2 CONTRIBUTIONS OF PAPER

- An image-based visual servoing (IBVS) approach based on stereo vision has been presented and mathematically discussed and compared to the case of Monocular IBVS.
- The method for stacking the proper image interaction matrices for the case of image based stereo visual servoing has been developed for two cases of parallel and non-parallel cameras and the exact depth information has been extracted from the geometry of the vision system and used in image interaction matrices.
- A method for trajectory estimation of a moving object has been proposed to predict the position of the object which is used in a stereo image-based visual servoing for a real-time grasping procedure. The system dynamics of the object has been modeled in both linear and nonlinear description in image plane instead of 3- D space. object pose estimation in S_IBVS using Recursive Least Square method.
- For increasing response speed, the image interaction matrix was divided into two separate parts related to translational and rotational motion, and it was found that only the translational motion part is affected by distance. The control method separates the camera motion to three stages based on pure rotation, pure translation, and hybrid motion, which has a better time response compared to the classical IBVS control methods.

3 PROPOSED METHODOLOGIES

The task in visual servoing is to control the pose of the robot's end-effector, relative to the goal, using visual features extracted from an image of the goal object. In this paper, the goal is to optimize the assembly of robotic parts without the need for an operator.

To increase the accuracy of assembling, the two cameras are mounted on the robot's end-effector to detect the position and direction of the parts. The processed information is sent to the robot controller for decision. Object trajectory in image planes is predicted by RLS filter to increase convergence velocity. Proposed methodology is shown in "Fig. 1".

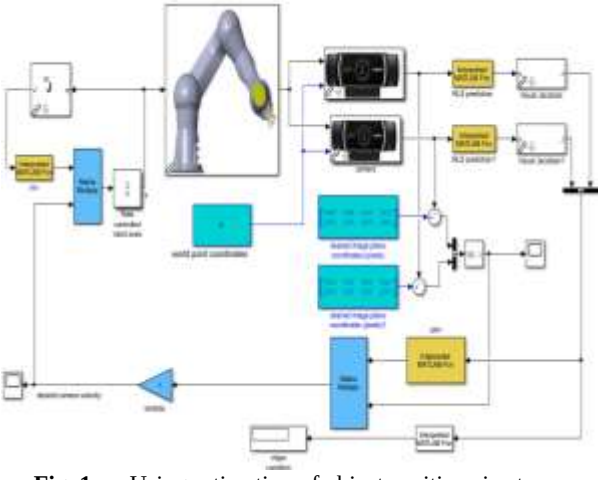

Fig. 1 Using estimation of object positions in stereo image-plane for an image-based servoing approach to grasp a moving target by 6 Dof PILZ robot.

As shown in "Fig .1", the object in the 3-D world viewed by stereo cams and recursive least square filter estimates the trajectory of object in both image planes. Because the cameras are mounted to the robot end-effector, so the output of the images is a motion gradient and the image interaction matrix must be obtained. Using the inverse of the image interaction matrix as well as the difference between the observed points and the desired point and multiplying these two by the system gain, the desired output speed can be obtained at any time. By multiplying the desired output speed by the inverse of the robot Jacobean and integrating the response, the desired angles for the joints can be calculated.

3.1. Dynamical Model of The Stereo-IBVS

Imagine a camera mounted on the end effector and move with a body velocity $\vartheta = (v, \omega)$ in the world frame and observe a world point P with camera relative coordinates $P = (X, Y, Z)$. The velocity of the point relative to the camera frame is

$$\dot{\boldsymbol{P}} = -\boldsymbol{\omega} \times \boldsymbol{P} - \boldsymbol{v} \tag{1}$$

Which can write in scalar form as:

$$\begin{aligned} \dot{\boldsymbol{X}} &= \boldsymbol{Y\omega_x} - \boldsymbol{Z\omega_y} - \boldsymbol{v_x} \\ \dot{\boldsymbol{Y}} &= \boldsymbol{X\dot{\omega}_z} - \boldsymbol{Z\omega_x} - \boldsymbol{v_y} \\ \boldsymbol{Z} &= \boldsymbol{X\omega_y} - \boldsymbol{Y\omega_x} - \boldsymbol{v_z} \end{aligned} \tag{2}$$

The perspective projection for normalized image-plane coordinates could write as:

$$\boldsymbol{x} = \frac{\boldsymbol{X}}{\boldsymbol{Z}} \ , \boldsymbol{y} = \frac{\boldsymbol{Y}}{\boldsymbol{Z}} \tag{3}$$

Using the quotient rule drive the temporal derivative as:

$$\dot{\boldsymbol{x}} = \frac{\dot{X}Z - X\dot{Z}}{Z^2} \ , \dot{\boldsymbol{y}} = \frac{\dot{Y}Z - Y\dot{Z}}{Z^2} \tag{4}$$

With placement $X = xZ$ and $Y = yZ$ in "Eq. (2)" then write in matrix form as:

$$\begin{pmatrix} \dot{\mathbf{x}} \\ \dot{\mathbf{y}} \end{pmatrix} = \begin{bmatrix} -\frac{1}{\mathbf{Z}} & \mathbf{0} & \frac{\mathbf{x}}{\mathbf{Z}} & \mathbf{xy} & -(\mathbf{1}+\mathbf{x}^{\mathbf{2}}) & \mathbf{y} \\ \mathbf{0} & -\frac{1}{\mathbf{Z}} & \frac{\mathbf{y}}{\mathbf{Z}} & \mathbf{1}+\mathbf{y}^{\mathbf{2}} & -\mathbf{xy} & -\mathbf{x} \end{bmatrix} \begin{bmatrix} \mathbf{v_x} \\ \mathbf{v_y} \\ \mathbf{v_z} \\ \boldsymbol{\omega}_{\mathbf{x}} \\ \boldsymbol{\omega}_{\mathbf{y}} \\ \boldsymbol{\omega}_{\mathbf{z}} \end{bmatrix} \tag{5}$$

Which maps camera spatial velocity to feature velocity in normalized image coordinates. If normalized image-plane coordinates change to the pixel coordinates:

$$\boldsymbol{u} = \frac{\boldsymbol{f}}{\boldsymbol{\rho_u}}\boldsymbol{x} + \boldsymbol{u_0} \ , \boldsymbol{v} = \frac{\boldsymbol{f}}{\boldsymbol{\rho_v}}\boldsymbol{y} + \boldsymbol{v_0} \tag{6}$$

In Eq. (6), f describes the focus length and (u_0, v_0) is principal point. By definition $\bar{u} = u - u_0$ and $\bar{v} = v - v_0$, Eq. (6) could be rearranged as $x = \frac{\rho_u}{f}\bar{u}$, $y = \frac{\rho_v}{f}\bar{v}$ by considering ρ_u, ρ_v and f is constant parameters, so the temporal derivative related to the pixel coordinates is:

$$\boldsymbol{x} = \frac{\boldsymbol{\rho_u}}{\boldsymbol{f}}\dot{\bar{\boldsymbol{u}}} \ , \boldsymbol{y} = \frac{\boldsymbol{\rho_v}}{\boldsymbol{f}}\dot{\bar{\boldsymbol{v}}} \tag{7}$$

And substituting "Eq. (7) and Eq. (5)" into Eq. leads to:

$$\begin{pmatrix} \dot{\bar{\boldsymbol{u}}} \\ \dot{\bar{\boldsymbol{v}}} \end{pmatrix} = \begin{bmatrix} -\frac{\boldsymbol{f}}{\boldsymbol{\rho_u Z}} & \mathbf{0} & \frac{\bar{\boldsymbol{u}}}{\boldsymbol{Z}} & \frac{\boldsymbol{\rho_v}\bar{\boldsymbol{u}}\bar{\boldsymbol{v}}}{\boldsymbol{f}} & -\frac{\boldsymbol{f^2}+\boldsymbol{\rho_u}^2\bar{\boldsymbol{u}}^2}{\boldsymbol{\rho_u f}} & \frac{\boldsymbol{\rho_v}\bar{\boldsymbol{v}}}{\boldsymbol{\rho_u}} \\ \mathbf{0} & -\frac{\boldsymbol{f}}{\boldsymbol{\rho_v Z}} & \frac{\bar{\boldsymbol{v}}}{\boldsymbol{Z}} & \frac{\boldsymbol{f^2}+\boldsymbol{\rho_v}^2\bar{\boldsymbol{v}}^2}{\boldsymbol{\rho_v f}} & -\frac{\boldsymbol{\rho_v}\bar{\boldsymbol{u}}\bar{\boldsymbol{v}}}{\boldsymbol{f}} & -\frac{\boldsymbol{\rho_u}\bar{\boldsymbol{v}}}{\boldsymbol{\rho_v}} \end{bmatrix} \begin{bmatrix} \boldsymbol{v_x} \\ \boldsymbol{v_y} \\ \boldsymbol{v_z} \\ \boldsymbol{\omega_x} \\ \boldsymbol{\omega_y} \\ \boldsymbol{\omega_z} \end{bmatrix} \tag{8}$$

To simplify assume $\rho = \rho_u = \rho_v$ and $\bar{f} = {}^{f}/_{\rho}$. The Jacobian matrix could be simplified as:

$$\boldsymbol{J_p(p,Z)} = \begin{bmatrix} -\frac{\bar{\boldsymbol{f}}}{\boldsymbol{Z}} & \mathbf{0} & \frac{\bar{\boldsymbol{u}}}{\boldsymbol{Z}} & \frac{\bar{\boldsymbol{u}}\bar{\boldsymbol{v}}}{\bar{\boldsymbol{f}}} & -\frac{\bar{\boldsymbol{f}}^2+\bar{\boldsymbol{u}}^2}{\boldsymbol{f}} & \bar{\boldsymbol{v}} \\ \mathbf{0} & -\frac{\bar{\boldsymbol{f}}}{\boldsymbol{Z}} & \frac{\bar{\boldsymbol{v}}}{\boldsymbol{Z}} & \frac{\bar{\boldsymbol{f}}^2+\bar{\boldsymbol{v}}^2}{\boldsymbol{f}} & \frac{\bar{\boldsymbol{u}}\bar{\boldsymbol{v}}}{\bar{\boldsymbol{f}}} & -\bar{\boldsymbol{u}} \end{bmatrix} \tag{9}$$

"Eq. (7)" can write concise matrix form as:

$$\dot{\boldsymbol{P}} = \boldsymbol{J_p(p,Z)}\boldsymbol{\vartheta} \tag{10}$$

Where, J_p, is the 2×6 image Jacobian matrix for a point feature at coordinate p and camera distance Z. Jacobean matrix $J_p(p,Z)$ could be divided in two parts of translation and angular:

$$\boldsymbol{J_p(p,Z)} = \begin{bmatrix} \underbrace{-\frac{\bar{\boldsymbol{f}}}{\boldsymbol{Z}} \quad \mathbf{0} \quad \frac{\bar{\boldsymbol{u}}}{\boldsymbol{Z}}}_{\frac{1}{Z}\boldsymbol{J_t}} & \underbrace{\frac{\bar{\boldsymbol{u}}\bar{\boldsymbol{v}}}{\bar{\boldsymbol{f}}} \quad -\frac{\bar{\boldsymbol{f}}^2+\bar{\boldsymbol{u}}^2}{\boldsymbol{f}} \quad \bar{\boldsymbol{v}}}_{\boldsymbol{J_\omega}} \\ \mathbf{0} \quad -\frac{\bar{\boldsymbol{f}}}{\boldsymbol{Z}} \quad \frac{\bar{\boldsymbol{v}}}{\boldsymbol{Z}} \quad \frac{\bar{\boldsymbol{f}}^2+\bar{\boldsymbol{v}}^2}{\boldsymbol{f}} \quad \frac{\bar{\boldsymbol{u}}\bar{\boldsymbol{v}}}{\bar{\boldsymbol{f}}} \quad -\bar{\boldsymbol{u}} \end{bmatrix} \tag{11}$$

The "Eq. (11)" can write in brevity as:

$$\dot{\boldsymbol{P}} = \left(\frac{\boldsymbol{1}}{\boldsymbol{Z}}\boldsymbol{J_t(p,Z)} \ \vdots \ \boldsymbol{J_\omega(p,Z)}\right)\boldsymbol{\vartheta} \tag{12}$$

Substitute "Eq. (12)" into "Eq. (8)":

$$\begin{pmatrix} \dot{\bar{\boldsymbol{u}}} \\ \dot{\bar{\boldsymbol{v}}} \end{pmatrix} = \frac{\boldsymbol{1}}{\boldsymbol{Z}}\boldsymbol{J_t v} + \boldsymbol{J_\omega \omega} \tag{13}$$

Rearranging Eq. (13) in linear form:

$$\frac{\boldsymbol{1}}{\boldsymbol{Z}}\boldsymbol{J_t v} = \begin{pmatrix} \dot{\bar{\boldsymbol{u}}} \\ \dot{\bar{\boldsymbol{v}}} \end{pmatrix} - \boldsymbol{J_\omega \omega} \tag{14}$$

Writing "Eq. (12)" in compact form $A\theta = B$, we have a simple linear equation. Computing the image Jacobian requires knowledge of the camera intrinsic, the principal point, and focal length, but in practice, it is quite tolerant of errors in these.

3.2. Interaction Matrix for Stereo Vision

Consider the pair of cameras are look at an arbitrary point in the world. The projected point in each image plane is showed by $\{p_i(x_i, y_{i)}, \ i = l, r\}$ so relative equation for projecting observed points in the left and right image planes could be written as:

$$\boldsymbol{x_l} = \frac{X + \frac{b}{2}}{Z} \quad , \ \boldsymbol{y_l} = \frac{Y}{Z} \tag{15-a}$$

$$\boldsymbol{x_r} = \frac{X - \frac{b}{2}}{Z} \quad , \ \boldsymbol{y_r} = \frac{Y}{Z} \tag{15-b}$$

Normalize the coordinates and describe "Eq. 15" in pixel dimensions:

$$\boldsymbol{x_l = \frac{u_l - u_0}{f^* \alpha}} \quad , \quad \boldsymbol{y_l = \frac{v_l - v_0}{f^*}} \tag{16-a}$$

$$\boldsymbol{x_r = \frac{u_r - u_0}{f^* \alpha}} \quad , \quad \boldsymbol{y_l = \frac{v_r - v_0}{f^*}} \tag{16-b}$$

In "Eq. (16)", u_0 and v_0 are the coordinates of the camera principal point, f is the focal length, α is the ratio of the pixel dimensions where $\frac{dy}{dx} = \alpha$ and f^* is focal length described in pixel dimensions. Taking the time derivative of the perspective projection Equations:

$$\boldsymbol{x_l = \frac{\dot{X} + x_l \dot{Z}}{Z}} \quad , \; \boldsymbol{y_l = \frac{\dot{Y} + y_l \dot{Z}}{Z}} \tag{17-a}$$

$$\boldsymbol{x_r = \frac{\dot{X} - x_r \dot{Z}}{Z}} \quad , \; \boldsymbol{y_l = \frac{\dot{Y} - y_r \dot{Z}}{Z}} \tag{17-b}$$

The velocity of a feature point in an image p_I can be written related to the velocity of a feature point in a camera frame P^c as:

$$\boldsymbol{\dot{p} = J_c^I \dot{P}^c} \tag{18}$$

Where of $p_I = [p_l, p_r]$ and:

$$\boldsymbol{J_C^I} = \begin{bmatrix} \frac{\partial x_l}{\partial X} & \frac{\partial y_l}{\partial X} & \frac{\partial x_r}{\partial X} & \frac{\partial y_r}{\partial X} \\ \frac{\partial x_l}{\partial Y} & \frac{\partial y_l}{\partial Y} & \frac{\partial x_r}{\partial Y} & \frac{\partial y_r}{\partial Y} \\ \frac{\partial x_l}{\partial Z} & \frac{\partial y_l}{\partial Z} & \frac{\partial x_r}{\partial Z} & \frac{\partial y_r}{\partial Z} \end{bmatrix}^T = \begin{bmatrix} \frac{1}{Z} & 0 & \frac{1}{Z} & \frac{1}{Z} \\ 0 & \frac{1}{Z} & 0 & \frac{1}{Z} \\ -\frac{X+\frac{b}{2}}{Z^2} & -\frac{Y}{Z^2} & -\frac{X-\frac{b}{2}}{Z^2} & -\frac{Y}{Z^2} \end{bmatrix}^T \tag{19}$$

The velocity of P^c related to spatial camera velocity can be written as:

$$\boldsymbol{\dot{P}^c = -\omega_c \times P^c - v_c} \tag{20}$$

Solve "Eq. 20":

$$\boldsymbol{\dot{P}^c = \begin{bmatrix} \dot{X} \\ \dot{Y} \\ \dot{Z} \end{bmatrix} = \begin{bmatrix} -\omega_y Z + \omega_x Y - v_x \\ -\omega_z X + \omega_x Z - v_x \\ -\omega_x Y + \omega_y X - v_Z \end{bmatrix} = \Lambda u_c} \tag{21}$$

Substituting Eq. 18 in Eq.21 can be written:

$$\boldsymbol{\dot{p}_I = J_c^I \dot{P}_c \;\; \mapsto \;\; \dot{p}_I = J_c^I \Lambda u_c = J_{st} u_c} \tag{22}$$

Where, J_{st} is the stereo-vision image interaction which expresses the relation between a velocity of a feature point in an image $\dot{p}_I$, and a moving velocity of a camera u_c. Considering $X = \frac{b(x_l + x_r)}{2(x_l - x_r)}$, $Y = y_l \frac{b}{(x_l - x_r)}$ and $Z = \frac{b}{(x_l - x_r)}$ rewrite the stereo-vision image interaction matrix as:

$$\boldsymbol{J_{st}} = \begin{bmatrix} -\frac{a}{b} & 0 & x_l \frac{a}{b} & x_l y & -\left(1 + \frac{x_l (x_l + x_r)}{2}\right) & y \\ 0 & -\frac{a}{b} & y \frac{a}{b} & 1 + y^2 & -y \frac{(x_l + x_r)}{2} & -\frac{(x_l + x_r)}{2} \\ -\frac{a}{b} & 0 & x_r \frac{a}{b} & x_r y & -\left(1 + \frac{x_l (x_l + x_r)}{2}\right) & y \\ 0 & -\frac{a}{b} & y \frac{a}{b} & 1 + y^2 & -y \frac{(x_l + x_r)}{2} & -\frac{(x_l + x_r)}{2} \end{bmatrix} \tag{23}$$

Where, $a = x_l + x_r$ is called feature point disparity and $y = y_l = y_r$. Eventually, the stereo-vision image interaction matrix could be obtained with the velocities expressed in the camera frame and then transformed into the sensor frame [20].

$$\boldsymbol{\dot{p}_I = \begin{bmatrix} J_l M_c^l \\ J_r M_c^r \end{bmatrix} u_c = J_{st} u_c} \tag{24}$$

Assume a camera spatial velocity be unit magnitude $v^T v = 1$, Due to "Eq. (24)", write the camera velocity in terms of the pseudo-inverse $v = J^+ \dot{p}$ where $J^+ \in R^{2n \times 6}$ the Jacobian stack and $\dot{p} \in R^{2n}$is the point velocities. Substitution this Eq's yields the equation of an ellipsoid in the point velocity space.

$$\boldsymbol{p^{\cdot T} J^{+T} J^+ \dot{p} = 1 \;\; \mapsto \;\; p^{\cdot T} (J J^T)^{-1} \dot{p} = 1} \tag{25}$$

The eigenvectors of JJ^T define the principal axes of the ellipsoid and the singular values of J are the radii. The ratio of the maximum to minimum radius is given by the condition number of JJ^T and indicates the anisotropy of the feature motion. A high value indicates that some of the points have low velocity in response to some camera motions. Next section explained how to design a proper controller via selecting features.

3.3. Design Controller

In general, the relationship between changes in image features and camera speed can be written as follows:

$$\boldsymbol{\dot{s}(t) = J_{st}(t) V_c(t)} \tag{26}$$

On the other hand, using the Jacobin robot matrix, the camera speed can be achieved:

$$\boldsymbol{V_c(t) = J_R(t) \dot{q}(t) = \begin{bmatrix} V_{ct}(t) \\ V_{cr}(t) \end{bmatrix} = \begin{bmatrix} J_{Rt}(t) \dot{q}(t) \\ J_{Rr}(t) \dot{q}(t) \end{bmatrix}} \tag{27}$$

Where, $J_R(t) = [J_{Rt}(t) \;\; J_{Rr}(t)]^T \in \mathbb{R}^{6*1}$ is decomposed to the translational and rotational part, by

considering "Eq. (26) and (27)" for the i[th] features $\dot{s}_i(t) \epsilon \mathbb{R}^{2*1}$ as:

$$\dot{\boldsymbol{s}}_{\boldsymbol{i}}(\boldsymbol{t}) = [\boldsymbol{J}_{\boldsymbol{t}}(\boldsymbol{t}) \quad \boldsymbol{J}_{\boldsymbol{r}}(\boldsymbol{t})] \begin{bmatrix} \boldsymbol{V}_{\boldsymbol{ct}}(\boldsymbol{t}) \\ \boldsymbol{V}_{\boldsymbol{cr}}(\boldsymbol{t}) \end{bmatrix} = \boldsymbol{J}_{\boldsymbol{t}}(\boldsymbol{t})\boldsymbol{V}_{\boldsymbol{ct}}(\boldsymbol{t}) + \boldsymbol{J}_{\boldsymbol{r}}(\boldsymbol{t})\boldsymbol{V}_{\boldsymbol{cr}}(\boldsymbol{t}) \quad (28)$$

By expanding the "Eq. (28)" and placing the relation (27) in this equation, the relation between the features and the speed of the camera is obtained as follows:

$$\dot{\boldsymbol{s}}_{\boldsymbol{i}}(\boldsymbol{t}) = \boldsymbol{J}_{\boldsymbol{t}}(\boldsymbol{t})\boldsymbol{J}_{\boldsymbol{Rt}}(\boldsymbol{q}(\boldsymbol{t}))\dot{\boldsymbol{q}}(\boldsymbol{t}) + \boldsymbol{J}_{\boldsymbol{r}}(\boldsymbol{t})\boldsymbol{J}_{\boldsymbol{Rr}}(\boldsymbol{q}(\boldsymbol{t}))\dot{\boldsymbol{q}}(\boldsymbol{t}) \quad (29)$$

Due to the three different stage of camera motion, the adaptive controller is designed based on the switch method. The first stage is only rotational, so the translational command is turned off. In the second stage, the translational movement is active and the rotational command is off. The third stage is the hybrid motion of rotation and translation.

In the first stage, the rotation command is off and controller decides just based on translational motion:

$$\dot{\boldsymbol{s}}_{\boldsymbol{i}}(\boldsymbol{t}) = \frac{\boldsymbol{1}}{\boldsymbol{Z}}\boldsymbol{J'}_{\boldsymbol{t}}(\boldsymbol{t})\boldsymbol{J}_{\boldsymbol{Rt}}(\boldsymbol{q}(\boldsymbol{t}))\dot{\boldsymbol{q}}(\boldsymbol{t}) \quad (30)$$

In "Eq. (30)" $J'_t(t) = ZJ_t(t)$. In the second stage, the camera is in pure rotation, so just the rotational part is turned on:

$$\dot{\boldsymbol{s}}_{\boldsymbol{i}}(\boldsymbol{t}) = \boldsymbol{J}_{\boldsymbol{r}}(\boldsymbol{t})\boldsymbol{J}_{\boldsymbol{Rr}}(\boldsymbol{q}(\boldsymbol{t}))\dot{\boldsymbol{q}}(\boldsymbol{t}) \quad (31)$$

Finally, in the third stage the camera motion is due to both translation and rotation movement, so the rotation and translation command in this stage switched on:

$$\dot{\boldsymbol{s}}_{\boldsymbol{i}}(\boldsymbol{t}) = \frac{\boldsymbol{1}}{\boldsymbol{Z}}\boldsymbol{J'}_{\boldsymbol{t}}(\boldsymbol{t})\boldsymbol{J}_{\boldsymbol{Rt}}(\boldsymbol{q}(\boldsymbol{t}))\dot{\boldsymbol{q}}(\boldsymbol{t}) + \boldsymbol{J}_{\boldsymbol{r}}(\boldsymbol{t})\boldsymbol{J}_{\boldsymbol{Rr}}(\boldsymbol{q}(\boldsymbol{t}))\dot{\boldsymbol{q}}(\boldsymbol{t}) \quad (32)$$

Depending on the position of the features relative to the desired position in the image space, the controller adjusts the movement of the cameras (and consequently the movement of the robot) and commands one of the mentioned positions.

If the current points of the corners of the quadrilateral are out of square shape, it is clear that the camera is farther away from the target object, so the translational mode is activated first. (See "Fig. 2").

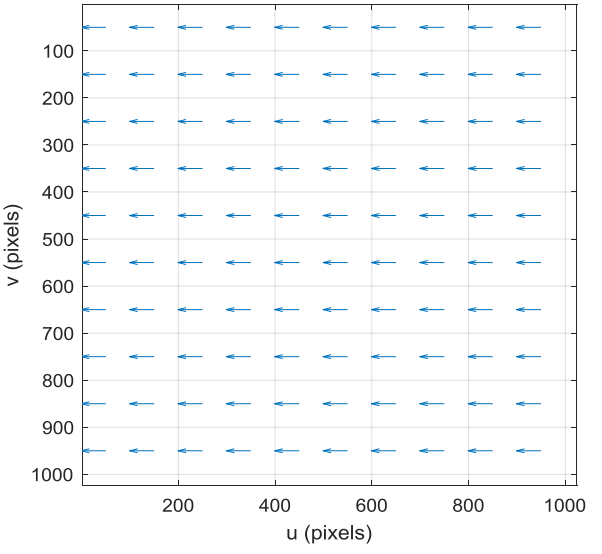

Fig. 2 Pure translation of camera movement.

If the target points differ from the desired points only in terms of orientation and positioning, only the rotation command is issued. (See "Fig. 3").

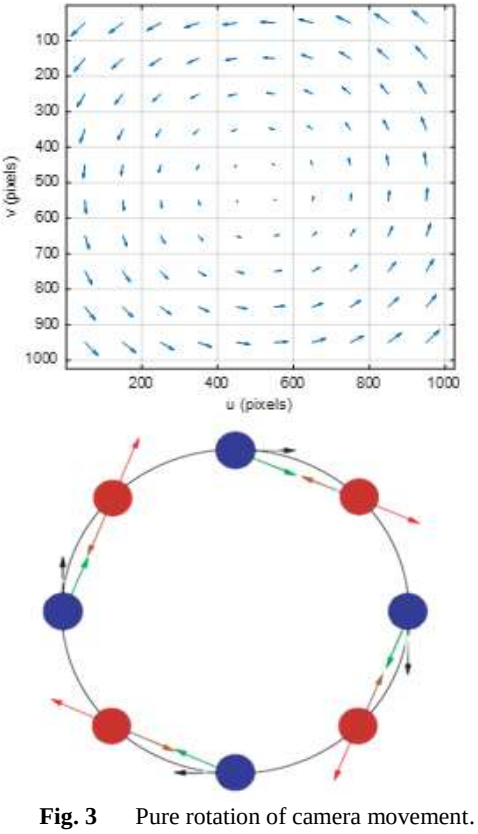

Fig. 3 Pure rotation of camera movement.

If they are slightly different in terms of position and rotation, then both rotation and translation commands

are activated by the controller and this is called fine-tuning. (See "Fig. 4").

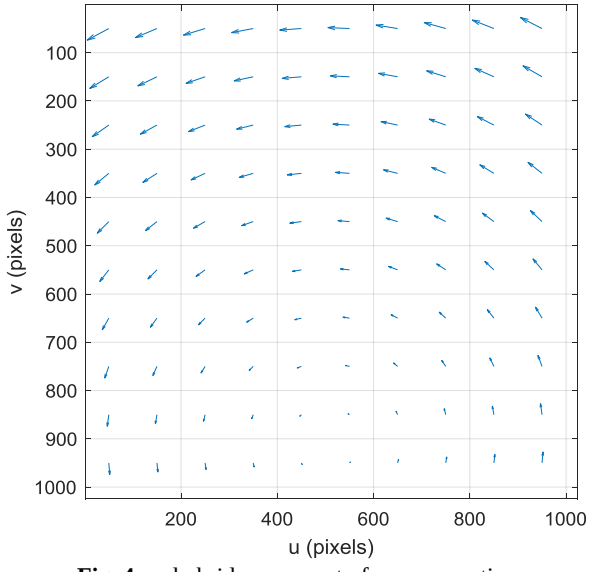

Fig. 4 hybrid movement of camera motion.

3.4. Moving Object Modeling

In order to provide essential position information for an image-based stereo visual servoing approach to grasp a moving object, it is possible to model the motion of the target in image-planes and to predict the trajectory and positions in a near future sequence. Based on the estimated velocity and acceleration of the moving object in right and left image planes and knowing the current position parameters, the estimated position of the object or the feature points in next instance, $(\hat{x}_k, \hat{y}_k)$ could be predicted as:

$$\hat{\boldsymbol{x}}_{\boldsymbol{k}} = \hat{\boldsymbol{x}}_{\boldsymbol{k-1}} + \hat{\boldsymbol{v}}_{\boldsymbol{k-1}}.\Delta \boldsymbol{T} + \frac{\boldsymbol{1}}{\boldsymbol{2}}\hat{\boldsymbol{a}}_{\boldsymbol{k-1}}.\Delta \boldsymbol{T^2} \tag{35}$$

ΔT is the sampling period. In order to model the moving object in a recursive procedure, "Eq. (35)" should be expressed in form of the discrete time state transition and its observation models are as follows:

$$X_k = \emptyset_{k,k-1} X_{k-1} + W_{k-1} \tag{36}$$

$$Z_k = H_k X_k + v_k \tag{37}$$

Where, $X_k = [x_k, y_k, dx_k, dy_k]^T$ is the state vector, $Z_k = [x_k, y_k]^T$ is the measurement vector, $\emptyset_{\boldsymbol{k,k-1}}$ is the state transition matrix which represents the transition from one state vector $Xk-1$ to the next vector Xk, Wk represents the process noises and are the measurement noises in both x and y direction. Hk is called observation matrix and represents the relationship between the measurement and the state vector. Now we are able to obtain the observation models as follows:
The measurement vector $Z_k = [x_k, y_k]^T$ is the actual position of an object or a feature point in x-y image planes in right and left cameras which could be obtained using the vision system.

$$\begin{bmatrix} \boldsymbol{x_k} \\ \boldsymbol{y_k} \end{bmatrix} = \begin{bmatrix} \boldsymbol{1} & \boldsymbol{0} & \boldsymbol{0} & \boldsymbol{0} \\ \boldsymbol{0} & \boldsymbol{1} & \boldsymbol{0} & \boldsymbol{0} \end{bmatrix} \begin{bmatrix} \boldsymbol{x_k} \\ \boldsymbol{y_k} \\ \boldsymbol{dx_k} \\ \boldsymbol{dy_k} \end{bmatrix} + \begin{bmatrix} \boldsymbol{\gamma_x} \\ \boldsymbol{\gamma_y} \end{bmatrix} \tag{38}$$

$$\begin{bmatrix} \boldsymbol{x_k} \\ \boldsymbol{y_k} \\ \boldsymbol{dx_k} \\ \boldsymbol{dy_k} \end{bmatrix} = \begin{bmatrix} \boldsymbol{1} & \boldsymbol{0} & \boldsymbol{\Delta t} & \boldsymbol{0} \\ \boldsymbol{0} & \boldsymbol{1} & \boldsymbol{0} & \boldsymbol{\Delta t} \\ \boldsymbol{0} & \boldsymbol{0} & \boldsymbol{1} & \boldsymbol{0} \\ \boldsymbol{0} & \boldsymbol{0} & \boldsymbol{0} & \boldsymbol{1} \end{bmatrix} \begin{bmatrix} \boldsymbol{x_{k-1}} \\ \boldsymbol{y_{k-1}} \\ \boldsymbol{dx_{k-1}} \\ \boldsymbol{dy_{k-1}} \end{bmatrix} + \begin{bmatrix} \boldsymbol{0.5 * d^2(x_{k-1}) * \Delta t^2} \\ \boldsymbol{0.5 * d^2(y_{k-1}) * \Delta t^2} \\ \boldsymbol{d^2(x_{k-1}) * \Delta t} \\ \boldsymbol{d^2(y_{k-1}) * \Delta t} \end{bmatrix} \tag{39}$$

4 TRAJECTORY ESTIMATION USING RECURSIVE LEAST SQUARE METHOD

Enough number of feature points projected in the camera plane are selected, a Recursive Least Squares method can be used to find the best estimation of the state variables of the object e.g., $X_k = [x_k, y_k, dx_k, dy_k]^T$ from the previous states data. The best estimation for time interval k can be computed as:

$$\hat{\boldsymbol{x}}_{\boldsymbol{k}} = \hat{\boldsymbol{x}}_{\boldsymbol{k-1}} + \boldsymbol{G_k}.[\boldsymbol{Z_k} - \boldsymbol{H_k}\hat{\boldsymbol{X}}_{\boldsymbol{k-1}}] \tag{40}$$

Where, G_k is the optimal gain matrix and H_k is the observation matrix. The gain matrix can be computed by $G_k = L_k H'_k$. L_k is the error covariance matrix for the estimation of the state of time interval k and can be expressed as:

$$\boldsymbol{L_k} = (\emptyset^{-\boldsymbol{T}}_{\boldsymbol{k,k-1}} \boldsymbol{L^{-1}_{k-1}} \emptyset^{\boldsymbol{T}}_{\boldsymbol{k,k-1}} + \boldsymbol{H^T_k H_k})^{\boldsymbol{-1}} \tag{41}$$

5 SIMULATION RESULTS

In this section the robotic stereo visual servoing system for PILZ robot is modeled. The effectiveness of the image-based stereo visual servoing system compared to the monocular system is validated. Then the system performance in a task of tracking and grasping a moving object is examined and the results for utilizing recursive least square method for predicting the position and trajectory of the moving target are presented and discussed. The object assumes to be a square cube and

the corners of this cube are the object image features extracted in both cameras.

The stereo system consists of two parallel cameras which are located at a distance of b/2 with respect to the origin of the sensor frame. In order to keep at least 3 selected feature points on the object in both cameras' fields of views, during the approaching phase, the distance b is selected to be equal to 10 cm. The simulation results for 6 Dof PILZ robot and object points are shown in Fig. 5.

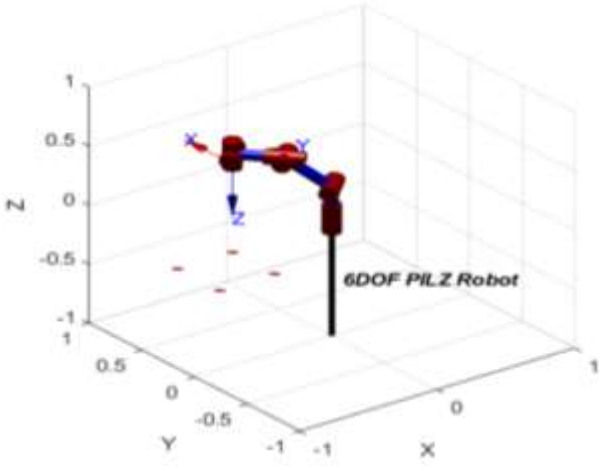

Fig. 5 6 Dof PILZ Robot and object simulation.

For the presented algorithm, a grasping algorithm with an object in a sinusoidal motion with a linear velocity of 4 cm/sec would be tested. As it was mentioned previously, the tracking and grasping task is performed by pre-defining desired positions for the object image features such that the robot moves and aligns the end-effector with the object and reaches towards it. (See "Fig. 6").

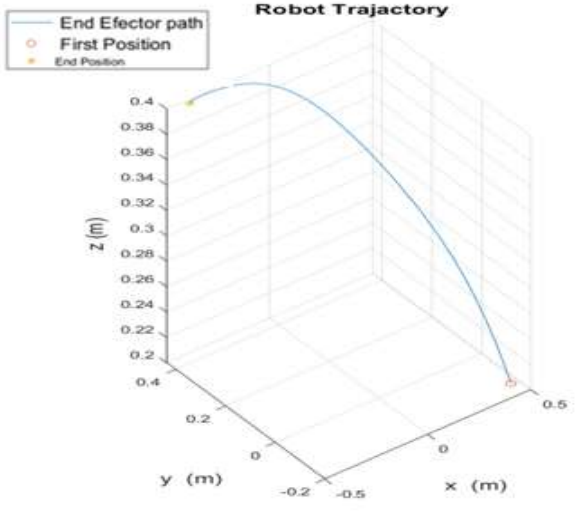

Fig. 6 The trajectory of end- effector in 3-D world for tracking the object.

Figure 7 illustrates the feature trajectory of the stereo image based visual servoing system with an RLS estimator for tracking and grasping a moving object in linear trajectory.

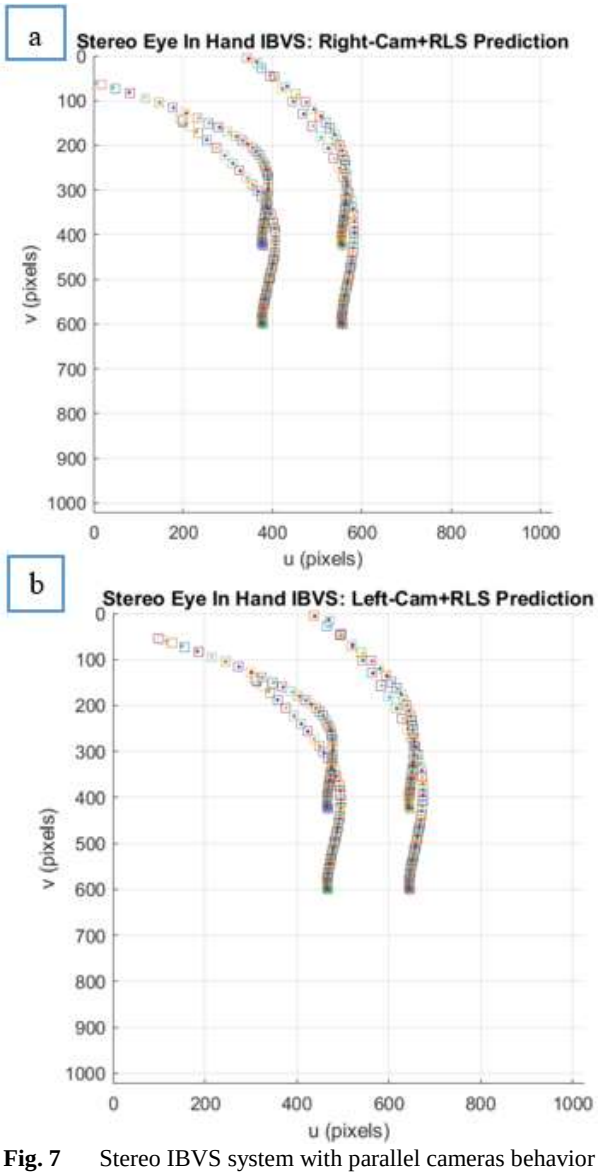

Fig. 7 Stereo IBVS system with parallel cameras behavior in a procedure of grasping a moving object using RLS method: (a): Image feature trajectories in right images, and (b): Image feature trajectories in left images.

From the simulation results shown in "Fig. 8 a and b", for a tracking and grasping task, the pixel error due to the measurement noise could be considerably reduced in both image plane by using Recursive Least Square (RLS) algorithms based on the moving object model.

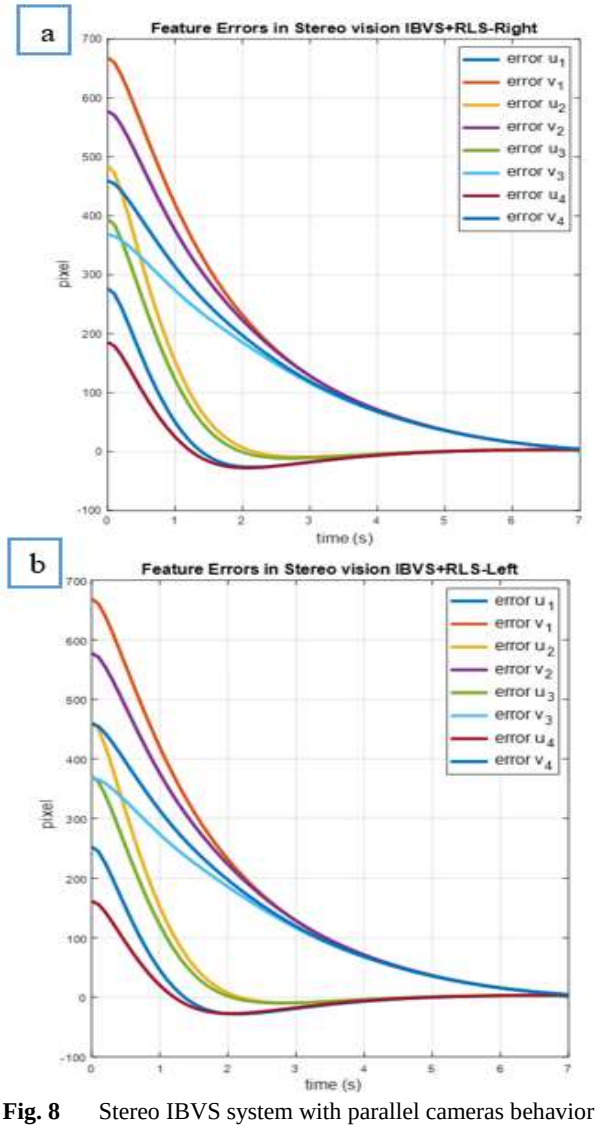

Fig. 8 Stereo IBVS system with parallel cameras behavior in a procedure of grasping a moving object using RLS method: (a): Image feature errors for right cameras, and (b): Image feature errors for left cameras.

The camera velocity components in the system with RLS prediction compared to the system without prediction, started with relatively low speeds. From the simulations shown in "Fig. 9", it is quite considerable that in comparison with the monocular system, the trajectories of the points in both images plane are smoother in the case of using the RLS estimator and the camera velocity components do not include large oscillations which lead to fewer energy consumptions.

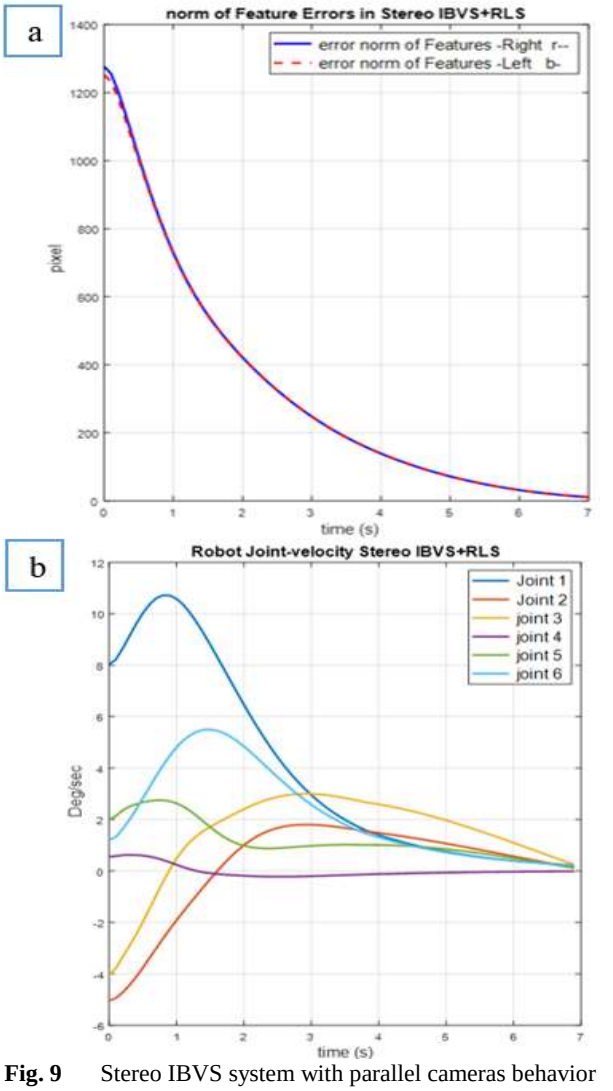

Fig. 9 Stereo IBVS system with parallel cameras behavior in a procedure of grasping a moving object using RLS method: (a): Norm of features errors in stereo IBVS, and (b): Camera frame velocity components.

In MATLAB software, the vision control system based on a single camera and stereo was simulated and the moving object was predicted by using the Recursive least squares. As mentioned in the previous sections, the image interaction matrix was divided into two parts, rotational and translational, according to the movement of the camera and the object. The rotational part is independent of the distance from the object to the camera, but to calculate the translation part, the distance from the object to the camera is required. The distance from the object to the camera is estimated at any given time by the epipolar plane. Separating the rotation and translation sections helped to reduce computations and speed up the system's time response. The simulation results are shown in "Table 1".

Table 1 Comparison results for all the IBVS cases for tracking and grasping of a moving object

Vision system	Convergence time(s)	Maximum tracking error (pixel)	Maximum joint velocity (deg /sec)
Mono-IBVS	12.4	650	8.1
Stereo-IBVS	7.8	780	9.2
Mono-IBVS+ RLS	8.1	700	8.7
Stereo-IBVS+RLS	6.9	680	10.6

"Table 1" show that the convergence time is reduced using the stereo image based visual servoing and tracking and grasping task, the pixel error due to the measurement noise could be considerably reduced in both image plane by using Recursive Least Square (RLS) algorithms based on the moving object model.

6 CONCLUSIONS

This article presents a novel eye- in- hand image-based stereo visual servoing system for a real-time task of tracking and grasping a moving object in an uncalibrated environment. An image-based visual servoing (IBVS) approach based on stereo vision has been presented and mathematically discussed and compared to the case of Monocular IBVS. The monocular and stereo visual servoing system are simulated on 6 Dof PILZ robot. From the results, it can be inferred that in the single-camera based vision system, the system is slow in convergence and the overshoot is too high. Conversely, in the stereo control system, stereo-based convergence is faster and less response is observed than in single-camera mode. This is because in stereo vision, the Jacobean image matrices can be updated at any time using the calculated depth information. Therefore, it is possible to create the correct feedback command that leads to the stability of the vision-based control system. For increasing response speed, the image interaction matrix was divided into two separate parts related to translational and rotational motion, and it was found that only the translational motion part is affected by distance. The control method separates the camera motion to three stages based on pure rotation, pure translation, and hybrid motion, which has a better time response compared to the classical IBVS control methods.

It can be also inferred from the results that the case with the RLS estimator shows better tracking and convergence performance and has better behavior in end-effector 3-D trajectories.

REFERENCES

[1] Hashimoto, K., A review on vision-based control of robot manipulators, Adv. Robot. Int. J. Robot. Soc. Japan, Vol. 17, No. 10, 2003, pp. 969–991.

[2] Corke, P., Robotics, Vision and Control: Fundamental Algorithms In MATLAB®Second, Completely Revised, Vol. 118, 2017.

[3] Chaumette, F., Hutchinson, S., Visual Servo Control, I. Basic Approaches, IEEE Robot. Autom. Mag., Vol. 13, No. 4, 2006, pp. 82–90.

[4] Chaumette, F., Hutchinson, S., Visual Servo Control, II. Advanced Approaches [Tutorial], IEEE Robot. Autom. Mag., Vol. 14, No. 1, 2007, pp. 109–118.

[5] Keshmiri, M., Xie, W. F., and Mohebbi, A., Augmented Image-Based Visual Servoing of A Manipulator Using Acceleration Command, IEEE Trans. Ind. Electron., Vol. 61, No. 10, 2014, pp. 5444–5452.

[6] Chaumette, F., Potential Problems of Stability and Convergence in Image-Based and Position-Based Visual Servoing, In The Confluence of Vision and Control, Springer, 1998, pp. 66–78.

[7] Xie, W. F., Li, Z., Tu, X. W., and Perron, C., Switching Control of Image-Based Visual Servoing With Laser Pointer in Robotic Manufacturing Systems, IEEE Trans. Ind. Electron., Vol. 56, No. 2, 2008, pp. 520–529.

[8] Shu, T., Gharaaty, S., Xie, W., Joubair, A., and Bonev, I. A., Dynamic Path Tracking of Industrial Robots with High Accuracy Using Photogrammetry Sensor, IEEE/ASME Trans. Mechatronics, Vol. 23, No. 3, 2018, pp. 1159–1170.

[9] Shen, Y., Xiang, G., Liu, Y. H., and Li, K., Uncalibrated Visual Servoing of Planar Robots, In Proceedings 2002 IEEE International Conference on Robotics and Automation (Cat. No. 02CH37292), Vol. 1, 2002, pp. 580–585.

[10] Ghasemi, A., Li, P., and Xie, W. F., Adaptive Switch Image-Based Visual Servoing for Industrial Robots, Int. J. Control. Autom. Syst., Vol. 18, No. 5, 2020, pp. 1324–1334.

[11] Ghasemi A., Xie, W. F., Decoupled Image-Based Visual Servoing for Robotic Manufacturing Systems Using Gain Scheduled Switch Control, In 2017 International Conference on Advanced Mechatronic Systems (ICAMechS), 2017, pp. 94–99.

[12] Liang, X., Wang, H., Liu, Y. H., Chen, W., and Zhao, J., A Unified Design Method for Adaptive Visual Tracking Control of Robots with Eye-In-Hand/Fixed Camera Configuration, Automatica, Vol. 59, 2015, pp. 97–105.

[13] Wang, H., Adaptive Visual Tracking for Robotic Systems Without Image-Space Velocity Measurement, Automatica, Vol. 55, 2015, pp. 294–301.

[14] Dong G., Zhu, Z. H., Kinematics-Based Incremental Visual Servo for Robotic Capture of Non-Cooperative Target, Rob. Auton. Syst., Vol. 112, 2019, pp. 221–228.

[15] Keshmiri M., Xie, W. F., Image-Based Visual Servoing Using an Optimized Trajectory Planning Technique, IEEE/ASME Trans. Mechatronics, Vol. 22, No. 1, 2016, pp. 359–370.

[16] Zheng, D., Wang, H., Chen, W., and Wang, Y., Planning and Tracking in Image Space for Image-

Based Visual Servoing of A Quadrotor, IEEE Trans. Ind. Electron., Vol. 65, No. 4, 2017, pp. 3376–3385.

[17] Zhao, Y., Xie, W. F., and Liu, S., Image-Based Visual Servoing Using Improved Image Moments in 6-DOF Robot Systems, Int. J. Control. Autom. Syst., Vol. 11, No. 3, 2013, pp. 586–596.

[18] Payeur, P., Le-Huy, H., and Gosselin, C. M., Trajectory Prediction for Moving Objects Using Artificial Neural Networks, IEEE Trans. Ind. Electron., Vol. 42, No. 2, pp. 147–158, 1995.

[19] Hashimoto, H., Kubota, T., Sato, M., and Harashima, F., Visual Control of Robotic Manipulator Based on Neural Networks, IEEE Trans. Ind. Electron., Vol. 39, No. 6, pp. 490–496, 1992.

[20] Martinet, P., Cervera, E., Stacking Jacobians Properly in Stereo Visual Servoing, In Proceedings 2001 ICRA. IEEE International Conference on Robotics and Automation (Cat. No. 01CH37164), Vol. 1, 2001, pp. 717–722.

[21] Kim, D. J., Lovelett, R., and Behal, A., Eye-in-Hand Stereo Visual Servoing of an Assistive Robot Arm in Unstructured Environments, In 2009 IEEE International Conference on Robotics and Automation, 2009, pp. 2326–2331.

Int. J. Advanced Design and Manufacturing Technology, 2023, Vol. 16, No. 1, pp. 57-64

DOI: 10.30486/admt.2023.1963260.1368 ISSN: 2252-0406 https://admt.isfahan.iau.ir

Design Construction and Evaluation of a Ring-like Karbandi Structure

Ahad Shah Hosseini[1,] *, Sajjad Pakzad[2]
Faculty of Design, Tabriz Islamic Art University, Iran
E-mail: ahad.shahhoseini@tabriziau.ac.ir, s.pakzad@tabriziau.ac.ir
*Corresponding author

Mohammad Mahdi Ranjbar Malek Shahi[3]
Faculty of Design, Tabriz Islamic Art University, Iran
E-mail: mm.ranjbar@tabriziau.ac.ir

Received: 16 July 2022, Revised: 18 October 2022, Accepted: 23 October 2022

Abstract: Due to the gold price increases in the Iranian market, the desired buyers have been attracted to LGJ (Lightweight Gold Jewelry). Meanwhile, because of the strength decreases in structure in LGJ., we investigated a structural solution in this research. The proposed solution was Karbandi as a supporting lattice-ordered structure in Iranian architecture. We used five types of primary Iranian architecture arches and a perfectly logical Karbandi plan to create ring-like structures. Arches and ring-like structures were compared based on maximum mises stress, strain, and weight using FEM analyses. The applied load and approximate area of it in analyses, according to the female mean Tip-pinch and the mean of minimum, thumb, and index finger width were chosen. Based on analyses results, a ring-like Karbandi structure was chosen for construction. The models were constructed in four alloys category based on sterling silver standard with Cu-nanoparticles as an admixture. A practical test was done to investigate the mean deformation time for each alloy's model category. A weight was used to investigate the observable deformation time-based capacity of the models. Results showed that the lowest mises max stress value was observed in the 1st arch, although the 3rd arch had the minimum strain among arches. In ring-like Karbandi structures made from 1st and 3rd arches, the minimum value of mises max stress and strain was related to the Karbandi. In the physical load applying process, the category that did not contain cu-nanoparticles had the highest deformation meantime among all categories.

Keywords: FEM Analyses, Iranian Architecture, Karbandi, Ring, Structure

Biographical notes: Ahad Shahhoseini received his Ph.D. in Architecture from Sapienza University of Rome, Rome, Italy, in 2012. He is currently an assistant professor in the Faculty of Design at Tabriz Islamic Art University, Tabriz, Iran. His research interests include Industrial Design, Eco-Design, and Design studies. **Sajjad Pakzad** received his Ph.D. in Mechanical Engineering from University of Tabriz, Tabriz, Iran, in 2018. He is currently an assistant professor in the Faculty of Design at Tabriz Islamic Art University, Tabriz, Iran. His research interests include Industrial Design, Parallel Mechanisms, and Robotics. **Mohammad Mehdi Ranjbar Malek Shahi** received his B.Sc. in Industrial Design from Tabriz Islamic Art University in 2020. He is currently an MSc student in industrial Design at the Faculty of Design at Tabriz Islamic Art University, Tabriz, Iran. His research interests include Design studies, mechanical structures, mechanical mechanisms and FEM analyses spatially in gold ornaments and Jewelry.

Research paper

1 INTRODUCTION

The price of gold in the Iranian market has increased significantly in recent years [1]. Hence, the desire of buyers and subsequent, production has been attracted to "lightweight gold jewelry" (LGJ.). Making LGJ. due to the metal and mechanical properties of gold alloy used in the Iranian market [2], structurally has reduced the strength of jewelry. One of the characteristics of buyers of LGJ., in particular a ring, is its relative observable mechanical strength against the normal pressure that is applied to both sides of the ring with two fingers. The result of this process is influential on buying willingness. Using lattice structures, it is possible to have lightweight and high strength together [3]. In many design applications, lattice structures are used for their excellent properties including the light-weighting, high specific strength, stiffness [4] and their positive effects on the total deformation capacity [5]. Therefore, in this study, we investigated the effects of a supporting lattice-ordered structure of Iranian architecture in LGJ. mechanical behavior. The selected structure was Karbandi. Karbandi is one of the supporting structures in Iranian architecture [6]. Each Karbandi structure is composed of arches [7]. Five types of arches were introduced in Jamshid Kashani's book "Mafatih al-Hesab" and considered as Karbandi basis in Iranian architecture [8]. These five arches were simulated in "Rhinoceros 7" software according to details and drawing methods presented in the partial translation of Mafatih al-Hesab [9]. The simulation results were compared using the Finite Element Method (FEM) analyses in Abaqus software. The criteria were maximum mises stress, strain, and weight at the same load, thickness, and material mechanical properties. The load applied to the samples was taken from a study that measured females' tip-pinch in Tabriz [10].

According to the results of the pre-stage (minimum of strain and mises stress), in this paper we selected two arches and used them to design a Karbandi structure with the most similarity to a women's gold ring. Then, due to a certain limit of the criteria and construction limitations of the ring, we chose one model for construction. Alloys in jewelry industry usually are made by using bulk metals as an admixture [11]. The overall positive strengthening effect of metal nanoparticles on alloys has been investigated [12]. Thus, for investigating the effects of nanoparticles on the deformation capacity of metals used in the jewelry industry we used silver (as base metal) Cu, and Cu-nanoparticles (as admixture) to make models in four different alloy types. Finally, we compared these four models' deformation capacity by a practical load applying procedure.

2 AN IRANIAN ARCHITECTURE SUPPORTING STRUCTURE

2.1. Arches

Arches are one of the first steps of development in architectural structures [13]. Ghiyath al-Din Jamshid Kashani (1380-1429) wrote a manuscript known as "Miftah al-hisab" (Key of Arithmetic) and introduced five main types of arches in Islamic architecture and methods of drawing them [8]. We use these arches types and methods of drawing in this study ("Fig. 1").

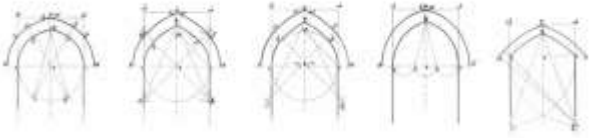

Fig. 1 Types of arches in the Persian translation of "Miftah al-hisab" [9].

2.2. Karbandi Structure

Karbandi is one of the identity elements of Iranian architecture that integrates architecture and structure and it is based on two criteria, a plan of n-sided Karbandi and an arch [7]. Plan of each n-sided Karbandi based on a circle that is divided into "n" equal parts. From a selected point of division, a connection distance is equal to "d" (which connects one point to another desired point), arches are placed on this distance, and circular arrayed "n" times. The shape with the sides of "a" and "b" are used to delete unwanted pieces according to the type of Karbandi ("Fig. 2").

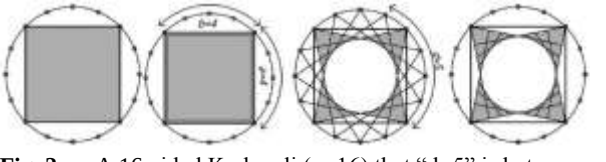

Fig. 2 A 16-sided Karbandi (n=16) that "d=5" is between "a=4" and "n/2=8" [7].

If "d" is between "a" and "n/2" then, the Karbandi is perfectly logical and geometrically correct [7]. We use this type of Karbandi to create a ring-like structure.

3 2D AND 3D MODELING

3.1. Arches Modelling

Two-dimensional Modeling of arches was done in generic overall dimensions in "Rhinoceros 7" according to "Miftah al-hisab" instructions ("Fig. 3").

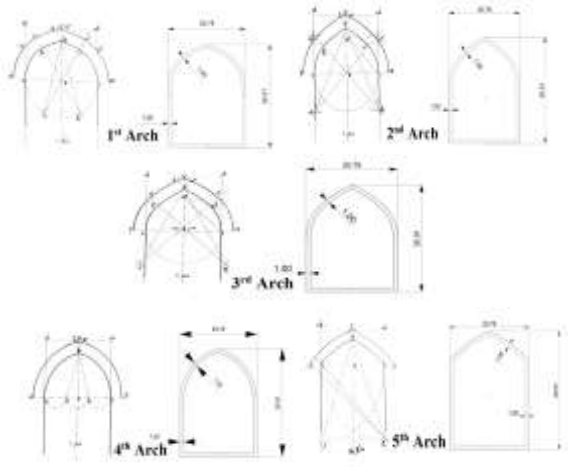

Fig. 3 Arches (left column) [9] and 2D modeling of them (right column) with "Rhinoceros 7".

3.2. Ring-Like Karbandi Structures

Using the geometrical perfect type of Karbandi [7], arches mentioned in the previous section, and "Rhinoceros 7" as 3D modeling software, the ring-like Karbandi structures were modeled. The plan of Krabandi is a 16-sided (n=16) and parameters "a" and "b" are set to 4 (a=b=4). The Karbandi circle diameter is 26.56 mm according to the ring size 59 (by European standard). All possible "d" quantities (d = 2, 3, 4, 5, 6, and 7) are considered due to the "a<d<n/2" relation. Finally, the deletion method and bottom connection of each structure were considered based on a ring-like shape creation ("Fig. 4" and "Fig. 5").

Fig. 4 Ring-like Karbandi structure created with specifications of a=b=4, d=6 and using the first arch in "Fig. 3".

Fig. 5 Ring-like Karbandi structures base on the first arch with all "d" possible quantities (d=2, 3, 4, 5, 6 and 7, left to right accordingly).

4 FINITE ELEMENT ANALYSES

4.1. Software and Analyses Specifications

We used "Abaqus DS Simulia Suite 2022" for all analyses in this study. All 2D and 3D models were converted to IGES. format for importing to Abaqus. The category of section applied to all models and their types were Shell and Homogenous, respectively. The Shell thickness is set to 0.3 mm based on a common gold ring shell thickness. All analyses were static in the category of mechanical. The meshing technique is set to free and "Tri" type, and mesh types were standard linear shells. The requested output fields were "Maximum Mises equivalent stress", "E, Max" (strain), and also weight calculated in the software environment.

4.1.1. Applied Load (Amount, Location, and, Direction)

Duo to the Tip-pinch which has the most similarities to fingers position in ring-wearing posture, we used the results of a cross-sectional study that took place in Tabriz which was conducted among 196 (96 males and 100 females) volunteers. The applied load and approximate area of it, according to the female mean Tip-pinch (4.7 Kgf[1] = 46.09 N) and the mean of minimum, thumb, and index finger width were chosen [10]. The mean amount of thumb and index finger width (1.3 cm) was used as the applying load area. ("Fig. 6").

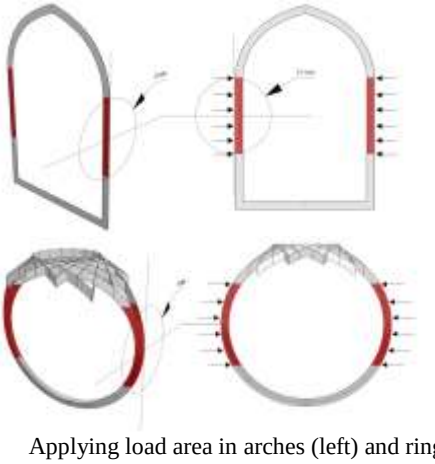

Fig. 6 Applying load area in arches (left) and ring-like Karbandi structure (right).

Exhaustive researches have been done on the behavior of arches under vertical loads [14-17] but less attention has been devoted to their horizontal endurance [18]. In this study due to fingers condition in ring-wearing posture (thumb and index finger), we considered the load direction horizontally symmetrical to structures at the applying load areas ("Fig. 6").

4.1.2. Material Properties

The most common precious metals in the fine jewelry industry are gold, platinum, palladium, and silver [19]. We used gold mechanical properties data ("Table 1") from the CATIA material library in all FEM analyses [20].

Table 1 Gold mechanical properties

Material	Gold
Density (kg/m^3)	19320
Young's modulus (N/m^2)	7.8e+10
Poisson's ratio	0.42
Yield stress (N/m^2)	2.05e+8

5 CONSTRUCTION PROCESS

5.1. Alloy Specifications and Categories

A decrease in structure weight can be the cause of a decrease in its strength [21], one solution to overcome this, is using alloys with more stiffness (less deformation capacity). Due to reduced production costs in this study, we used sterling silver alloy to construct ring-like structures. Sterling silver is an alloy of silver and copper, known as silver 925 which contains 92.5% silver and 7.5% copper by weight [22]. Copper is a metal that exists in both gold and silver alloys as an admixture [22], hence, its degree of mixture variation can be generalizable for gold alloys' capacity of deformation too.

The positive effects of metal nanoparticles on the mechanical behavior of alloys have been investigated [12-24]. Thus, in this study, we used some variations of copper and its nanoparticles to investigate their effect on the deformation capacity of ring-like Karbandi structures.

The melting point of metal nanoparticles is lower than the bulk metal and has a direct relationship with their size of it [25]. Thus, with increases in metal nanoparticle size, the melting point temperature is increased. Due to the preservation of metal nanoparticle properties because of the close melting point temperature of silver and copper (Ag, 961.78 °C and Cu, 1.085 °C), we used the largest Cu-nanoparticles size (100 nm) available on the market ("US NANO" brand) and to ensure purity, Cu-microparticles ("Armina" brand) in constructing categories of sterling silver alloys ("Table 2").

Table 2 Categories of sterling silver alloys (based on 20 g weight of each category).

Categories	Silver	Cu-Nanoparticles	Cu-Microparticles
First	18.5 G	-	1.5 G
Second	18.5 G	1.5 G	-
Third	18.5 G	1 G	0.5 G
Fourth	18.5 G	0.5 G	1 G

5.2. 3D Printing

We used the "Form Labs 2" 3D printer for printing the models. The resin brand was similar to the 3D printer (purple castable wax). Totally 24 models were printed (6 models for each alloy category). The thickness of the layers was 50 µm, the total number of them was 530 and, 32 mL resin was used for the 3D printing process.

5.3. Casting Process Specifications

We used a vacuum casting machine and oxy-acetylene torch for melting silver and copper (nanoparticles and microparticles) in the casting process. The casting plaster brand was Optima (green model-resin specific) and 1 kg plaster was used for each casting process (a total of 4 casting process was done). A 10 centimetres height flask was used for casting. Baking time and casting temperatures were 7 h and 720 °C, respectively, and casting was done under 600 psi vacuum pressure ("Fig. 7").

Fig. 7 Several views of a casting model (first alloy's category).

6 PRACTICAL LOAD APPLICATION

To investigate the observable deformation of constructed models (in 4 alloys categories), we used a dial thickness gauge (0-20 mm range - 0.1 mm graduation), standard 50 g, and 2000 g (about 40% of Tip-pinch [10]) calibration weights and a mini table clamp. The 50 g calibration weight was used to measure the models' diameter in the initial state, then the 2000 g weight was used to investigate the observable deformation capacity of the models. All models of each alloy's category were used to calculate the mean (time-based) deformation capacity ("Fig. 8").

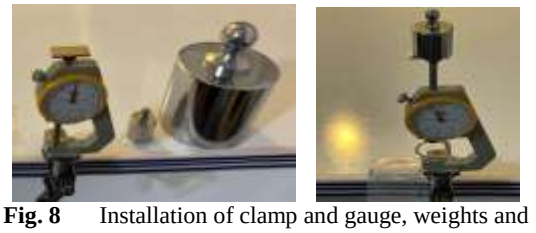

Fig. 8 Installation of clamp and gauge, weights and models (we used a neodymium magnet (1.3g) for more fixity of weights during measurement).

7 RESULTS

7.1. Software Analyses

7.1.1. Arches

The results of finite element method analyses for maximum Mises stress, maximum strain, and weight

calculation of each arch were shown ("Fig. 9" and "Table 3").

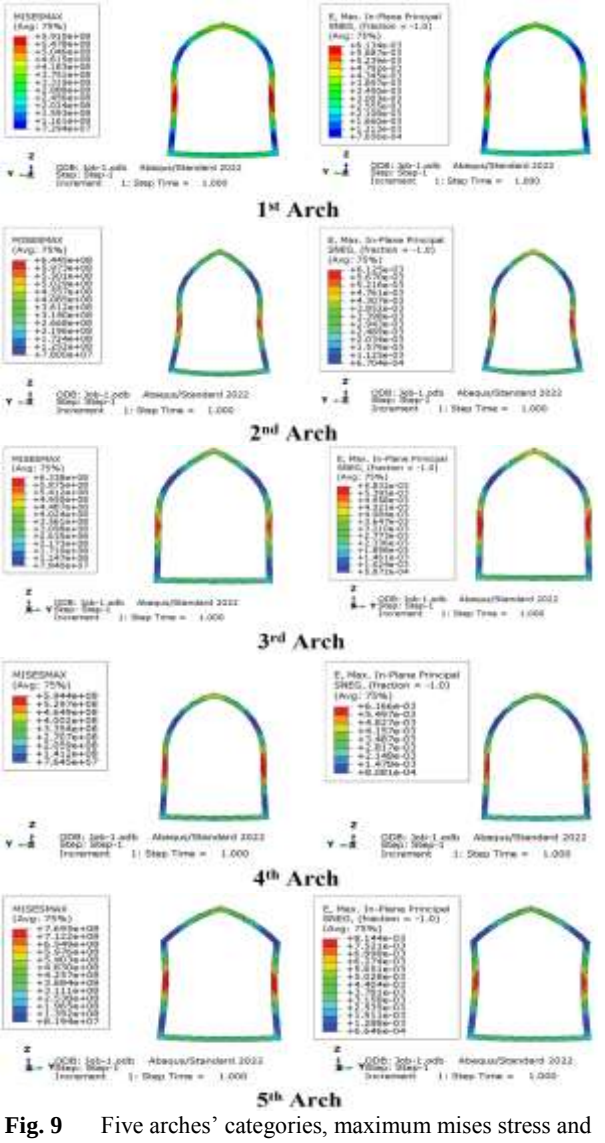

Fig. 9 Five arches' categories, maximum mises stress and maximum strain.

Table 3 Arches' mises max, strain, and weight

Arches	Mises Max (N/m^2)	Strain	Mass (Kg)
1	5.910e+8	6.134e-3	5.54e-4
2	6.445e+8	6.125e-3	5.43e-4
3	6.338e+8	5.832e-3	5.42e-4
4	5.944e+8	6.166e-3	5.49e-4
5	7.695e+8	8.144e-3	5.57e-4

Two aches with the minimum of mises max stress (1st arch) and a minimum of strain (3rd arch) were used to create ring-like Karbandi structure variations.

7.1.2. Ring Like Karbandi Structures

The results of finite element method analyses for maximum von mises stress, maximum strain, and weight calculation of each ring-like Karbandi structure with all "d" possible quantities (d=2, 3, 4, 5, 6, and 7) were shown ("Fig. 10", "Fig. 11", "Fig. 12", "Fig. 13" and "Table 4").

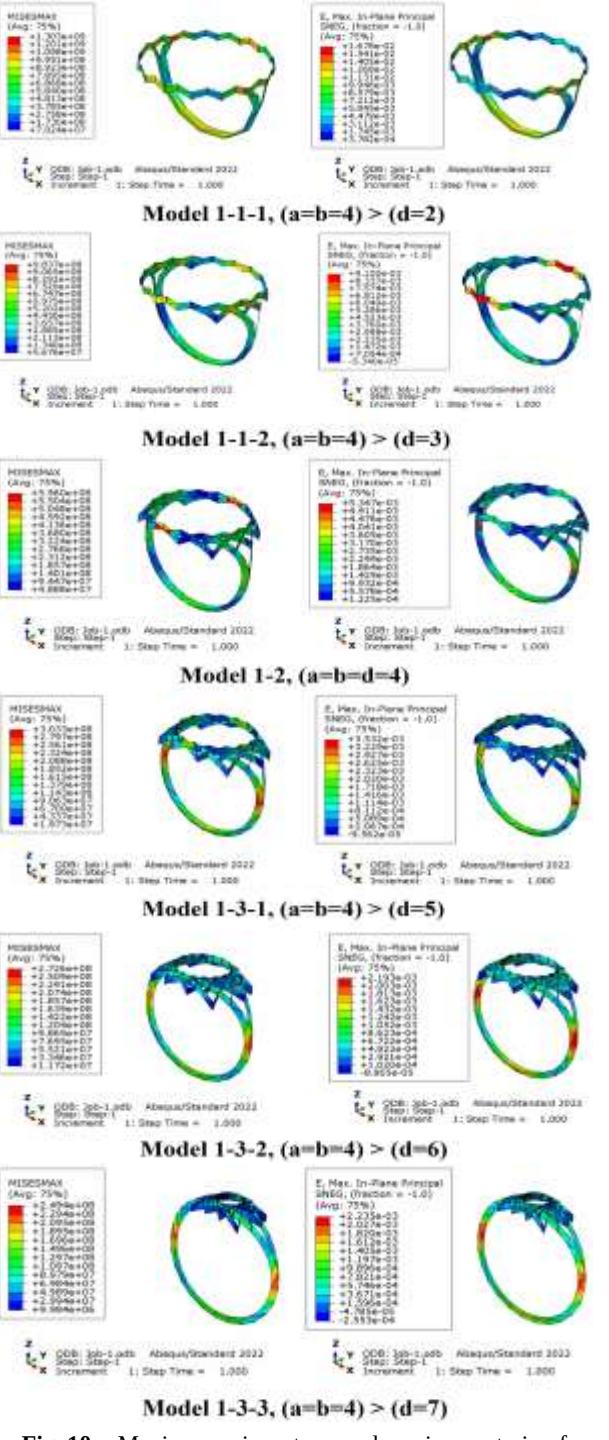

Fig. 10 Maximum mises stress and maximum strain of ring-like Karbandi structures with all "d" possible quantities (d=2, 3, 4, 5, 6 and 7) using the 1st arch.

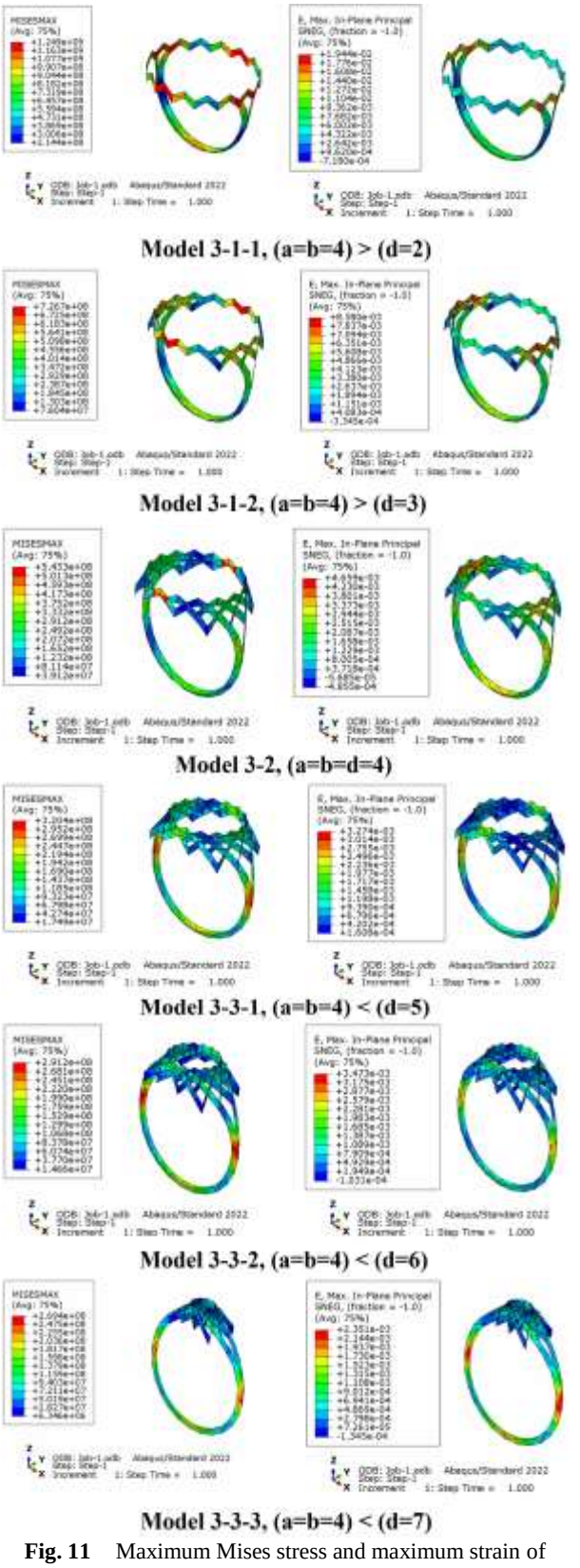

Fig. 11 Maximum Mises stress and maximum strain of ring-like Karbandi structures with all "d" possible quantities (d=2, 3, 4, 5, 6 and 7) using the 3rd arch.

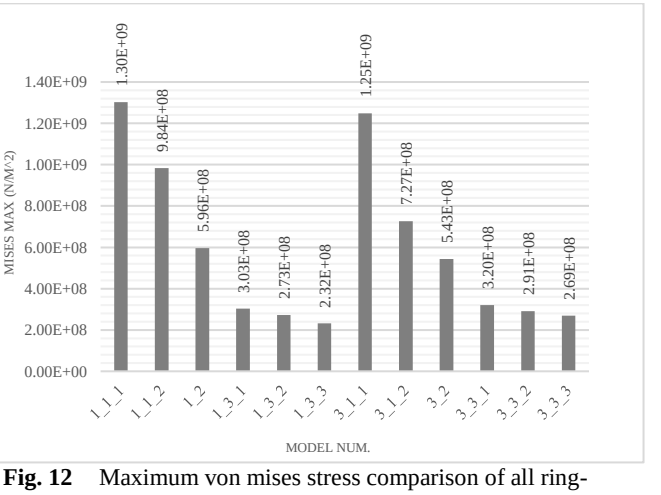

Fig. 12 Maximum von mises stress comparison of all ring-like Karbandi structures.

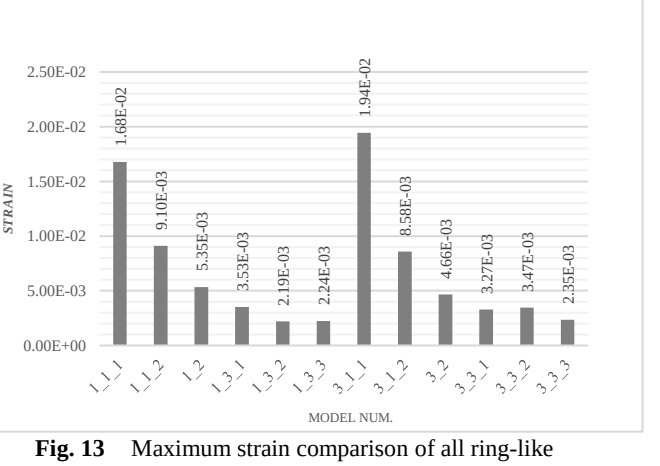

Fig. 13 Maximum strain comparison of all ring-like Karbandi structures**.**

Table 4 Ring-like Karbandi structures von mises maximum stress, strain, and weight

Model Num.	Mises Max (N/m^2)	Strain	Weight (kg)
1_1_1	1.30E+09	1.68E-02	9.24E-04
1_1_2	9.84E+08	9.10E-03	1.13E-03
1_2	5.96E+08	5.35E-03	1.42E-03
1_3_1	3.03E+08	3.53E-03	1.65E-03
1_3_2	2.73E+08	2.19E-03	1.71E-03
1_3_3	2.32E+08	2.24E-03	1.52E-03
3_1_1	1.25E+09	1.94E-02	9.93E-04
3_1_2	7.27E+08	8.58E-03	1.20E-03
3_2	5.43E+08	4.66E-03	1.52E-03
3_3_1	3.20E+08	3.27E-03	1.76E-03
3_3_2	2.91E+08	3.47E-03	1.82E-03
3_3_3	2.69E+08	2.35E-03	1.62E-03

7.2. Practical Experiments

The results of all model's diameters on 50 g and their mean deformation time on 2000 g weights are shown ("Fig. 14" and "Table. 5").

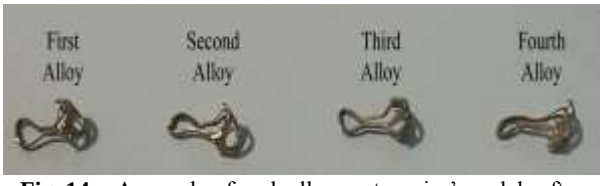

Fig. 14 A sample of each alloys categories' models after deformation.

Table 5 Admixtures weight (base metal, MP (microparticles), and NP (nanoparticles)), the diameter of models on 50 g and 2000 g weights, and deformation mean time of each 6 models of each category

Alloys category	Admixtures' weights	D on 50 g	D on 2000 g	Meantime (S)
First	18.8g Ag + 1.5g Cu(MP)	19.3mm	Pressed	3.97
Second	18.8g Ag + 1.5g Cu(NP)	19.4mm	Pressed	1.96
Third	18.8g Ag + 1g Cu(NP) + 0.5g Cu(MP)	19.3mm	Pressed	2.23
Fourth	18.8g Ag + 1g Cu(MP) + 0.5g Cu(NP)	19.5mm	Pressed	2.77

8 CONCLUSIONS

Using structures as a combination of members connected in such a way to support more loads can be a solution to increase solidity in LGJ. In this research, we tried to introduce a structure for this problem. The proposed structure was Karbandi. Arches and Karbandi-plan as the most important factors in this structure were investigated. The results showed that in the first arch, the lowest mises max stress value was observed due to the application of the same load, and the arch's weight was fourth among the five weights. Although the third arch had the minimum strain and the lowest weight among arches. In model 1-3-3 from ring-like Karbandi structures, the lowest mises max stress value was observed and it had the fifth place in terms of the most weight. In model 1-3-2, the lowest strain value was observed and it had the sixth place in terms of the most weight in its category (ring-like Karbandi structures based on the first arch). The minimum value of mises max stress and also strain was related to the Karbandi plan with the "(a=b) < d" relation. This condition was observable in structures that were made from the first and third arches.

In the physical load applying process, because of clamp surface decrease of load applying area to approximately 1/12 of the area considered in the FEM analyses, the physical stress increased 12 times and an inevitable complete deformation occurred. The first category that did not contain cu-nanoparticles had the highest deformation meantime among all categories. The lowest deformation meantime was related to the second category that contains the most Cu-nanoparticles as an alloy's admixture. Also, in the third and fourth alloy categories, it is observable that the more presence of Cu-nanoparticles led to increase in deformation meantime. One cause of this phenomenon can be the airflow in the oxy-acetylene flame. Because of the very low weight of nanoparticles, this flow can pour out Cu-nanoparticles out of the melting pot before the melting process. On the other hand, the flammability of Cu- nanoparticles can be the reason for the lack of influence or the absence of Cu-nanoparticles' mechanical properties in the alloy categories.

APPENDIX

[1]. Kgf (Kilogram-Force) is a non-SI dimension of force that is generally used in medical research and is equal to the magnitude of the force exerted on one kilogram of mass in a 9.80665 m/s^2 gravitational field [26].

ACKNOWLEDGMENTS

We acknowledge the Islamic Art University of Tabriz, the Design department, and Skyseas gold gallery, for supporting this work.

REFERENCES

[1] Dastranj, E., Sahebi Fard, H., Abdolbaghi, A., and Reza Hejazi, S., Power Option Pricing Under the Unstable Conditions (Evidence of Power Option Pricing Under Fractional Heston Model in The Iran Gold Market), Physica A: Statistical Mechanics and its Applications, Vol. 537, 2020, pp. 122690, https://doi.org/10.1016/j.physa.2019.122690.

[2] Saradesh, K., Vinodkumar, G., Metallurgical Processes for Hardening of 22karat Gold for Light Weight and High Strength Jewelry Manufacturing, Journal of Materials Research and Technology, Vol. 9, No. 2, 2020, pp. 2009-2020, https://doi.org/10.1016/j.jmrt.2019.12.033.

[3] Pan C, Han Y, Lu J., Design and Optimization of Lattice Structures: A Review, Applied Sciences, Vol. 10, No. 18, 2020, pp. 63-74, https://doi.org/10.3390/app10186374.

[4] Dong, G., Yunlong, T., and Yaoyao F. Zh., A Survey of Modeling of Lattice Structures Fabricated by Additive Manufacturing, Journal of Mechanical Design, Vol. 139, No. 10, 2017, 100906.

[5] Großmann, A., Gosmann, J., and Mittelstedt, C., Lightweight Lattice Structures in Selective Laser Melting: Design, Fabrication and Mechanical

Properties, Materials Science and Engineering: A, Vol. 766, 2019, pp. 138356, https://doi.org/10.1016/j.msea.2019.138356.

[6] Pour Ahmadi, M., Sohrabi, M., Design of Persian Karbandi: The Problem of Dividing the Base from a Mathematical Viewpoint, Jria.iust.ac.ir. Vol. 7, 2019, pp. 21-36, Online access, http://jria.iust.ac.ir/article-1-1171-en.html.

[7] Amjad Mohamadi, A., Nejad Ebrahimi, A., and Shahbazi, Y., Geometric Design of a Masonry Lattice Space Dome Titled Karbandi in Persian Architecture, International Journal of Space Structures, Vol. 34, No. 2, 2019, pp. 22-39, https://doi.org/10.1177/0956059919845631.

[8] Koliji, H. Revisiting the Squinch: From Squaring the Circle to Circling the Square, Nexus Netw Journal, Vol. 14, 2012, pp. 291–305, https://doi.org/10.1007/s00004-012-0113-9.

[9] Jazbi, A., Risaaleh Taaq va Ajaz, Soroush Publications, Tehran, Iran, 1987, pp. 27 (Partial Translation of Miftah al-hisab).

[10] Maleki-Gahfarokhi, A., Dianat, I., Feizi, H., and Asghari-Jafarabadi, M., Influences of Gender, Hand Dominance, and Anthropometric Characteristics on Different Types of Pinch Strength: A Partial Least Squares (PLS) Approach, Applied Ergonomics, Vol. 79, 2019, pp. 9-16, https://doi.org/10.1016/j.apergo.2019.04.002.

[11] Klotz, U. E., Tiberto, D., and Held, F., Optimization of 18-Karat Yellow Gold Alloys for The Additive Manufacturing of Jewelry and Watch Parts, Gold Bull, No. 50, 2017, pp. 111–121 https://doi.org/10.1007/s13404-017-0201-4.

[12] Pang, X., Xian, Y., Wang, W., and Zhang, P., Tensile Properties and Strengthening Effects of 6061Al/12 wt%B4C Composites Reinforced with Nano-Al2O3 Particles, Journal of Alloys and Compounds, Vol. 768, 2018, pp. 476-484, https://doi.org/10.1016/j.jallcom.2018.07.072.

[13] Buzurgmehri, Z., Hindisa dar Mimari (Geometry in Persian Architecture), Iranian Cultural Heritage Organization, Tehran, Iran, 1992, pp. 154 (In Farsi).

[14] Marano, G. C., Trentadue, F., and Petrone, F., Optimal Arch Shape Solution Under Static Vertical Loads, Acta Mech, Vol. 225, 2014, pp. 679–686, https://doi.org/10.1007/s00707-013-0985-0.

[15] Guo, Y., Chen, H., Pi, Y., and Bradford, M., In-Plane Strength of Steel Arches with a Sinusoidal Corrugated Web Under a Full-Span Uniform Vertical Load: Experimental and Numerical Investigations, Eng Struct, Vol. 110, 2016, pp.105-115, https://doi.org/10.1016/j.engstruct.2015.11.056.

[16] Marano, G., Trentadue, F., Greco, R., Vanzi, I., and Briseghella, B., Volume/Thrust Optimal Shape Criteria for Arches Under Static Vertical Loads, Journal of Traffic and Transportation Engineering (English Edition), Vol. 5, 2018, pp. 503-509, https://doi.org/10.1016/j.jtte.2018.10.005.

[17] Zampieri, P., Tetougueni, C., Maiorana, E., and Pellegrino, C., Post-Buckling of Network Arch Bridges Subjected to Vertical Loads, Structure and Infrastructure Engineering, Vol. 17, 2020, pp. 941-959, https://doi.org/10.1080/15732479.2020.1778742.

[18] Brandonisio, G., Mele, E., and De Luca, A., Limit Analysis of Masonry Circular Buttressed Arches Under Horizontal Loads, Meccanica, Vol. 52, 2017, pp. 2547-2565, https://doi.org/10.1007/s11012-016-0609-6.

[19] Sensoy, A., Dynamic Relationship Between Precious Metals, Resources Policy, Vol. 38, 2013, pp. 504-511, https://doi.org/10.1016/j.resourpol.2013.08.004.

[20] CATIA, Material Library (Mechanical properties), Dassault Systemes, Package 3, Ver. 5-6, Service Pack 1, 2021.

[21] Addisu, H., Koricho, E., Structural Weight and Stiffness Optimization of a Midibus Using the Reinforcement and Response Surface Optimization (RSO) Method in Static Condition, Modelling and Simulation in Engineering, Vol. 2022, 2022, pp. 1-15, https://doi.org/10.1155/2022/6812744.

[22] Grimwade, M., Introduction to Precious Metals; Metallurgy for Jewelers and Silversmiths, Brynmorgen press, USA, First Edition, 2009, pp. 91-102.

[23] Aarts, W., Jarvis, R., The Change in Resistivity, On Plastic Deformation, Of Silver-Copper and Silver-Gold Alloys, Acta Metallurgica, Vol. 2, No. 1, 1954, pp. 87-91, https://doi.org/10.1016/0001-6160(54)90098-x.

[24] Gain, A., Zhang, L., The Effects of TiO2 Nanoparticles Addition on The Thermal Shock Resistance, Shear Strength and IMC Layer Growth of SAC305 Alloy, Materialia (Oxf), Vol. 3, 2018, pp. 64-73, https://doi.org/10.1016/j.mtla.2018.10.009

[25] Aliofkhazraei, M., Handbook of Nanoparticles, Springer Cham, 2020, pp. 664-665, https://doi.org/10.1007/978-3-319-13188-7.

[26] Cholewickl, J., Wolf, S., Unit of Measurement: Newton (N) Versus Kilogram Force (kgf), Journal of Hand Surgery, Vol. 23, No. 5, 1998, pp. 952, https://doi.org/10.1016/s0363-5023(98)80181-0.

Int. J. Advanced Design and Manufacturing Technology, 2023, Vol. 16, No. 1, pp. 65-74

DOI: 10.30486/admt.2022.1942847.1328 ISSN: 2252-0406 https://admt.isfahan.iau.ir

The Effect of Sintering and Compaction Conditions on the Microstructure and Properties of AZ31 Magnesium Alloy

Amin Saghafi[1,] *, Seyed Ehsan Eftekhari Shahri[2], Hossein Jamshidi[3], Mohammad Kazem Salari[4]

Department of Mechanical Engineering,
Birjand University of Technology, Birjand, Iran
E-mail: a.saghafi@ birjandut.ac.ir, e.eftekhari@birjandut.ac.ir, ai.hjamshidi@gmail.com, mk.salari@gmail.com
*Corresponding author

Razieh Khoshhal[5]

Department of Materials and Metallurgical Engineering,
Birjand University of Technology, Birjand, Iran
E-mail: rkhoshhal@birjandut.ac.ir

Received: 16 December 2021, Revised: 17 April 2022, Accepted: 23 April 2022

Abstract: Magnesium and its alloys are attractive materials in industrial applications due to the low density and high strength. The properties of AZ31 magnesium alloy can be much improved by choosing proper sintering conditions. In this study, the microstructure and mechanical properties of AZ31 prepared by mechanical alloying, compaction, and sintering of elemental powder, were studied. The effect of parameters such as compaction pressure, heating rate, and sintering time were investigated to determine the optimal sintering condition of AZ31 magnesium alloys. Previous researches have focused on the specific conditions of sintering, while in this study, various factors of sintering were examined simultaneously. The results showed that sintering time is one of the major variables that have a considerable effect on the final properties of AZ31. In short sintering times, recrystallization leads to small grain formation inside the powder. However, as the sintering time increases, the growth of new grains slows down and no trace of them can be detected in the microstructure. Furthermore, the conditions for recrystallization were also determined, which can be used to provide small grain size and, consequently, better properties after the initial powder milling and sintering. At optimal sintering conditions, the average grain size, porosity percentage and hardness of the samples AZ31 magnesium alloy was obtained as 104 μm and 2.05%, and 79.5 HV, respectively which is expectable result in comparison to the bulk AZ31.

Keywords: AZ31 Magnesium Alloy, Microstructure, Powder Metallurgy, Sintering

Biographical notes: Amin Saghafi is Associate Professor at the Department of Mechanical Engineering, Birjand University of Technology, Birjand, Iran. He received his PhD in Mechanical Engineering from Ferdowsi University of Mashhad, Mashhad, Iran in 2015. **Seyed Ehsan Eftekhari Shahri** received his PhD in Mechanical Engineering/Manufacturing branch from University of Birjand, Birjand, Iran in 2013. He is Assistant Professor at the Department of Mechanical Engineering, Birjand University of Technology, Birjand, Iran. **Hossein Jamshidi** is MSc student of Mechanical engineering/ Manufacturing branch at the Birjand University of Technology, Birjand, Iran. He received his BSc. in Mechanical engineering from Islamic Azad University, Eqlid Branch, Eqlid, Iran in 2014. **Mohammad Kazem Salari** is MSc student of Mechanical engineering/Manufacturing branch at the Birjand University of Technology, Birjand, Iran. He received his BSc. in Mechanical engineering from Islamic Azad University/ Mashhad Branch, Mashhad, Iran in 2006. **Razieh Khoshhal** received her PhD in Metallurgy and Materials Engineering from Iran University of Science and Technology, Tehran, Iran in 2014. She is Assistant Professor at the Department of Materials and Metallurgical Engineering, Birjand University of Technology, Birjand, Iran.

Research paper

1 INTRODUCTION

Magnesium and its alloys are widely used in various applications such as automotive, electronics, aerospace, and medicine because of its lightweight, low density, high strength and biocompatibility properties [1-2]. However, these alloys have some limitations such as low elastic modulus, and poor corrosion resistance [3-5].

The improvement of the mechanical properties of AZ31 magnesium alloys is important. Previous researchers have pursued this goal under various conditions. Reinforcing particles in metal-based composites and powder metallurgy (PM) techniques are commonly used to increase mechanical properties [6-10]. Powder metallurgy refers to the method in which a solid formed product can be achieved through 3 basic steps powder mixing, compression, and sintering. Magnesium and its alloys are often produced by casting. Applying the powder metallurgy on Magnesium requires special preparations. A high tendency to react with oxygen leads to surface oxidation and makes the sintering process difficult. Argon and nitrogen are usually used to solve this problem [11-12]. The microstructure and mechanical properties of alloys formed by powder metallurgy can be affected by the porosity and the contact surface of the particles [13-14]. It also can be improved by choosing the proper sintering conditions. The researchers showed that the properties of materials after sintering depend on various factors such as temperature, time, particle size, and compacting pressure [15-16]. Ram Kim et al. [17] investigated the microstructural evolution and mechanical properties of 6% Al Mg alloy in the spark plasma sintering (SPS) process by degassing before sintering. Due to the type of grafting at the grain boundaries and the improvement of mechanical properties, optimal temperature and compaction pressure were reported as 530°C and 130 MPa, respectively. Mondet et al. [18] performed spark plasma sintering on AZ91 magnesium alloy to improve the compressive strength of the AZ91. The influence of the sintering temperature was investigated. The optimum microstructure was obtained for a sintering temperature of 380ºC. Burke et al. [19] investigated the effect of pressing pressure, and temperature of sintering on AZ31 magnesium alloy produced by traditional sintering. They found that the sintering temperature and time have the greatest effect on the properties of the sample. The maximum tensile strength was observed at 20 min and 500°C. The SPS process to prepare compact samples from gas-atomized and attritor-milled AE42 magnesium powder was studied by Minarik et al. [20]. After the short attritor-milling, the powder was sintered in the range of 400-550°C for 3 minutes. It was found that a short milling time applied on magnesium alloy powder before SPS can be effectively used to improve the mechanical properties. In magnesium-based metal composites, the addition of reinforcing particles improves tensile strength. Similarly, Jayakumar et al. [21] prepared AZ31 alloy composite reinforced with multiwall carbon nanotubes (MWCNTs) by mechanical alloying and powder metallurgy technique. The results showed that an addition of 1 wt% carbon nanotubes leads to an improvement in 0.2% yield strength without any losing ductility. Galindes et al. [22] examined three alloys of magnesium AZ31, AZ61, AZ91 produced by high energy milling and hot sintering. It was found that as milling speed and time increased, the particles were fractured to the size of 10 μm, and the improvement of hardness was also achieved.

The main objective of this research was to improve the properties of AZ31 magnesium alloy by choosing proper sintering conditions. Based on the above literature, the previous researches have focused on specific conditions of sintering, while in this study, various factors of sintering were examined simultaneously. The effect of sintering parameters on the microstructure and mechanical properties of the AZ31 magnesium alloys were evaluated in terms of grain size, porosity, and hardness. Then, the optimal sintering conditions (sintering time, heating rate, and compaction pressure) were determined to achieve improved mechanical properties.

2 EXPERIMENTAL PROCEDURE

Powder metallurgy and mechanical alloying have been used to fabrication of AZ31 magnesium alloy. Elemental powders of Mg, Al, Zn and Mn were selected based on AZ31 stoichiometry (“Table 1”).

Table 1 Specifications of powders used for powder metallurgy of AZ31 magnesium alloy

Materials	Mg	Al	Zn	Mn
Purity (%)	>99.9	>99.8	>99.8	>99.8
Particle size (μm)	100	40	10	10
Wt%	Base	3	1	0.35

The mechanical alloying was conducted on mixed powders using a high energy ball mill with RPM of 300, a ball ratio of 20:1 for 3h (in which a break time of 8 min was performed every 20 minutes). Stearic acid (3 wt%) was added to prevent excessive cold welding. Also, argon was utilized to prevent oxidation. The milled powders were compacted under the pressures of

500, 600, 700 MPa for 3 min at room temperature to obtain samples with dimensions of Ø14×21 mm. Subsequently, the samples were sintered at 520°C in a tube furnace. XRD (X-ray diffraction) analysis was used to determine the phase composition and crystallite size in the range of 5-90° by Cu Kα radiation.

In order to examine the effect of the sintering factors, the specimens were prepared for microstructure and hardness tests. Microstructure investigations were carried out using an optical microscope and scanning electron microscope (TESCAN MIRA-3 FE-SEM). The grain size and the porosity percentage of the phases were evaluated using MIP (microstructural image processing) software. The results were obtained based on 3 repetitions for each experiment to minimize the errors. Finally, the hardness of each sample was determined by using a Vickers hardness tester with a load of 1 kg and a holding time of 5 seconds. It was measured at 5 places for each sample and the average value was reported.

3 RESULTS AND DISCUSSION

3.1. Determination of the Optimal Compaction Pressure

A series of recent studies have indicated that compacting pressure plays an important role in the properties of sintered products [23]. This part of the study, therefore, set out to assess the effect of compacting pressure (500, 600, and 700 MPa) on the microstructure, porosity, and hardness of sintered AZ31. Images obtained by optical microscope and porosity percentage are shown in "Fig. 1". The grain size and Vickers hardness results of AZ31 alloy samples are shown in "Fig. 2". As shown in these figures, the sampled pressed under 600 MPa has the least porosity while it delivered the most hardness. When the compacting pressure was increased from 500 MPa to 600 MPa, the porosity percentage of the samples decreased significantly from 12.88% to 5.6%. Also, the hardness increased from 44.7 HV to 81.2 HV, and the grain size decreased from 74 µm to 71 µm. The reason could be the weak contact between the raw materials in low pressure (500 MPa), and more work hardening created at the grain boundaries which spread into the grains and causes more porosity as a result of the high pressure in hardened regions (700 MPa). Accordingly, the pressure of 600 MPa was selected as the proper compaction pressure for the subsequent experiments based on the high enough hardness and minimum porosity and grain size.

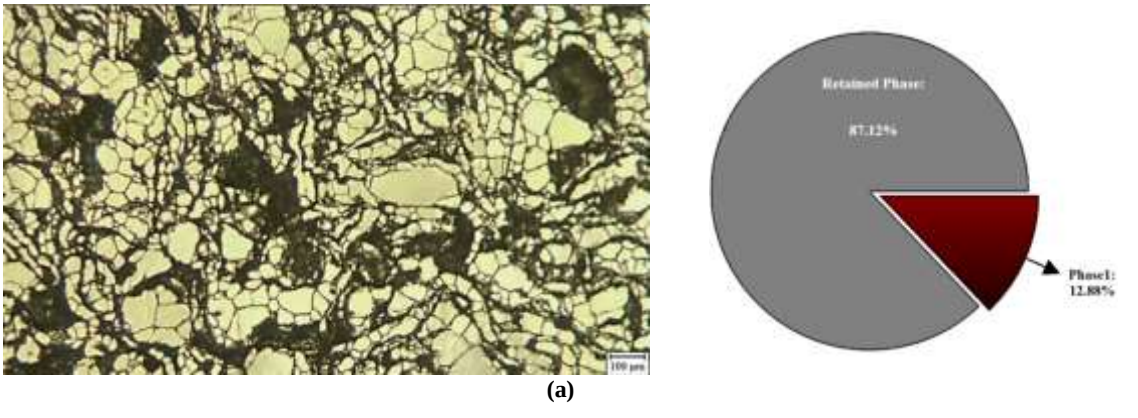

(a)

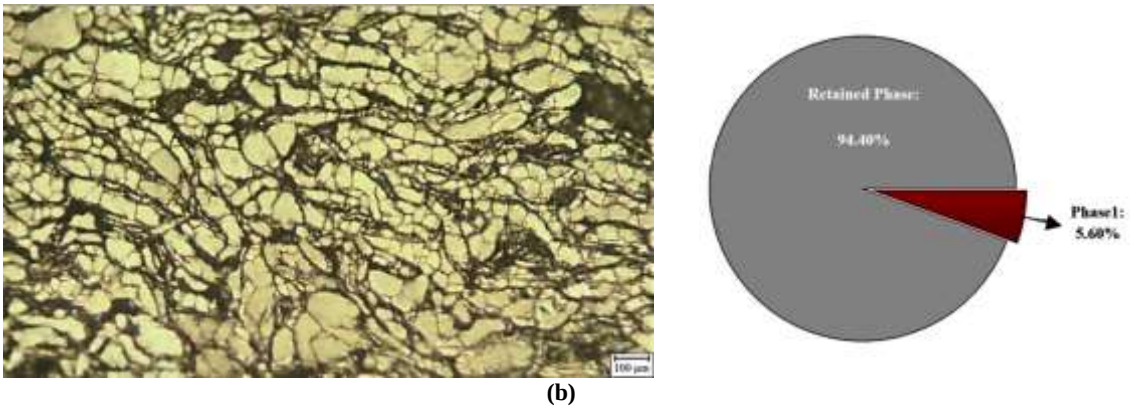

(b)

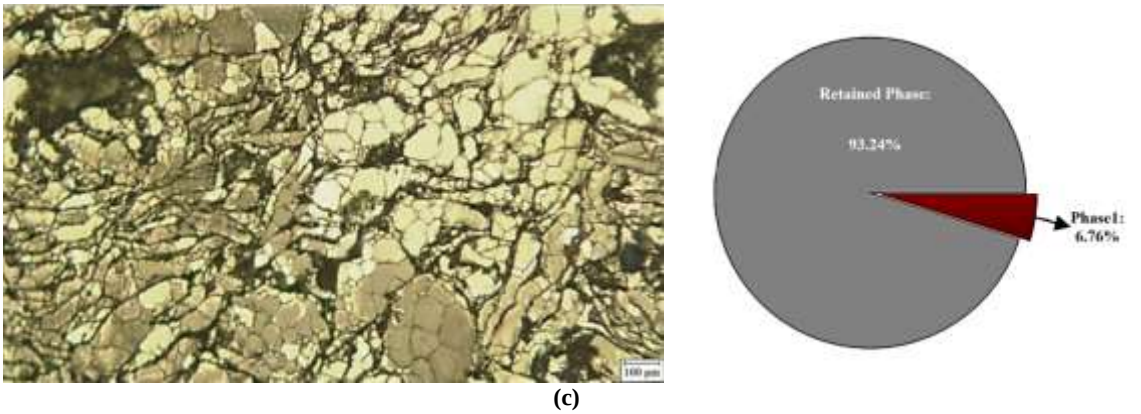

(c)

Fig. 1 The optical microscope images and the porosity percentage of samples pressed under: (a): 500, (b): 600, and (c): 700MPa and sintered at 520°C for 3h.

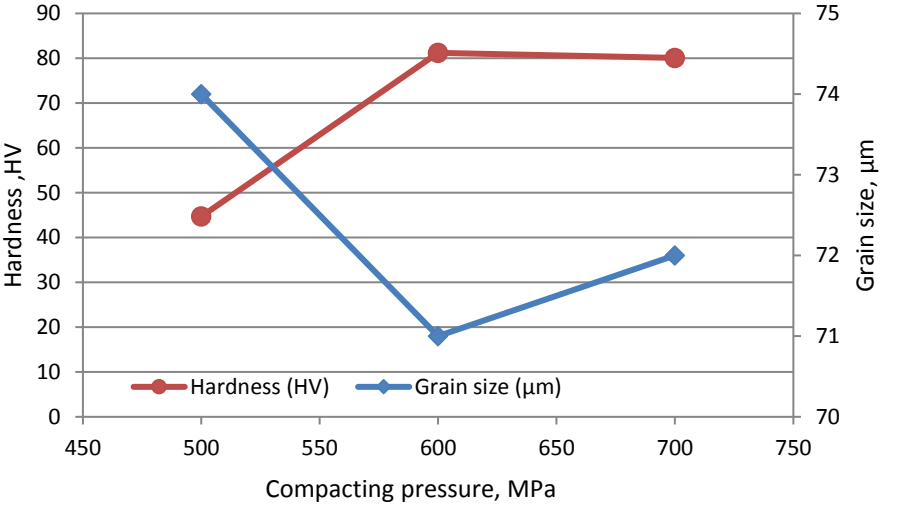

Fig. 2 The hardness and grain size of samples pressed under 500, 600, and 700MPa and sintered at 520°C for 3h.

3.2. The Effect of Sintering Cycles

It has previously been observed that 520°C is the best temperature for sintering of AZ31 [24]. The heating rate and sintering time were considered as the factors that could affect the microstructure and mechanical properties of AZ31. Figure 3 shows the microstructure of samples pressed under 600MPa and sintered with different heating rates. Figure 4 shows the grain size and hardness values of each sample. As illustrated in "Fig. 3(a) and Fig. 4", by interring the pressed sample directly at 520°C without applying a heating rate, the obtained product has low hardness and high porosity, which can be attributed to the thermal shock. To reduce the negative effects of heat shock, the samples were preheated at a specified rate.

As can be seen in "Fig. 3", in short sintering times, small grains are formed inside the powder particles. A possible explanation for this might be the recrystallization process. Since the samples have been milled, a lot of strain is stored in powders, which are released at the temperature of sintering in the form of new strain-free grains. However, as the sintering time increases, these new grains grow slowly and no trace of them can be detected in the microstructure ("Fig. 5"). Another reason that can confirm the recrystallization process in the early times of sintering is the shape of the particles which is stretched and shows the stored strain ("Fig. 3"), while with increasing the sintering time, there is no trace of these distorted particles. Comparing "Fig. 5 b and c", it can be seen that sintering time does not have any effect on the microstructure of the sample while it can reduce the hardness by releasing more strain or the grain growth ("Fig. 6"). The optimum microstructure was obtained for sintering time 16h, for which the average grain size, porosity percentage, and hardness were measured 104 µm, 2.05%, and 79.5 HV, respectively. These conditions are recommended as the proper conditions for sintering.

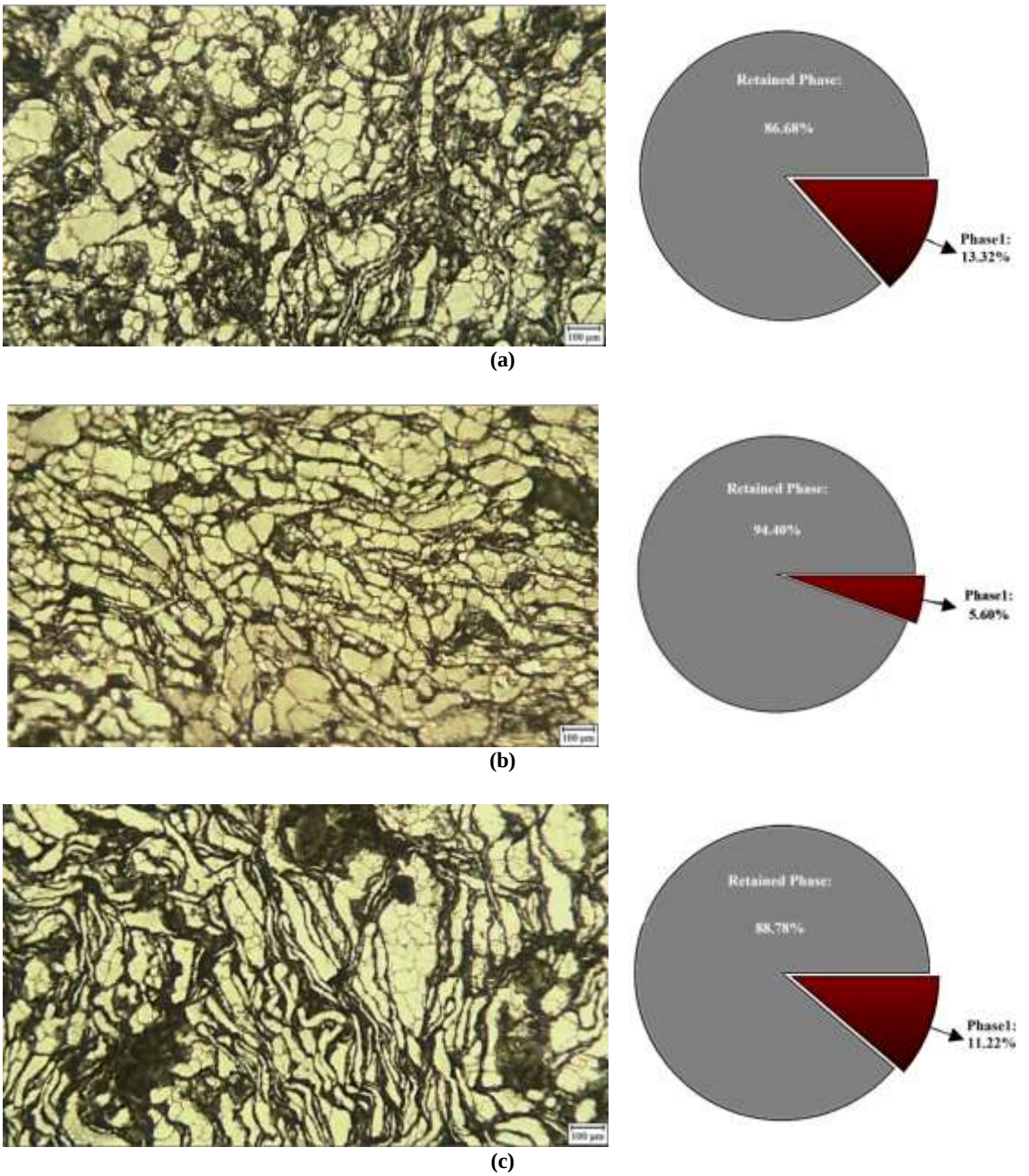

Fig. 3 Optical micrographs and the porosity percentage of AZ31 magnesium alloys for 3h sintering time with different heating rate: (a): by interring the sample directly in tube furnace, (b): 9 ^{o}C/min heating rate, and (c): 5 ^{o}C/min heating rate.

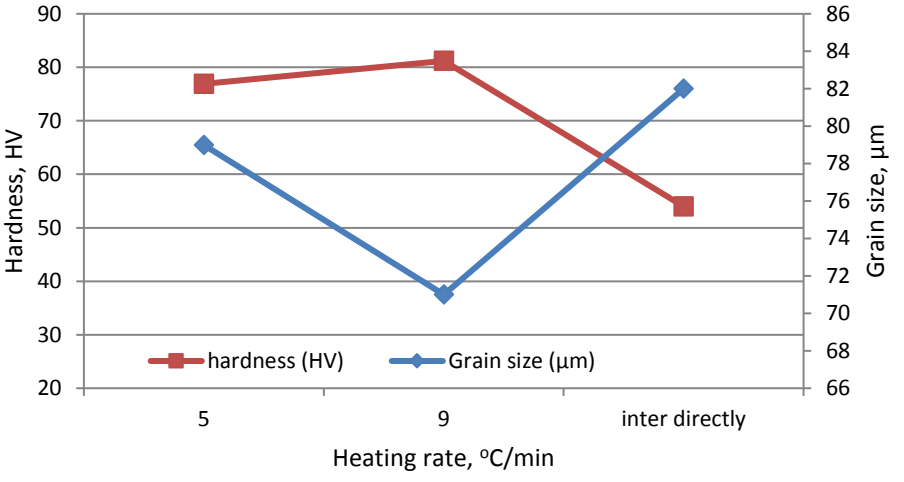

Fig. 4 The hardness and grain size of samples with different heating rate.

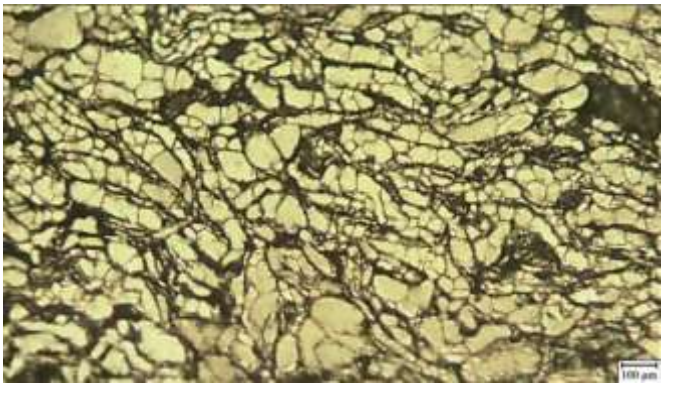

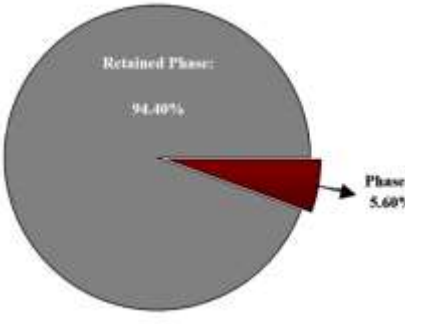

(a)

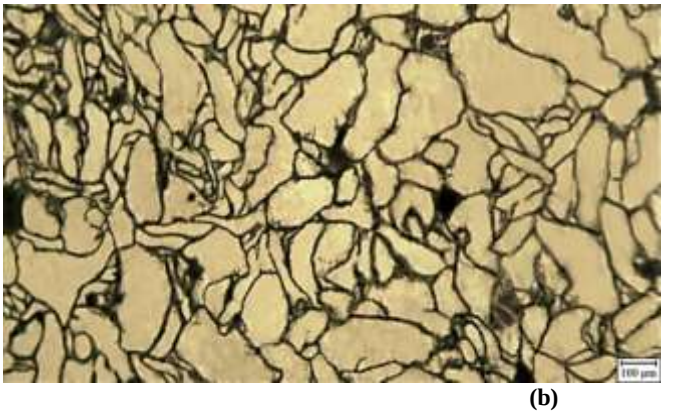

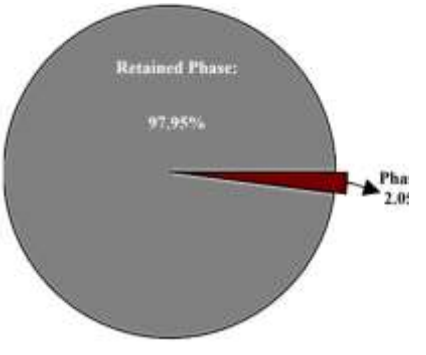

(b)

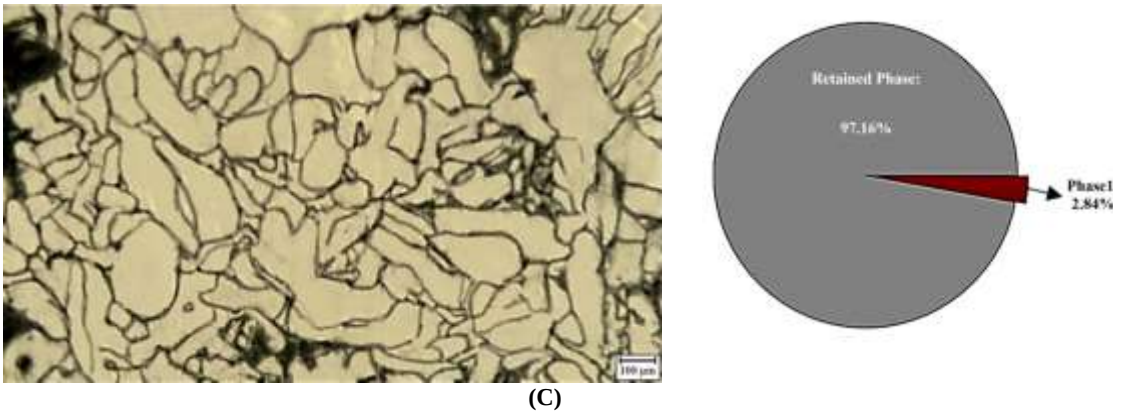

(C)

Fig. 5 Optical micrographs and the porosity percentage of AZ31 magnesium alloys sintered with 9 °C/min heating rate and different sintering time: (a): 3h, (b): 16 h, and (c): 24 h.

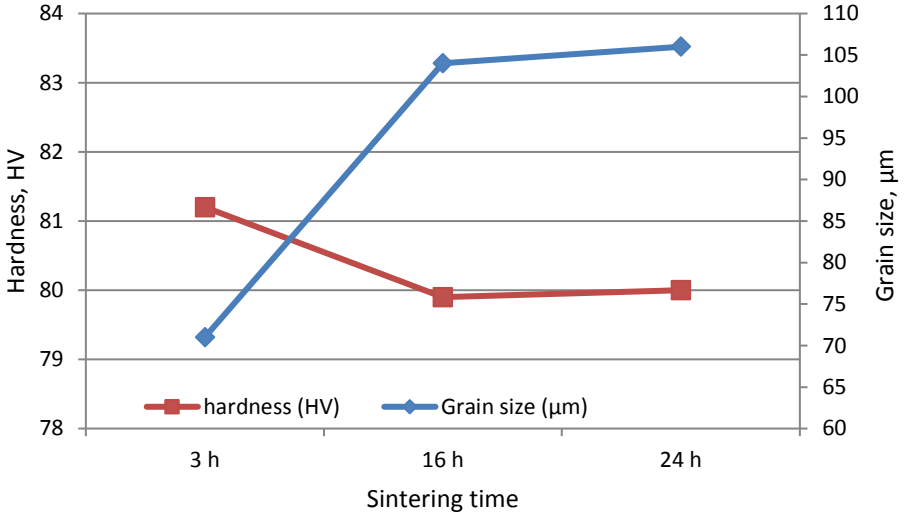

Fig. 6 The hardness and grain size of samples with different sintering time.

3.3. XRD Results

The milling process was applied for the mechanical alloying of raw materials to make them active. It was also conducted to improve the sintering procedure. To study the possible changes, the XRD results for the primary mixed sample and the milled one have been compared as illustrated in "Fig. 7". The crystallite size for both the mixed and milled powder was calculated via the Scherrer method which was equal to 1155 and 701 Å, respectively. These results confirm the association between the milling process and crystallite size. The data can be interpreted with the mechanical alloying energy which leads to lattice distortion and increase in defect quantity and lattice strain, subsequently. These two phenomena lead to the breaking of crystals and making them smaller. The Scherrer method can be described as the following Equation:

$$\tau = \frac{K\lambda}{\beta\cos\theta} \quad (1)$$

In which, τ is the crystalline mean, K is the shape factor, which is often equal to 0.9, X-ray wavelength is shown by λ; β is equal to full width at half maximum (FWHM), and θ is the Bragg angle.

After the sintering process at 520°C for 3h, the new component of Al12Mg17 has appeared in XRD pattern as is shown in "Fig. 8". This is due to the reaction of aluminium and magnesium. This pattern was utilized for the calculation of crystallite size of magnesium after sintering which was equal to 484 Å. The most striking finding is that the magnesium crystallite size decreased during the sintering process. One possible explanation for this may be that the defects in the milling stage lead to recrystallization as the temperature rises, which ultimately causes the newly formed grains to become smaller. α-Mg phase and secondary β-Al12Mg17 phase are the two main phases of AZ31 alloy.

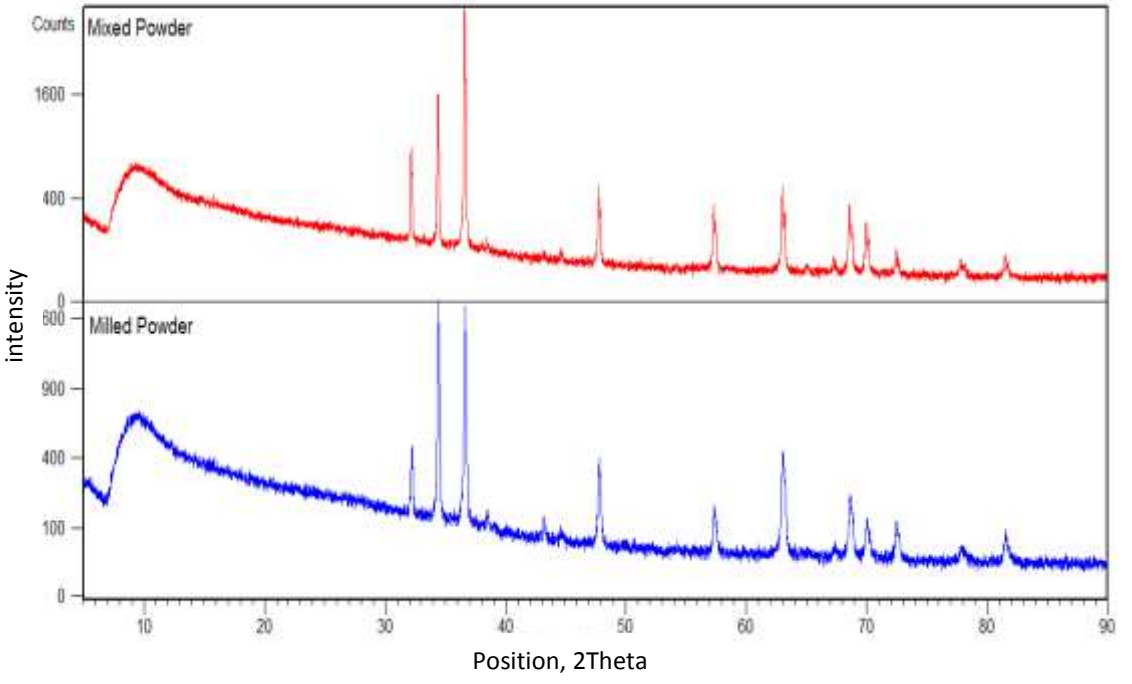

Fig. 7 The XRD results for the mixed and milled powder.

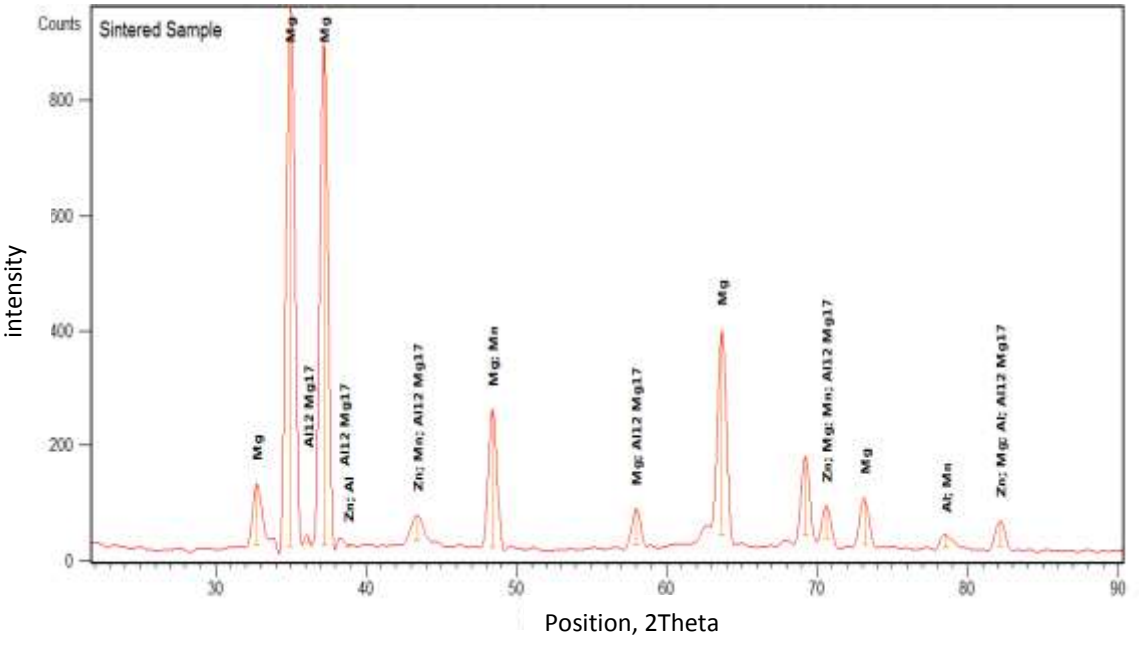

Fig. 8 The XRD results after the sintering process.

The SEM results of the sample sintered at 520°C for 3h, were shown in "Fig. 9". As can be seen, white components are detectable between the magnesium grains ("Fig. 9(a)"). EDX showed that this component is rich in Mg and Al. It means that MgAl was formed at the grain boundaries of Mg. EDX also showed that MgO presents in all grain boundaries of Mg. This is unavoidable due to the high tendency of magnesium to oxidize.

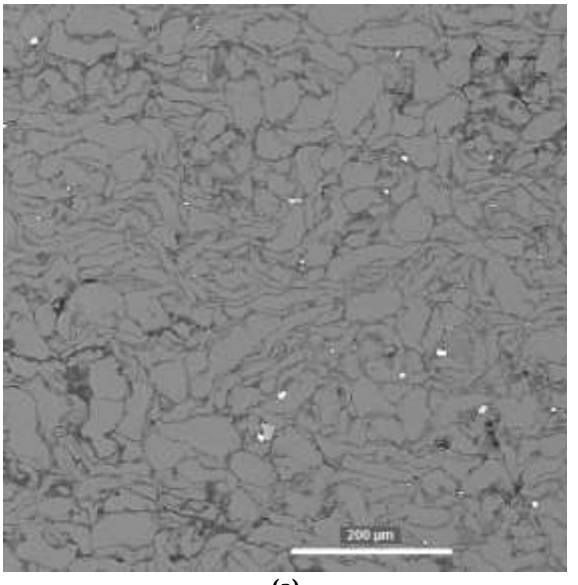

(a)

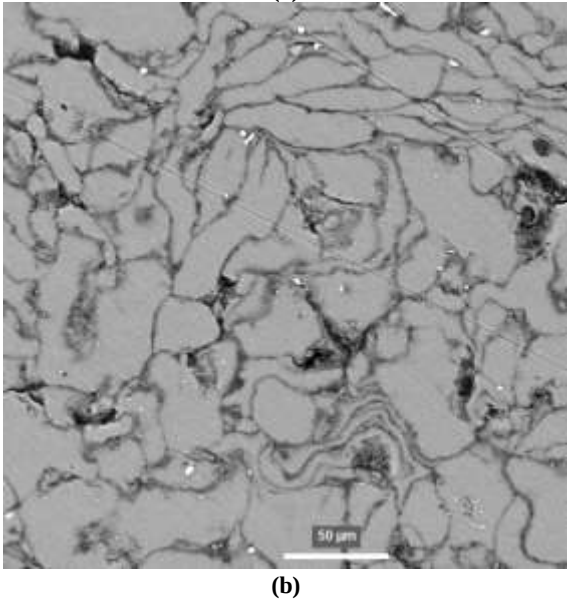

(b)

Fig. 9 The SEM image of the sintered sample at 520°C for 3h in two different magnifications.

4 CONCLUSIONS

AZ31 magnesium alloy was prepared based on its stoichiometry from elemental powders with ball milled, pressed and sintered in different conditions. The microstructure and the mechanical properties of AZ31 magnesium alloy were investigated to determine the effect of sintering parameters. The results showed that the sintering time is one of the major variables. In short sintering times, recrystallization leads to small grain formation inside the powder. However, as the sintering time increases, these new grains grow slowly and no trace of them can be detected in the microstructure. The high performance of sintered AZ31 magnesium alloy were obtained at sintering temperature of 520 °C, sintering time of 16h, and heating rate 9°C/min, for which values of grain size, porosity percentage and hardness of the samples were measured as 104 µm, 2.05%, and 79.5 HV, respectively.

CONFLICT OF INTEREST

The author(s) declared no potential conflicts of interest with respect to the research, authorship and publication of this article.

REFERENCES

[1] Pollock, T. M., Weight Loss with Magnesium Alloys, Materials Science, Vol. 328, No. 5981, 2010, pp. 986-987, DOI: 10.1126/science.1182848.

[2] Ren, L., Fan, L., Zhou, M., Guo, Y., Zhang, Y., Boehlert, C. J., and Quan, G., Magnesium Application in Railway Rolling Stocks: A New Challenge and Opportunity for Light Weighting, International Journal of Lightweight Materials and Manufacture, Vol. 1, No. 2, 2018, pp. 81-88, DOI:10.1016/j.ijlmm.2018.05.002.

[3] Polmear, I. J., Metallurgy of the Light Metals, Light Alloys, Third ed., Edward Arnold, London, 1995.

[4] Avedesian, M. M., Baker, H., ASM Specialty Handbook: Magnesium and Magnesium Alloys, ASM International, 1999.

[5] Anyanwu, I. A., Kamado, S., and Kojima, Y., Aging Characteristics and High Temperature Tensile Properties of Mg-Gd-Y-Zr Alloys, Materials Transactions, Vol. 42, No. 7, 2001, pp. 1206-1211, DOI: 10.2320/matertrans.42.1206.

[6] Watanabe, H., Mukai, T., Mabuchi, M., and Higashi, K., Superplastic Deformation Mechanism in Powder Metallurgy Magnesium Alloys and Composites, Acta Materialia, Vol. 49, No. 11, 2001, pp. 2027-2037, DOI:10.1016/S1359-6454(01)00101-X.

[7] Watanabe, H., Mukai, T., Ishikawa, K., Mohri, T., Mabuchi, M., and Higashi, K., Superplasticity of a Particle-Strengthened WE43 Magnesium Alloy, Materials Transactions, Vol. 42, No. 1, 2001, pp. 157-162, DOI:10.2320/matertrans.42.157.

[8] Watanabe, H., Mukai, T., Ishikawa, K., Mabuchi, M., and Higashi, K., Realization of High-Strain-Rate Superplasticity at Low Temperatures in a Mg–Zn–Zr alloy, Materials Science and Engineering: A, Vol. 307, No. 1-2, 2001, pp. 119-128, DOI: 10.1016/S0921-5093(00)01974-2.

[9] Nieh, T. G., Schwartz, A. J., and Wadsworth, J., Superplasticity in a 17 Vol.% Sic Particulate-Reinforced ZK60A Magnesium Composite (ZK60/SiC/17p), Materials Science and Engineering: A, Vol. 208, 1996, pp. 30–36, DOI:10.1016/0921-5093(95)10060-1.

[10] Mabuchi, M., Higashi, K., High-Strain-Rate Superplasticity in Magnesium Matrix Composites

Containing Mg2Si Particles, Philosophical Magazine A, Vol. 74, No. 4, 1996, pp. 887-905, DOI: 10.1080/01418619608242166.

[11] Agrawal, D., Microwave Sintering of Metal Powders, Advances in Powder Metallurgy: Properties, Processing and Applications, Elsevier Inc., 2013, pp. 361-379, DOI: 10.1533/9780857098900.3.361.

[12] Straffelini, G., Nogueira, A. P., Muterlle, P., and Menapace, C., Spark Plasma Sintering and Hot Compression Behaviour of AZ91 Mg Alloy, Materials Science and Technology, Vol. 27, No. 10, 2011, pp. 1582-1587, DOI:10.1179/1743284710Y.0000000007.

[13] Meng, F., Rosalie, J. M., Singh, A., and Tsuchiya, K., Precipitation Behavior of An Ultra-Fine Grained Mg–Zn Alloy Processed By High-Pressure Torsion, Materials Science and Engineering: A, Vol. 644, 2015, pp. 386-391, DOI:10.1016/j.msea.2015.07.086.

[14] Brezina, M., Minda, J., Dolezal, P., Krystynova, M., Fintova, S., Zapletal, J., and Ptacek, P., Characterization of Powder Metallurgy Processed Pure Magnesium Materials for Biomedical Applications, Metals, Vol. 7, No. 11, 2017, pp. 461, DOI: 10.3390/met7110461.

[15] Diatta, J., Antou, G., Courreges, F., Georges, M., Pradeilles, N., and Maitre, A., Effect of the Current Pulse Pattern During Heating in A Spark Plasma Sintering Device: Experimental and Numerical Modeling Approaches, Journal of Materials Processing Technology, Vol. 246, 2017, pp. 93-101, DOI: 10.1016/j.jmatprotec.2017.03.004.

[16] Mondal, A., Upadhyaya, A., and Agrawal, D., Effect of Heating Mode and Sintering Temperature on The Consolidation of 90W–7Ni–3Fe Alloys, Journal of Alloys and Compounds, Vol. 509, No. 2, 2011, pp. 301-310, DOI: 10.1016/j.jallcom.2010.09.008.

[17] Kim, K. R., Kim, H. S., Kwon, S. H., and Hwang, D. Y., The Effect of Sintering Pressure on The Microstructure and Properties of a Nanocrystalline Magnesium Alloy in Spark Plasma Sintering, Journal of the Korean Physical Society, Vol. 65, No. 10, 2014, pp. 1669-1674, DOI:10.3938/jkps.65.1669.

[18] Mondet, M., Barraud, E., Lemonnier, S., Guyon, J. Allain, N., and Grosdidier, T., Microstructure and Mechanical Properties of AZ91 Magnesium Alloy Developed by Spark Plasma Sintering, Acta Mater. Vol. 119, 2016, pp. 55–67, DOI:10.1016/ j.actamat.2016.08.006.

[19] Burke, P., Kipouros, G. J. Development of Magnesium Powder Metallurgy AZ31 Alloy Using Commercially Available Powders, High Temperature Materials and Processes, Vol. 30, No. 1-2, 2011, pp. 51-61, DOI:10.1515/htmp.2011.007.

[20] Minarik, P., Zemkova, M., Knapek, M., Sasek, S., Dittrich, J., Lukac, F., and Kral, R., Effect of Short Attritor-Milling of Magnesium Alloy Powder Prior to Spark Plasma Sintering, Materials, Vol. 13, No. 18, 2020, pp. 3973, DOI:10.3390/ma13183973.

[21] Jayakumar, J., Raghunath, B. K., and Rao, T. H., Enhancing Microstructure and Mechanical Properties of AZ31-MWCNT Nanocomposites Through Mechanical Alloying, Advances in Materials Science and Engineering, Vol. 2013, 2013, Article ID 539027, DOI: 10.1155/2013/539027.

[22] Galindez, Y., Correa, E., Zuleta, A. A., Valencia-Escobar, A., Calderon, D., Toro, L., Chacon, P., and Echeverria, F., Improved Mg–Al–Zn Magnesium Alloys Produced by High Energy Milling and Hot Sintering, Met. Mater. Int., Vol. 27, 2021, pp. 1113–1130, DOI: 10.1007/s12540-019-00490-1.

[23] Grasso, S., Biesuz, M., Zoli, L., Taveri, G., Duff, A. I., Ke, D., Jiang, A., and Reece, M. J., A Review of Cold Sintering Processes, Advances in Applied Ceramics, Vol. 119, No. 3, 2020, pp. 115-143, DOI: 10.1080/17436753.2019.1706825.

[24] Wolff, M., Ebel, T., and Dahms, M., Sintering of Magnesium, Advanced Engineering Materials, Vol. 12, No. 9, 2010, pp. 829-836, DOI: 10.1002/adem.201000038.

Int. J. Advanced Design and Manufacturing Technology, 2023, Vol. 16, No. 1, pp. 75-79

DOI: 10.30486/admt.2023.1962339.1360 ISSN: 2252-0406 https://admt.isfahan.iau.ir

Effect of Deposition Time on the Morphological Features and Structure of DLC Coatings on Aluminuim-T6 by PACVD

Seyed Mohammad Mahdi Shafiei [1, *]
Department of Mechanical Engineering,
West Tehran Branch, Islamic Azad University, Tehran, Iran
Department of Mechanical Engineering,
Roudehen Branch, Islamic Azad University, Tehran, Iran
E-mail: shafiei.mohammad@wtiau.ac.ir
*Corresponding author

Hamed Raeisifard[2]
Department of Mechanical Engineering,
West Tehran Branch, Islamic Azad University, Tehran, Iran
E-mail: raeiesifard.ha@wtiau.ac.ir

Kameleh Jafari[3]
Department of Art and Architecture,
West Tehran Branch, Islamic Azad University, Tehran, Iran
E-mail: jafarii@gmail.com

Received: 2 July 2022, Revised: 12 August 2022, Accepted: 18 August 2022

Abstract: Diamond like Carbon (DLC) was deposited on aluminum substrate using Plasma Assisted Chemical Vapor Deposition (PACVD) route. Spattering, the surface was activated before deposition for increasing adhesion. Deposition time was varied from 60 minutes to 5 hours. Deposit was characterized using with grazing incidence X-ray diffraction and atomic force microscope. The mechanical property was measured using microhardness and roughness tester. The analysis showed that the deposit consisted of columnar growth of submicron and micron meter scale. Compared to substrate material, deposit showed higher hardness and roughness. These results show that growth of DLC layer includes three stages. The first stage is primary growth of nuclei, and then these nuclei join together in second stage. In third stage, secondary growth of these nuclei happens.

Keywords: Coating, DLC, Deposition Time, PACVD, Tribology

Biographical note: Seyed Mohammad Mahdi Shafiei is Assistant Professor at Islamic Azad University. He received his PhD from Iran University of Science and Technology in 2015. His current research interest is surface engineering**. Hamed Raeisifard** is Assistant Professor at Islamic Azad University. He received his PhD from Islamic Azad University Science and Research Branch, Tehran in 2014. His current research interest is Mechanical engineering**. Kameleh Jafari** is BSc Student in Department of Art and Architecture from University of West Tehran Islamic Azad Branch, Iran. Her current research is manufacturing processes.

Research paper

1 INTRODUCTION

The PACVD technique is an appropriate method to deposit wear and corrosion resistant hard coatings which have excellent properties for several applications. In comparison to PVD methods, it offers the possibility of coating work pieces with complicated shapes homogeneously. Other advantage of PACVD method is the high adhesion. Tools deposited with hard coatings, like TiN, DLC, TiC, have already been used successfully for many industrial applications [1–3].

The PACVD process is influenced by several process parameters, like discharge voltage, current density, gas pressure and gas composition and flow rate [4–5].

Titanium nitrides have been successfully applied as coating materials due to their tribological properties, biocompatibility and affordable price. TiN is one of the most studied ceramic coatings [6–14], however other nitrides such as TiNbN and DLC may be interesting alternatives. In recent fifteen years, ternary TiBN and DLC coatings have been a subject of interest both for scientific research and for industrial application [6–20]. In comparison with the earlier developed TiN, TiB2 and TiC binary coatings, the ternary coatings often combine the individual advantages of these binary coatings and have high hardness, wear resistance, low friction coefficient and good adhesion to substrate. The ternary coatings can be conveniently deposited on a substrate through a Plasma Assisted Chemical Vapor Deposition (PACVD) process. Combining some of the advantages of Chemical Vapor Deposition (CVD) and Physical Vapor Deposition (PVD), PACVD is operated at a temperature usually below the tempering temperature of most tool aluminums. Therefore, it is particularly suitable for large and complexly shaped extrusion dies and die-casting moulds [21].

The previous research [26] was on investigation of effect of gas flow ratio on characterizes DLC coating but in the present research, the influence of deposition time on properties of PACVD DLC coating on the 6061-T6 aluminum has been investigated.

2 EXPERIMENTAL DETAILS

DLC coatings with compositional gradients were deposited on a 6061-T6 aluminum substrate using a PACVD coating system equipped with a voltage-controlled pulse generator. The PACVD DLC deposition was conducted in the same industrial set plant. The cylindrical vacuum chamber, which is 500 mm in diameter and 700 mm in height, can be heated with an auxiliary heating system, the temperature of which is controlled by a thermocouple and kept constant at 270 °C. The substrate is put directly on the charging plate, which is also used as the cathode of the system. The surrounding wall of the chamber is used as the anode of the system and the potential earth.

During coating, process parameters such as gas flow ratio, wall temperature, voltage duration of pulse-on and pulse-off time and total pressure were monitored. H2, Ar, N2 and CH4 gases were used as process gases for coating deposition. Total pressure was kept at 2 mbar and substrate temperature was controlled at 270°C to avoid exceeding the tempering temperature of the 6061-T6 aluminum. Plasma Nitriding (PN) was used as pre-treatment to decrease hardness gradient between substrate and coating and spattering surface. The processing parameters for deposition are listed in "Table 1".

Table 1 PACVD and PN variables

Variable	PACVD	PN
$CH_4/(CH_4+N_2)$	0.3	-
N_2	0.25 mL/min	0.25 mL/min
CH_4	mL/min 0.1	-
H_2	1.6 mL/min	1.6mL/min
Ar	0.6 mL/min	0.6mL/min
%33	%33	Duty cycle
8 KHz	8 KHz	Frequency
650 V	650 V	Voltage
2 mA	2 mA	Current
2 mbar	2 mbar	Pressure
270 °C	270 °C	Temperature
120 min	60 to 300 min	Time

The crystalline structure of the coatings was determined by grazing incidence X-ray diffraction (GIXRD) in the continuous scanning mode using CuKα radiation (λ = 0.154056 nm). The full-width at half-maximum (FWHM) of the Bragg peaks is used to approximate grain size based on the Scherrer formula [22]:

$$D = (0.9\lambda) \big/ (\beta.\cos\theta) \tag{1}$$

Where, D is grain size, β is the FWHM of the Bragg peak, and θ is the Bragg reflection angle. The film morphology is studied by atomic force microscopy (AFM).

3 RESULTS AND DISCUSSION

Figures 1(a) to 1(d) show morphology of DLC deposits deposited for time intervals of 60 ,120, 150 minutes and 5 hours, respectively. DLC deposit deposited for 60 min ("Fig. 1(a)") is incomplete. The nuclei of DLC deposited over substrate materials are clearly visible.

Compared to that, deposit deposited for 120 minutes and above covers the substrate almost completely. Black part in "Fig. 1(a)" was interpreted as a porosity of DLC film. The existence of the porosity means the DLC deposit is incomplete, i.e., it does not cover the surface completely. On the other hands, "Fig. 1(b)" almost does not have black part. This means that DLC deposit in "Fig. 1(b)" covers the substrate almost completely. The surface topography of DLC deposit showed the columnar structure very fine. Island growth of DLC coating is formed in columnar structure.

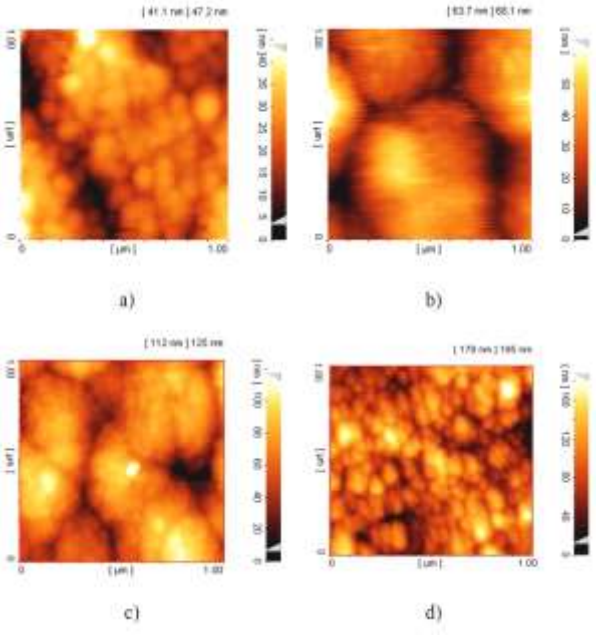

Fig. 1 Microstructures of DLC deposits deposited for times: (a): 60, (b): 120, (c): 150, and (d): 300 minutes, respectively.

Figure 2 shows nucleation size distribution measured over a large number of nuclei. We see that in all cases the nucleation size is relatively small and all deposits show a clear peak in the distribution curve. Only in 150 minutes, nucleation size distribution show two peaks. Then in 300 minutes, that shows a clear peak. These results show that growth of DLC layer includes three stages. The first stage is primary growth of nuclei, and then these nuclei join together in second stage. In third stage, secondary growth of these nuclei happens.

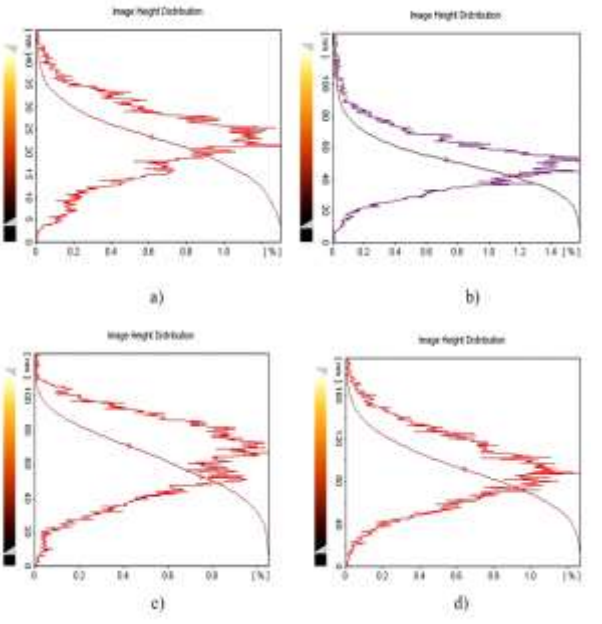

Fig. 2 Nucleation size distribution in samples deposited for various times: (a): 60 minutes, (b): 120 minutes, (c): 150 minutes, and (d): 300 minutes.

DLC deposition is a nucleation and growth phenomena which are time dependent. Nucleation is an important step in forming an adherent DLC coating. Nucleation activity itself is a probabilistic phenomenon. Hence, DLC island density and island size distribution are time dependent functions during the existence period in the CVD reactor [23]. DLC deposit deposited for 60 min shows the form of islands. This is because the nucleation events occurring on a catalyzed surface are a probabilistic process. Once nucleation events take place, the DLC grains grow into columnar structure. The number of nucleating sites increases with time, creating more columnar structure. In the next stage, the nuclei acted as the deposition sites for the deposition reaction and the coating was extended into 2D direction, centering on the columnar structure and covering full surface.

The deposits deposited for longer times (120 min and greater) also show the additional nuclei present above the base layer. This is because the substrates like aluminuim become catalytic when surface of substrate spatters. The catalytic sites on the initial deposits act as nucleating sites for additional nuclei.

The as-formed coating has the catalytic activity required for the autocatalytic reaction, and this promoted the nucleation and growth of the coating in the third direction. The formation of a new layer on the previously deposited layer could be seen in the coatings deposited for longer existence time and such morphologies are also reported [24]. It may be noted

that the mean roughness is much larger by increasing time ("Fig. 3").

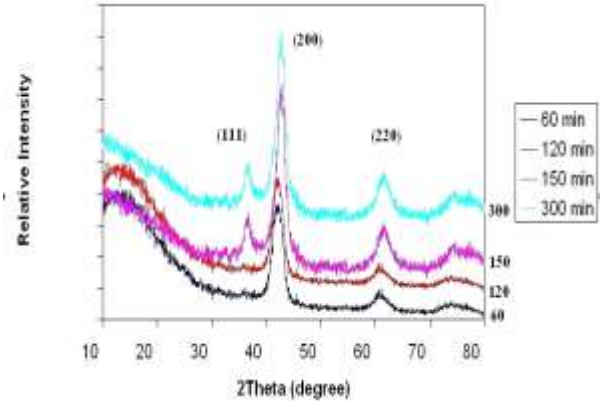

Fig. 3 Change of roughness with deposition time.

Figure 4 shows XRD plots for DLC deposits deposited for various time durations. Peaks are wide which suggest that coating is semicrystalline a mixture of amorphous and microcrystalline. He et al. [25] have reported a semicrystalline DLC coating on aluminum.

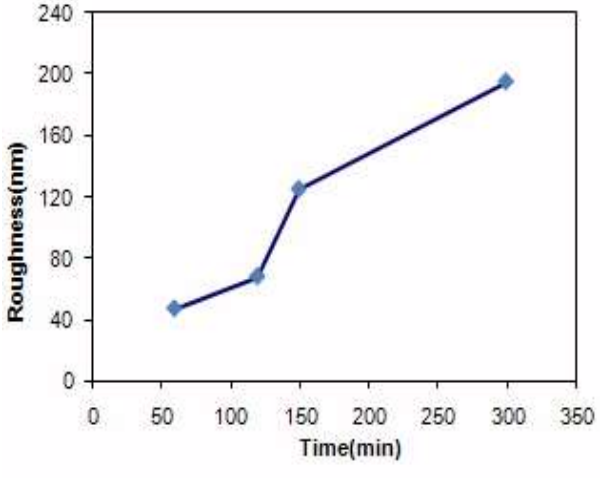

Fig. 4 2XRD plots for DLC deposits deposited for various times.

A single broad peak indicates that the deposit is microcrystalline with preferred orientation (200). This orientation is dense, so DLC layer shows high hardness. By increasing deposition time, structure was denser and also hardness increased ("Fig. 5")
SEM images show the thickness of layer plus the rate of growth, both of them increased by increasing time. ("Fig. 5")

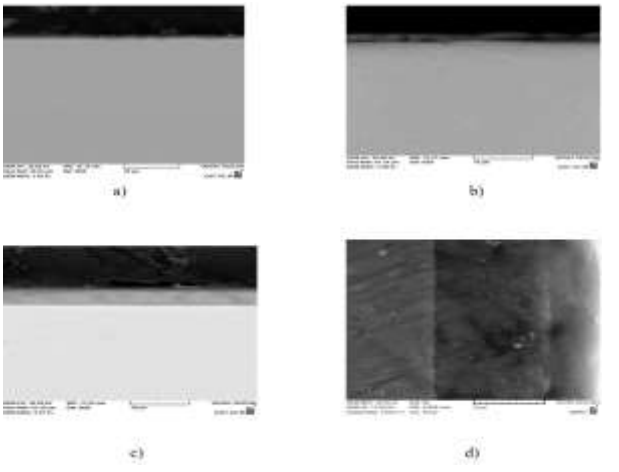

Fig. 5 SEM images of deposited DLC thin films for various time: (a): 60, (b): 120, (c): 150, and (d): 300 minutes.

To assess the mechanical properties of the DLC coating, microhardness measurements were done with a load of 50 g, and "Fig. 6" presents statistics of 4 measurements. The micro hardness of the substrate before and after nitriding is 440 HV0.05 and 960 HV0.05. It must be mentioned that the load is high enough to have both coating and substrate materials as interacting materials during indentation. Increase in deposition time produces a thicker coating. For a fixed indentation load, as the deposition time increases, contribution from coating towards measured hardness increases. This in turn leads to an increase in the hardness value. This clearly shows that coating is much harder than the substrate material.

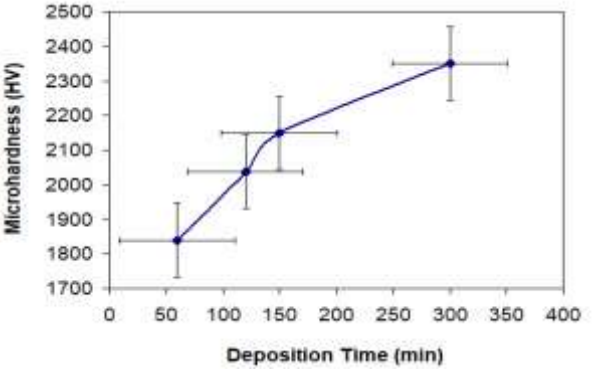

Fig. 6 Measured hardness values of the coating deposited for different durations.

4 CONCLUSIONS

- DLC deposits were deposited on aluminum for different time durations. Very fine nuclei in the deposit were observed the form of islands.

- These results show that growth of DLC layer includes three stages. The first stage is primary growth of nuclei, and then these nuclei join together in second stage. In third stage, secondary growth of these nuclei happens.
- Compared to substrate material, deposit showed higher hardness and roughness.
- XRD plots show a single broad peak which indicates that the deposit is microcrystalline with preferred orientation (200). This orientation is dense, so DLC layer shows higher hardness than plasma nitriding and substrate. By increasing deposition time, structure was denser and also hardness increased.

REFERENCES

[1] Rie, K. T., Gebauer, A., Woehle, J., To¨nshoff, H. K., and Blawit, C., Synthesis of TiN/DLC/TiC Layer Systems on Aluminuim and Cermet Substrates by PACVD, Surf. Coat. Technol., Vol. 74/75, 1995, pp. 375–381.

[2] Hedenqvist, P., Olsson, M., Wallen, P., Kassman, A., Hogmark, and Jacobson, S., How TiN Coatings Improve the Performance of High-Speed Tools, Surf. Coat. Technol., Vol. 41, 1990, pp. 243–256.

[3] Sundgren, J. E., Structure and Properties of TiN Coatings, Thin Solid Films, Vol. 128, 1985, pp. 21–44.

[4] Rie, K. T., Gebauer, A., and Woehle, J., Investigation of PA-CVD of TiN: Relations Between Process Parameters Spectroscopic Measurements and Layer Properties, Surf. Coat. Technol., Vol. 60, 1993, pp. 385–388.

[5] Ishii, Y., Ohtsu, H., Adachi, T., Ichimura, H., and Kobayashi, K., TiN Film Formation by Plasma Chemical Vapour Deposition and Its Plasma Diagnostics, Surf. Coat. Technol., Vol. 49, 1991, pp. 279–283.

[6] Dion, I., Rouais, F., Trut, L., Baquey, C., Monties, J. R., and Havlik, P., TiN coating: surface characterization and haemocompatibility, Biomaterials, Vol. 14, Issue 3, 1993, pp. 169-176.

[7] Dion, X. Roques, N. More, L. Labrousse, J. Caix, F. Lefebvre, F. Rouais, and et al, Ex Vivo Leucocyte Adhesion and Protein Adsorption on TiN, Biomaterials, Vol. 14, 1993, pp. 712-719.

[8] Narayan, J., Fan, W. D., Narayan, R. J., Tiwari, P., and Stadelmaier, H. H., Mater. Sci. Eng., Vol. B25, No. 5, 1995.

[9] Raimondi, M. T., Pietrabissa, R., The In-Vivo Wear Performance of Prosthetic Femoral Heads with Titanium Nitride Coating, Biomaterials, Vol. 21, No. 9, 2000, pp. 907–913.

[10] Hubler, R., Cozza, A., Marcondes, T. L., Souza, R. B., and Fiori, F., Surf. Coat. Tech., Vol. 142, 2001, pp. 1078.

[11] Oñate, J. I., Comin, M., Braceras, I., Garcia, A., Viviente, J. L., Brizuela, M., Garagorri, N., and et al, Wear Reduction Effect on Ultra-High-Molecular-Weight Polyethylene by Application of Hard Coatings and Ion Implantation on Cobalt Chromium Alloy, As Measured in A Knee Wear Simulation Machine, Surf. Coat. Tech., Vol. 142–144, 2001, pp. 1056-1062.

[12] Tamura, Y., Yokoyama, A., Watari, F., and Kawasaki, T., Dent. Mater. J., Vol. 21, 2002, pp. 355-372.

[13] Gutmanas, E. Y., Gotman, I., PIRAC Ti Nitride Coated Ti-6Al-4V Head Against UHMWPE Acetabular Cup-Hip Wear Simulator Study, J. Mater. Sci.: Mater. Med., Vol. 15, 2004, pp. 327–330.

[14] M.P. Gispert, A.P. Serro, R. Colaço, A.M. Botelho do Rego, E. Alves, R.C. da Silva, P., Brogueira, et al Wear, Vol.262, 2007, pp.1337.

[15] R. Kullmer, R., Lugmair, C., Figueras, A., Bassas, J., Stoiber, M., and Mitterer, C., Microstructure, Mechanical and Tribological Properties of PACVD Ti(B,N) and TiB2 Coatings, Surf. Coat. Technol. Vol. 174–175, 2003, pp. 1229-1233.

[16] Klimek, K. S., Ahn, H., Seebach, I., Wang, M., and Rie, K. T., Duplex Process Applied for Die-Casting and Forging Tools, Surf. Coat. Technol., Vol. 174–175, 2003, pp. 677-680.

[17] Stoiber, M., Perlot, S., Mitterer, C., Beschliesser, M., Lugmairand C., and Kullmer, R., Surf. Coat. Technol., Vol. 177–178, 2004, pp. 348.

[18] Mayrhofer, P. H., Stoiber, M., and Mitterer, C., Age Hardening of PACVD TiBN Thin Films, Scr. Mater., Vol. 53, No. 2, 2005, pp. 241.

[19] Ma, Sh., Xu, K., and Jie, W., Plasma nitrided and TiCN coated AISI H13 steel by pulsed dc PECVD and Its Application for Hot-Working Dies, Surf. Coat. Technol., Vol. 191, No. 2-3, 2005, pp. 201-205.

[20] Bull, S. J., Bhat, D. G., and Staia, M. H., Properties and Performance of Commercial TiCN Coatings, Part 2: Tribological Performance, Surf. Coat. Technol., Vol. 163–164, 2003, pp. 507-514.

[21] Mitterer, C., Holler, F., Reitberger, D., Badisch, E., Stoiber, M., Lugmair, C., Nöbauer, R., and et al, Industrial Applications of PACVD Hard Coatings, Surf. Coat. Technol. Vol. 163–164, 2003, pp. 716-722.

[22] B.D. Cullity, Elements of X-ray Diffraction, second ed., Addison Wesley, 1978.

[23] O. Salas, K. Kearns, S. Carrera and J. Moore, Tribological Behavior of Candidate Coatings for Al Die Casting Dies, Surface and Coatings Technology Vol. 172, No. 2-3, 2003, pp.117–127.

[24] H.L. Wang, J.L. He and M.H. Hon, Sliding Wear Resistance of TiCN Coatings on Tool Steel Made by Plasma-Enhanced Chemical Vapour Deposition, Wear, Vol. 169, 1993, pp. 195-200.

[25] Y. He, I. Apachitei, J. Zhou, T. Walstock and J. Duszczyk, Effect of Prior Plasma Nitriding Applied to A Hot-Work Tool Steel on The Scratch-Resistant Properties of PACVD TiBN and TiCN Coatings, Surface & Coatings Technology, Vol. 201, 2006, pp. 2534–2539.

[26] S.M.M.Shafiei, M. Divandari, S.M.A.Boutorabi and R. Naghizadeh, Materials Research, Vol.17(6), 2014, pp. 1651-1657.

Int. J. Advanced Design and Manufacturing Technology, 2023, Vol. 16, No. 1, pp. 81-88

DOI: 10.30486/admt.2022.1943233.1321 ISSN: 2252-0406 https://admt.isfahan.iau.ir

Effect of Inter-Cavity Spacing and Heat Treatment in Friction Stir Processing/Welding (FSP/FSW) Al7075 Composites Containing Al_2O_3 and Graphene Nanomaterials using Charpy Impact Test

Ali Hossein zadeh[1,] *, Mahmood Shariati[2]
Department of Mechanical Engineering,
Ferdowsi University of Mashhad, Iran
E-mail: a.hosseinzadeh.PhD@mail.um.ac.ir, mshariati44@um.ac.ir
*Corresponding author

Danial Ghahremani-moghadam[3]
Department of Mechanical Engineering,
Quchan University of Technology
E-mail: d.ghahremani@qiet.ac.ir

Mohammad Reza Maraki[4]
Department of Material Engineering,
Birjand University of Technology
E-mail: maraki@birjandut.ac.ir

Received: 23 October 2021, Revised: 28 March 2022, Accepted: 31 March 2022

Abstract: In this research, the friction stir process by adding Al_2O_3 and graphene nanoparticles at two different distances have been investigated. Nanoparticles are inserted in cavities with a diameter of 2 mm and a depth of 3 mm. Nanoparticles of Al_2O_3, graphene, and equal compositions of Al_2O_3 and graphene, each with two cavity spacings of 8 and 10 mm, have been performed in six different groups of friction stir process. From each group, Six Charpy specimens were separated. Charpy impact test was performed on six samples, three of which were heat-treated after the friction stir process. Charpy impact test has shown that the specimens have higher fracture energy after heat treatment. Also, in all cases, the fracture energy at the distance between the two cavities are10 mm more than the distance of 8 mm, this is since nanoparticles do not accumulate at a more distance. Also, to observe the resulting microstructures using optical microscopy and scanning electron microscopy on the friction welding process and the fracture surface of Charpy impact specimens were performed. The results show that the nanoparticles are accumulated in some samples and well dispersed in the materials in others.

Keywords: Aluminum Matrix Composites, Al_2O_3, Charpy Impact Test, Friction Stir Processing, Grapheme, Nanoparticle

Biographical notes: Ali Hosseinzadeh is a PhD candidate at Ferdowsi University of Mashhad, Iran. His main research interests are fatigue, fracture and impact mechanic. **Mahmood Shariati** received his PhD in Mechanical Engineering from Tarbiat Modares University, Iran in 1999. He is currently Full Professor at the Department of Mechanical Engineering in Ferdowsi University of Mashhad, Iran. **Danial Ghahremani-moghadam** received his PhD in Mechanical Engineering from Ferdowsi University of Mashhad, Iran in 2016. He is currently Assistant Professor at the Department of Mechanical Engineering in Quchan University of Technology, Iran. **Mohammad Reza Maraki** is an Instructor of Material Engineering at Birjand University of Technology. He received his MSc in Material Engineering from Iran University of Science and Technology in 2002. His current research focuses on the welding process and fracture mechanic.

Research paper

1 INTRODUCTION

The quality and mechanical properties of welds depend greatly on the presence of weld defects such as cavities, cracks, pores and components during traditional welding. Friction stir welding (FSW), invented in the 1990's by the Welding Institute (UK), is a solid-state welding process [1].

This welding method is used for welding materials with less weldability or almost welding by fusion and also for welding dissimilar alloys. Unlike traditional joint welding, in FSW, the bonding process takes place below the solid temperature, which causes less distortion, residual stress and various defects in the final products. FSW has other advantages such as simple sample preparation, precise external control and high connection speed, less energy consumption and less pollution reduction [2]. Given these advantages, FSW has received widespread attention as a process of joining similar and different alloys [3-6] for use in various industries, such as shipbuilding, vehicle construction, railways, aerospace and marine construction [7-9].

Recently, FSP has been widely used to fabricate Al-matrix surface nanocomposites with various nanoscale enhancers (including SiC [10-12], Al_2O_3 [13-15], B_4C [16-17], TiC [18], fullerene [19], SiO_2 [20-21], TiO_2 [22-24], TiB_2 [25], intermetallic [26]) or nanotubes (including single carbon nanotubes [27] and multi-wall carbon nanotube (CNT) [28-29]).

Nandipati et al. [30] investigated friction stir welded AA6061 metal matrix nanocomposites (MMNC) reinforced with SiC nanoparticles. Butola et al. [31] studied the measurement of residual stress on H13 tool steel during machining for fabrication of FSW/FSP tool pins. Zhang et al. [32] investigated microstructure, mechanical properties and fatigue crack growth behavior of friction stir welded joint of 6061-T6 aluminum alloy. Duan et al. [33] investigated microstructure, crystallography, and toughness in the nugget zone of friction stir welded high-strength pipeline steel. Shaikh et al. [34] used FSW for joining of high-densitypolyethylene (HDPE) composites that were formed through the additions of SiC, SiO_2, nano-alumina, and graphite powders during welding at the rotational speed of 1800 rpm, traveling speed of 16 mm/min and the other selected welding parameters. Khan et al. [35] investigated the effect of inter-cavity spacing in friction stir processed Al 5083 composites containing carbon nanotubes and boron carbide particles.

2 MATERIALS AND EXPERIMENTAL PROCEDURES

2.1. Nanoparticles

In this research, graphene and Al_2O_3 nanomaterials have been used. Graphene nanoplates with a purity of 99.9%, thickness of 2-4 μm, diameter less than 2 nm, specific surface area of 700 m^2/g, black color and true density of 1.9-2.2 g/cm^3 have been used. Aluminum oxide nanopowders (Al_2O_3, Gamma) with 99.9% purity, average particle size of 20-30 nm, specific surface area of 130-220 m^2/g, white color, true density of 3.5-3.9 g/cm^3, and crystal form nearly spherical (Gamma) have been used.

2.2. Friction Stir Processing/Welding (FSP/FSW)

In this paper, the alloy used for FSP/FSW is 7075-T651 aluminum. This alloy has heat treatment ability and the characteristic of T6 indicates heat treatment of solubilized and artificially aged type and the number 51 indicates de-stressing by stretching after heat treatment. Also, this alloy has excellent mechanical strength and is widely used in the aerospace industry. "Table 1" shows the chemical composition of this alloy, which was determined using chemical analysis with the Solaris OES Plus quantimeter manufactured by the Italian company GNR. The mechanical properties of the alloy are also given in "Table 2". The six plates used have dimensions of 120×120 mm and a thickness of 5 mm and the nanoparticles are inserted in cavities with a diameter of 2 mm and a depth of 3 mm (Figure 1). Cavities of diameter 2mm and depth 3mm were prepared on an Al7075 plate using a drilling machine. Two different spacing between the cavities were selected, i.e. 8mm and 10mm. Also a plate without inserting nanoparticles, FSP/FSW is performed.

Table 1 Chemical composition of 7075-T651 Aluminum Alloy

No.	E	%	No.	E	%
1	Fe	0.162	9	V	0.097
2	Cu	1.043	10	Zr	0.020
3	Mn	0.01	11	Ag	0.3
4	Mg	1.071	12	Ga	0.018
5	Cr	0.198	13	Sb	0.15
6	Zn	4.046	14	Bi	92.642
7	Ti	0.074	15	Al	
8	Pb	0.012	-	-	-

Table 2 Mechanical Properties of 7075-T651 Aluminum Alloy

Mechanical Properties	Value
Modulus of elasticity (GPa)	72
Yield strength (MPa)	529.78
Ultimate strength (MPa)	593.45
Poison ratio	0.33
Micro Hardness (MicroVickers)	39
Elongation%	13.2

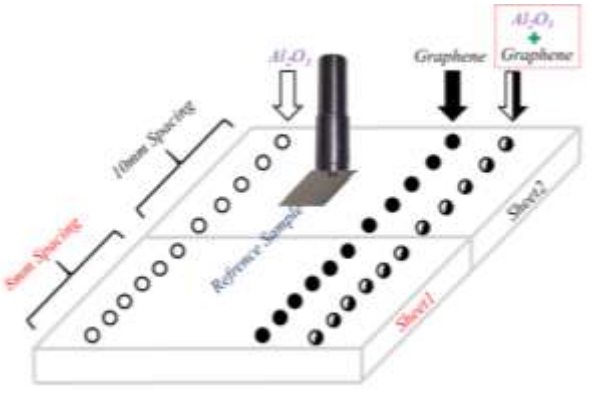

Fig. 1 Schematic of FSP.

For plate welding, a threaded pin shoulder was used to better dissolve the nanoparticles as shown in "Fig. 2". The shoulder is made of SPK2436 steel alloy with a hardness of 50 Rockwell (HCR), the tool shoulder diameter is 20, pin diameter is 4 mm and pin height is 4 mm, and threads with a step of 1 mm are created on it while an angle of 2□ was made from the shoulder to pin root to accumulate the possible spreading of reinforcement from cavities.

Fig. 2 Photographs of FSP/FSW shoulder.

The angle of deviation of the tool from the piece was also chosen to be 2 degrees. The proper angle between the tool pin and the workpiece as the tool shoulder travels through the FSW process allow the tool shoulder to cover the softened and moved material. At a deflection angle of 2 degrees, the materials that have become plastic when the tool penetrates and moves under the tool shoulder return to the workpiece with great pressure using the forging force behind the tool.
To perform the process, FP4M manual milling machine was used. The FP4M milling machine has the ability to withstand the forces during the process and also the ability to move automatically in different directions. Since the workpiece fixture closes on the table, the machine table must be such that it does not vibrate during the process. If the machine is vibrating or has another defect, it has a great effect on the resulting process. Therefore, the obtained results will be with high error and unacceptable. The tool is advancing manually and slowly until it reaches the ideal linear speed. According to the material and thickness of the specimens, the rotational speed of 750 rpm, the advancing speed of the tool is 16 mm / min and the penetration depth of 0.3 mm has been selected, ("Fig. 3").

Fig. 3 Photograph of the process showing machine, tool and plate processed by FSP.

After the FSP/FSW, the specimens are first polished, next etched, and next prepared for macrography in the mount ("Fig. 4"). The different regions of the FSP/FSW are shown in "Fig. 5".

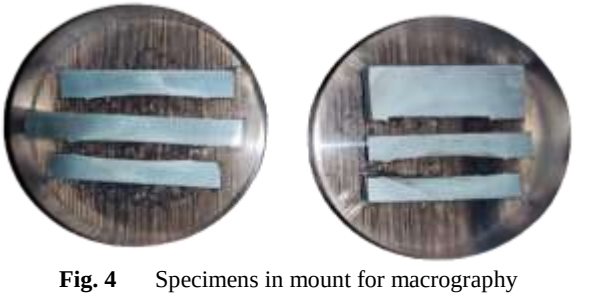

Fig. 4 Specimens in mount for macrography

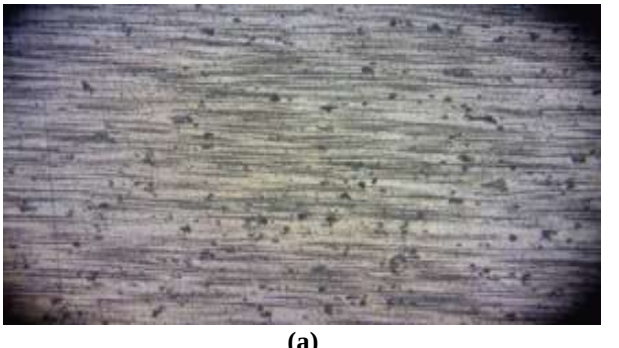

(a)

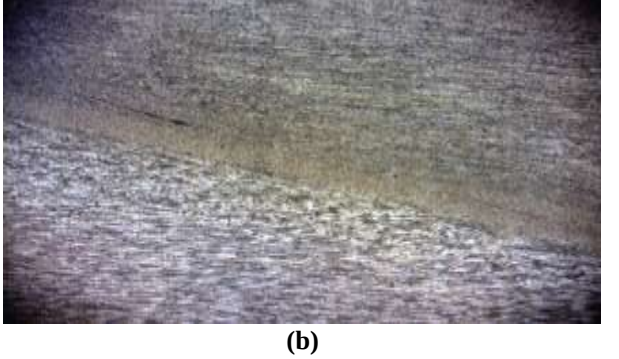

(b)

(c)

Fig. 5 Different FSP/FSW zones: (a): Base Metal, (b): HAZ and, (c): Weld Metal.

Imaging was also performed by scanning electron microscopy to observe the nanoparticles. Figure 6 shows the graphene and Al_2O_3 nanoparticles. The Al_2O_3 nanoparticles shown in "Fig. 6" correspond to a specimen with a distance of 8 mm showing that the nanoparticles have accumulated in one place due to their short distance from each other.

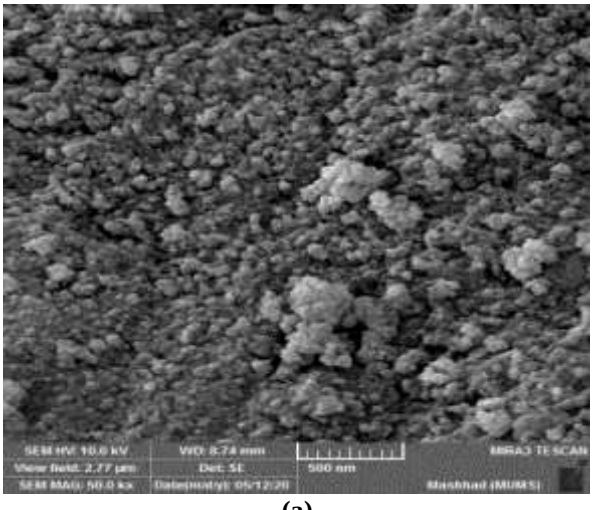

(a)

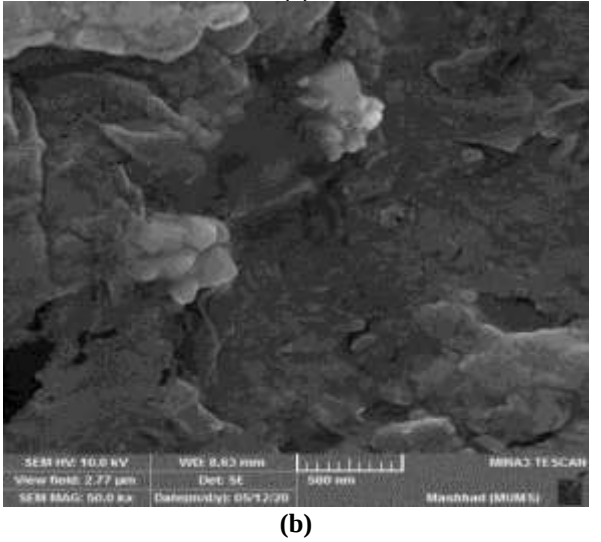

(b)

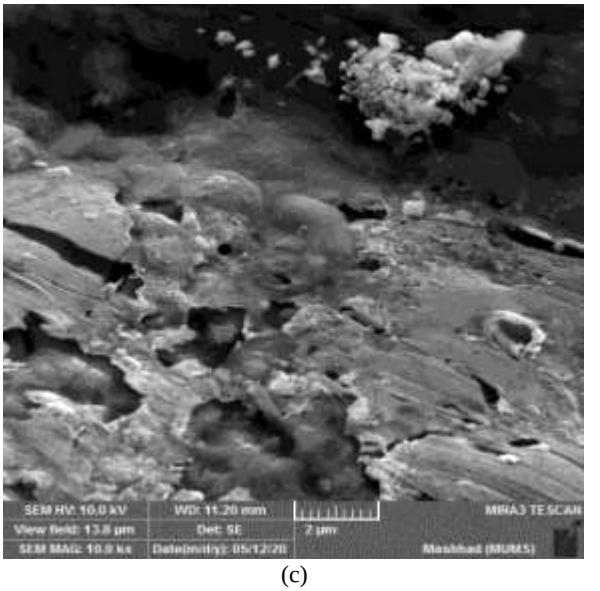

(c)

Fig. 6 SEM images of Al7075 reference with: (a): Al_2O_3 nanoparticles, (b): Graphene nanoplates, and (c): Al_2O_3 + Graphene.

2.3. Heat Treatment

After FSP/FSW process, from each group, three specimens were subjected to the T6 heat treatment cycle (dissolution at 480 ° C for 120 minutes and cooling in water and then precipitation at 120 ° C for 24 hours). Figure 7 shows a triple group of Charpy impact specimens before and after heat treatment.

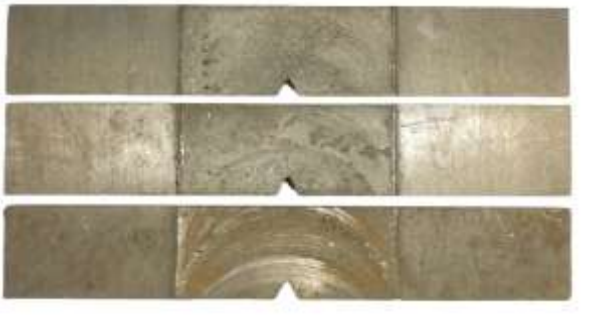

(a)

(b)

Fig. 7 Charpy specimens: (a): before and, (b): after heat treatment.

The specimens are categorized according to "Table 3".

Table 3 Grouping and naming specimens by adding nanoparticles

Number of Group	Nanoparticles	Distance cavities (mm)	Description
1	Gr + Al_2O_3	8	-
2	Gr + Al_2O_3	10	-
3	Al_2O_3	8	-
4	Al_2O_3	10	-
5	Graphene	8	-
6	Graphene	10	-
7	-	-	Specimen without nanoparticle (only FSP)
8	-	-	Specimen without nanoparticle and FSP

2.4. Charpy Impact Test

From 7075 aluminum plate, which made the friction stir welding process, as shown in "Fig. 8", Charpy impact specimens are separated according to ASTM E23 so that the notch is in the center of the weld. Specimen notches can be pressed or machined (Chevron V-notch) according to the API 5L3 standard, which is created by a wirecut machine. The press notch created in the laboratory specimen by pressing the chisel is sharp enough and there are no residual stresses in the notch tip zone and also the type of notch can affect the fracture start energy [36].

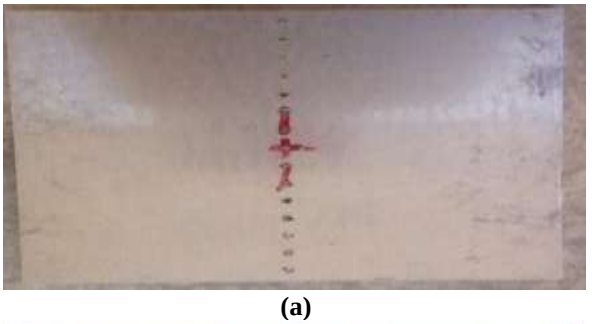

(a)

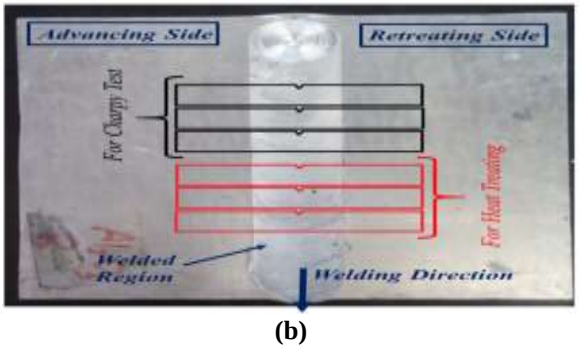

(b)

Fig. 8 (a): The cavities to be prepared by drilling and Al7075 plate after drilling and, (b): after FSP and Schematic diagram of the Charpy specimens selector of the plate.

In this study, notches were created on the specimens using a wire-cut machine. Subsize specimens with dimensions of 55 × 5 × 10 mm and notch angle of 45 degrees, notch tip radius of 0.25 mm, and notch depth of 2 mm have been made with sufficient precision and compliance with standard requirements. The specimens are then smoothed and polished by a grinding machine to smooth the surface.

Impact testing was performed using a 25-joules Charpy impact machine, C-shaped striker, hammer with an 8 mm radius at 23 ° C ("Fig. 9").

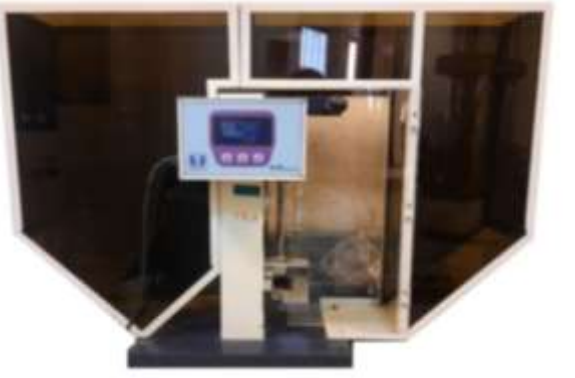

Fig. 9 Charpy impact machine used experimental test

Charpy impact test was repeated 3 times for each specimen and the average fracture energy obtained was reported as the final fracture energy.

3 RESULTS AND DISCUSSION

3.1. Hardness

Six examples of FSP/FSW by Vickers microhardness have been investigated. Hardness results are reported in "Fig. 10". Hardness is done in the zones of HAZ, TMAZ, SZ, TMAZ, HAZ and is W-shaped. In specimens with a distance between two cavities of 10 mm, the hardness in all three specimens of nanoparticles is higher than in specimens with a distance of 8 mm. Hardness results and microscopic observations show that nanoparticles have accumulated at shorter distances and reduced the hardness of the specimen. The best hardness results are for Al_2O_3 nanoparticles, then the combination of graphene nanoplate and Al_2O_3 nanoparticles. The lowest hardness is related to graphene nanoplates, which is even less hardness than the specimen without nanomaterials.

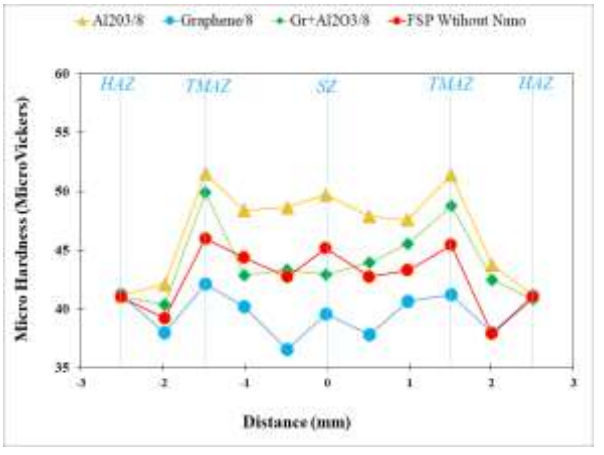

(a)

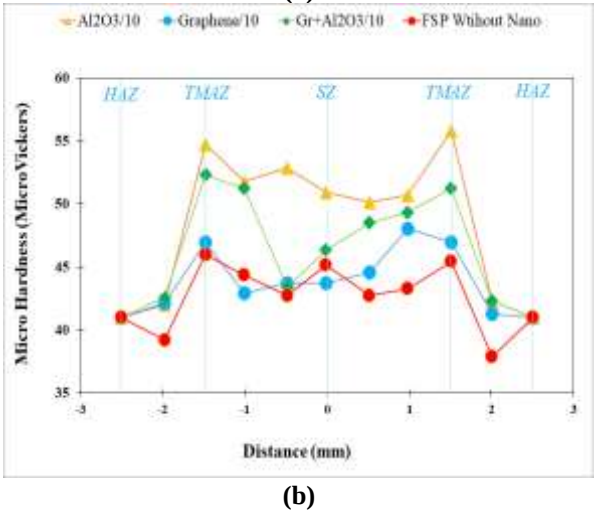

(b)

Fig. 10 Microhardness values of FSP/FSW composites: (a): 8mm spacing and, (b): 10mm spacing specimens.

3.2. Charpy Impact Test

Seven specimens of friction stir welding were tested by a 25-joule Charpy impact machine. The results of the Charpy impact test are reported in "Fig. 11".

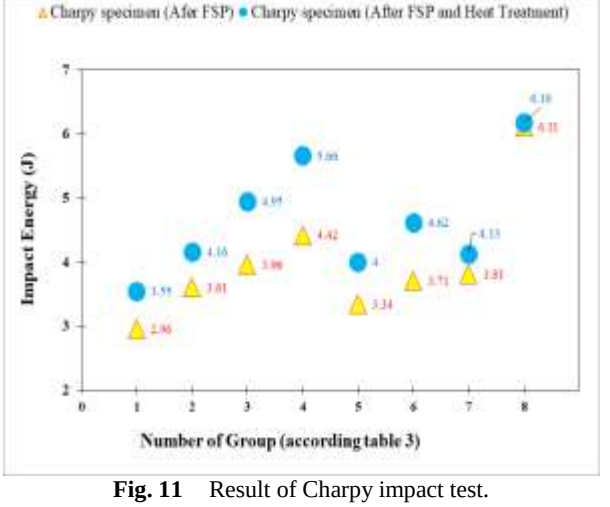

Fig. 11 Result of Charpy impact test.

Experimental results show that the fracture energy of specimens with nanomaterials at a distance of 10 mm is higher. This shows that in specimens with a distance of 8 mm nanomaterials accumulated and reduced the fracture energy.

In all specimens, after heat treatment, higher fracture energy was reported, which indicates that heat treatment has caused the nanomaterials to penetrate well into the material and become part of the material structure.

The highest fracture energy is related to the specimen in which the Al_2O_3 nanoparticles are set at a distance of 10 mm. The lowest fracture energy is related to a specimen that combines Al_2O_3 and graphene nanomaterials at a distance of 8 mm, which is even lower in a specimen where the FSP/FSW is performed alone. In all cases, the fracture energy of specimens with a distance of 10 mm is higher than that of specimens with a distance of 8 mm. This is due to the accumulation of nanomaterials at shorter distances, which reduces the strength of the material.

4 CONCLUSIONS

In the present study, the Effect of inter-cavity spacing and heat treatment in friction stir Processing/welding (FSP/FSW) Al7075 composites containing Al_2O_3 and Graphene nanomaterials using Charpy impact test was investigated. 24 specimens were tested in eight specimens series (each specimen 3 times) with standard subsize specimens. The specimens were also heat treated and Charpy tested again. The Charpy impact machine used in this experiment had the capacity of 25 joules, which is selected according to ASTM E23. Also, fractography of the samples was performed by optical microscopy and SEM. the results are summarized as follows:

1- The hardness in specimens with a distance of 10 mm is higher than the specimens with a distance of 8 mm in all three specimens with different nanoparticles.

2- Hardness results and microscopic observations show that nanoparticles have accumulated at shorter distances and reduced the hardness of the specimen.

3- The best hardness results are for alumina nanoparticles, then the combination of graphene nanoplate and Al_2O_3 nanoparticles. The lowest hardness is related to graphene nanoplates, which is even less hardness than the specimen without nanomaterials.

4- In the Charpy test, all specimens reported higher fracture energy after heat treatment, indicating that heat treatment caused the nanomaterials to penetrate well into the material and become part of the material structure.

5- The highest fracture energy is related to the specimen where the Al_2O_3 nanoparticles are placed at a distance of 10 mm.
6- The lowest fracture energy is related to a specimen that combines Al_2O_3 and graphene nanomaterials at a distance of 8 mm, which is even lower in a specimen where the FSP/FSW is performed alone.
7- In all cases, the fracture energy of specimens with a distance of 10 mm is higher than that of specimens with a distance of 8 mm. This is due to the accumulation of nanomaterials at shorter distances, which reduces the strength of the material.

REFERENCES

[1] Wahid, M. A., Khan, Z. A., and Siddiquee, A. N., Review on Underwater Friction Stir Welding: A Variant of Friction Stir Welding with Great Potential of Improving Joint Properties Transactions of Nonferrous Metals Society of China, Vol. 28, No. 2, 2018, pp. 193-219.

[2] Subramanya, P., Amar, M., Arun, S., Mervin, H., and Shrikantha, R., Friction Stir Welding of Aluminium Matrix Composites–A Review, MATEC Web Conf., Vol. 144, 2018, pp. 03002, http://dx.doi.org/10.1051/matecconf/201814403002

[3] Murr, L., A Review of FSW Research on Dissimilar Metal and Alloy Systems, J. Mater. Eng. Perform., Vol. 19, No. 8, 2010, pp. 1071-1089, http://dx.doi.org/10.1007/s11665-010-9598-0.

[4] Chen, T., Process Parameters Study on FSW Joint of Dissimilar Metals for Aluminum–Steel, J. Mater. Sci., Vol. 44, No. 10, 2009, pp. 2573-2580, http://dx.doi.org/10.1007/s10853-009-3336-8.

[5] Carlone, P., Astarita, A., Palazzo, G. S., Paradiso, V., and Squillace, A., Microstructural Aspects in Al–Cu Dissimilar Joining by FSW, Int. J. Adv. Manuf. Technol., Vol. 79, No. 5-8, 2015, pp. 1109-1116, http://dx.doi.org/10.1007/s00170-015-6874-z.

[6] Moghadam, D. G., Farhangdoost, K., Influence of Welding Parameters on Fracture Toughness and Fatigue Crack Growth Rate in Friction Stir Welded Nugget of 2024-T351 Aluminum Alloy Joints, Trans. Nonferrous Met. Soc. China, Vol. 26, No. 10, 2016, pp. 2567-2585, http://dx.doi.org/10.1016/S1003-6326(16)64383-2.

[7] Zhao, J., Jiang, F., Jian, H., Wen, K., Jiang, L., and Chen, X., Comparative Investigation of Tungsten Inert Gas and Friction Stir Welding Characteristics of Al–Mg–Sc Alloy Plates, Mater. Des. Vol. 31, No. 1, 2010, pp. 306-311, http://dx.doi.org/10.1016/j.matdes.2009.06.012.

[8] Cavaliere, P., Cabibbo, M., Panella, F., and Squillace, A., 2198 Al–Li Plates Joined by Friction Stir Welding: Mechanical and Microstructural Behavior, Mater. Des., Vol. 30, No. 9, 2009, pp. 3622 - 3631, http://dx.doi.org/10.1016/j.matdes.2009.02.021.

[9] Thomas, W., Nicholas, E., Friction Stir Welding for The Transportation Industries, Mater. Des., Vol. 18, No. 4-6, 1997, pp. 269-273.

[10] Ni, D., Chen, D., Wang, D., Xiao, B., and Ma, Z., Influence of Microstructural Evolution on Tensile Properties of Friction Stir Welded Joint of Rolled SiCp/AA2009-T351 Sheet, Mater. Des., Vol. 51, 2013, pp. 199-205, http://dx.doi.org/10.1016/j.matdes.2013.04.027.

[11] Khodabakhshi, F., Gerlich, A., and Švec, P., Fabrication of a High Strength Ultra-Fine-Grained Al-Mg-SiC Nanocomposite by Multi-Step Friction-Stir Processing, Mater. Sci. Eng. A, Vol. 698, 2017, pp. 313-325, http://dx.doi.org/10.1016/j.msea.2017.05.065.

[12] Khodabakhshi, F., Simchi, A., Kokabi, A., and Gerlich, A., Similar and Dissimilar Friction-Stir Welding of an PM Aluminum-Matrix Hybrid Nanocomposite and Commercial Pure Aluminum: Microstructure and Mechanical Properties, Mater. Sci. Eng. A, Vol. 666, 2016, pp. 225-237, http://dx.doi.org/10.1016/j.msea.2016.04.078.

[13] Ashjari, M., Asl, A. M., and Rouhi, S., Experimental Investigation on The Effect of Process Environment on The Mechanical Properties of AA5083/Al_2O_3 Nanocomposite Fabricated Via Friction Stir Processing, Mater. Sci. Eng. A, Vol. 645, 2015, pp. 40-46, http://dx.doi.org/10.1016/j.msea.2015.07.093.

[14] Khodabakhshi, F., Yazdabadi, H. G., Kokabi A., and Simchi, A., Friction Stir Welding of a P/M Al–Al_2O_3 Nanocomposite: Microstructure and Mechanical Properties, Mater. Sci. Eng. A, Vol. 585, 2013, pp. 222-232, http://dx.doi.org/10.1016/j.msea.2013.07.062.

[15] Khodabakhshi, F., Simchi, A., Kokabi, A., Gerlich, A., Nosko, M., and Švec, P., Influence of Hard Inclusions on Microstructural Characteristics and Textural Components During Dissimilar Friction-Stir Welding of an PM Al–Al_2O_3–SiC Hybrid Nanocomposite with AA1050 Alloy, Sci. Technol. Weld. Join., Vol. 22, No. 5, 2017, pp. 412-427, http://dx.doi.org/10.1080/13621718.2016.1251714.

[16] Narimani, M., Lotfi, B., and Sadeghian, Z., Evaluation of the Microstructure and Wear Behavior of AA6063-B4C/TiB2 Mono and Hybrid Composite Layers Produced by Friction Stir Processing, Surf. Coat. Tech.,Vol. 285, 2016, pp. 1-10,http://dx.doi.org/10.1016/j.surfcoat.2015.11.015.

[17] Yuvaraj, N., Aravindan, S., Fabrication of Al5083/B4C Surface Composite by Friction Stir Processing and Its Tribological Characterization Journal of Materials Research and Technology, Vol. 4, No. 4, 2015, pp. 398-410, http://dx.doi.org/10.1016/j.jmrt.2015.02.006.

[18] Rejil, C. M., Dinaharan, I., Vijay, S., and Murugan, N., Microstructure and Sliding Wear Behavior of AA6360/(TiC+ B4C) Hybrid Surface Composite Layer Synthesized by Friction Stir Processing on Aluminum Substrate, Mater. Sci. Eng. A, Vol. 552, 2012, pp. 336-344, http://dx.doi.org/10.1016/j.msea.2012.05.049.

[19] Morisada, Y., Fujii, H., Nagaoka, T., Nogiand K., Fukusumi, M., Fullerene/A5083 Composites Fabricated by Material Flow During Friction Stir Processing, Compos., Part A Appl. Sci. Manuf., Vol. 38, No. 10, 2007, pp. 2097-2101,

http://dx.doi.org/10.1016/j.compositesa.2007.07.004.

[20] Ramesh, S., Sivasamy, A., Rhee, K., Park, S., and Hui, D., Preparation and Characterization of Maleimide–Polystyrene/SiO2–Al2O3 Hybrid Nanocomposites by An In-Situ Sol-Gel Process and Its Antimicrobial Activity, Compos., Part B Eng., Vol. 75, 2015, pp. 167-175, http://dx.doi.org/10.1016/j.compositesb.2015.01.040.

[21] You, G., Ho, N., and Kao, P., In-Situ Formation of Al2O3 Nanoparticles During Friction Stir Processing of AlSiO2 Composite, Mater. Charact., Vol. 80, 2013, pp. 1-8, http://dx.doi.org/10.1016/j.matchar.2013.03.004.

[22] Khodabakhshi, F., Gerlich, A., Simchi, A., and Kokabi, A., Hot Deformation Behavior of An Aluminum-Matrix Hybrid Nanocomposite Fabricated by Friction Stir Processing, Mater. Sci. Eng. A, Vol. 626, 2015, pp. 458-466, http://dx.doi.org/10.1016/j.msea.2014.12.110.

[23] Khodabakhshi, F., Gerlich, A., Simchi, A., and Kokabi, A., Cryogenic Friction-Stir Processing of Ultrafine-Grained Al-Mg–TiO2 Nanocomposites, Mater. Sci. Eng. A, Vol. 620, 2015, pp. 471-482, http://dx.doi.org/10.1016/j.msea.2014.10.048.

[24] Khodabakhshi, F., Simchi, A., Kokabi, A., Sadeghahmadi, M., and Gerlich, A., Reactive Friction Stir Processing of AA 5052–TiO2 Nanocomposite: Process–Microstructure–Mechanical Characteristics, Mater. Sci. Technol., Vol. 31, No. 4, 2015, pp. 426-435, http://dx.doi.org/10.1179/1743284714Y.0000000573.

[25] Eskandari, H., Taheri, R., and Khodabakhshi, F., Friction-Stir Processing of an AA8026-TiB2-Al2O3 Hybrid Nanocomposite: Microstructural Developments and Mechanical Properties, Mater. Sci. Eng. A, Vol. 660, 2016, pp. 84-96, http://dx.doi.org/10.1016/j.msea.2016.02.081.

[26] Khodabakhshi, F., Simchi, A., Kokabi, A., and Gerlich, A., Friction Stir Processing of An Aluminum-Magnesium Alloy with Pre-Placing Elemental Titanium Powder: In-Situ Formation of an Al3Tireinforced Nanocomposite and Materials Characterization, Mater.Charact., Vol. 108, 2015, pp. 102-114, http://dx.doi.org/10.1016/j.matchar.2015.08.016.

[27] Liu, Z., Xiao, B., Wang, W., and Ma, Z., Singly Dispersed Carbon Nanotube/Aluminum Composites Fabricated by Powder Metallurgy Combined with Friction Stir Processing, Carbon, Vol. 50, No. 5, 2012, pp. 1843-1852, http://dx.doi.org/10.1016/j.carbon.2011.12.034.

[28] Kim, W., Lee, T., and Han, S., Multi-Layer Graphene/Copper Composites: Preparation Using High-Ratio Differential Speed Rolling, Microstructure and Mechanical Properties, Carbon, vol. 69, 2014, pp. 55-65, http://dx.doi.org/10.1016/j.carbon.2013.11.058.

[29] Kondoh, K., Fukuda, H., Umeda, J., Imai, H., and Fugetsu, B., Microstructural and Mechanical Behavior of Multi-Walled Carbon Nanotubes Reinforced Al–Mg–Si Alloy Composites in Aging Treatment, Carbon, Vol. 72, 2014, pp. 15-21, http://dx.doi.org/10.1016/j.carbon.2014.01.013.

[30] Nandipati, G., Damera, N., and Nallu, R., Effect of Microstructural Changes on Mechanical Properties of Friction Stir Welded Nano SiC Reinforced AA6061 Composite, Int. J. Eng. Sci. Technol., Vol. 2, No. 11, 2010, pp. 6491-6499.

[31] Butola, R., Choudhary, N., Kumar, R., Kumar Mouria, P., Zubair, M., Ranganath, M., and Singari, M., Measurement of Residual Stress on H13 Tool Steel During Machining for Fabrication of FSW/FSP Tool Pins, Materials Today: Proceedings, Vol. 43, No. 1, 2021, pp. 256-262.

[32] Zhang, L., Zhong, H., Li, Sh., Zhao, H., Chen, J., and Qi, L., Microstructure, Mechanical Properties and Fatigue Crack Growth Behavior of Friction Stir Welded Joint of 6061-T6 Aluminum Alloy, International Journal of Fatigue, Vol. 135, 2020, 105556, ISSN 0142.

[33] Duan, R. H., Xie, G. M., Luo, Z. A., Xue, P., Wang, C., Misra, R. D. K., and Wang, G. D., Microstructure, Crystallography, And Toughness in Nugget Zone of Friction Stir Welded High-Strength Pipeline Steel, Materials Science and Engineering: A, Vol. 791, 2020, 139620, ISSN 0921-5093.

[34] Shaikh, A. S., Tahir, M. S., and Qureshi, M. K. A., Experimental Investigation of Mechanical Properties of Friction Stir Welded HDPE with Additions of Silicon Carbide, Silica, Nano-Alumina, And Graphite, Materials Science and Technology, Joining of Advanced and Specialty Materials, 2012, pp. 316-323.

[35] Khan, M., Rehman, A., Aziz, T., Shahzad, M., Naveed, K., and Subhani, T., Effect of Inter-Cavity Spacing in Friction Stir Processed Al 5083 Composites Containing Carbon Nanotubes and Boron Carbide Particles, Journal of Materials Processing Technology, Vol. 253, 2018, pp. 72-85, ISSN 0924-0136.

[36] Majidi, A., Hashemi, S. H., Study of Macroscopic Fracture Surface Characteristics of Spiral Welded API X65 Gas Transportation Pipeline Steel, Modares Mechanical Engineering, Vol. 17, No. 11, 2018, pp. 219-228.

Int. J. Advanced Design and Manufacturing Technology, 2023, Vol. 16, No. 1, pp. 89-97

DOI: 10.30486/admt.2022.1949157.1332 ISSN: 2252-0406 https://admt.isfahan.iau.ir

Multi-Objective Optimization of Plate Heat Exchangers by Employing an Imperialist Competitive Algorithm

Mohammad Javad Mahmoodabadi[1,] *, Soodeh Zarnagar[2]

Department of Mechanical Engineering,
Sirjan University of Technology, Sirjan, Iran
E-mail: Mahmoodabadi@sirjantech.ac.ir
*Corresponding author

Received: 6 January 2022, Revised: 20 April 2022, Accepted: 23 April 2022

Abstract: In this paper, the multi-objective optimum design of plate fin heat exchangers is investigated. To this end, the efficiency and cost as two important factors for the design of heat exchangers are regarded as the objective functions. Fin pitch, fin height, fin offset length, cold stream flow length, no-flow length and hot stream flow length are considered as six design parameters. The ε-NTU method is applied to estimate the heat exchanger pressure drop and its effectiveness. A case study related to a gas furnace in Barez tire group located in the northwest of Kerman, Iran is considered for the constant parameters. The Imperialist Competitive Algorithm (ICA) is used to find the optimal design parameters to achieve the maximum thermal efficiency and minimum consumption cost. The method of the weighting coefficients is applied to change the considered multi-objective optimization problem as a single objective one. Furthermore, the effects of variations of the design parameters on the objective functions are independently investigated, and the related graphs are presented.

Keywords: Consumption Cost, Imperialist Competitive Algorithm, Multi-Objective Optimization, Plate Fin Heat Exchanger, Thermal Efficiency

Biographical notes: Mohammad Javad Mahmoodabadi received his BS and MS degrees in Mechanical Engineering from Shahid Bahonar University of Kerman, Iran in 2005 and 2007, respectively. He received his Ph.D. degree in Mechanical Engineering from the University of Guilan, Rasht, Iran in 2012. During his research, he was a scholar visitor with Robotics and Mechatronics Group, University of Twente, Enchede, Netherlands for 6 months. Now, he is an Associate Professor of Mechanical Engineering at the Sirjan University of Technology, Sirjan, Iran. His research interests include optimization algorithms, nonlinear and robust control, robotics and computational methods. **Soodeh Zarnegar** received her BSc in mechanical engineering from the Sirjan University of Technology, Sirjan, Iran in 2015. Her current research focuses on optimization algorithms, and heat exchangers design.

Research paper

1 INTRODUCTION

Compact heat exchangers are characterized by a large heat transfer surface area per unit volume of the system. A plate fin heat exchanger (PFHE) as a typical compact heat exchanger is widely used in many industries such as cooling process coupled with ortho-para hydrogen conversion [1], superfluid helium cryogenic systems [2], evaporation heat transfer plants [3], cryogenic mechanisms [4], superfluid helium system [5], supercritical carbon dioxide Brayton cycle [6], thermally-induced flow maldistribution mechanisms [7], two-phase flow boiling in offset strip fin channels [8], heat transfer and friction factors correlations for offset strip fin and wavy fin [9], and transient three-dimensional thermo-fluid cryogenic plant [10].

In fact, fins or extended surfaces as the plate elements are implemented to increase the heat transfer area [11]. Moreover, offset strip fins with high compactness, high heat transfer efficiency and high reliability are widely employed in heat exchangers for cooling systems of aircrafts, automobiles etc. [12]. Offset strip fins have higher heat transfer performance than plain fins, whereas, those have higher strength and reliability than louver fins [13]. On the other hands, meta-heuristic algorithms have effectively been exploited for optimum design of complicated nonlinear problems. Moreover, most of real-world problems involve more than one objective function to be optimized simultaneously. In this way, a summation of all objective functions could be regarded to form a single-objective optimization problem. Especially, for a heat exchanger design problem, the system efficiency should be increased, while minimum values of the total cost would be utilized. To name but a few, the following research works clearly illustrate the feasibility of the meta-heuristic algorithms to solve heat exchanger design problems: optimal design of heat exchanger network considering the fouling throughout the operating cycle by Hang et al. in 2022 [14], multi-objective optimum design for double baffle heat exchangers by Abolpour et al. in 2021 [15], optimal shape design and performance investigation of helically coiled tube heat exchangers by Wang et al. in 2021 [16], optimal design of variable-path heat exchangers for energy efficiency improvement of air-source heat pump systems by Sim et al. in 2021 [17], a fast reduced model for a shell-and-tube based latent heat thermal energy storage heat exchangers and its application for cost optimal design by nonlinear programming by Pan et al. in 2021 [18], optimum design of heat exchanging device for efficient heat absorption using high porosity metal foams by Prakash et al. [19], an optimal design for hollow fiber heat exchangers by Bohacek et al. [20], design of optimal heat exchanger networks with fluctuation probability using break-even analysis by Hafizan et al. [21], optimal design parameter selection for performance of alumina nano-material particles and turbulence promotors in heat exchangers by Kumar et al. [22], optimization of propane pre-cooling cycle by optimal Fin design of heat exchangers by Allahyarzadeh-Bidgoli et al. [23].

In this paper after thermal modeling of a PFHE, this equipment is optimized as maximizing the effectiveness as well as minimizing the total annual cost. The imperialist competitive algorithm is applied to provide a set of Pareto multiple optimum solutions. The sensitivity analysis for variations of the design parameters on the effectiveness and total annual cost is performed and the results are reported.

The structure of the paper is organized as follows. Section 2 represents the mathematical modelling of the thermal behavior of the plate heat exchangers. The objective functions, design variables and constraints are illustrated in Section 3. The considered case study is described in Section 4. The imperialist competitive algorithm and multi-objective optimization method are described in Section 5. Results and analysis are illustrated in Section 6. Finally, Section 7 concludes the paper.

2 THERMAL MODELING

In this paper, the $\varepsilon - \mathrm{NTU}$ scheme is employed for modelling the dynamics of the heat exchanger. The effectiveness of a cross-flow heat exchanger having unmixed fluids is computed by the following Equation [24]:

$$\varepsilon = 1 - \exp[-(1+C^*)\mathrm{NTU}] \times [I_0(2\mathrm{NTU}\sqrt{C^*}) + \sqrt{C^*} I_1(2\mathrm{NTU}\sqrt{C^*} - \frac{1-C^*}{C^*} \sum_{n=2}^{\infty} C^{*\frac{n}{2}} I_n(2\mathrm{NTU}\sqrt{C^*})] \quad (1)$$

Where, I is the modified Bessel function. The Number of Transfer Units (NTU) and heat capacity ratio C^* are calculated by the following relations [11]:

$$\mathrm{NTU} = \frac{UA_{tot}}{C_{min}} \quad (2)$$

$$C^* = C_{min}/C_{max} \quad (3)$$

Where, U denotes the overall heat transfer coefficient, and A_{tot} states the total heat transfer surface area that can be calculated by the fallowing Equations:

$$U = \frac{1}{\frac{1}{h_c \eta_{s,c}} + \frac{1}{\frac{A_{tot,h}}{A_{tot,c}}(h_h \eta_{s,h})}} \quad (4)$$

$$A_{tot} = (\beta V_p)_c + (\beta V_p)_h \quad (5)$$

Where, h represents the convection heat transfer coefficient. Moreover, β shows the heat transfer surface area per unit volume and can be found by the following relations [25]:

$$\beta = \frac{A_{cell}}{V_{cell}} = \frac{2(b-t_f)x+2(c-t_f)x+2(b-t_f)t_f+ct_f}{bcx} \quad (6)$$

Where, b, t_f, x and c denote the height, thickness, pitch and length of the fin, respectively. Further, $V_{p,h}$ and $V_{p,c}$ respectively illustrate the volume between plates for hot and cold stream sides of the heat exchanger:

$$V_{p,c} = L_c L_h b_c (N_p + 1) \quad (7)$$

$$V_{p,h} = L_c L_h b_h N_P \quad (8)$$

IF $N_p$is regarded as the number of the passages for the hot side, while N_p+ 1 passages are considered for the cold side, then:

$$N_p = \frac{L_n - b_c + 2t_w}{b_h + b_c + 2t_w} \quad (9)$$

Where, t_w demonstrates the plate thickness. Moreover, L_c, L_h and $L_n$mention the cold stream flow length, hot stream flow length and no-flow length, respectively. Besides, $\eta_s$in "Eq. (4)" as overall surface efficiency could be calculated as follows [11]:

$$\eta_s = 1 - \frac{A_f}{A_{cell}}(1-\eta_f) \quad (10)$$

Where, A_f defines the fin heat transfer area (for a single fin without base area) formulated as follows [25]:

$$A_f = 2(b - t_f)x + 2(b - 2t_f)t_f + ct_f \quad (11)$$

$$\eta_f = \tanh(ml)/(ml) \quad (12)$$

Where,

$$m = \sqrt{\frac{2h}{k_f t_f}} \quad (13)$$

and:

$$l = \frac{b}{2} \quad (14)$$

Where, k_f shows the heat conductivity of the material. The above Equations are valid for 120 < Re <10^4. For ratios, the fallowing relations are defined.

$$\alpha = \frac{c}{b} \qquad \delta = \frac{t_f}{x} \qquad \gamma = \frac{t_f}{c} \quad (15)$$

The specifications of the considered system are according to a PFHE of a gas furnace in Barez tire factory located in the northwest of Kerman city, Iran

3 OBJECTIVE FUNCTIONS, DESIGN VARIABLES AND CONSTRAINTS

In this study, the efficiency and total annual cost of the PFHE system are considered as two objective functions. The total annual cost includes the investment cost (annualized cost of the heat transfer surface area) and the operating cost of the compressor to flow the fluid as calculated by the following Equations [26]:

$$C_{total} = aC_{inv} + C_{ope} \quad (16)$$

$$C_{inv} = C_A A_{tot}^n \quad (17)$$

$$C_{ope} = \left(k_{el}\tau\frac{\Delta p V_t}{\eta}\right)_c + \left(k_{el}\tau\frac{\Delta p V_t}{\eta}\right)_h \quad (18)$$

Where, C_A and k_{el} present the heat exchanger investment cost per unit surface area and the electricity unit cost, respectively. Moreover, n is a constant, and τ denotes the operation hours of the exchanger per year. Further, Δp, V_t and η represent the pressure drop, volume flow rate and compressor efficiency, respectively. Finally, a denotes the annual cost coefficient defined as follows [11]:

$$a = \frac{r}{1-(1+r)^{-y}} \quad (19)$$

Where, r and y demonstrate the interest rate and depreciation time, respectively. In this study, fin pitch (c), fin height (b), fin offset length (x), cold stream flow length (L_c), no-flow length (L_n) and hot stream flow length (L_c) are regarded as the design variables. The following constraints are imposed to insure that parameters α, δ and γ are selected from the acceptable ranges 0.134 <α< 0.997, 0.012 <δ< 0.048 and 0.041 <γ< 0.121 with respect to the physical configurations related the case study.

4 CASE STUDY

The design parameters of a plate fin heat exchanger would be optimized for a case related to a gas furnace in Barez tire factory located in Kerman, Iran. The temperature of the furnace is about 500 K at first and around 1500 K at end. The hot gases go out from the middle stage with 1.45 kg/s flow rate of the mass and temperature 700 K. The environmental air moves with 1.35 kg/s flow rate of the mass and 300 K temperature.

The PFHE is made from Aluminum having thermal conductivity k_w= 239 W/m K. Numerical values of other operating conditions are given in "Table 1". The thermophysical properties of air such as Prandtl number, viscosity and specific heat are regarded as temperature dependent. The effects of the design parameters on the efficiency and normal total cost (objective functions) are plotted in "Figs. 1 to 6".

Table 1 Thermophysical and process data of the considered PFHE (input data for modeling)

Symbol	Operating conditions	measured value
$\dot{m}_{fc}$	Flow rate of hot fluid (kg/s)	1.45
$\dot{m}_{fh}$	Flow rate of cold fluid (kg/s)	1.35
T_h	Hot gas temperature (K)	700
T_c	Cold gas temperature (K)	300
C_A	Price per unit area ($/m2)	90
P_c	Cold pressure (kPa)	150
P_h	I tot pressure (kPa)	200
k_{el}	Electrical energy pṅce ($ MWh_1)	20
η	Efficiency of the compressor	0.6
τ	Operation hours per year (h/year)	5000

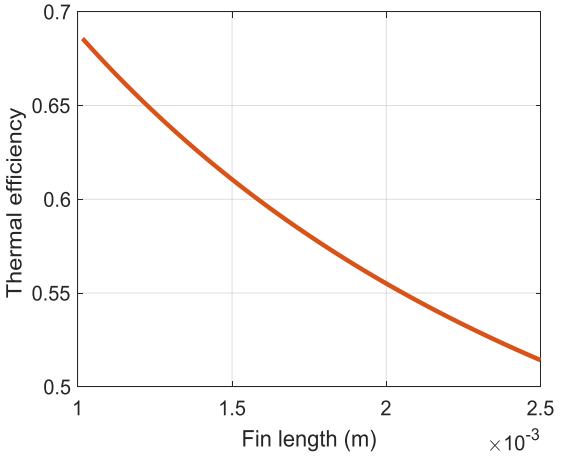

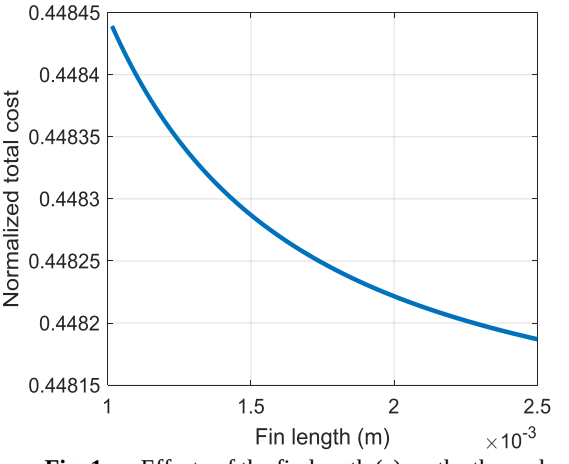

Fig. 1 Effects of the fin length (c) on the thermal efficiency (ϵ) and normalized total cost (C^N_{total}).

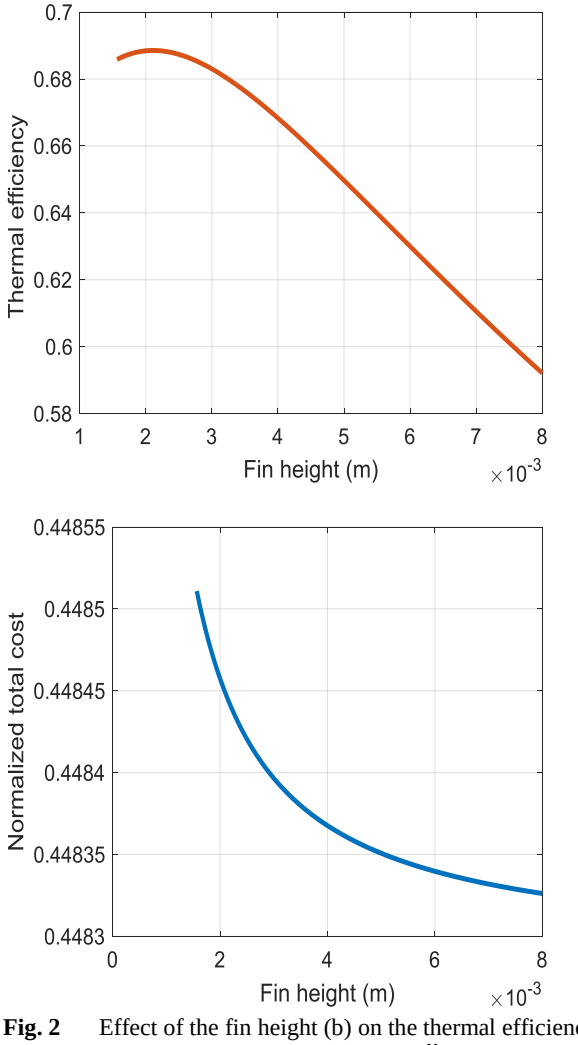

Fig. 2 Effect of the fin height (b) on the thermal efficiency (ϵ) and normalized total cost (C^N_{total}).

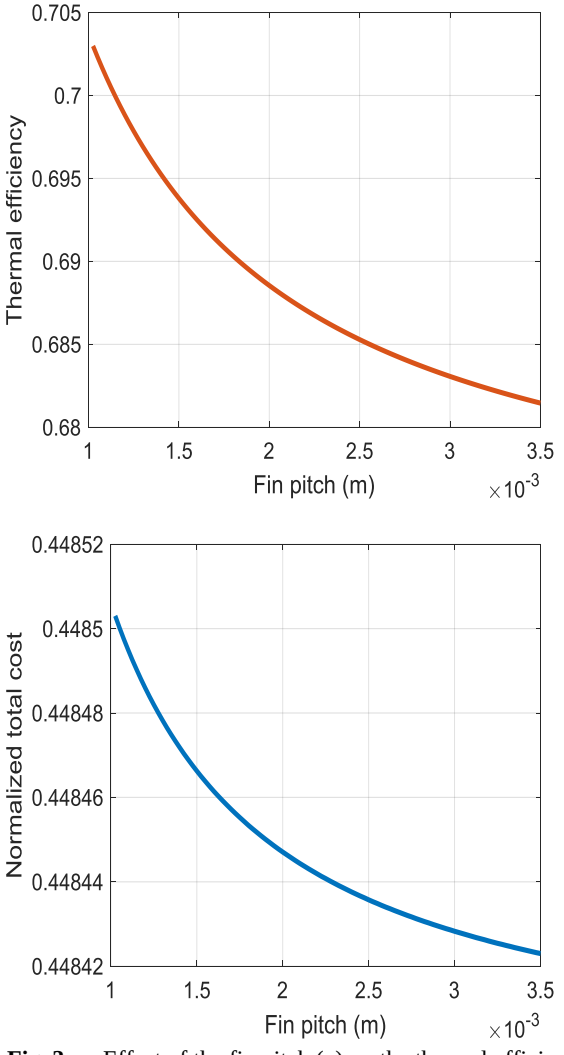

Fig. 3 Effect of the fin pitch (x) on the thermal efficiency (ϵ) and normalized total cost ($\mathbf{C_{total}^{N}}$).

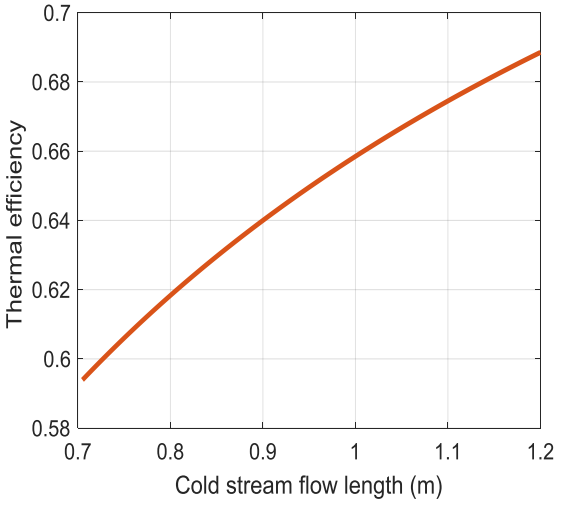

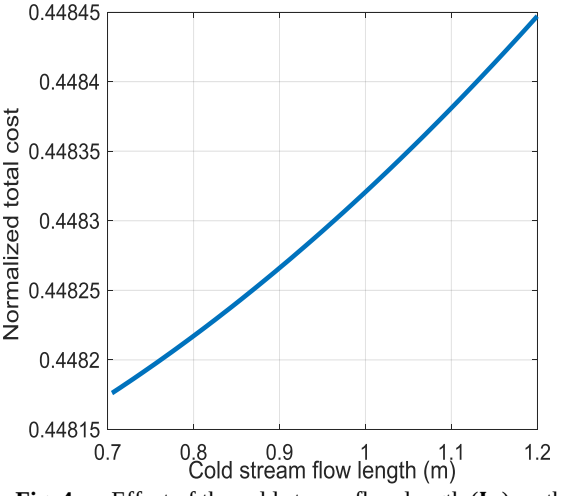

Fig. 4 Effect of the cold stream flow length ($\mathbf{L_c}$) on the thermal efficiency (ϵ).

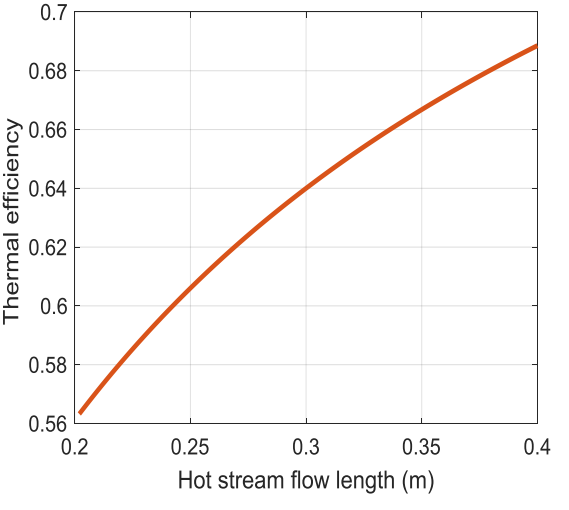

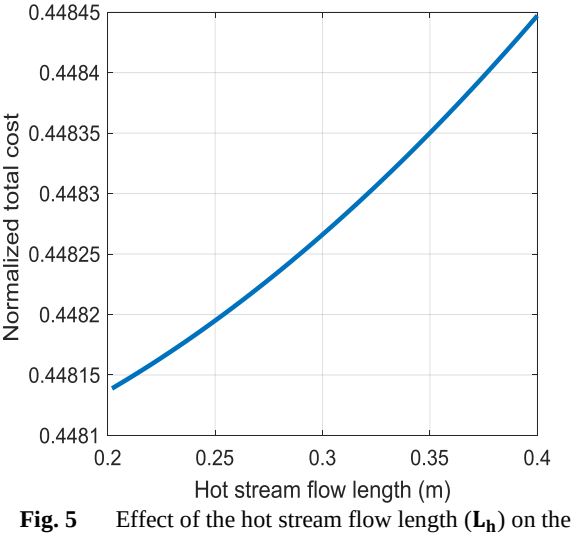

Fig. 5 Effect of the hot stream flow length ($\mathbf{L_h}$) on the thermal efficiency (ϵ).

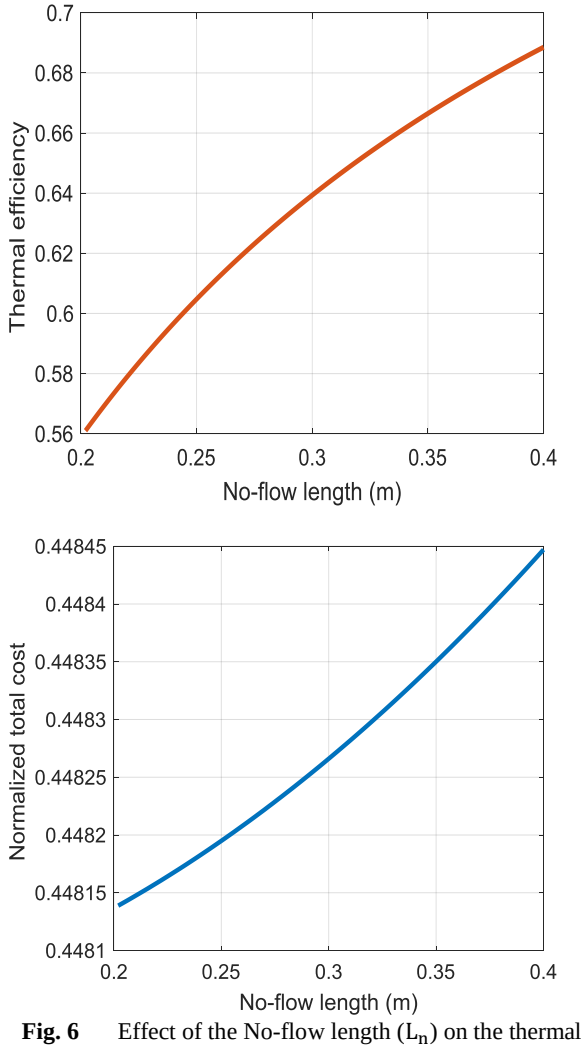

Fig. 6 Effect of the No-flow length (L_n) on the thermal efficiency (ϵ).

5 IMPERIALIST COMPETITIVE ALGORITHMS

The Imperialist Competitive Algorithm (ICA) [27-28], as a successful meta-heuristic algorithm has been widely utilized to solve different types of optimization problems in various areas of engineering and sciences such as environmental constrained energy management of microgrids [29], energy and operational management of virtual power plants [30], environmental emissions for walnut production [31], combined heat and power economic dispatch problems [32]. Like other optimization algorithms, the ICA does not need the gradient of the objective function in its operation process. The block diagram of the ICA as a mathematical model and a computer simulation of human social evolution is depicted in "Fig. 7". This algorithm starts from a set of candidate random solutions, called initial countries, in the feasible search space of the optimization problem. The cost function of the optimization problem determines the power of each country, and the best countries (the countries having the least cost function) are regarded as the imperialists that control other countries (called colonies) [27].

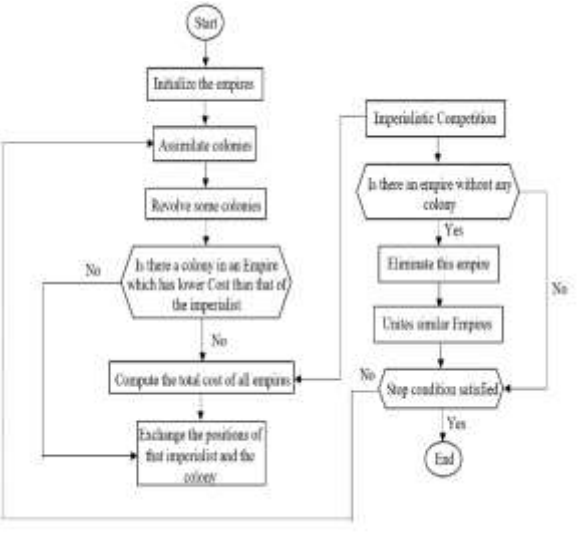

Fig. 7 Flowchart of the imperialist competitive algorithm.

Two main operators of the imperialist competitive algorithm are assimilation and revolution. The assimilation operator makes classification for the colonies in the space of socio-political characteristics. The revolution operator makes sudden random variations in the position of the selected countries in the search space. During the assimilation and revolution operations, a colony might reach a better position and has the chance to control the entire empire and replace the current imperialist of the empire [28]. Besides, in this algorithm, all the empires try to win this game and take the colonies of other empires.

Finally, in competition step, any empire has the chance to control the colonies of the weakest empire based on its power [27]. The algorithm continues via the mentioned steps (assimilation, revolution, competition) until the pre-defined stop criterion is satisfied.

In this paper, the method of the weighting coefficients is applied to solve the considered multi-objective optimization problem via the introduced single objective ICA [33]. In other words, the two objective functions are combined with each other by using weighting coefficients and to make a single cost function. The weighting coefficient of an objective function is related to its importance and the more important objective function has a greater weighting coefficient. Hence, this multi-objective optimization problem is converted into a single objective problem as follows:

$$F(x)= \sum_{i=1}^{k} w_i F_i (x) \qquad (20)$$

$$\sum_{i=1}^{k} w_i = 1 \quad (21)$$

Where, k is the number of objective functions, w_i denotes the i-th weighting coefficient, $F_i(x)$ demonstrates the i-th objective function, and F(x) represents the total objective function. In fact, $F_1(x)$ represents the thermal efficiency, whereas $F_2(x)$ signifies the normal value of the total cost. By changing the weighting coefficients, total objective function F(x) would be varied and a new point in the Pareto front would be obtained.

6 MULTI-OBJECTIVE OPTIMIZATION OF THE PLATE FIN HEAT EXCHANGER

In this section, the proposed multi-objective imperialist competitive algorithm is utilized to optimize the PFHE system modeled in the Sections 2 to 4. The numerical values of the objective function, weighting summation of the efficiency and total cost, obtained via the optimization process are depicted in "Table 2" for different values of the weighting coefficients.

Table 2 Objective functions for different values of the weighting coefficients achieved by the ICA

w_1	w_2	F
0	1	0.44803
0.1	0.9	0.54884
0.2	0.8	0.64922
0.3	0.7	0.74961
0.4	0.6	0.8500
0.5	0.5	0.95039
0.6	0.4	1.0508
0.7	0.3	1.1512
0.8	0.2	1.2516
0.9	0.1	1.3519
1	0	1.4523

The evolutionary trajectories for the optimum design of the PFHE and for various values of the weighting coefficients found by applying the imperialist competitive algorithm are illustrated in "Fig. 8".

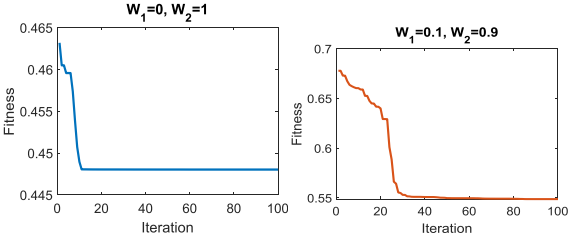

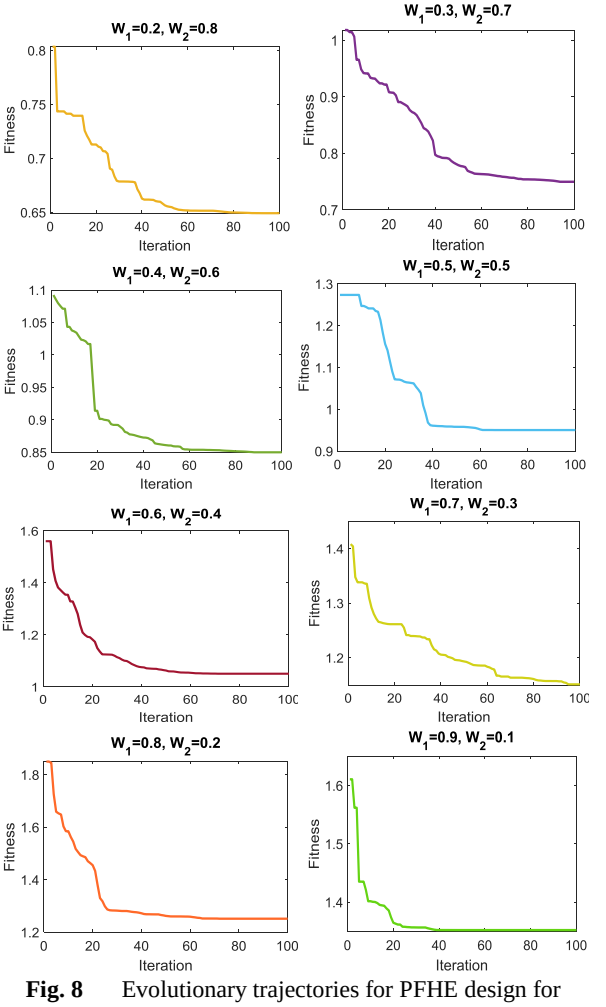

Fig. 8 Evolutionary trajectories for PFHE design for various values of the weighting coefficients found by applying the imperialist competitive algorithm

Moreover, the related Pareto front is illustrated in "Fig. 9", and the found optimum design variables (optimum point B) are represented in "Table 3".

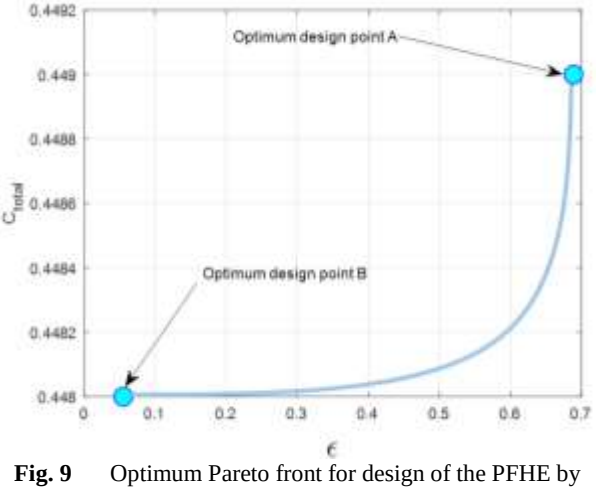

Fig. 9 Optimum Pareto front for design of the PFHE by using the empiricist competitive algorithm.

Table 3 Design parameters (decision variables) related to the optimum solution found by the ICA

Variables	Optimum value
Pitch of the fin (mm)	1.00
Height of the fin (mm)	2.116
Length of the fin (mm)	1.85
Length of the hot gas flow (m)	0.4
Length of the cold gas flow (m)	1.2
No-flow length (m)	0.4

In "Fig. 9", points A and B stand for the best efficiency and the total cost, respectively. It is clear from this chart that all optimum points could be selected by the designer to represent optimum plate heat exchangers. In fact, choosing a better value for any objective function in the Pareto front would cause a worst value for another one. In other words, the found design variables related to the non-dominated solutions are the best possible design points. This figure illustrates that if any other vector of the design variables is selected, the related point to the objective functions would be located in the top/left side of "Fig. 9". Such important design facts could not be reached without applying a multi-objective optimization process.

7 CONCLUSIONS

Appendix or nomenclature, if needed, appears before the acknowledgements. This research has investigated the Pareto optimal design of the plate heat exchangers by using the imperialist competitive algorithm. The $\varepsilon - NTU$ method has been applied for mathematically modelling the considered plate heat exchanger. The constant parameters of the model have been selected from a case study existing in Barez tire group, Kerman, Iran. The nonlinear effects of the design parameters on the efficiency and total cost have been investigated. The weighting coefficient method has been implemented to transfer the multi-objective optimization problem to a single objective one. The numerical values of the obtained results have been reported, and the related Pareto front has been displayed to provide several different choices as the non-dominated solutions for designers.

REFERENCES

[1] Xu, P., Lei, G., Xu, Y., Wen, J., Wang, S., and Li, Y., Study on Continuous Cooling Process Coupled with Ortho-Para Hydrogen Conversion in Plate-Fin Heat Exchanger Filled with Catalyst, International Journal of Hydrogen Energy, Vol. 11, No. 074, 2021, DOI: 10.1016/j.ijhydene.2021.11.074.

[2] Wen, J., Li, C., Hao, H., Zhao, X., Lei, G., Wang, S., and Li, Y., Numerical Investigation on Fin Configuration Improvement of 2 K Sub-Atmospheric Plate-Fin Heat Exchangers for The Superfluid Helium Cryogenic Systems, Applied Thermal Engineering, Vol. 196, 2021, DOI:10.1016/j.applthermaleng.2021.117290 .

[3] Kota, D., NorihiroInoue, S., Evaporation Heat Transfer and Flow Characteristics of Vertical Upward Flow in A Plate-Fin Heat Exchanger, International Journal of Refrigeration, Vol. 133, 2022, pp. 165-171, DOI: 10.1016/j.ijrefrig.2021.09.030.

[4] Haider, P., Freko, P., Acher, T., Rehfeldt, S., and Klein, H., Influence of Inlet Configuration and Distributor Geometry on The Performance of Cryogenic Plate-Fin Heat Exchangers, Applied Thermal Engineering, Vol. 195, 2021, DOI:10.1016/j.applthermaleng.2021.117197.

[5] Xu, P., We, J., Zhao, X., Hao, H, Wang, S., and Li, Y., Numerical Investigation on Serrated Fin of Sub-Atmosphere Plate-Fin Heat Exchanger Used in Superfluid Helium System, Cryogenics, Vol. 119, 2021, DOI: 10.1016/j.cryogenics.2021.103351.

[6] Lian, J., Xu, D., Chang, H., Xu, Z., Lu, X., Wang, Q., and Ma, T., Thermal and Mechanical Performance of A Hybrid Printed Circuit Heat Exchanger Used for Supercritical Carbon Dioxide Brayton Cycle, Energy Conversion and Management, Vol. 245, 2021, DOI: 10.1016/j.enconman.2021.114573.

[7] Niroomand, R., Saidi, M. H., and Hannani, S. K., A New Multiscale Modeling Framework for Investigating Thermally-Induced Flow Maldistribution in Multi-Stream Plate-Fin Heat Exchangers, International Journal of Heat and Mass Transfer, Vol. 180, 2021, DOI:10.1016/j.ijheatmasstransfer.2021.121779.

[8] Hu, H., Li, J., Experimental Investigation on Heat Transfer Characteristics of Two-Phase Flow Boiling in Offset Strip Fin Channels of Plate-Fin Heat Exchangers, Applied Thermal Engineering, Vol. 185, 2021, DOI: 10.1016/j.applthermaleng.2020.116404.

[9] Kedam, N., Dmitry, U., Evgeniy, A., Gorshkalev, V., and Alexey, A., Heat Transfer Factor J and Friction Factor F Correlations for Offset Strip Fin and Wavy Fin of Compact Plate-Fin Heat-Exchangers, Case Studies in Thermal Engineering, Vol. 28, 2021, DOI: 10.1016/j.csite.2021.101552.

[10] Haider, P., Freko, P., Acher, T., Rehfeldt, S., and Klein, H., A Transient Three-Dimensional Model for Thermo-Fluid Simulation of Cryogenic Plate-Fin Heat Exchangers, Applied Thermal Engineering, Vol. 180, 2020, DOI: 10.1016/j.applthermaleng.2020.115791.

[11] Kays, W., London, A., Compact Heat Exchangers, 3rd ed. New York: McGraw Hill, 1984.

[12] Guo, L., Qin, F., Chen, J., and Chen, Z., Lubricant Side Thermal–Hydraulic Characteristics of Steel Offset Strip Fins with Different Flow Angles, Applied Thermal Engineering, Vol. 28, 2008, pp. 907–14, DOI: 10.1016/j.applthermaleng.2007.07.005.

[13] Lihua, G., Jiangping, C., Feng, Q., and Zhijiu, C., Geometrical Optimization and Mould Wear Effect on HPD Type Steel Offset Strip Fin Performance, Energy Convers Manage, Vol. 48, 2007, pp. 2473-2480, DOI:10.1016/j.enconman.2007.04.003.

[14] Hang, P., Zhao, L., Liu, G., Optimal Design of Heat Exchanger Network Considering the Fouling Throughout the Operating Cycle, Energy, Vol. 241, 2022, DOI:10.1016/j.energy.2021.122913.

[15] Abolpour, B., Hekmatkhah, R., and Shamsoddini, R., Multi-Objective Optimum Design for Double Baffle Heat Exchangers, Thermal Science and Engineering Progress, Vol. 26, 2021, DOI: 10.1016/j.tsep.2021.101132.

[16] Wang, G., Liu, A., Dbouk, T., Wang, D., Peng, X., and Ali, A., Optimal Shape Design and Performance Investigation of Helically Coiled Tube Heat Exchanger Applying MO-SHERPA, International Journal of Heat and Mass Transfer, 2021, DOI: 10.1016/j.ijheatmasstransfer.2021.122256.

[17] Sim, J., Lee, H., and Jeong, J. H., Optimal Design of Variable-Path Heat Exchanger for Energy Efficiency Improvement of Air-Source Heat Pump System, Applied Energy, Vol. 290, 2021, DOI: 10.1016/j.apenergy.2021.116741.

[18] Pan, C., Vermaak, N., Wang, X., Romero, C., and Neti, S., A Fast Reduced Model for A Shell-And-Tube Based Latent Heat Thermal Energy Storage Heat Exchanger and Its Application for Cost Optimal Design by Nonlinear Programming, International Journal of Heat and Mass Transfer, Vol. 176, 2021, DOI:.10.1016/j.ijheatmasstransfer.2021.121479.

[19] Prakash, H., Gnanase, J., karan, N., Optimum Design of Heat Exchanging Device for Efficient Heat Absorption Using High Porosity Metal Foams, International Communications in Heat and Mass Transfer, Vol. 126, 2021, DOI:10.1016/j.icheatmasstransfer.2021.105475.

[20] Bohacek, J., Raudensky, M., Astrouski, I., and Karimi-Sibaki, E., An Optimal Design for Hollow Fiber Heat Exchanger: A Combined Numerical and Experimental Investigation, Energy, Vol. 229, 2021, DOI:10.1016/j.energy.2021.120571.

[21] Hafizan, A. M., Alwi, S. R. W., Manan, Z. A., Klemeš, J. J., and Hamid, M .K. A., Design of Optimal Heat Exchanger Network with Fluctuation Probability Using Break-Even Analysis, Energy, Vol. 212, 2020, DOI:10.1016/j.energy.2020.118583.

[22] Kumar, S., Maithani, R., and Kumar, A., Optimal Design Parameter Selection for Performance of Alumina Nano-Material Particles and Turbulence Promotors in Heat Exchanger: An AHP-TOPSIS Technique, Materialstody: Proceedings, Vol. 43, 2021, pp. 3152-3155, DOI:10.1016/j.matpr.2021.01.654.

[23] Allahyarzadeh-Bidgoli, A., Dezan, D. J., and Yanagihara, J. I., COP Optimization of Propane Pre-Cooling Cycle by Optimal Fin Design of Heat Exchangers: Efficiency and Sustainability Improvement, Journal of Cleaner Production, Vol. 271, 2020, DOI: 10.1016/j.jclepro.2020.122585.

[24] Franco, A., Giannini, N., Optimum Thermal Design of Modular Compact Heat Exchangers Structure for Heat Recovery Steam Generators, Applied Thermal Engineering, Vol. 25, 2005, pp.1293-1313, DOI: 10.1016/j.applthermaleng.2004.08.018.

[25] Smith, E. M., Advances in Thermal Design of Heat Exchangers, John Wiley and Sons, Ltd. 2005.

[26] Xie, G. N., Sunden, B., and Wang, Q. W., Optimization of Compact Heat Exchangers by A Genetic Algorithm, Applied Thermal Engineering, Vol. 28, 2008, pp. 895-906, DOI: 10.1016/j.applthermaleng.2007.07.008.

[27] Atashpaz-Gargari, E., Lucas, C., Imperialist Competitive Algorithm: An algorithm for Optimization Inspired by Imperialistic Competition, IEEE Congress on Evolutionary Computation, 2007, DOI: 10.1109/CEC.2007.4425083.

[28] Nazari-Shirkouhi, S., Eivazy, H., Ghodsi, R., Rezaie, K., and Atashpaz-Gargari, E., Solving the Integrated Product Mix-Outsourcing Problem by a Novel Meta-Heuristic Algorithm: Imperialist Competitive Algorithm, Expert Systems with Applications, Vol. 37, 2010, pp. 7615-7626, DOI: 10.1016/j.eswa.2010.04.081.

[29] Rabiee, A., Sadeghi, M., and Aghaei, J., Modified Imperialist Competitive Algorithm for Environmental Constrained Energy Management of Microgrids, Journal of Cleaner Production, Vol. 202, 2018, pp. 273-292, DOI: 10.1016/j.jclepro.2018.08.129.

[30] Kasaei, M. J., Energy and Operational Management of Virtual Power Plant Using Imperialist Competitive Algorithm, Electrical Energy System, Vol. 28, 2018, DOI: 10.1002/etep.2617.

[31] Khanali, M., Akram, A., Behzadi, J., Mostashari-Rad, F., Saber, Z., Chau, K., and Nabavi-Pelesaraei, A., Multi-Objective Optimization of Energy Use and Environmental Emissions for Walnut Production Using Imperialist Competitive Algorithm, Applied Energy, Vol. 284, 2021, DOI: 10.1016/j.apenergy.2020.116342

[32] Nourianfar, H., Abdi, H., The Application of Imperialist Competitive Algorithm to the Combined Heat and Power Economic Dispatch Problem, Energy Management and Technology, Vol. 2, 2018, 5pp. 9-69, DOI:10.22109/JEMT.2018.141453.1111.

[33] Arora, J. S., Introduction to Optimum Design, Elsevier Inc, Academic Press, 2017, ISBN 978-0-12-800806-5.

Preparation of Papers - Paper Title

Author 1*
Department of Xxxxxxx Engineering,
University of Xxxxxxxx, Country
E-mail: Jmechanic@iaumajlesi.ac.ir
*Corresponding author

Author 2
Department of Xxxxxxx Engineering,
University of Xxxxxxxx, Country
E-mail: Jmechanic@iaumajlesi.ac.ir

Received: 13 November 2011, Revised: 19 May 2012, Accepted: 23 July 2012

Abstract: These instructions give you guidelines for preparing papers for International Journal of Advanced Design and Manufacturing Technology. Use this document as a template if you are using Microsoft Word. Otherwise, use this document as an instruction set. This first paragraph is formatted in the abstract style. Abstracts are required only for regular, full-length papers. Be sure to define all symbols used in the abstract, and do not cite references in this section. Do not delete the blank line immediately above the abstract; it sets the footnote at the bottom of this column. Page margins are 2.26 cm top and 2.54 down; 1.69 cm gutter.

Keywords: About four key words or phrases in alphabetical order, separated by commas

Reference: to this paper should be made as follows: Author 1 and Author 2, ‘Paper Title’, Int J of Advanced Design and Manufacturing Technology, Vol. 2/No. 1, 2008, pp. 43–54, .

Biographical notes: T. H. Mohamadi received his PhD in Mechanical Engineering from University of IAU, Science and Research Branch, 2003. He is currently Assistant Professor at the Department of Mechanical Engineering, Majlesi University, Isfahan, Iran. His current research interest includes Rapid prototyping and Rapid Tooling. **B. M. Mansori** is Associate Professor of Mechanical engineering at the University of Majlesi, Iran. She received her PhD in Mechanical engineering from Isfahan University of Iran and a BSc in Manufacturing from the University of MIT, USA. Her current research focuses on fluid mechanics, thermodynamics and heat transfer.

NOTE AUTHORS

1 INTRODUCTION

This document is a template for Word (doc) versions. If you are reading a paper version of this document, so you can use it to prepare your manuscript. When you open template.doc, select "Page Layout" from the "View" menu in the menu bar (View | Page Layout), which allows you to see the footnotes. Then type over sections of template.doc or cut and paste from another document and then use mark up styles. The pull-down style menu is at the left of the Formatting Toolbar at the top of your Word window (for example, the style at this point in the document is "Text"). Highlight a section that you want to designate with a certain style, then select the appropriate name on the style menu. The style will adjust your fonts and line spacing. Do not change the font sizes or line spacing to squeeze more text into a limited number of pages. To insert images in Word, position the cursor at the insertion point and either use Insert | Picture | From File or copy the image to the Windows clipboard and then Edit | Paste Special | Picture (with "Float over text" unchecked). ADMT will do the final formatting of your paper.

2 PROCEDURE FOR PAPER SUBMISSION

All manuscripts are to be submitted online at MJME.ir. Select "Submit to ADMT," then click "Start New." Once you enter your e-mail address, you will receive an e-mail message containing your tracking number and password. This information will allow you to track your manuscript's status, update submission data, upload your manuscript and subsequent revisions, and communicate with the editors, through your Author Status Page, at anytime during the publication process. After entering all required submission data, you must use the "Upload Manuscript" feature of the Author Status Page to upload your submission. Remember that your document must be double spaced before you upload it. Please be sure the name of the file you upload for processing is short and simple (i.e., "msc12345.doc") with no spaces, tildes, symbols, or other unusual characters. Authors are encouraged to upload PDF and doc files. Failure to meet these requirements could result in a processing error that would require you to re-upload your manuscript. Once you have uploaded your manuscript, please inspect the file for accuracy. This step is required to complete your submission. If you experience difficulties with the upload and/or conversion of your manuscript, please submit your manuscript electronically for review as e-mail attachments. (jmechanic@iaumajlesi.ac.ir or journalmechanic@gmail.com)

3 EQUATIONS, NUMBERS, SYMBOLS, AND ABBREVIATIONS

Equations are centred and numbered consecutively, with equation numbers in parentheses flush right, as in Eq. (1). Insert a blank line on either side of the equation. First use the equation editor to create the equation. If you are using Microsoft Word, use either the Microsoft Equation Editor or the Math Type add-on (http://www.mathtype.com) for equations in your paper, use the function (Insert>Object>Create New>Microsoft Equation or Math Type Equation) to insert it into the document. Please note that "Float over text" should not be selected. To insert the equation into the document, do the following:

1. Select the "Equation" style from the pull-down formatting menu and hit "tab" once.
2. Insert the equation, hit "tab" again,
3. Enter the equation number in parentheses.

A sample equation is included here, formatted using the preceding instructions. To make your equation more compact, you can use the solid us (/) or appropriate exponents when the expression is five or fewer characters. Use parentheses to avoid ambiguities in denominators.

$$\int_0^{r_2} F(r,\varphi)\, dr\, d\varphi = [\sigma r_2 / (2\mu_0)] \cdot \int_0^{\infty} \exp(-\lambda\,|z_j - z_i\,|)\,\lambda^{-1}\, J_1(\lambda r_2)\, J_0(\lambda r_i)\, d\lambda\,. \tag{1}$$

Be sure that the symbols in your equation are defined before the equation appears, or immediately following. Italicize symbols (T might refer to temperature, but T is the unit tesla). Refer to "Eq. (1)," not "(1)" or "equation (1)" except at the beginning of a sentence: "Equation (1) is…" Equations can be labeled other than "Eq." should they represent inequalities, matrices, or boundary conditions. If what is represented is really more than one equation, the abbreviation "Eqs." can be used. Define abbreviations and acronyms the first time they are used in the main text. Very common abbreviations such as SI, ac, and dc do not have to be defined. Abbreviations that incorporate periods should not have spaces: write "P.R.," not "P. R." Delete periods between initials if the abbreviation has three or more initials; e.g., U.N. but ESA. Do not use abbreviations in the title unless they are unavoidable.

4 GENERAL GRAMMAR AND PREFERRED USAGE

Use only one space after periods or colons. Hyphenate complex modifiers: "zero-field-cooled magnetization." Avoid dangling participles, such as, "Using Eq. (1), the potential was calculated." [It is not clear who or what used

Eq. (1).] Write instead “The potential was calculated using Eq. (1),” or “Using Eq. (1), we calculated the potential.”Use a zero before decimal points: “0.25,” not “.25.” Use “cm2,” not “cc.” Indicate sample dimensions as “0.1 cm × 0.2 cm,” not “0.1 x 0.2 cm2.” The preferred abbreviation for “seconds” is “s,” not “sec.” Do not mix complete spellings and abbreviations of units: use “Wb/m2” or “webers per square meter,” not “webers/m2.” When expressing a range of values, write “7–9,” not “7~9.”A parenthetical statement at the end of a sentence is punctuated outside of the closing parenthesis (like this). (A parenthetical sentence is punctuated within parenthesis.) In American English, periods and commas are placed within quotation marks, like “this period.” Other punctuation is “outside”! Avoid contractions; for example, write “do not” instead of “don’t.” The serial comma is preferred: “A, B, and C” instead of “A, B and C.” If you wish, you may write in the first person singular or plural and use the active voice (“I observed that…” or “We observed that…” instead of “It was observed that…”). Remember to check spelling. If your native language is not English, please ask a native English-speaking colleague to proofread your paper. The word “data” is plural, not singular (i.e., “data are,” not “data is”). The subscript for the permeability of vacuum μ0 is zero, not a lowercase letter “o.” The term for residual magnetization is “remanence”; the adjective is “remanent”; do not write “remnance” or “remnant.” The word “micrometer” is preferred over “micron” when spelling out this unit of measure. A graph within a graph is an “inset,” not an “insert.” The word “alternatively” is preferred to the word “alternately” (unless you really mean something that alternates). Use the word “whereas” instead of “while” (unless you are referring to simultaneous events). Do not use the word “essentially” to mean “approximately” or “effectively.” Do not use the word “issue” as a euphemism for “problem.” When compositions are not specified, separate chemical symbols by en-dashes; for example, “NiMn” indicates the intermetallic compound Ni0.5Mn0.5 whereas “Ni–Mn” indicates an alloy of some composition NixMn1-x. Be aware of the different meanings of the homophones “affect” (usually a verb) and “effect” (usually a noun), “complement” and “compliment,” “discreet” and “discrete,” “principal” (e.g., “principal investigator”) and “principle” (e.g., “principle of measurement”). Do not confuse “imply” and “infer.”Prefixes such as “non,” “sub,” “micro,” “multi,” and “"ultra” are not independent words; they should be joined to the words they modify, usually without a hyphen. There is no period after the “et” in the abbreviation “et al.” The abbreviation “i.e.,” means “that is,” and the abbreviation “e.g.,” means “for example” (these abbreviations are not italicized).

5 UNITS

Use either SI (MKS) or CGS as primary units. (SI units are strongly encouraged.) English units may be used as secondary units (in parentheses). This applies to papers in data storage. For example, write “15 Gb/cm^2 (100 Gb/in^2).” An exception is when English units are used as identifiers in trade, such as “3½ in disk drive.” Avoid combining SI and CGS units, such as current in amperes and magnetic field in oersteds. This often leads to confusion because equations do not balance dimensionally. If you must use mixed units, clearly state the units for each quantity in an equation. The SI unit for magnetic field strength H is A/m. However, if you wish to use units of T, either refers to magnetic flux density B or magnetic field strength symbolized as μ0H. Use the center dot to separate compound units, e.g., “A·m^2.”

6 FIGURES, TABLES, AND OTHER IMAGES

Insert tables and figures within your document either scattered throughout the text or all together at the end of the file. Use the Table drop-down menu to create your tables; do not insert your figures in text boxes. Figures should have no background, borders, or outlines. In the electronic template, use the “Figure” style from the pull-down formatting menu to type caption text. You may also insert the caption by going to the Insert menu and choosing Caption. Make sure the label is “Fig.,” and type your caption text in the box provided. Captions are bold with a single tab (no hyphen or other character) between the figure number and figure description. See the Table 1 example for table style and column alignment. If you wish to centre tables that do not fill the width of the page, simply highlight and “grab” the entire table to move it into proper position.

Table 1 Transitions selected for thermometry

ν″	Frequency, cm^{-1}	FJ, cm^{-1}	Gν, cm^{-1}
0	44069.416	73.58	948.66
1	42229.348	73.41	2824.76
2	40562.179	71.37	4672.68
0	42516.527	1045.85	948.76

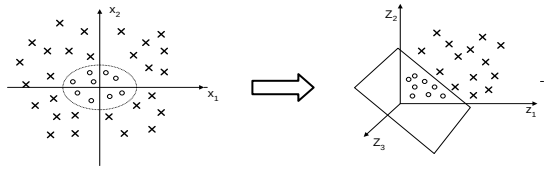

Fig. 1 Mapping nonlinear data to a higher dimensional feature space

Place figure captions below all figures. If your figure has multiple parts, include the labels "a)," "b)," etc., below and to the left of each part, above the figure caption. Please verify that the figures and tables you mention in the text actually exist. When citing a figure in the text, use the abbreviation "Fig." except at the beginning of a sentence. Do not abbreviate "Table." Number each different type of illustration (i.e., figures, tables, images) sequentially with relation to other illustrations of the same type. Figure axis labels are often a source of confusion. Use words rather than symbols wherever possible. As in the Fig. 1 example in this document, write the quantity "Magnetization" rather than just "M." Do not enclose units in parentheses, but rather separate them from the preceding text by commas. Do not label axes only with units. As in Fig. 1, for example, write "Magnetization, A/m" or "Magnetization, A · m−1," not just "A/m." Do not label axes with a ratio of quantities and units. For example, write "Temperature, K," not "Temperature/K." Multipliers can be especially confusing. Write "Magnetization, kA/m" or "Magnetization, 10^3A/m." Do not write "Magnetization (A/m) × 1000" because the reader would not then know whether the top axis label in Fig. 1 meant 16000 A/m or 0.016 A/m. Figure labels must be legible (approximately 8–12 point type).

7 CONCLUSION

Although a conclusion may review the main points of the paper, it must not replicate the abstract. A conclusion might elaborate on the importance of the work or suggest applications and extensions. Do not cite references in the conclusion as all points should have been made in the body of the paper. Note that the conclusion section is the last section of the paper to be numbered. The appendix (if present), acknowledgment, and references are listed without numbers.

8 APPENDIX OR NOMENCLATURE

Appendix or nomenclature, if needed, appears before the acknowledgements.

ACKNOWLEDGMENTS

The preferred spelling of the word "acknowledgment" in American English is without the "e" after the "g." Avoid expressions such as "One of us (S.B.A.) would like to thank…" Instead, write "F. A. Author thanks…" Sponsor and financial support acknowledgments are also to be listed in the "acknowledgments" section.

REFERENCES

Number citations consecutively in square brackets [1]. The sentence punctuation follows the brackets [2]. Multiple references [2], [3] are each numbered with separate brackets [1–3]. When citing a section in a book, please give the relevant page numbers [2]. In sentences, refer simply to the reference number, as in [3]. Do not use "Ref. [3]" or "reference [3]" except at the beginning of a sentence: "Reference [3] shows ...." Please note that the references at the end of this document are in the preferred referencing style. All references should be in 9-point font, with reference numbers inserted in superscript immediately before the corresponding reference. You are not required to indicate the type of reference; different types are shown here for illustrative purposes only.

Periodicals

[1] Vatistas, G. H., Lin, S., and Kwok, C. K., "Reverse Flow Radius in Vortex Chambers," AIAA Journal, Vol. 24, No. 11, 1986, pp. 1872- 1873.

[2] Dornheim, M. A., "Planetary Flight Surge Faces Budget Realities," Aviation Week and Space Technology, Vol. 145, No. 24, 9 Dec. 1996, pp. 44–46.

[3] Terster, W., "NASA Considers Switch to Delta 2," Space News, Vol. 8, No. 2, 13-19 Jan. 1997, pp., 1- 18.

All of the preceding information is required. The journal issue number ("No. 11" in Ref. 1) is preferred, but the month (Nov.) can be substituted if the issue number is not available. Use the complete date for daily and weekly publications. Transactions follow the same style as other journals; if punctuation is necessary, use a colon to separate the transactions title from the journal title.

Books

[4] Peyret, R., and Taylor, T. D., Computational Methods in Fluid Flow, 2nd ed., Springer-Verlag, New York, 1983, Chaps. 7, 14.

[5] Oates, G. C. (ed.), Aerothermodynamics of Gas Turbine and Rocket Propulsion, AIAA Education Series, AIAA, New York, 1984, pp. 19- 136.

[6] Volpe, R., "Techniques for Collision Prevention, Impact Stability, and Force Control by Space Manipulators," Teleoperation and Robotics in Space, edited by S. B. Skaar and C. F. Ruoff, Progress in Astronautics and Aeronautics, AIAA, Washington, DC, 1994, pp. 175–212.

Publisher, place, and date of publication are required for all books. No state or country is required for major cities: New York, London, Moscow, etc. A differentiation must always be made between Cambridge, MA, and Cambridge, England, UK. Note that series titles are in Roman type.

Proceedings

[7] Thompson, C. M., "Spacecraft Thermal Control, Design, and Operation," AIAA Guidance, Navigation, and Control Conference, CP849, Vol. 1, AIAA, Washington, DC, 1989, pp. 103–115

[8] Chi, Y., (ed.), Fluid Mechanics Proceedings, SP-255, NASA, 1993.

[9] Morris, J. D., "Convective Heat Transfer in Radially Rotating Ducts," Proceedings of the Annual Heat Transfer Conference, edited by B. Corbell, Vol. 1, Inst. of Mechanical Engineering, New York, 1992, pp. 227–234.

Reports, Theses, and Individual Papers

[10] Chapman, G. T., and Tobak, M., "Nonlinear Problems in Flight Dynamics," NASA TM-85940, 1984.

[11] Steger, J. L., Jr., Nietubicz, C. J., and Heavey, J. E., "A General Curvilinear Grid Generation Program for Projectile Configurations," U.S. Army Ballistic Research Lab., Rept. ARBRL-MR03142, Aberdeen Proving Ground, MD, Oct. 1981.

[12] Tseng, K., "Nonlinear Green's Function Method for Transonic Potential Flow," Ph.D. Dissertation, Aeronautics and Astronautics Dept., Boston Univ., Cambridge, MA, 1983.

Government agency reports do not require locations. For reports such as NASA TM-85940, neither insert nor delete dashes; leave them as provided. Place of publication should be given, although it is not mandatory, for military and company reports. Always include a city and state for universities. Papers need only the name of the sponsor; neither the sponsor's location nor the conference name and location are required. Do not confuse proceedings references with conference papers.

Electronic Publications

CD-ROM publications and regularly issued, dated electronic journals are permitted as references. Archived data sets also may be referenced as long as the material is openly accessible and the repository is committed to archiving the data indefinitely. References to electronic data available only from personal Web sites or commercial, academic, or government ones where there is no commitment to archiving the data are not permitted in the reference list.

[13] Richard, J. C., and Fralick, G. C., "Use of Drag Probe in Supersonic Flow," AIAA Meeting Papers on Disc [CD-ROM], Vol. 1, No. 2, AIAA, Reston, VA, 1996.

[14] Atkins, C. P., and Scantelbury, J. D., "The Activity Coefficient of Sodium Chloride in a Simulated Pore Solution Environment," Journal of Corrosion Science and Engineering [online journal], Vol. 1, No. 1, Paper 2, URL: http://www.cp/umist.ac.uk/JCSE/vol1/vol1.html [cited 13 April 1998].

[15] Vickers, A., "10-110 mm/hr Hypodermic Gravity Design A," Rainfall Simulation Database [online database], URL: http://www.geog.le.ac.uk/bgrg/lab.htm [cited 15 March 1998].

.

Always include the citation date for online references. Break Web site addresses after punctuation, and do not hyphenate at line breaks.

Computer Software

[16] TAPP, Thermochemical and Physical Properties, Software Package, Ver. 1.0, E. S. Microware, Hamilton, OH, 1992.

Include a version number and the company name and location of software packages.

Patents

Patents appear infrequently. Be sure to include the patent number and date.

[17] Scherrer, R., Overholster, D., and Watson, K., Lockheed Corp., Burbank, CA, U.S. Patent Application for a "Vehicle," Docket No. P-01-1532, filed 11 Feb. 1979.

Private Communications and Web Sites

References to private communications and personal Web site addresses are not permitted. Private communications can be defined as privately held unpublished letters or notes or conversations between an author and one or more individuals. Depending on the circumstances, private communications and Web site addresses may be incorporated into the main text of a manuscript or may appear in footnotes.

Unpublished Papers and Books

Unpublished works can be used as references as long as they are being considered for publication or can be located by the reader (such as papers that are part of an archival collection). If a journal paper or a book is being considered for publications choose the format that reflects the status of the work (depending upon whether it has been accepted for publication):

[18] Doe, J., "Title of Paper," Name of Journal (to be published).

[19] Doe, J., "Title of Chapter," Name of Book, edited by Publisher's name and location (to be published).

[20] Doe, J., "Title of Work," Name of Archive, Univ. (or organization) Name, City, State, Year (unpublished).

Unpublished works in an archive must include the name of the archive and the name and location of the university or other organization where the archive is held. Also include any cataloging information that may be provided. Always query for an update if a work is about to be published